
JSCSEN 77(8)983–1127(2012)

ISSN 1820-7421 (Online)

Journal of the Serbian Chemical Society



VOLUME 77

No 8

BELGRADE 2012

Available on line at



www.shd.org.rs/JSCS/

The full search of JSCS

is available through

DOAJ DIRECTORY OF
OPEN ACCESS
JOURNALS
www.doaj.org

Штампање ове свеске је субфинансирао ЛУКОИЛ Србија АД



Publication of this issue is financially co-supported by LUKOIL Srbija AD





CONTENTS

Organic Chemistry

- H. G. Kathroliya, R. G. Patel and M. P. Patel: Microwave-assisted multi-component synthesis of indol-3-yl substituted pyrano[2,3-*c*]pyrazoles and their antimicrobial activity 983

- S. Ž. Drmanić, A. D. Marinković, J. B. Nikolić and B. Ž. Jovanović: The substituent effects on the ¹³C chemical shifts of the azomethine carbon atom of *N*-(substituted phenyl)salicylaldimines 993

Biochemistry and Biotechnology

- J. Ognjenović, Z. O. Tantoush, R. Jankov, T. Ćirković Veličković and J. Vukmirica: Isolation of functional total RNA from *Tilia cordata* leaves and pollen 1003

Inorganic Chemistry

- R. K. Jain and A. P. Mishra: Microwave synthesis and spectral, thermal and antimicrobial activities of some novel transition metal complexes with tridentate Schiff base ligands 1013

Theoretical Chemistry

- I. Gutman and B. Furtula: Vertex-degree-based molecular structure descriptors of benzenoid systems and phenylenes 1031

- M. M. Ristić, M. Petković and M. Etinski: Quantum-chemical investigation of the photo-product of a reaction of two 1-methylthymine molecules: the pyrimidine(6-4)pyrimidone adduct 1037

Electrochemistry

- I. Jevremović, A. Debeljković, M. Singer, M. Achour, S. Nešić and V. Mišković-Stanković: A mixture of dicyclohexylamine and oleylamine as a corrosion inhibitor for mild steel in NaCl solution saturated with CO₂ under both continual immersion and top of the line corrosion 1047

Analytical Chemistry

- S. Stanchev, I. Pencheva, S. Konstantinov, D. Obreshkova and V. Hadjimitova: Application of UV–Vis spectrophotometric and chemiluminescent methods for the evaluation of the antioxidant action of curcumin (Short communication) 1063

Polymers

- Y. Liu, F. Zhao, C. Zhang, J. Zhang and W. Yang: Solvent-free preparation of poly(lactic acid) fibers by melt electrospinning using an umbrella-like spray head and alleviation of the problematic thermal degradation 1071

Thermodynamics

- A. B. Knežević-Stevanović, G. M. Babić, M. Lj. Kijevčanin, S. P. Šerbanović and D. K. Grozdanović: Correlation of the liquid mixture viscosities (Short communication) 1083

Materials

- D. Poleti, L.J. Karanović, M. Zdujić and Č. Jovalekić: Phase composition of Bi₂O₃ specimens doped with Ti, Zr and Hf (Note) 1091

Environmental

- M. Prica, M. Dalmacija, B. Dalmacija, J. Tričković and S. Maletić: The use of cardboard factory sludge in the remediation of zinc-contaminated sediment 1097

Geochemistry

- K. Stojanović, D. Životić, A. Šajnović, O. Cvetković, H. P. Nytoft and G. Scheeder: Drmno lignite field (Kostolac Basin, Serbia): origin and palaeoenvironmental implications from petrological and organic geochemical studies 1109

Published by the Serbian Chemical Society

Karnegijeva 4/III, 11000 Belgrade, Serbia

Printed by the Faculty of Technology and Metallurgy
Karnegijeva 4, P.O. Box 35-03, 11120 Belgrade, Serbia

Available online at www.shd.org.rs/JSCS/



Microwave-assisted multi-component synthesis of indol-3-yl substituted pyrano[2,3-*c*]pyrazoles and their antimicrobial activity

HARSHAD G. KATHROTIYA, RANJAN G. PATEL and MANISH P. PATEL*

Department of Chemistry, Sardar Patel University, Vallabh
Vidyanagar-388120, Gujarat, India

(Received 5 August, revised 19 October 2011)

Abstract: A series of pyrano[2,3-*c*]pyrazole derivatives of indole was synthesized by multi-component reactions using the conventional and microwave irradiation approach. Particularly valuable features of this method include high yield, broad substrate scope, shorter reaction times and straightforward procedure. Antimicrobial screening of the synthesized derivatives against eight human pathogens, namely *Bacillus subtilis*, *Clostridium tetani*, *Streptococcus pneumoniae*, *Salmonella typhi*, *Vibrio cholerae*, *Escherichia coli*, *Aspergillus fumigatus* and *Candida albicans*, was realized by employing the broth micro-dilution minimum inhibition concentration method, as recommended by National Committee for Clinical Laboratory Standards (NCCLS).

Keywords: indole; pyranopyrazole; multi-component reaction; microwave irradiation; antimicrobial activity.

INTRODUCTION

Indole derivatives are a topic of substantial research interest in contemporary heterocyclic and medicinal chemistry due to their great significance in the view of their *i*) occurrence in nature as a prominent sub-structure of a large number of alkaloids¹ and *ii*) wide-ranging biological activities, which include antimicrobial,² antitubercular,³ anticancer,⁴ antioxidant,⁵ antiviral,⁶ antimalarial,⁷ etc. Moreover, the 4H-pyran nucleus is a fertile source of biologically important molecules possessing a wide spectrum of pharmacological activities, such as antimicrobial,⁸ antiviral,⁹ mutagenic,¹⁰ sex pheromone,¹¹ antitumour,¹² cancer therapy¹³ and central nervous system activity.¹⁴

The conventional procedures for the synthesis of indole-based pyrano[2,3-*c*]pyrazole are not satisfactory with regards to operational simplicity, effective-

*Corresponding author. E-mail: patelmanish1069@yahoo.com
doi: 10.2298/JSC110805199K

ness and yield. An alternative synthetic approach is microwave irradiation.¹⁵ In recent years, microwave irradiation has been demonstrated not only to dramatically accelerate many organic reactions, but also to improve yield and selectivity. The optimizations of reaction strategies¹⁶ *via* three-component one-pot conventional synthesis and four-component microwave assisted synthesis were aimed at improving the yield and selectivity, and reducing the use of hazardous organic bases, such as piperidine. A literature survey revealed that a number of pyranopyrazole derivatives have been synthesized using various aldehydes⁸ but not a single report existed in which 2-phenyl-1*H*-indole-3-carbaldehyde was used.

It must be emphasized that a combination of the pyranopyrazole template with other heterocycles is a well-known approach for the build-up of drug-like molecules, which allows the achievement of new pharmacological profiles, action strengthening or toxicity lowering. As part of ongoing research aimed at the discovery of new active antimicrobial compounds,¹⁷ in this work an attempt was made to study the influence of the combination of the pyranopyrazole moiety and the 2-phenyl-1*H*-indole scaffold on antimicrobial effect of the resulting compounds. Hence, herein, the synthesis of some new derivatives of pyranopyrazole **5a–h** *via* the multi-component reaction approach under microwave irradiation is reported. The newly synthesized compounds were characterized by elemental analysis, and FT-IR, ¹H-NMR, ¹³C-NMR and mass spectrometry. All the compounds were screened for their *in vitro* antimicrobial activity against a representative panel of bacteria and fungi using the broth microdilution MIC (minimum inhibitory concentration) method.¹⁸

RESULTS AND DISCUSSION

Chemistry

The title derivatives were synthesized in two ways, *i.e.*, three-component piperidine catalyzed reaction and microwave-assisted four-component one pot reaction catalyzed by NaOH. The comparative study based on the optimization of both methods is depicted in Table I, which indicates that the reactions were efficiently promoted by microwave irradiation. The reaction time was strikingly shortened from 2–2.5 h (under traditional heating conditions) to 5–6 min (under microwave irradiation) and quantitative yields were obtained.

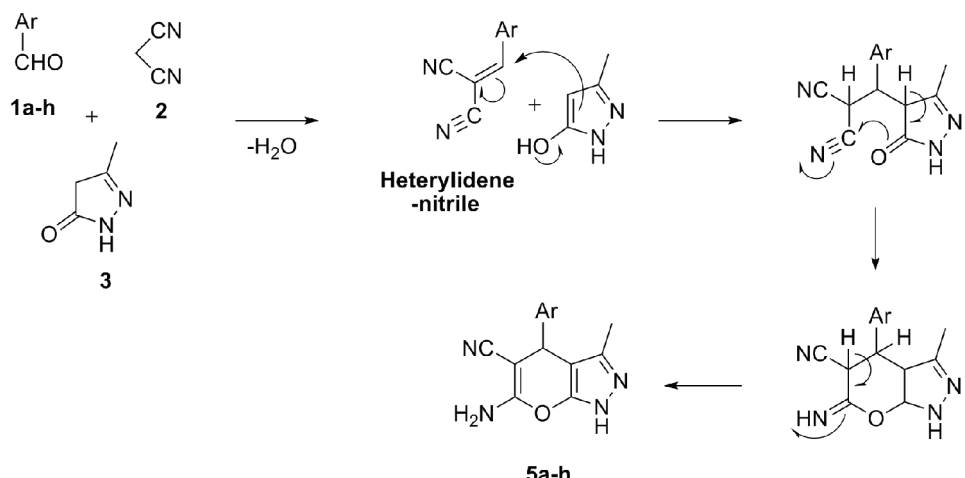
The key intermediates substituted 2-phenyl-1*H*-indole-3-carboxaldehydes **1a–h** were prepared by the Vilsmeier–Haack Reaction of 2-phenyl-1*H*-indole according to a literature procedure.¹⁹ The title compounds **5a–h** were synthesized by microwave-assisted four-component synthesis with good yields (73–84 %) (Table I).

The reaction occurred *via* initial *in situ* formation of the heterylidenenitriles (Scheme 1), containing the electron-poor C=C double bond, from the Knoevenagel condensation between 2-phenyl-1*H*-indole-3-carbaldehyde **1a–h** and malono-

nitrile **2** by loss of water molecules. Finally, Michael addition of 3-methyl-1*H*-pyrazol-5(4*H*)-one **3** to the initially formed unsaturated nitrile, *i.e.*, nucleophilic attack of the hydroxyl moiety on the cyano moiety afforded the cyclised 4*H*-pyran derivatives **5a–h**. A similar mechanism maybe operative in the four-component reaction.

TABLE I. Comparison of microwave and conventional method and physical data of the compounds **5a–h**

Compd.	R	Microwave		Conventional		M.p. / °C (after crystallization)
		Time min	Isolated yield %	Time h	Isolated yield %	
5a	H	5	74	2	65	206–208
5b	CH ₃		73		61	201–203
5c	OCH ₃		68		59	200
5d	Cl	6	79	2.5	70	214–216
5e	Br		82		73	204–206
5f	F	5	80	2	69	210
5g	NO ₂		76		67	209–211
5h	SO ₂ CH ₃		84		74	214



Ar = 2-(4-(Un)-substitutedphenyl)-1*H*-indole

Scheme 1. Plausible mechanistic pathway of the synthesis of pyranopyrazole derivatives **5a–h**.

The structures of all the newly synthesized compounds were established by ¹H-NMR, ¹³C-NMR, FT-IR and mass spectrometry, and elemental analysis. The IR spectrum of compound **5c** exhibited characteristic absorption bands at 3415 and 3320 cm⁻¹ (asym. & sym. str.) for –NH₂ and at 2195 (C≡N stretching) and 1250 cm⁻¹ (asym. str. of cyclic C–O–C ether). The ¹H-NMR spectrum of com-

pound **5c** indicated the presence of one singlet peak at δ 4.95 ppm of the –CH proton and the disappearance of a singlet at δ 10.50 ppm of –CHO, which clearly confirmed the cyclization of the Knoevenagel intermediate. The singlet at δ 6.82 ppm arose from the NH₂ protons of the pyran ring. All the aromatic protons resonated as multiplets at δ 7.03–7.60 ppm. The singlets at δ 1.54 and 11.92 ppm are due to the presence of the methyl and secondary amine of the fused pyrazole ring, respectively. The singlet peaks at δ 3.08 and δ 11.11 ppm are due to OCH₃ and the secondary amine of the indole ring, respectively. The ¹³C-NMR spectrum of compound **5c** exhibited a distinctive signal at δ 9.87 ppm for the methyl of the fused pyrazole ring and at δ 27.52 ppm for the C4 of the pyran ring. All the aromatic carbons and C≡N of **5c** showed signals at δ 111.76–155.27 ppm. Moreover, distinctive signals at δ 161.32 ppm for C6 (C–NH₂), δ 55.69 ppm for OCH₃, δ 57.23 ppm for C5 C–C≡N), δ 97.88 ppm for C3a and δ 159.51 ppm for C7a in the ¹³C-NMR spectrum confirmed the structure of **5c**. Furthermore, the structures of all the new compounds were confirmed by mass spectral studies. The mass spectra detected the expected molecular ion signals corresponding to respective molecular formula of the synthesized compounds. The mass spectrum of compound **5c** gave a molecular ion peak at 398 (M⁺+1), corresponding to the molecular formula C₂₃H₁₉N₅O₂. The elemental analysis values and the mass spectral data are in good agreement with the theoretical data.

The analytic and spectroscopic data of all the synthesized compounds are given in the Supplementary Material to this paper together with representative spectra of **5e** and **5f**, the two compounds showing outstanding and excellent antibacterial activity, respectively.

Biological evaluation

The results of the antimicrobial activity screening are presented in Table II. Examination of the data revealed that the majority of the compounds showed good antibacterial and antifungal activity when compared with ampicillin, nystatin and griseofulvin. Compound **5f** (R = F) was found to be exceedingly potent against most of the employed strains.

In particular, compound **5f** (R = F) showed outstanding activity (*MIC* 62.5 µg mL⁻¹) against the Gram-negative bacteria *Escherichia coli*, as compared to the standard ampicillin (*MIC* 100 µg mL⁻¹) and compound **5e** (R = Br) displayed excellent activity (*MIC* 125 µg mL⁻¹) against the Gram-positive bacteria *Bacillus subtilis*, as compared to the standard ampicillin (*MIC* 250 µg mL⁻¹). Compounds **5b** (R = CH₃), **5d** (R = Cl), **5f** (R = F) and **5h** (R = NO₂) against *B. subtilis* (*MIC* 200 µg mL⁻¹) and compounds **5c** (R = OCH₃), **5f** (R = F) and **5h** (R = NO₂) against *Clostridium tetani* (*MIC* 200 µg mL⁻¹) were found significantly active in comparison to ampicillin (*MIC* 250 µg mL⁻¹). Against fungal pathogen *Candida albicans*, compounds **5b** (R = CH₃) and **5f** (R = F) were found to possess better



activity (*MIC* 250 µg mL⁻¹) as compared to the standard griseofulvin (*MIC* 500 µg mL⁻¹).

TABLE II. Antimicrobial activity of the compounds **5a–h** (minimum inhibitory concentration, *MIC* / µg L⁻¹); *S.p.*, *S. pneumoniae*; *C.t.*, *C. tetani*; *B.s.*, *B. subtilis*; *S.t.*, *S. typhi*; *V.c.*, *V. cholerae*; *E.c.*, *E. coli*; *A.f.*, *A. fumigatus*; *C.a.*, *C. albicans*; “–“ represents “not tested”

Compound	Gram-positive bacteria			Gram-negative bacteria			Fungi	
	<i>B.s.</i>	<i>C.t.</i>	<i>S.p.</i>	<i>E.c.</i>	<i>S.t.</i>	<i>V.c.</i>	<i>A.f.</i>	<i>C.a.</i>
				MTCC				
	441	449	1936	443	98	3906	3008	227
5a (R = H)	250	250	200	250	200	500	1000	500
5b (R = CH ₃)	200	500	200	500	500	200	>1000	250
5c (R = OCH ₃)	250	200	250	200	200	200	>1000	>1000
5d (R = Cl)	200	500	200	500	500	250	1000	1000
5e (R = Br)	125	250	250	250	250	200	250	500
5f (R = F)	200	200	200	62.5	200	250	1000	250
5g (R = SO ₂ CH ₃)	500	250	250	250	250	250	1000	1000
5h (R = NO ₂)	200	200	200	200	250	200	1000	1000
Ampicillin	250	250	100	100	100	100	–	–
Griseofulvin	–	–	–	–	–	–	100	500
Nystatin	–	–	–	–	–	–	100	100

Compounds **5a** (R = H) and **5c** (R = OCH₃) against *B. subtilis*, and compounds **5a** (R = H), **5e** (R = Br) and **5g** (R = SO₂CH₃) against *C. tetani* were found to be equipotent to ampicillin (*MIC* 250 µg mL⁻¹). In the case of the fungal pathogen *C. albicans*, compounds **5a** (R = H) and **5e** (R = Br) were equally active to griseofulvin (*MIC* 500 µg mL⁻¹). Unfortunately, none of the synthesized compounds were found sufficiently potent to inhibit *Streptococcus pneumoniae*, *Salmonella typhi*, *Vibrio cholerae* or the fungal pathogen *Aspergillus fumigatus*.

The investigation of the structure–activity relationship of the antibacterial screening revealed that the compound with 4-fluorophenyl ring at the 2-position of the indole nucleus gave excellent results towards *E. coli*. Whereas, towards *B. subtilis*, the compounds with 4-methyl-, chloro-, bromo-, fluoro and nitro-phenyl ring substitutions were found to be highly active, while compounds with a 4-methoxy substituted and an unsubstituted phenyl ring showed equal activity to that of ampicillin. Against *C. tetani*, compounds carrying a 4-methoxy, fluoro and nitro phenyl ring were found to be more potent than ampicillin, while the compounds with 4-bromo, methylsulphonyl and unsubstituted phenyl ring and ampicillin gave equal results. Antifungal evaluation showed that 4-methyl and fluoro phenyl ring containing compounds were the most potent, while compounds with 4-bromo and unsubstituted phenyl ring displayed similar activity to griseofulvin



against fungal species *C. albicans*. Except the nitro substituted title compound, all derivatives displayed excellent antimicrobial activity.

Reviewing and comparing the activity data, it is worthy to mention that the antimicrobial activity of the target compounds depended not only on the bicyclic heteroaromatic pharmacophore, but also on the nature of the peripheral substituents.

EXPERIMENTAL

Materials, instruments and methods

Required acetophenone, phenylhydrazine, polyphosphoric acid, phosphorous oxychloride, ethyl acetoacetate and hydrazine hydrate were obtained commercially. Solvents were purified and dried before use. The microwave-assisted reactions are conducted in a "RAGA's modified electromagnetic microwave system" whereby the microwaves were generated by a magnetron at a frequency of 2450 MHz having adjustable output power levels, *i.e.*, 10 levels from 140 to 700 W and with an individual sensor for temperature control (a fibre optic was used as the individual sensor for temperature control) with the attachment of a reflux condenser under constant stirring (thus avoiding the risk of high pressure development). All melting points were taken in open capillaries and are uncorrected. Thin-layer chromatography (TLC, on aluminium plates pre-coated with silica gel, $^60\text{F}_{254}$, 0.25 mm thickness) (Merck, Darmstadt, Germany) was used for monitoring the progress of all reactions, and the purity and homogeneity of the synthesized compounds; the eluent was 5:5 hexane:ethyl acetate and UV radiation and/or iodine were used as the visualizing agents. Elemental analysis (% C, H, N) was realised using a Perkin-Elmer 2400 series-II elemental analyzer (Perkin-Elmer, USA) and the values for all compounds are within ± 0.4 % of the theoretical values. The IR spectra were recorded in KBr on a Perkin-Elmer Spectrum GX FT-IR Spectrophotometer (Perkin-Elmer, USA) and only the characteristic peaks are reported in cm^{-1} . The $^1\text{H-NMR}$ and $^{13}\text{C-NMR}$ spectra were recorded in $\text{DMSO}-d_6$ on a Bruker Avance 400F (MHz) spectrometer (Bruker Scientific Corporation Ltd., Switzerland) using the solvent peak as an internal standard at 400 and 100 MHz, respectively. Chemical shifts are reported in parts per million (ppm). Mass spectra were scanned on a Shimadzu LCMS 2010 spectrometer (Shimadzu, Tokyo, Japan).

*General procedures for the synthesis of 6-amino-4-(2-(4-(*un*-substituted phenyl)-1*H*-indol-3-yl)-3-methyl-1,4-dihydropyrano[2,3-*c*]pyrazole-5-carbonitriles 5a-h*

Method a: three-component one pot reaction. 2-Phenyl-1*H*-indole-3-carbaldehydes **1a-h** (1 mmol), malononitrile **2** (1 mmol), 3-methyl-1*H*-pyrazol-5(4*H*)-one **3** (1 mmol) and ethanol (15 mL) containing piperidine (0.1 mmol) were charged into a 100-mL round bottom flask with mechanical stirrer and condenser. The reaction mixture was slowly heated and refluxed for 2–2.5 h. After completion of the reaction (checked by TLC), the reaction mixture was cooled to room temperature and the solid that separated was filtered and washed with equimolar mixture of chloroform and methanol to obtain the pure compounds.

Method b: four-component microwave irradiation method. 2-Phenyl-1*H*-indole-3-carbaldehydes **1a-h** (1 mmol), malononitrile **2** (1 mmol), ethyl acetoacetate **4** (1 mmol), hydrazine hydrate **6** (1.1 mmol) and NaOH (5 mol %) were thoroughly mixed in ethanol (10 mL). The mixture was irradiated for 5–6 min at 280 W output power. After the completion of reaction (checked by TLC), the reaction mixture was cooled to room temperature and the solid that separated was filtered and washed with equimolar mixture of chloroform and methanol to obtain the pure compounds.



The physical data of compounds are reported in Table I.

Antimicrobial activity

All the employed glass equipment was sterilized before use. Antimicrobial activity of all the synthesized compounds was carried out by the broth microdilution method. Mueller Hinton broth was used as the nutrient medium to grow and dilute the compound suspension for the test bacteria and Sabouraud dextrose broth was used for fungal nutrition. The inoculum size for the test strain was adjusted to 10^8 CFU (colony forming unit) per milliliter by comparing the turbidity. The strains used for the activity were procured from (MTCC – Microbial Type Culture Collection) Institute of Microbial Technology, Chandigarh. Each synthesized compound was diluted to obtain a concentration of $2000\text{ }\mu\text{g mL}^{-1}$, as the stock solutions. The results were recorded in the form of primary and secondary screening. Compounds **5a–h** were screened for their antimicrobial activity against a representative panel of bacteria and fungi at concentrations of 1000, 500 and $250\text{ }\mu\text{g mL}^{-1}$ as the primary screening. DMSO was used as the vehicle to obtain the desired test concentrations of the compounds. The compounds found to be active in the primary screening were further screened in a second set of dilution at concentrations of 200, 100, 62.5 and $50\text{ }\mu\text{g mL}^{-1}$. $10\text{ }\mu\text{L}$ suspensions from each well were further inoculated and growth was noted after 24 and 48 h. The lowest concentration that allowed no visible growth (turbidity) of the micro-organisms after the spot subculture was considered as the *MIC* for each compound. In the present study, ampicillin was used as standard antibacterial drug, whereas griseofulvin and nystatin were used as standard antifungal drugs. The protocols are summarized in Table II.

CONCLUSIONS

Rapid, simple, and efficient method has been developed for the synthesis of some new indole based pyrano[2,3-*c*]pyrazole derivatives under microwave irradiation conditions in the presence of the non-hazardous base NaOH. The engaged synthetic strategy allows the construction of a relatively complicated nitrogen and oxygen carrying heterocyclic system as well as the introduction of various (hetero) aromatic substitutions into 4-position of the 4*H*-pyran system. It can be concluded from antimicrobial screening against a panel of human pathogens, that most of the synthesized 4*H*-pyran derivatives were highly active against *B. subtilis* and *C. tetani* as well as against *C. albicans* compared to the standard drugs. It is worth mentioning that minor changes in molecular structure of these compounds profoundly influenced the activity. The present study throws light on the identification of this new structural class as antimicrobials, which could be of interest for further detailed preclinical investigations.

SUPPLEMENTARY MATERIAL

Analytical and spectral data of the synthesized compound are available electronically from <http://www.shd.org.rs/JSCS/>, or from the corresponding author on request.

Acknowledgements. The authors are thankful to Department of Chemistry, Sardar Patel University for providing the $^1\text{H-NMR}$ and $^{13}\text{C-NMR}$ spectra and research facilities. Mr. H. G. Kathroliya is grateful to UGC, New Delhi for a Research Fellowship in Sciences for Meritorious Students.



ИЗВОД

СИНТЕЗА 3-ИНДОЛИЛ СУПСТИТУИСАНИХ ПИРАНО[2,3-с]ПИРАЗОЛА ПОД
ДЕЈСТВОМ МИКРОТАЛАСА И ЊИХОВА АНТИМИКРОБНА АКТИВНОСТ

HARSHAD G. KATHROTIYA, RANJAN G. PATEL и MANISH P. PATEL

Department of Chemistry, Sardar Patel University, Vallabh Vidyanagar-388120, Gujarat, India

Серија деривата пирано[2,3-с]пиразола синтетисана је конвенционалним поступцима и под дејством микроталаса. Поступак са микроталасима карактеришу висок принос, широк опсег супстрата који могу да се користе, краће реакционо време и директан поступак. Извршено је тестирање антимикробне активности синтетисаних једињења према осам патогена *Bacillus subtilis*, *Clostridium tetani*, *Streptococcus pneumoniae*, *Salmonella typhi*, *Vibrio cholerae*, *Escherichia coli*, *Aspergillus fumigatus* и *Candida albicans* поступком микроразблаживања у бујону према препоруци NCCLS.

(Примљено 5. августа, ревидирано 19. октобра 2011)

REFERENCES

1. a) M. Somei, F. Yamada, *Nat. Prod. Rep.* **30** (2003) 2016; b) S. Hibino, T. Chosi, *Nat. Prod. Rep.* **19** (2002) 148; c) S. Hibino, T. Chosi, *Nat. Prod. Rep.* **18** (2001) 66
2. a) R. K. Tiwari, D. Singh, J. Singh, V. Yadav, A. K. Pathak, R. Dabur, A. K. Chhillar, R. Singh, G. L. Sharma, R. Chandra, A. K. Verma, *Bioorg. Med. Chem. Lett.* **16** (2006) 413; b) R. A. Al-Qawasmeh, M. Huesa, V. Nedanuri, R. Peralta, J. Wright, Y. Lee, A. Young, *Bioorg. Med. Chem. Lett.* **20** (2010) 3518
3. a) S. V. Karthikeyan, S. Perumal, K. A. Shetty, P. Yogeeshwari, D. Sriram, *Bioorg. Med. Chem. Lett.* **19** (2009) 3006; b) O. Guzel, N. Karali, A. Salman, *Bioorg. Med. Chem.* **16** (2008) 8976
4. a) P. Singh, M. Kaur, P. Verma, *Bioorg. Med. Chem. Lett.* **19** (2009) 3054; b) A. S. Gergis, *Eur. J. Med. Chem.* **44** (2009) 1257; c) C. Q. Shi, Z. Q. Liu, W. Q. Lin, Y. W. Chen, *Chin. Chem. Lett.* **18** (2007) 899
5. N. V. Lakshmi, P. Thirumurgan, K. M. Noorulla, P. T. Perumal, *Bioorg. Med. Chem. Lett.* **20** (2010) 5054
6. M. Giampieri, A. Balbi, M. Mazzei, P. L. Collab, C. Ibbab, R. Loddob, *Antiviral Res.* **83** (2009) 179
7. J. L. Kgokong, P. P. Smith, G. M. Matsabisa, *Bioorg. Med. Chem.* **13** (2005) 2935
8. N. J. Thumar, M. P. Patel, *Arkivoc* (2009) 363
9. A. G. Martinez, L. J. Marco, *Bioorg. Med. Chem. Lett.* **7** (1997) 3165
10. K. Hiramoto, A. Nasuhara, K. Michiloshi, T. Kato, K. Kikugawa, *Mutat. Res.* **47** (1997) 395
11. G. Bianchi, A. Tava, *Agric. Biol. Chem.* **51** (1987) 2001
12. J. Mohr, M. A. Chirigos, F. S. Fuhrman, J. W. Pryor, *Cancer Res.* **35** (1975) 3750
13. D. R. Anderson, S. Hegde, E. Reinhard, L. Gomez, W. F. Vernier, L. Lee, S. Liu, A. Sambandam, P. A. Snider, L. Masih, *Bioorg. Med. Chem. Lett.* **15** (2005) 1587
14. F. Eiden, F. Denk, *Arch. Pharm. (Weinheim Ger.)* **324** (1991) 353
15. a) X. Jing, Q. Zhu, F. Xu, X. Ren, D. Li, C. Yan, *Synth. Commun.* **36** (2006) 2597; b) J. P. Nirmal, M. P. Patel, R. G. Patel, *Indian J. Chem.* **48B** (2009) 712; c) D. C. Mungra, M. P. Patel, R. G. Patel, *Med. Chem. Res.* **20** (2011) 782



16. a) F. M. Abdelrazek, P. Metz, O. Kataeva, A. Jaeger, S. F. El-Mahrouky, *Arch. Pharm. Chem.* **340** (2007) 543; b) G. Vasuki, K. Kumaravel, *Tetrahedron Lett.* **49** (2008) 5636; c) F. Lehmann, M. Holm, S. J. Laufer, *Comb. Chem.* **10** (2008) 364; d) S. Gogoi, C.-G. Zhao, *Tetrahedron Lett.* **50** (2009) 2252; e) S. Muramulla, C. -G. Zhao, *Tetrahedron Lett.* **52** (2011) 3905
17. a) D. C. Mungra, M. P. Patel, D. P. Rajani, R. G. Patel, *Eur. J. Med. Chem.* **46** (2011) 4192; b) J. A. Makawana, M.P. Patel, R.G. Patel, *Bioorg. Med. Chem. Lett.* **21** (2011) 6166; c) N. M. Shah, M. P. Patel, R. G. Patel, *J. Heterocycl. Chem.* (2011), doi: 10.1002/jhet.918; d) J. A. Makawana, M.P. Patel, R.G. Patel, *Med. Chem. Res.* **21** (2012) 616; e) P. M. Shah, M. P. Patel, *Med. Chem. Res.* **21** (2012) 1188; f) N. J. Thumar, M. P. Patel, *Med. Chem. Res.* **21** (2012) 1751; g) N. J. Thumar, M. P. Patel, *J. Het. Chem.* (2011), accepted; h) N. J. Thumar, M. P. Patel, *Arch. Pharm.* **344** (2011) 91; i) D. C. Mungra, M. P. Patel, R. G. Patel, *Arkivoc* **xiv** (2009) 64; j) J. A. Makawana, M.P. Patel, R.G. Patel, *Chemical Papers* **65** (2011) 700; k) N. K. Ladani, M .P. Patel, R. G. Patel, *Arkivoc* (2009) 292; l) C. B. Sangani, M. P. Patel, R. G. Patel, *Cent. Eur. J. Chem.* **9** (2011) 635
18. National Committee for Clinical Laboratory Standards (NCCLS), 940, West Valley Road, Suite 1400, Wayne, Pennsylvania 19087-1898, USA. Performance Standards for Antimicrobial Susceptibility Testing; Twelfth Informational Supplement (ISBN 1-56238-454 -6), 2002, M100-S12 (M7)
19. J. Qu, N. Kumar, M. Alamgir, D. S. Black, *Tetrahedron Lett.* **50** (2009) 5628.





SUPPLEMENTARY MATERIAL TO
Microwave-assisted multi-component synthesis of 3'-indol-3-yl substituted pyrano[2,3-*c*]pyrazoles and their antimicrobial activity

HARSHAD G. KATHROTIYA, RANJAN G. PATEL and MANISH P. PATEL*

Department of Chemistry, Sardar Patel University, Vallabh
Vidyanagar-388120, Gujarat, India

J. Serb. Chem. Soc. 77 (8) (2012) 983–991

ANALYTICAL AND SPECTRAL DATA OF THE SYNTHESIZED COMPOUNDS

6-Amino-3-methyl-4-(2-phenyl-1H-indol-3-yl)-1,4-dihydropyrano[2,3-*c*]pyrazole-5-carbonitrile (5a). Anal. Calcd. for C₂₂H₁₇N₅O (FW: 367.14): C, 71.92; H, 4.66; N 19.06 %. Found: C, 71.86; H, 4.48; N, 19.15 %; IR (KBr, cm⁻¹): 3410 and 3385, 3270 (asym. and sym. str. of –NH₂ and –NH– str.), 2210 (–C≡N str.), 1220 (asym. str. of cyclic C–O–C ether); ¹H-NMR (400 MHz, DMSO-*d*₆, δ / ppm): 1.53 (3H, *s*, CH₃), 4.99 (1H, *s*, H4), 6.82 (2H, *s*, NH₂), 6.84–8.31 (9H, *m*, Ar–H), 11.21 (1H, *s*, NH of indole ring), 11.94 (1H, *s*, NH of pyrazole ring); ¹³C-NMR (100 MHz, DMSO-*d*₆, δ / ppm): 9.85 (CH₃), 27.41 (C4), 57.38 (C5), 97.59 (pyran C5), 111.71, 112.38, 114.55, 119.21, 120.92, 121.08, 126.11, 126.35, 127.25, 130.33, 135.21, 136.05, 136.93, 156.56 (Ar–C and C≡N), 158.32 (C7a), 162.38 (C6); MS (*m/z*): 368 (M⁺⁺¹).

6-Amino-3-methyl-4-(2-(4-methylphenyl)-1H-indol-3-yl)-1,4-dihydropyrano[2,3-*c*]pyrazole-5-carbonitrile (5b). Anal. Calcd. for C₂₃H₁₉N₅O (FW: 381.16): C, 72.42; H, 5.02; N, 18.36 %. Found: C, 72.33; H, 5.11; N, 18.24 %; IR (KBr, cm⁻¹): 3395 and 3360, 3285 (asym. and sym. str. of –NH₂ and –NH– str.), 2190 (–C≡N str.), 1235 (asym. str. of cyclic C–O–C ether); ¹H-NMR (400 MHz, DMSO-*d*₆, δ / ppm): 1.52 (3H, *s*, CH₃), 2.47 (3H, *s*, CH₃), 4.91 (1H, *s*, H4), 6.85 (2H, *s*, NH₂), 6.95–8.13 (8H, *m*, Ar–H), 11.15 (1H, *s*, NH of indole ring), 11.94 (1H, *s*, NH of pyrazole ring); ¹³C-NMR (100 MHz, DMSO-*d*₆, δ / ppm): 9.96 (CH₃), 21.42 (CH₃), 27.15 (C4), 58.25 (C5), 97.46 (C3a), 112.05, 112.67, 115.28, 120.11, 120.87, 121.45, 127.05, 127.88, 128.31, 131.18, 135.33, 136.81,

*Corresponding author. E-mail: patelmanish1069@yahoo.com

137.25, 157.36 (Ar-C and C≡N), 158.92 (C7a), 161.81 (C6); MS (*m/z*): 382.1 (M⁺⁺1).

6-Amino-4-(2-(4-methoxyphenyl)-1H-indol-3-yl)-3-methyl-1,4-dihydropyrano[2,3-c]pyrazole-5-carbonitrile (5c). Anal. Calcd. for C₂₃H₁₉N₅O₂ (FW: 397.15): C, 69.51; H, 4.82; N, 17.62 %. Found: C, 69.85; H, 4.75; N, 17.59 %; IR (KBr, cm⁻¹): 3415 and 3320, 3250 (asym. and sym. str. of –NH₂ and –NH– str.), 2195 (–C≡N str.), 1250 (asym. str. of cyclic C–O–C ether); ¹H-NMR (400 MHz, DMSO-*d*₆, δ / ppm): 1.54 (3H, s, CH₃), 3.08 (3H, s, OCH₃), 4.95 (1H, s, H4), 6.82 (2H, s, NH₂), 7.03–7.60 (8H, m, Ar–H), 11.11 (1H, s, NH of indole ring), 11.92 (1H, s, NH of pyrazole ring); ¹³C-NMR (100 MHz, DMSO-*d*₆, δ / ppm): 9.87 (CH₃), 27.52 (C4), 55.69 (OCH₃), 57.31 (C5), 97.88 (C3a), 111.76, 112.49, 114.71, 119.09, 121.48, 121.72, 125.37, 125.95, 127.00, 130.54, 135.88, 135.97, 136.74, 155.27 (Ar-C and C≡N), 159.51 (C7a), 161.32 (C6); MS (*m/z*): 398 (M⁺⁺1).

6-Amino-4-(2-(4-chlorophenyl)-1H-indol-3-yl)-3-methyl-1,4-dihydropyrano[2,3-c]pyrazole-5-carbonitrile (5d). Anal. Calcd. for C₂₂H₁₆ClN₅O (FW: 401.10): C, 65.76; H, 4.61; N, 17.43 %. Found: C, 65.69; H, 4.72; N, 17.57 %; IR (KBr, cm⁻¹): 3410 and 3355, 3280 (asym. and sym. str. of –NH₂ and –NH– str.), 2200 (–C≡N str.), 1210 (asym. str. of cyclic C–O–C ether); ¹H-NMR (400 MHz, DMSO-*d*₆, δ / ppm): 1.57 (3H, s, CH₃), 5.00 (1H, s, H4), 6.88 (2H, s, NH₂), 7.05–8.11 (8H, m, Ar–H), 11.25 (1H, s, NH of indole ring), 11.96 (1H, s, NH of pyrazole ring); ¹³C-NMR (100 MHz, DMSO-*d*₆, δ / ppm): 10.03 (CH₃), 27.45 (C4), 58.38 (C5), 97.23 (C3a), 112.13, 113.21, 114.77, 119.25, 120.99, 121.37, 125.12, 125.77, 126.89, 131.22, 136.05, 136.28, 138.45, 157.31 (Ar-C and C≡N), 158.66 (C7a), 161.27 (C6); MS (*m/z*): 402.0 (M⁺⁺1).

6-Amino-4-(2-(4-bromophenyl)-1H-indol-3-yl)-3-methyl-1,4-dihydropyrano[2,3-c]pyrazole-5-carbonitrile (5e). Anal. Calcd. for C₂₂H₁₆BrN₅O (FW: 445.05): C, 59.21; H, 3.61; N, 15.69 %. Found: C, 59.44; H, 3.82; N, 15.38 %; IR (KBr, cm⁻¹): 3405 and 3360, 3285 (asym. and sym. str. of –NH₂ and –NH– str.), 2190 (–C≡N str.), 1255 (asym. str. of cyclic C–O–C ether); ¹H-NMR (400 MHz, DMSO-*d*₆, δ / ppm): 1.61 (3H, s, CH₃), 4.96 (1H, s, H4), 6.81 (2H, s, NH₂), 6.95–7.89 (8H, m, Ar–H), 11.20 (1H, s, NH of indole ring), 11.97 (1H, s, NH of pyrazole ring); ¹³C-NMR (100 MHz, DMSO-*d*₆, δ / ppm): 10.15 (CH₃), 27.50 (C4), 57.17 (C5), 97.68 (C3a), 111.88, 112.95, 114.03, 120.11, 121.12, 121.89, 125.23, 126.17, 126.93, 130.73, 135.27, 137.34, 138.36, 148.86 (Ar-C and C≡N), 156.27 (C7a), 162.09 (C6); MS (*m/z*): 445.9 (M⁺⁺1).

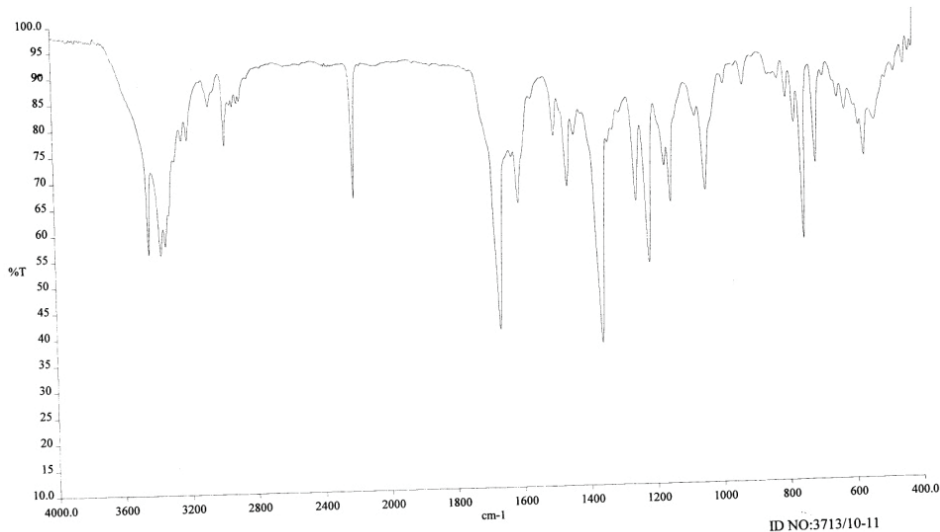
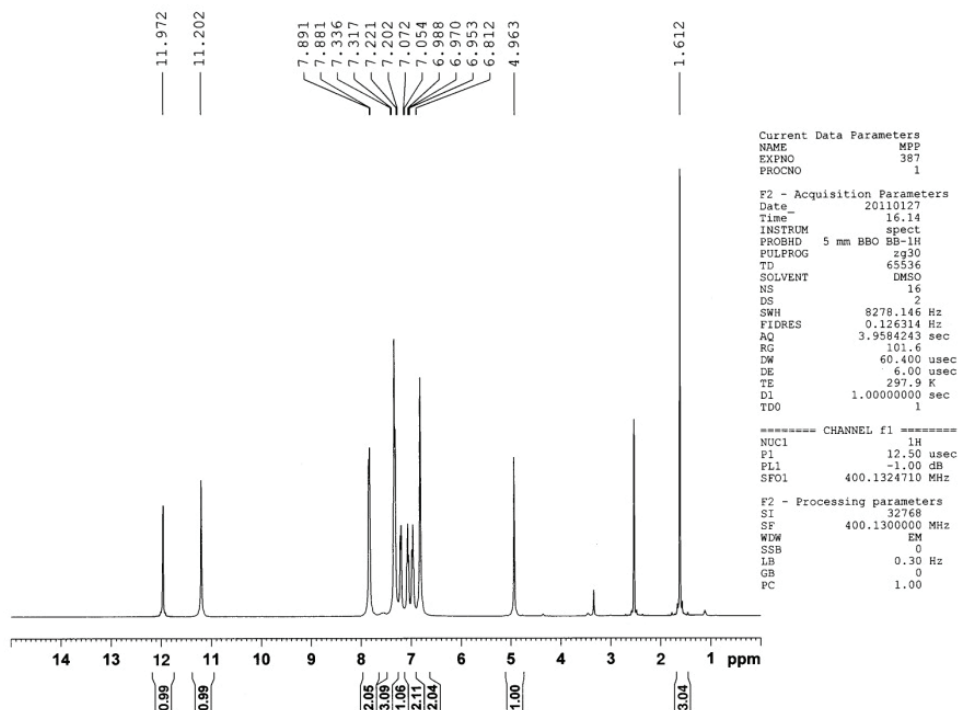
6-Amino-4-(2-(4-fluorophenyl)-1H-indol-3-yl)-3-methyl-1,4-dihydropyrano[2,3-c]pyrazole-5-carbonitrile (5f). Anal. Calcd. for C₂₂H₁₆FN₅O (FW: 385.13): C, 68.56; H, 4.18; N, 18.17 %. Found: C, 68.81; H, 4.03; N 17.98 %; IR (KBr, cm⁻¹): 3400 and 3370, 3285 (asym. and sym. str. of –NH₂ and –NH– str.), 2190 (–C≡N str.), 1255 (asym. str. of cyclic C–O–C ether); ¹H-NMR (400 MHz,

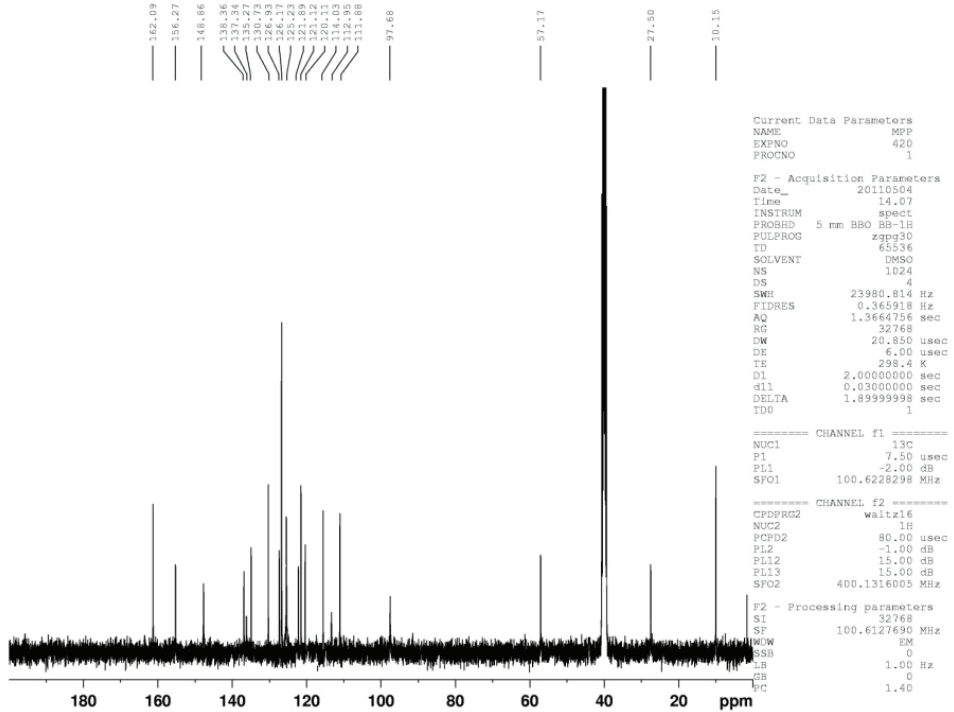


DMSO-*d*₆, δ / ppm): 1.54 (3H, *s*, CH₃), 5.01 (1H, *s*, H4), 6.79 (2H, *s*, NH₂), 6.93–8.03 (8H, *m*, Ar–H), 11.11 (1H, *s*, NH of indole ring), 11.92 (1H, *s*, NH of pyrazole ring); ¹³C-NMR (100 MHz, DMSO-*d*₆, δ / ppm): 9.91 (CH₃), 27.36 (C4), 57.49 (C5), 97.48 (C3a), 112.08, 113.25, 114.92, 116.08, 120.06, 120.86, 125.03, 126.28, 126.73, 131.25, 134.93, 136.23, 137.48, 156.49 (Ar–C and C≡N), 159.29 (C7a), 161.45 (C6); MS (*m/z*): 386.0 (M⁺+1).

6-Amino-3-methyl-4-(2-(4-(methylsulphonyl)phenyl)-1H-indol-3-yl)-1,4-dihydropyrano[2,3-c]pyrazole-5-carbonitrile (5g). Anal. Calcd. for C₂₃H₁₉N₅O₃S (FW: 445.12): C, 62.01; H, 4.30; N, 15.72 %. Found: C, 61.92; H, 4.19; N, 15.69 %; IR (KBr, cm⁻¹): 3385 and 3345, 3270 (asym. and sym. str. of –NH₂ and –NH– str.), 2195 (–C≡N str.), 1250 (asym. str. of cyclic C–O–C ether); ¹H-NMR (400 MHz, DMSO-*d*₆, δ / ppm): 1.58 (3H, *s*, CH₃), 3.35 (3H, *s*, SO₂CH₃), 5.07 (1H, *s*, H4), 6.86 (2H, *s*, NH₂), 6.91–8.09 (8H, *m*, Ar–H), 11.43 (1H, *s*, NH of indole ring), 11.97 (1H, *s*, NH of pyrazole ring); ¹³C-NMR (100 MHz, DMSO-*d*₆, δ / ppm): 10.00 (CH₃), 27.48 (C4), 44.00 (SO₂CH₃), 57.06 (C5), 97.57 (C3a), 112.19, 114.88, 119.50, 119.66, 121.55, 112.64, 126.79, 127.86, 129.77, 134.03, 136.02, 137.30, 138.00, 140.18 (Ar–C and C≡N), 155.25 (C7a), 161.29 (C6); MS (*m/z*): 446.1 (M⁺+1).

6-Amino-3-methyl-4-(2-(4-nitrophenyl)-1H-indol-3-yl)-1,4-dihydropyrano[2,3-c]pyrazole-5-carbonitrile (5h). Anal. Calcd. for C₂₂H₁₆N₆O₃ (FW: 412.13): C, 64.07; H, 3.91; N, 20.38 %. Found: C, 64.15; H, 4.22; N, 20.06 %; IR (KBr, cm⁻¹): 3395 and 3350, 3240 (asym. and sym. str. of –NH₂ and –NH– str.), 2185 (–C≡N str.), 1245 (asym. str. of cyclic C–O–C ether); ¹H-NMR (400 MHz, DMSO-*d*₆, δ / ppm): 1.55 (3H, *s*, CH₃), 4.99 (1H, *s*, H4), 6.98 (2H, *s*, NH₂), 7.11–8.15 (8H, *m*, Ar–H), 11.24 (1H, *s*, NH of indole ring), 12.01 (1H, *s*, NH of pyrazole ring); ¹³C-NMR (100 MHz, DMSO-*d*₆, δ / ppm): 9.78 (CH₃), 27.39 (C4), 57.00 (C5), 97.65 (C3a), 112.23, 114.72, 120.13, 120.54, 121.31, 123.25, 125.68, 125.99, 130.72, 135.21, 135.98, 137.53, 139.05, 149.35 (Ar–C and C≡N), 157.43 (C7a), 161.63 (C6); MS (*m/z*): 413.0 (M⁺+1).

REPRESENTATIVE SPECTRA OF COMPOUNDS **5e** AND **5f**Fig. S1. IR Spectrum of compound **5e**.Fig. S2. ¹H-NMR Spectrum of compound **5e**.

Fig. S3. ^{13}C -NMR Spectrum of compound **5e**.

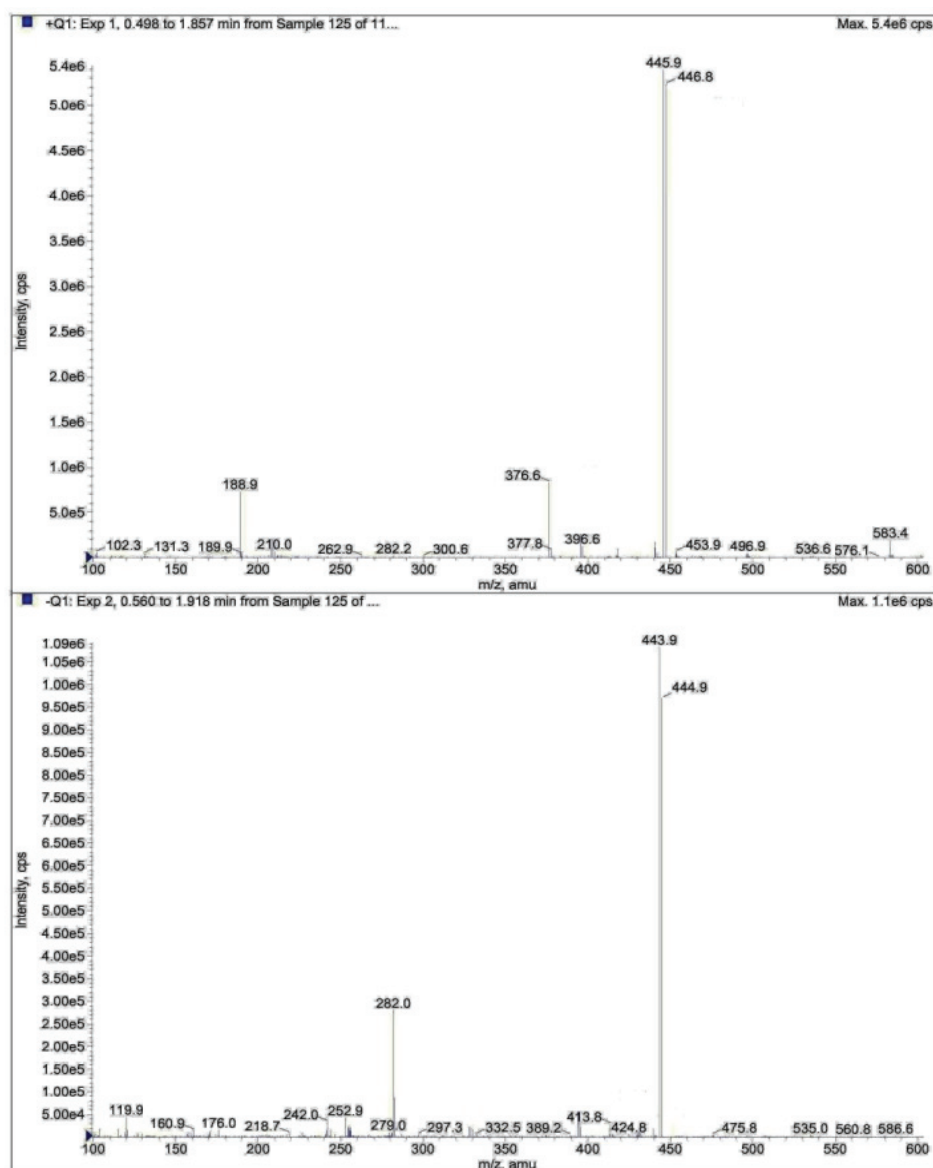
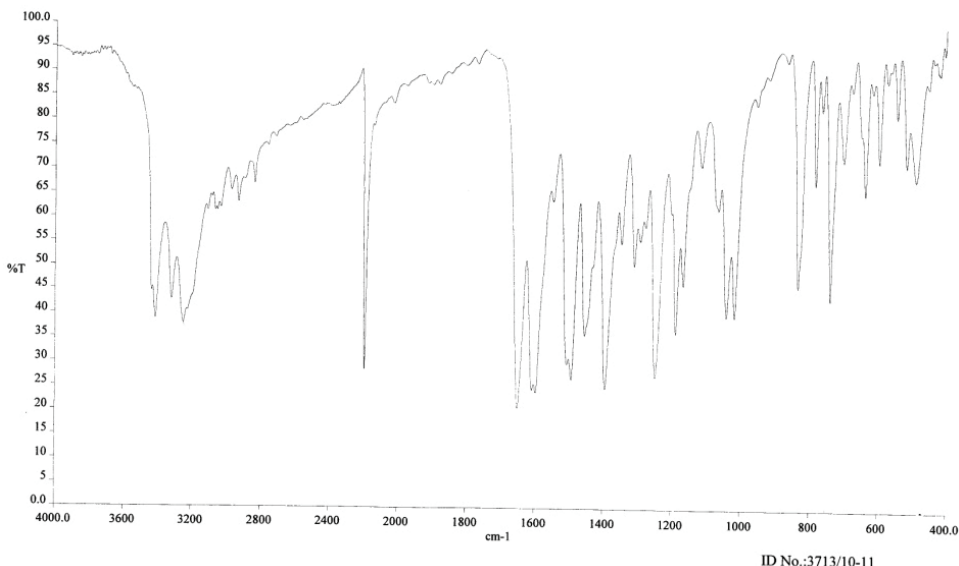
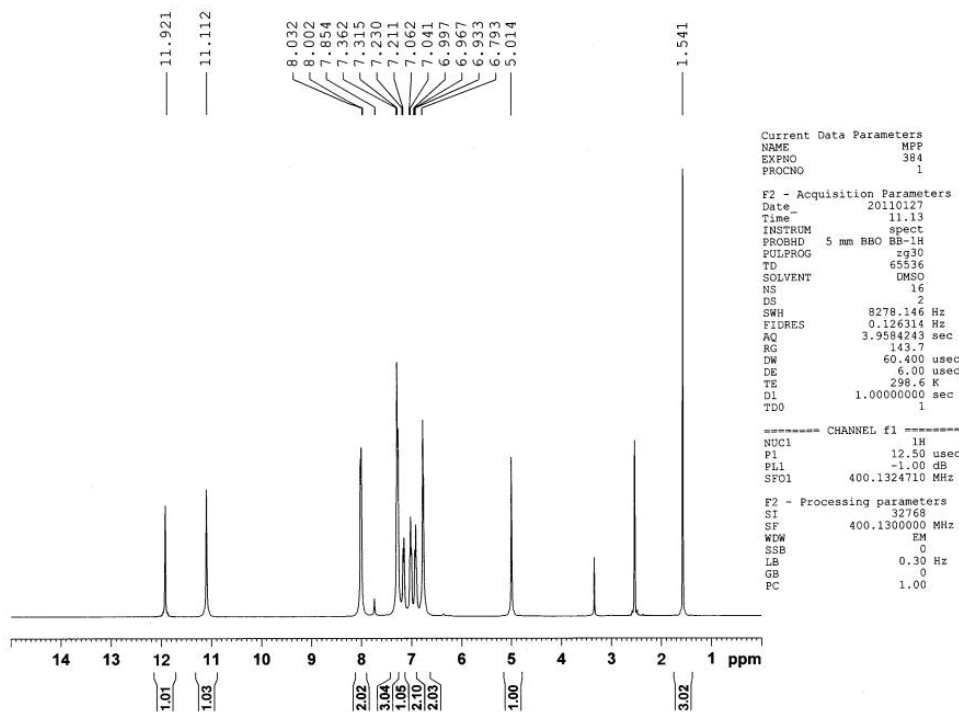
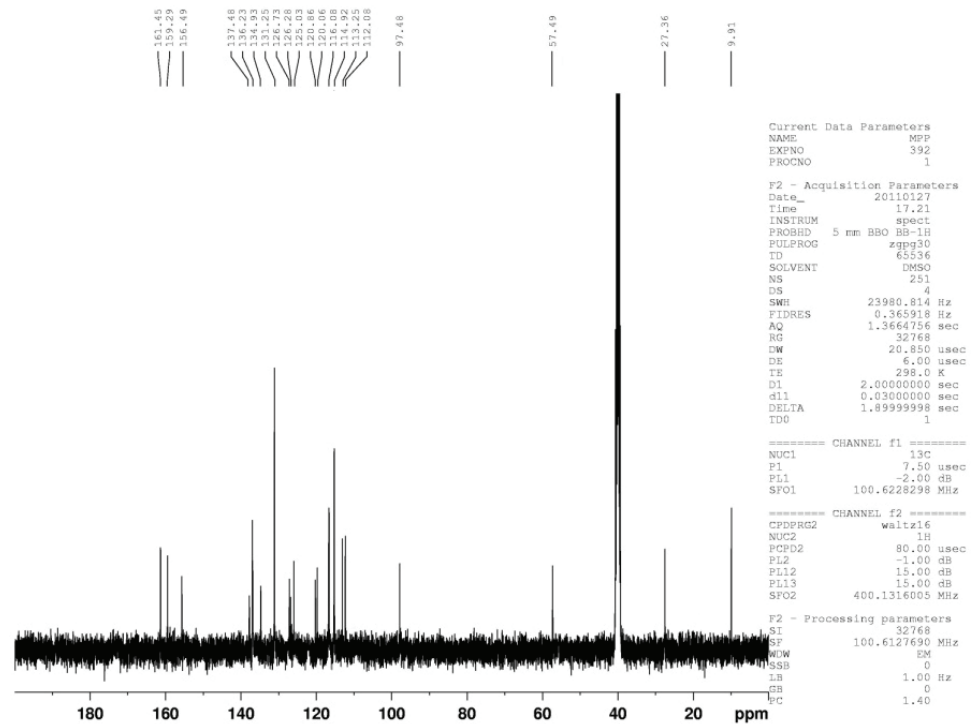


Fig. S4. Mass spectrum of compound 5e.

Fig. S5. IR Spectrum of compound **5f**.Fig. S6. ¹H-NMR Spectrum of compound **5f**.

Fig. S7. ^{13}C -NMR Spectrum of compound 5f.

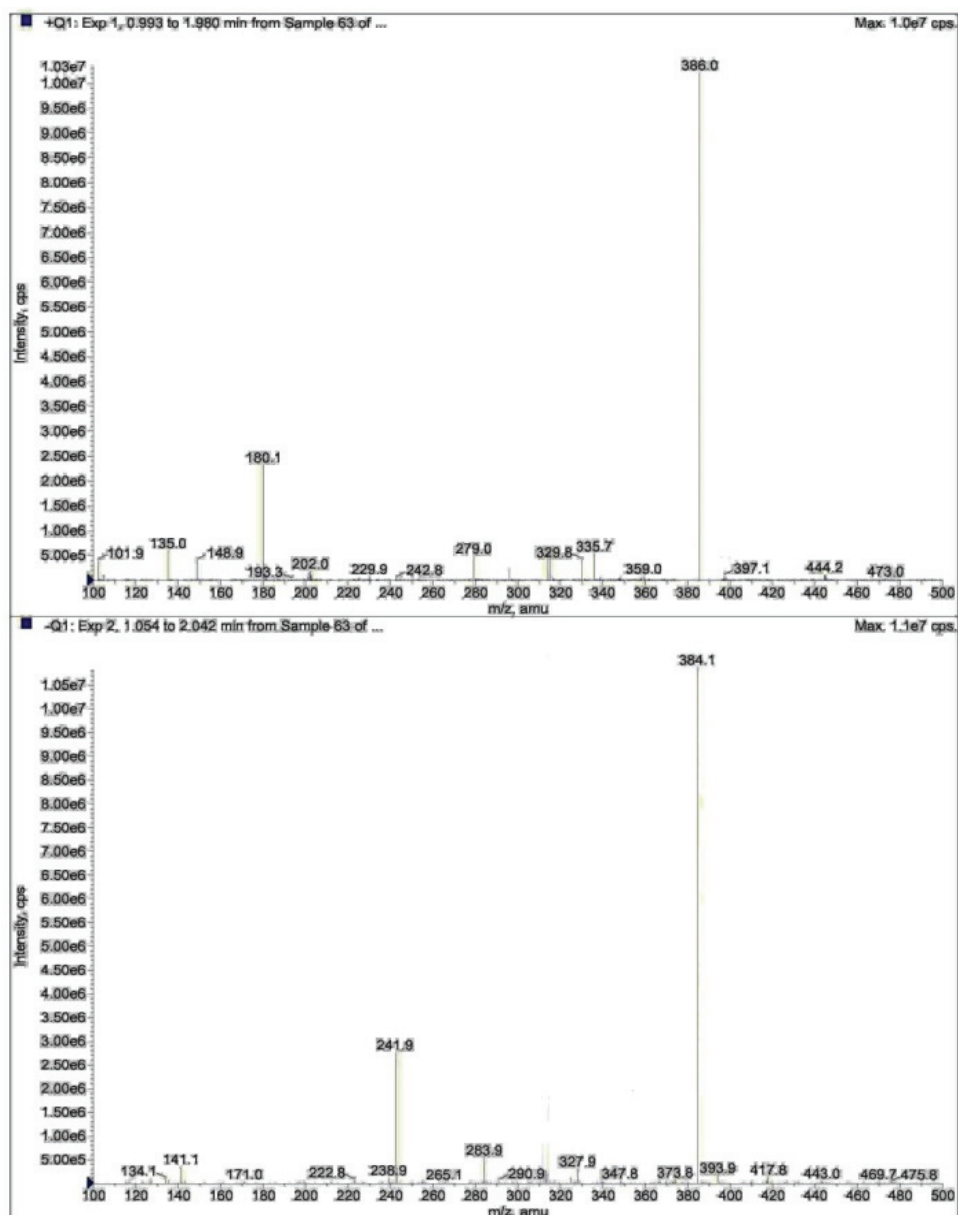


Fig. S8. Mass spectrum of compound 5f.



The substituent effects on the ^{13}C chemical shifts of the azomethine carbon atom of *N*-(substituted phenyl)salicylaldimines

SAŠA Ž. DRMANIĆ^{1**#}, ALEKSANDAR D. MARINKOVIĆ^{1#}, JASMINA B. NIKOLIĆ^{1#}
and BRATISLAV Ž. JOVANOVIĆ^{2#}

¹Department of Organic Chemistry, Faculty of Technology and Metallurgy, University of Belgrade, Kneževićevo 4, Belgrade and ²Institute of Chemistry, Technology and Metallurgy, University of Belgrade, Njegoševa 12, Belgrade, Serbia

(Received 19 March, revised 3 April 2012)

Abstract: Hammett correlations between the ^{13}C -NMR chemical shifts of the azomethine carbon atom and the corresponding substituent constants were established for thirteen Schiff bases. The successful correlation of the chemical shifts with the electrophilic substituent constants σ^+ indicate a significant resonance interaction of the substituents on the aniline ring with the azomethine carbon atom in the examined series of imines. The demand for electrons in the investigated compounds was compared to that of the *N*-benzylideneanilines and *N*-(substituted phenyl)pyridinealdimines. The manner of transmission of the substituent effects is discussed and they were separated into resonance and inductive effects. The inductive effects prevail over the resonance effects.

Keywords: ^{13}C -NMR chemical shifts; Hammett Equation; substituent constants; *N*-(substituted phenyl)salicylaldimines.

INTRODUCTION

N-(Substituted phenyl)pyridine aldimines have been in the field of interest for years.^{1,2} They are important intermediates for the synthesis of aminoalkylpyridines³ and pharmacologically active triazoles and triazolines.^{4,5} In this latter context, it has also been established that substituents both from the aniline ring and from the aryl group at the azomethine carbon can influence the yields of the triazole products.⁴

Schiff bases of salicyldehydes with anilines, aminopyridines and benzylamines were also investigated because of their photochromic and thermochromic

* Corresponding author. E-mail: drmana@tmf.bg.ac.rs

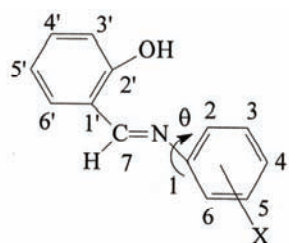
Serbian Chemical Society member.

doi: 10.2298/JSC120319033D

properties,⁶ as well as the role they play in biological systems,⁷ in addition to some other applications.⁸

Numerous previous investigations of the molecular structures of *N*-benzylideneanilines,^{9–11} showed that the substituents in the aniline ring have a significant influence on the deflection of the angle θ between the rings by their electronic and/or steric effects (the general formula is given in Fig. 1) and consequently determine the conformation of the corresponding molecules.

The general formula of the investigated *N*-(substituted phenyl)salicylaldimines is shown in Fig. 1.



X: H (1); *p*-CH₃ (2); *p*-Br (3); *p*-Cl (4); *p*-OCH₃ (5); *p*-N(CH₃)₂ (6); *p*-NO₂ (7); *p*-COCH₃ (8); 2N (9); 3N (10); 2N, 4-CH₃ (11); 3N, 5CH₃ (12); 3,5-diCl (13).

Fig 1. The general formula of *N*-(substituted phenyl)salicylaldimines.

The intention of the present investigation was to study the effects of the substituents at the aniline ring and of the 2'-hydroxyphenyl group present on the azomethine carbon (C-7) on the ¹³C-NMR chemical shifts of the azomethine carbon, as a continuation of previous studies of 2-, 3- and 4-*N*-(substituted phenyl)pyridine aldimines.^{1,2} Based on the studied effects, it was possible to draw conclusions about the conformations of the investigated molecules.

EXPERIMENTAL

The *N*-(substituted phenyl)salicylaldimines used in this study were synthesized by procedures described in the literature.^{4,5,12,13} Equimolar amounts of salicylaldehyde and substituted anilines in ethanol were heated to 60–70 °C under constant stirring for 2–3 h. The products were recrystallized from analytical grade ethanol to constant melting point. The purity of the obtained compounds was confirmed by their melting points, elemental analyses and NMR spectra, which were in agreement with literature data.^{4,5,12,13}

The ¹³C-NMR chemical shifts data of the investigated compound were obtained using a Bruker AC 250 spectrometer at 62.896 MHz. The spectra were recorded at room temperature in deuterated dimethyl sulfoxide (DMSO-*d*₆) in 5 mm tubes. The chemical shifts are expressed in ppm values referenced to the residual solvent signal at 39.5 ppm.

RESULTS AND DISCUSSION

The ¹³C-NMR chemical shifts of the azomethine carbon atom (δ_{C}) in the solvent DMSO-*d*₆ and the differences in the chemical shifts ($\Delta\delta_{\text{C}}$) together with

the corresponding σ^{14} and σ^{+15} constants for substituents in the *m*- and *p*-position of the aniline ring are given in Table I.

TABLE I. ¹³C-NMR chemical shifts of the azomethine carbon atoms of *N*-(substituted phenyl)salicylaldimines in DMSO-*d*₆ solution and the corresponding substituent constants

Substituent	X	δ_{C-7} / ppm	$\Delta\delta_{C-7}$ / ppm	σ_m or σ_p	σ_m^+ or σ_p^+
(1)	H	162.60	0.00	0.00	0.00
(2)	<i>p</i> -CH ₃	161.66	-0.94	-0.17	-0.31
(3)	<i>p</i> -Br	162.98	0.37	0.23	0.15
(4)	<i>p</i> -Cl	162.93	0.32	0.23	0.11
(5)	<i>p</i> -OCH ₃	160.43	-2.17	-0.27	-0.78
(6)	<i>p</i> -N(CH ₃) ₂	157.55	-5.05	-0.83	-1.70
(7)	<i>p</i> -NO ₂	165.35	2.75	0.78	0.79
(8)	<i>p</i> -COCH ₃	164.18	1.52	0.50	0.50
(9)	2N	164.72	2.13	0.73	0.72
(10)	3N	164.55	1.94	0.62	0.78
(11)	2N, 4CH ₃	163.71	1.11	0.56 ^a	0.41 ^a
(12)	3N, 5CH ₃	164.54	1.93	0.67 ^a	0.65 ^a
(13)	3,5-diCl	164.59	1.98	0.74 ^b	0.78 ^b

^a σ and σ^+ values were calculated as the sum of the σ or σ^+ substituent constants of a methyl group in the *m*- or *p*-position and the corresponding constant for the aza-substituent; ^b σ and σ^+ values were calculated as double values of the σ or σ^+ constants of a chlorine atom in the *m*- position.

The values of $\Delta\delta_C$ are the differences between the ¹³C-NMR chemical shifts of the substituted imines and the ¹³C-NMR chemical shift of the unsubstituted imine:

$$\Delta\delta_C = \delta_{C(\text{subst.})} - \delta_{C(\text{unsubst.})} \quad (1)$$

The general conclusion derived from the data in Table I is that all the substituents on the aniline ring of the imine influence *via* their electronic effects the value of the ¹³C-NMR chemical shifts of the azomethine carbon atom. For electron donor substituents, these were upfield shifts, while downfield shifts were registered for electron acceptor substituents.

For a quantitative assessment of the effects of substituents on the ¹³C-NMR chemical shifts, the Hammett Equation of the type:

$$\Delta\delta_C = \rho\sigma \quad (2)$$

was applied, where ρ is the reaction constant reflecting the sensitivity of the ¹³C-NMR chemical shift to the substituent effects.

Using the data from Table I, the following correlation equation for *N*-(substituted phenyl) salicylaldimines was obtained:

$$\begin{aligned} \Delta\delta_{C-7} &= (4.31 \pm 0.26)\sigma_{m/p} - 0.47 \\ (r &= 0.981; s = 0.44; n = 13) \end{aligned} \quad (3)$$



where r is the correlation coefficient, s the standard deviation and n the number of data included in the correlation.

In order to examine the influence of the electron-donor and the electron-acceptor substituents, the obtained data were separated according to their electronic effects, as shown in Eqs. (4) and (5):

For electron-donors:

$$\Delta\delta_{C-7} = (6.05 \pm 0.56)\sigma_p - 0.12 \quad (4)$$

$(r = 0.992; s = 0.35; n = 4)$

For electron-acceptors:

$$\Delta\delta_{C-7} = (3.31 \pm 0.35)\sigma_{m/p} - 0.47 \quad (5)$$

$(r = 0.961; s = 0.28; n = 10)$

From these correlations, it could be noticed that the electron-donor substituents influence the shifts of the azomethine carbon atom more than electron-acceptor substituents.

When σ^+ , the value of the electrophilic substituent constants, are used instead of σ (Eq. (3)), an even more precise correlation for *N*-(substituted phenyl)-salicylaldimines was obtained:

$$\Delta\delta_{C-7} = (2.91 \pm 0.08)\sigma_{m/p}^+ - 0.02 \quad (6)$$

$(r = 0.996; s = 0.20; n = 13)$

This correlation is presented in Fig. 2.

For electron-donor substituents, the following correlation equation was obtained:

$$\Delta\delta_{C-7} = (2.96 \pm 0.07)\sigma_p^+ + 0.02 \quad (7)$$

$(r = 0.999; s = 0.09; n = 4)$

while for electron-acceptor substituents, the following was obtained:

$$\Delta\delta_{C-7} = (2.89 \pm 0.25)\sigma_{m/p}^+ - 0.02 \quad (8)$$

$(r = 0.971; s = 0.23; n = 10)$

The better correlation coefficients obtained when the electrophilic substituent constant σ^+ was employed for both electron-acceptor and electron-donor substituents undoubtedly shows a considerable resonance interaction of the substituents on the aniline ring with the azomethine carbon atom.

Based on the obtained results and the correlation (6), it could be concluded that the electronic effect of substituents influence the ^{13}C chemical shifts of azomethine carbon atom, and that this influence depends on the position of the substituent in the aniline part of the molecule. The fact that the majority of substituted aldimine molecules are non-planar comes from the deviation of the phenyl ring from the molecular plane, which creates a special geometry of the molecule. The change of the angle between the rings (θ) is the consequence of the presence



of substituents. The electron-acceptor substituents cause an increase in the angle between the rings, while electron-donor substituents decrease this angle, tending to make the molecular structure more planar.

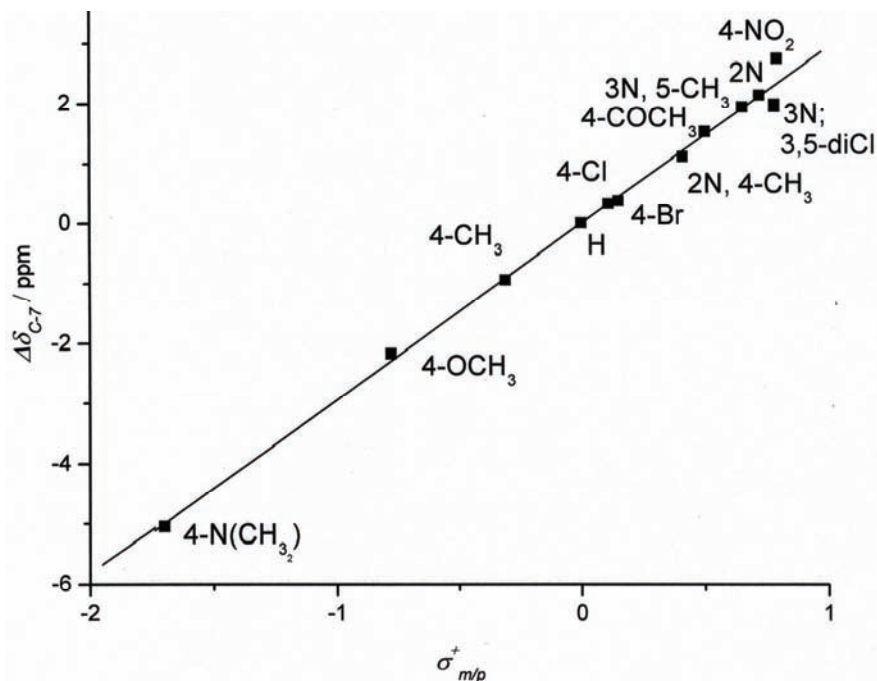


Fig. 2. $\Delta\delta_{C_7}$ as a function of the substituent constant σ^+ .

It was deemed of interest to compare the obtained values of $\rho^+ = 2.96$, Eq. (7), for *N*-(substituted phenyl)salicylaldimines with those found for 2*N*, 3*N*, and 4*N* *N*-(substituted phenyl)pyridinealdimines, $\rho^+ = 3.06$, 3.01 and 3.40, respectively, and with that for substituted *N*-benzylideneanilines,¹⁶ $\rho^+ = 2.81$ carrying the same substituents: H, *p*-CH₃, *p*-Cl, *p*-OCH₃ and *p*-N(CH₃)₂. In the case of both *N*-(substituted phenyl)salicylaldimines and the various *N*-(substituted phenyl)pyridinealdimines, there was an increased demand for the electrons of the azomethine carbon atom relative to the demand of the corresponding carbon in *N*-benzylideneanilines. Most probably, this could be attributed to the effect of the 2-hydroxyphenyl and the substituted pyridine groups bound to the azomethine carbon atom. It is evident that the electron donating effect of the substituents on the aniline ring of the azomethine carbon atom for *N*-(substituted phenyl)salicylaldimines lies between the same effect for the *N*-benzylideneanilines and the *N*-(substituted phenyl)pyridinealdimines.

In addition, it was considered very interesting to compare the values of the reaction constant ρ^+ for the series of substituted *N*-(substituted phenyl)salicylal-

dimines with those for *N*-benzylideneanilines and isomeric pyridinealdimines investigated in previous studies,^{1,2} with electron donating substituents in the *p*-position of the aniline ring (*p*-CH₃, *p*-OCH₃ and *p*-N(CH₃)₂), where these substituents probably allow a nearly planar conformation of the investigated compounds. The calculated ρ^+ values for the previously examined compounds, with the same substituents, are as follow: 2.81 for *N*-benzylideneanilines;¹ 3.36 for 4-pyridinealdimines;¹ 3.05 for 2-pyridinealdimines and 2.92 for 3-pyridinealdimines² and 2.96 for the *N*-(substituted phenyl)salicylaldimines, giving the following order for ρ^+ :



According to this comparison, it could be concluded that the inductive and resonance effects of the nitrogen atom in the pyridine ring affect the degree of resonance interaction through the molecule as a whole.

When the literature values^{1,16,17} of the ¹³C-NMR chemical shifts of *N*-benzylideneanilines (H, 160.31; *p*-CH₃, 159.45; *p*-OCH₃, 158.36; *p*-NO₂, 162.59; *p*-N(CH₃)₂, 155.52 and *p*-Cl, 160.69) are correlated with the ¹³C-NMR chemical shifts from both investigated series with the same substituents in the aniline ring, the following relationships were obtained:

$$\delta_{C-7(2OH,X)} = (1.09 \pm 0.03)\delta_{C(H,X)} - 12.51 \quad (9)$$

$(r = 0.999; s = 0.153; n = 6)$

The high correlation coefficient obtained, as well as those reported earlier for pyridinealdimines,^{1,2} proved that the mechanism of transmission of polar substituent effects to the azomethine carbon atom is the same as in the case of the substituted *N*-benzylideneanilines. This also implies that the dihedral angle for these two cases is not significantly different. However, the above intercorrelation includes both electron acceptor and electron donor substituents.

In order to separate the inductive and resonance effects of the substituents in the aniline ring and to observe their individual influence on the ¹³C-NMR chemical shifts of the azomethine carbon atom, it is useful to apply the Taft equation in the form:

$$\Delta\delta_{C-7} = \rho_I\sigma_I + \rho_R^+\sigma_R^+ \quad (10)$$

If the substituents on the aniline ring with dominantly electron-donor properties (*p*-CH₃, *p*-OCH₃ and *p*-N(CH₃)₂) are taken into consideration, using literature values¹⁸ of σ_I and σ_R^+ (substituent constants describing the inductive and the positive resonance effects, respectively) for *N*-(substituted phenyl)salicylaldimines, the following correlation is obtained:

$$\Delta\delta_{C-7} = (3.51 \pm 0.01)\sigma_I + (3.00 \pm 0.03)\sigma_R^+ - 0.03 \quad (11)$$

$(r = 0.999; s = 0.04; n = 4)$



Based on the obtained ratio ρ_R^+/ρ_I , which was $3.00/3.51=0.86$ for the *N*-(substituted phenyl)salicylaldimines, it may be concluded that the inductive effect prevails over the positive resonance effect of the substituents. However, the same approach for the *N*-(substituted phenyl)pyridine-4-aldimines, with the same substituents on the aniline ring, gives the result ρ_R^+/ρ_I of $3.35/2.98 = 1.12$,¹ meaning that the influence of the resonance effect was considerably higher for these previously examined compounds than for *N*-(substituted phenyl)salicylaldimines.

The observation that the positive resonance effect was less pronounced than the inductive one can be explained by the fact that the hydroxy group in position 2' decreases the possibility for any resonance interaction in the molecule. This is probably due to the existence of a hydrogen bond between it and the nitrogen atom (Fig. 3), which causes an increase in the demand for electrons of the azomethine carbon atom. The lone electron pair on the nitrogen is blocked by the described hydrogen bond, which prevents the transmission of the resonance effect of the substituents to the aniline ring.

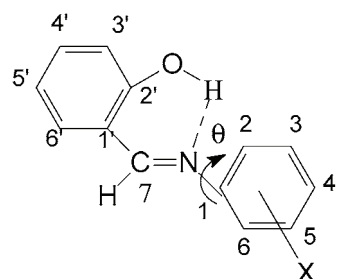


Fig. 3. Hydrogen bond between the 2'-hydroxy group and nitrogen in the molecule of *N*-(substituted phenyl)salicylaldimine.

The observation that the 2'-hydroxy group causes a decrease in the positive resonance effects, compared to pyridinealdimines, can also be explained by the deflection from planarity of the molecule, caused by repulsion between the lone electron pair of the hydroxyl oxygen and the π -electrons from the azomethine bond.

CONCLUSIONS

It has been shown that linear free energy relationships can be applied to the study of the transmission of substituent effects in *N*-(substituted phenyl)salicylaldimines using the data from ¹³C-NMR chemical shifts. It can be seen from the applied linear free energy relationships that both inductive and resonance effects influence the electron demand of the azomethine carbon.

Reliable correlations with the Hammett σ constants for *N*-(substituted phenyl)salicylaldimines, and the excellent correlation coefficients obtained with σ^+ and ρ_R^+ for predominantly electron donating substituents in the aniline ring, indicate extensive delocalization and significant resonance interactions in these

systems. Therefore, it is probably true that as long as electron-donating substituents are present in the aniline ring, there is a substantial decrease in the θ angle, so the molecule attains nearly planar conformation and the resonance interaction increases. This is in accordance with the conclusions reported in the literature that in special cases, strong electron donor substituents present in the aniline ring and strong electron acceptor substituents on the benzylidene ring can cause near-planar conformation of the corresponding molecules due to the complete delocalization through the whole molecule.^{16,17} Considering the ρ_R^+/ρ_I^- ratio, it is seen that the positive resonance effect decreases in the presence of the 2'-hydroxy group in the molecule of *N*-(substituted phenyl)salicylaldimine in comparison to the *N*-(substituted phenyl)pyridine-4-aldimine. This fact could be tentatively explained by the formation of a hydrogen bond between the 2'-hydroxy group and the nitrogen or by the repulsion of the electrons of the azomethine bond and the hydroxyl oxygen. Both factors could increase the angle (θ) between the phenyl rings, thereby decreasing the planarity of the molecule and the resonance effects of the substituents on the aniline ring on the azomethine carbon atom.

Acknowledgement. Authors are grateful to the Ministry of Education, Science and Technological Development of the Republic of Serbia for financial support (Project 172013).

ИЗВОД

ЕФЕКАТ СУПСТИТУЕНАТА НА ^{13}C ХЕМИЈСКА ПОМЕРАЊА АЗОМЕТИНСКОГ УГЉЕНИКА *N*-(СУПСТИТУИСАНИ ФЕНИЛ)САЛИЦИЛАДИМИНА

САША Ј. ДРМАНИЋ¹, АЛЕКСАНДАР Д. МАРИНОВИЋ¹, ЈАСМИНА Б. НИКОЛИЋ¹
и БРАТИСЛАВ Ж. ЈОВАНОВИЋ²

¹Каљегра за органску хемију, Технолошко-металуршки факултет, Универзитет у Београду,
Карнејева 4, Београд и ²Институт за хемију, технологију и металургију,
Универзитет у Београду, Његошева 12, Београд

^{13}C -NMR хемијска померања 13 Шифових база корелисана су са константама супституената коришћењем Хаметове једначине. Добра корелација хемијских померања азометинског угљеника са електрофилним константама супституената (σ^+) показује да постоји изражена резонантна интеракција супституената на анилинском прстену са азометинским угљеником. Испитиван је пренос електронских ефеката супституената и они су раздвојени на индуктивне и резонантне ефекте, а показано је да преовлађују индуктивни ефекти.

(Примљено 13. марта, ревидирано 3. априла 2012)

REFERENCES

1. B. Ž. Jovanović, M. Mišić-Vuković, A. D. Marinković, V. Vajs, *J. Mol. Struct.* **482** (1999) 375
2. B. Ž. Jovanović, M. Mišić-Vuković, A. D. Marinković, V. Vajs, *J. Mol. Struct.* **642** (2002) 113
3. J. E. Robertson, H. J. Biel, T. F. Mitchell, *J. Med. Chem.* **6** (1963) 805
4. P. K. Kabada, *J. Heterocycl. Chem.* **12** (1975) 143



5. P. K. Kabada, *J. Med. Chem.* **31** (1998) 196
6. E. Hadjoudis, M. Vittorakis, I. Moustakali-Mavridis, *Tetrahedron* **43** (1987) 1345
7. R. J. Johnson, C. M. Metzler, *J. Am. Chem. Soc.* **102** (1980) 6075
8. B. L. Feringa, W. F. Jager, B. de Lange, *Tetrahedron* **49** (1993) 8267
9. R. Akaba, K. Tokumaru, T. Kobayashi, *Bull. Chem. Soc. Jpn.* **53** (1980) 1993
10. R. Akaba, K. Tokumaru, T. Kobayashi, C. Utsunomiya, *Bull. Chem. Soc. Jpn.* **53** (1980) 2002
11. P. Skrabal, J. Steiger, H. Zollinger, *Helv. Chim. Acta* **58** (1975) 800
12. C. T. Bahner, R. Neely, *J. Org. Chem.* **22** (1957) 1109
13. G. E. Matsubayashi, M. Okunaka, T. Tanaka, *J. Organomet. Chem.* **56** (1973) 215
14. D. H. McDaniel, H. C. Brown, *J. Org. Chem.* **23** (1958) 420
15. H. C. Brown, Y. Okamoto, *J. Am. Chem. Soc.* **80** (1958) 4979
16. A. Kawasaki, *J. Chem. Soc., Perkin Trans 2* (1990) 223
17. R. Akaba, H. Sakuragi, K. Tokumaru, *Bull. Chem. Soc. Jpn.* **58** (1985) 1186
18. S. Ehrenson, R. T. C. Brownlee, R. W. Taft, *Prog. Phys. Org. Chem.* **10** (1973) 13.



Isolation of functional total RNA from *Tilia cordata* leaves and pollen

JANA OGNJENOVIC^{1*}, ZIYAD OMAR TANTOUSH¹, RATKO JANKOV^{1#},
TANJA ĆIRKOVIĆ VELIČKOVIC^{1#} and JELENA VUKMIRICA²

¹Faculty of Chemistry, University of Belgrade, Studentski trg 16, P. O. Box 158,
11001 Belgrade, Serbia and ²Faculty of Medicine, University of
Ottawa, 451 Smyth Rd., Ottawa, Ontario, Canada

(Received 30 November 2011, revised 23 February 2012)

Abstract: The conditions required for the isolation of high quality total RNA from European linden (*Tilia cordata*) leaves and pollen were determined. Pure total RNA was isolated from linden leaves utilizing a Qiagen plant mini kit, while the total RNA isolated from linden pollen using this method was degraded. Successful isolation of total RNA from both linden pollen and leaves, however, was achieved following TRIzol™ preparation of the total RNA. The total RNA isolated using TRIzol™ was contaminated with genomic DNA but treatment with the enzyme DNase, in solution or on-column, efficiently removed the genomic DNA. Furthermore, the conditions for the elimination of genomic DNA contamination on-column and isolation of pure total RNA from leaves were optimized. The isolated total RNA from both leaves and pollen was used successfully in first- and second-strand cDNA synthesis reactions and in a reverse transcription polymerase chain reaction (RT-PCR), demonstrating that the total RNA isolated using this method was functional. In conclusion, pure and functional total RNA from *T. cordata* leaves and pollen ($27.8 \pm 7.9 \mu\text{g g}^{-1}$ leaves; $25.7 \pm 1.1 \mu\text{g g}^{-1}$ pollen) could be obtained and was suitable for application in further molecular biology studies.

Keywords: *Tilia cordata*; leaves; pollen; total RNA; RT-PCR; cDNA.

INTRODUCTION

The European species of linden, *Tilia cordata*, is the most common species of *Tilia*.¹ The outer layer of the linden pollen grain is composed of a complex polymer of carotenoids and carotenoid esters, which are quite resistant to chemical and biological decay. In addition to carotenoids, linden pollen also contains proteins, nucleic acids, carbohydrates and lipids, making it a complex biochemical

* Corresponding author. E-mail: jognjenovic@chem.bg.ac.rs

Serbian Chemical Society member.

doi: 10.2298/JSC111130018O

source.² The European linden pollen is highly allergenic.^{3,4} Seasonal exposure to allergens in linden pollen can cause asthma, allergic rhinitis and allergic conjunctivitis.^{3–5} A study assessing the aeroallergen sensitization in an allergic population in Portugal found that linden tree is one of the most representative aero-allergens.⁶ Contact dermatitis due to *T. cordata* has also been documented.^{7,8}

Hitherto, very little biochemical research has been realized on the molecular properties of *T. cordata* leaves and pollen. Genetic analysis revealed that *T. cordata* has a disomic inheritance despite being an allopolyploid.⁹ Regarding protein analysis of *T. cordata*, a putative 50 kDa allergen was isolated from linden pollen but has not yet been fully characterized.⁵ An attempt was made to isolate RNA from *T. cordata* leaf and flower.¹⁰

To utilize molecular biology techniques in order to prepare a complementary DNA library from *T. cordata* genes, it is necessary to obtain a large quantity of pure and functional total RNA. In the present paper, a method for the total isolation of pure and functional RNA from *T. cordata* leaves and pollen is reported. Furthermore, the optimized conditions for the isolation of functional total RNA from both leaves and pollen of *T. cordata* are described.

EXPERIMENTAL

Chemicals. The RNeasy plant mini kit was from Qiagen (Hilden, Germany). TRIzol™ was from Invitrogen (Carlsbad, CA, USA). The enzymes DNase, DNA polymerase I and RNase H were from Qiagen, Stratagene (La Jolla, CA, USA), and Invitrogen, respectively. The RNA marker was from Sigma (St. Louis, MO, USA). The molecular biology reagents were supplied by Fermentas (Burlington, Canada), Invitrogen, or Qiagen. All other chemicals were from Sigma. *T. cordata* leaves were collected and stored at –80 °C, while the linden pollen was a generous gift from the Torlak Institute of Virology, Vaccines and Sera, Belgrade, Serbia.

Isolation of total RNA. For the total RNA isolation using the Qiagen RNeasy plant mini kit, up to 100 mg linden leaves or pollen were ground in liquid nitrogen, lysed, homogenized and applied onto spin columns according to the Qiagen protocol. The spin columns were eluted using 40 µl RNase-free water. For total RNA isolation using TRIzol™, from 300 mg up to 1 g linden leaves or pollen were used as the starting material and isolation was performed following the manufacturer's instructions. The obtained RNA pellet was resuspended in 150 or 200 µl RNase-free water per 300 mg leaves or pollen, respectively, and stored at –80 °C.

For DNase treatment in solution, 50 µl TRIzol™-prepared total RNAs were incubated with 2.5 µl of the stock solution (10 U µl^{–1}) of DNase for 15 min at room temperature followed by application onto a Qiagen spin column. For on-column DNase treatment, various amounts of isolated total RNA were applied onto Qiagen spin-columns and 10 µl of the stock solution of the DNase enzyme were added directly onto the column and incubated at room temperature for 15 min. Following on-column DNase treatment, the spin columns were washed and the total RNA eluted according to the Qiagen protocol.

The profile of total RNA was determined by agarose–formaldehyde denaturing electrophoresis.¹⁰

RNA purity, concentration and yield quantification. Concentration and purity of RNA were determined by measuring the absorbance at 260 nm (A_{260} nm) and the ratio between the



absorbance values at 260 nm and 280 nm (A_{260}/A_{280}), respectively. To determine the concentration of RNA, the following formula was used: $A_{260} \times 44 \mu\text{g mL}^{-1} \times \text{dilution factor}^{11}$

Total RNA isolated from linden leaves and pollen using TRIzol™ was used for first- and second-strand cDNA synthesis following the manufacturer's protocol (Stratagene).

Reverse transcription polymerase chain reaction (RT-PCR). Following first-strand cDNA synthesis reaction using total RNA isolated from leaves or pollen as the template, RNase H digestion was performed by incubating at 37 °C for 20 min. The PCRs were set up as follows: 5 µl RNase H-digested single stranded cDNA, 5 µl 10×PCR buffer, 4 µl 25 mM MgCl₂, 1 µl 10 mM dNTP mix, 1 µl (10 µM) of each primer (forward and reverse), 4U recombinant *Pfu* polymerase, and water up to 50 µl. After initial incubation at 95 °C for 2 min, 35 cycles of PCR amplification were performed with the following cycling parameters: 95 °C (30 s), 55 °C (1 min), 72 °C (2 min). A final extension at 72 °C for 5 min was performed. In order to amplify a fragment of the actin gene in *T. cordata*, the following actin primer sequences were used according to van den Berg *et al.*¹² actin primer (forward): 5'-ACCGAAGCCCCT-CTTAACCC-3' and actin primer (reverse): 5'-GTATGGCTGACACCATCAC-3'. Following RT-PCR, aliquots of the samples were migrated by 2 % agarose gel electrophoresis.

RESULTS AND DISCUSSION

Hitherto, only one article has been published describing an attempt to isolate total RNA from various plant sources, including the leaves and flower of *T. cordata*.¹³ In that study, the authors did not specify the yield of total RNA obtained. Furthermore, an $A_{260}/280$ of 1.1 was reported for the total RNA isolated from leaves and flower, which is a value much lower than that expected for pure RNA (usually an $A_{260}/280$ in the range of 1.9 to 2.1), suggesting that the RNA isolated was impure.

In the present study, total RNA was initially isolated from the leaves of *T. cordata* using a Qiagen RNeasy plant mini kit. Agarose-formaldehyde gel electrophoresis showed distinct RNA bands, indicating that RNA molecules of various sizes had been isolated and that no RNA degradation had occurred (Fig. 1A). Total leaf RNA was isolated and eluted from the Qiagen spin-column using 50 mg of the starting material; however, a higher yield of total RNA was obtained using 100 mg of the starting material (Fig. 1A). Furthermore, an increased yield of total RNA was observed when the leaf lysates were incubated at 65 °C instead of 56 °C (Fig. 1A). As recommended in the protocol for Qiagen RNeasy plant mini kit, re-elution of the spin-column increased slightly the yield of isolated total RNA (data not shown). On the other hand, agarose-formaldehyde gel electrophoresis for the total RNA isolated from *T. cordata* pollen indicated RNA degradation (Fig. 1B). Even under conditions which seemed to improve the yield of total RNA isolation from leaves, using a higher amount of starting material (100 mg) or increasing the temperature during lysis of the sample (65 °C), the total RNA isolated from pollen was completely degraded (Fig. 1B).



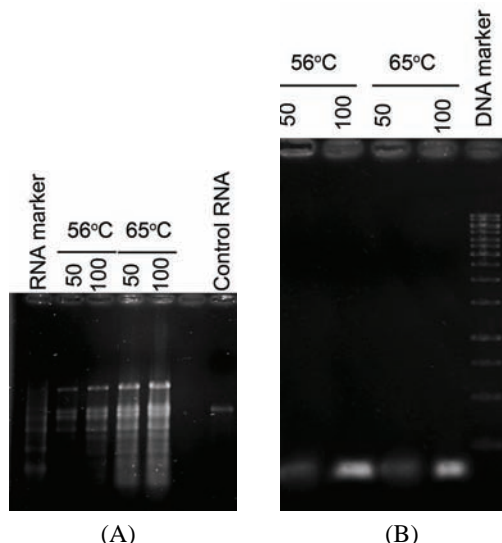


Fig. 1. Electrophoretic profile after isolation of total RNA from linden leaves and pollen using Qiagen plant mini kit. Total RNA from 50 or 100 mg of *T. cordata* leaves or pollen was purified with a Qiagen plant mini kit. The RNA samples were analyzed by 1.2 % formaldehyde–agarose electrophoresis and ethidium bromide staining. RNA marker, RNA control (1.6 kb), and/or DNA marker were run as size standards. *T. cordata* leaves (A) or pollen (B) were ground in liquid nitrogen and lysates were incubated at 56 or 65 °C for 5 min prior to homogenization and application onto Qiagen spin columns.

Subsequently, total RNA isolation using the commercial reagent TRIzol™ followed by chloroform extraction and 2-propanol precipitation was attempted. Using this method, total RNA was isolated from both linden leaves and pollen (Fig. 2) However, the total RNA obtained using this method was contaminated with genomic DNA. In order to eliminate the genomic DNA, DNase treatment was performed in solution or on-column, and total RNA was eluted after Qiagen RNA column clean-up. DNase treatment, both in solution and on-column, was effective in removing the genomic DNA, whereby the total RNA isolated from either leaves or pollen remained intact (Fig. 2).

The yields of total RNA isolated from leaves and pollen after DNase treatment to remove the genomic DNA contamination were 27.7 $\mu\text{g g}^{-1}$ for leaves and 25.7 $\mu\text{g g}^{-1}$ for pollen. The isolated RNA was of adequate purity (average A_{260}/A_{280} of 1.91 for leaves and 1.94 for pollen). Before DNase treatment, the total RNA isolated from both leaves and pollen was impure with average A_{260}/A_{280} values of 1.58 and 1.11, respectively (Table I).

While the yields of isolated total RNA from *T. cordata* leaves and pollen were similar, the relatively low yields of isolated total RNA compared to the total RNA isolated from other plant sources can be explained by the fact that linden

represents a difficult source due to its chemical and molecular composition. Linden pollen is an especially difficult starting material because it contains a variety of molecules, including carotenoids, flavonoids, phenols and lipids, all of which can make the RNA isolation process difficult. Indeed, the isolation of the RNA from *T. cordata* pollen with the Qiagen plant mini kit, unlike from *T. cordata* leaves, was unsuccessful, rendering almost completely degraded RNA (Fig. 1B). Furthermore, even using TRIzol™, which allowed for the successful isolation of total RNA from both leaves and pollen, some RNA isolated from pollen was still degraded. Hence, *T. cordata* leaves and pollen probably differ in their molecular composition and may require different strategies for the most effective biochemical manipulation and possible improvement in the yield of isolated total RNA.

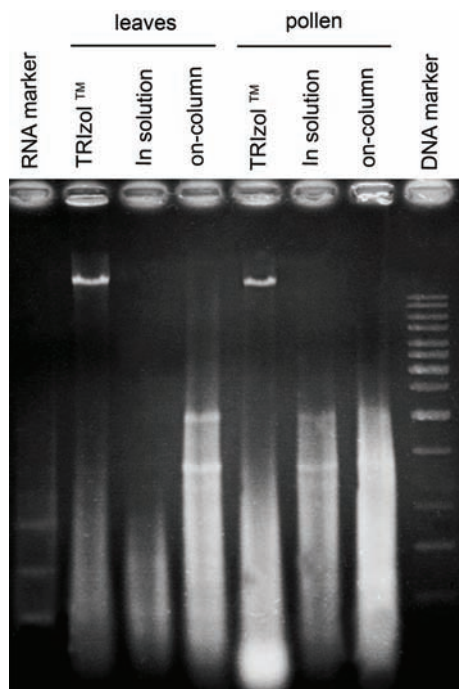


Fig. 2. Electrophoretic profile after isolation of total RNA from linden leaves and pollen using TRIzol™. *T. cordata* leaves or pollen (300 mg) were ground in liquid nitrogen and the total RNA was isolated using TRIzol™ and chloroform extraction. DNase treatment was performed either in solution or on-column. The RNA samples eluted after Qiagen on-column clean-up were analyzed by 1.2 % formaldehyde–agarose electrophoresis and ethidium bromide staining. RNA and DNA markers were run as size standards.

TABLE I. Concentration and purity of the total RNA isolated from *T. cordata* leaves and pollen with TRIzol™, before and after treatment with DNase (in solution or on-column)

Specimen	Sample	A_{260}/A_{280}
Leaves	TRIzol™	1.58±0.19
	After DNase treatment in solution	1.74±0.09
	After DNase treatment on-column	1.91±0.05
Pollen	TRIzol™	1.11±0.16
	After DNase treatment in solution	1.71±0.29
	After DNase treatment on-column	1.94±0.21

The next goal was to optimize the isolation of total RNA and elimination of genomic DNA using on-column DNase treatment. Up to 100 µg RNA can be loaded onto Qiagen plant mini kit columns and hence the optimal amount of TRIzol™-prepared total RNA that could be loaded onto a Qiagen spin column in order to efficiently remove the genomic DNA and isolate the highest possible amount of pure total RNA was determined. Various amounts of TRIzol™-prepared total RNA isolated from *T. cordata* leaves, ranging from 25 up to 150 µl, were applied onto Qiagen spin columns, treated with DNase enzyme for 15 min at room temperature, and eluted with RNase-free water. Samples from each on-column treatment were loaded and migrated on 1 % agarose gel. Genomic DNA was efficiently removed and pure RNA that was not degraded was obtained with samples, ranging from 25 to 150 µl, of TRIzol™-prepared total RNA applied for on-column DNase treatment (Fig. 3A). However, the optimal amount of TRIZOL™-prepared total RNA applied for on-column DNase treatment that resulted in the highest yield of eluted RNA was 100 µl (Fig. 3A). Furthermore, using three independent measurements of total RNA concentration by spectrophotometry (A_{260}), it was confirmed that applying 100 µl of TRIzol™-prepared RNA for on-column treatment was an optimal amount (Fig. 3B). Interestingly, for amounts over 100 µl of TRIzol™-isolated total RNA applied on-column, there was a decrease in the yield of isolated pure RNA.

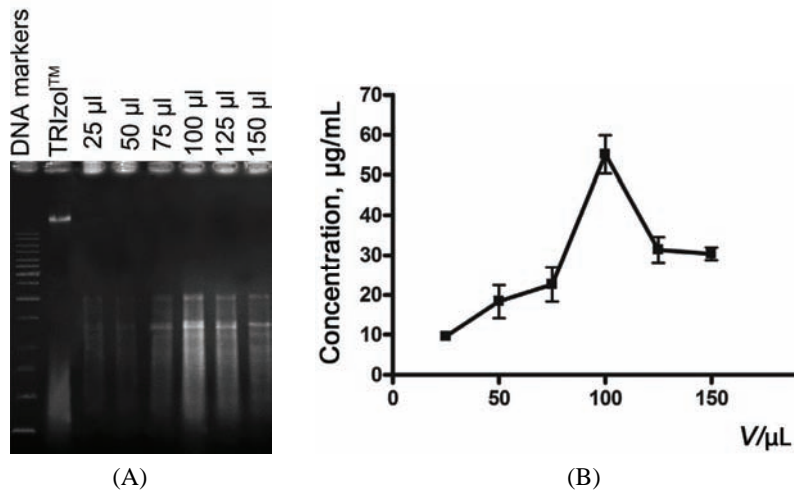


Fig. 3. Electrophoretic profile after optimization of the total RNA isolation following on-column DNase treatment. DNase treatment was performed on Qiagen mini spin columns after applying 25, 50, 75, 100, 125, or 150 µl of the total isolated RNA. A) Total RNA samples were analyzed by 1 % agarose electrophoresis and ethidium bromide staining. DNA markers were run as size standards. B) Yield of total RNA eluted ($\mu\text{g mL}^{-1}$ eluted volume) after on-column treatment with DNase, determined by measuring the concentration of eluted RNA using spectrophotometry (A_{260}).

Concentration and purity of total RNA isolated from leaves and pollen using TRIzolTM, before and after DNase treatment, on-column or in solution, were determined by measuring in triplicate the absorbance at 260 nm (A_{260}) and the ratio between absorbance at 260 and 280 nm (A_{260}/A_{280}), respectively. However, following DNase treatment on-column, the isolated RNA was pure with an average A_{260}/A_{280} of 1.91 for leaves and 1.94 for pollen. In terms of concentration, the A_{260} values of the TRIzolTM samples prior to DNase treatment were not taken into account because the contamination with genomic DNA obviously leads to overestimation of the real RNA concentration. Three measurements of the A_{260} value following on-column DNase treatment were used to calculate the average concentration of eluted total RNA following on-column DNase treatment, which was approximately $55.4 \pm 15.8 \mu\text{g mL}^{-1}$ for the total RNA isolated from leaves and $38.6 \pm 2.2 \mu\text{g mL}^{-1}$ for the total RNA isolated from pollen (Fig. 4A). These concentration values were further used to determine the average yield of isolated total RNA and a yield of $27.7 \pm 7.9 \mu\text{g g}^{-1}$ starting material was obtained for leaves compared to $25.7 \pm 1.1 \mu\text{g g}^{-1}$ starting material for pollen (Fig. 4B).

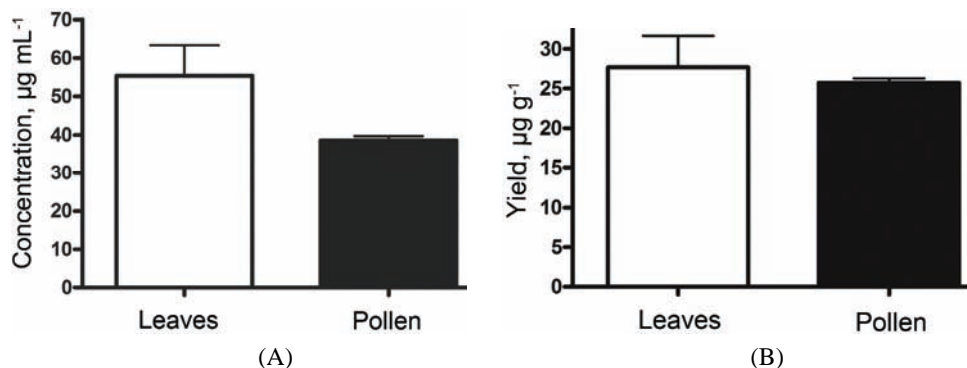


Fig. 4. Concentration, purity, and yield of total RNA isolated from *T. cordata* leaves and pollen. A) Concentration of total RNA ($\mu\text{g mL}^{-1}$) isolated from *T. cordata* leaves or pollen using TRIzolTM and digested on-column with DNase enzyme. B) Yield of total RNA ($\mu\text{g g}^{-1}$ of starting material) isolated from *T. cordata* leaves or pollen using TRIzolTM and digested on-column with DNase enzyme. Values were obtained using RNA samples from different isolations and three independent measurements.

To check the functionality of the isolated RNA, cDNA synthesis was performed using the total RNA isolated from linden leaves or pollen as a template. Using total RNA isolated from leaves with TRIzolTM and digested on-column with DNase, first- and second-strand cDNA synthesis reactions were performed, which resulted in the synthesis of single- and double-stranded cDNA, respectively, as shown by the broad range smears on the agarose gel after electrophoresis (Fig. 5A). Similar results were observed using total RNA isolated from linden pollen (Fig. 5B). To confirm further the functionality of the RNA preparations,

isolated total RNA was used in an RT-PCR reaction aimed at detecting and amplifying a fragment of the actin gene in *T. cordata* leaves and pollen (Fig. 5C). Indeed, a PCR-amplified fragment of identical size of less than 250 bp was observed in the RT-PCR using either total RNA isolated from leaves or pollen as template, showing that the isolated total RNA was functional.

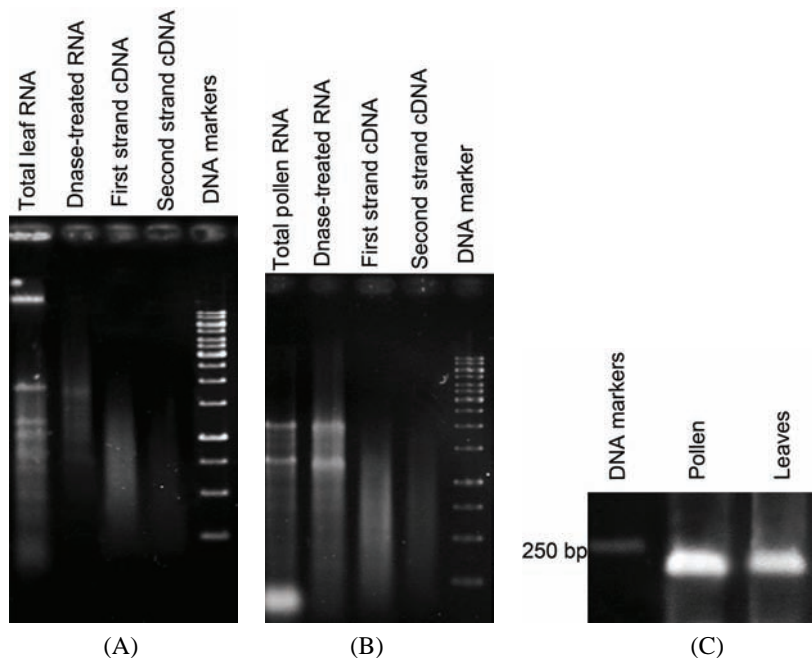


Fig. 5. Electrophoretic profile during cDNA synthesis and RT-PCR using total RNA isolated from *T. cordata* leaves and pollen. A) Total RNA isolated from *T. cordata* leaves using TRIzol™ was digested on-column with DNase and used as the template for first- and second-strand cDNA synthesis. B) Total RNA isolated from *T. cordata* pollen using TRIzol™ was digested on-column with DNase and used as the template for first- and second-strand cDNA synthesis. C) RT-PCR to amplify a fragment of the actin gene was realized using total RNA isolated from leaves or pollen. The samples were analyzed by 1 % agarose (A and B) or 2 % agarose gel electrophoresis (C) and ethidium bromide staining. DNA markers were run as size standards.

CONCLUSION

In the present paper, conditions for the isolation of functional RNA from *T. cordata* leaves and pollen are reported. This is the first report of the isolation of total RNA from *T. cordata* pollen. The total RNA isolated from leaves and pollen using TRIzol™ and DNase on-column digestion was functional, as confirmed by cDNA synthesis and RT-PCR reactions of the linden leaves and pollen actin gene (Fig. 5C). Stemming from these results, it was demonstrated that it is possible to isolate RNA from *T. cordata* leaves and pollen and, furthermore, that the ob-

tained total RNA could be of use for further molecular biology research aimed at characterizing the biochemical properties of *T. cordata*.

Acknowledgments. This research was realized with support from the Ministry of Education, Science and Technological Development of the Republic of Serbia, GA No.172024 and by the European Commission, under the Framework 7 Project RegPot FCUB ERA, GA No. 256716. This publication reflects only authors' views and the Community is not liable for any use that may be made of the information contained in this publication. We would also like to thank Nataša Martinović for technical help.

ИЗВОД

ИЗОЛОВАЊЕ ФУНКЦИОНАЛНЕ УКУПНЕ РНК ИЗ ЛИШЋА И ПОЛЕНА ЛИПЕ (*Tilia cordata*)

ЈАНА ОГЊЕНОВИЋ¹, ZIYAD OMAR TANTOUSH¹, РАТКО ЈАНКОВ¹, ТАЊА ЂИРКОВИЋ ВЕЛИЧКОВИЋ¹
и ЈЕЛЕНА ВУКМИРИЦА²

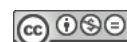
¹Hemjiski fakultet, Univerzitet u Beogradu, Studentski trg 16, 11000 Beograd и ²Faculty of Medicine,
University of Ottawa, 451 Smyth Rd. Ottawa, Ontario, Canada

Успостављени су услови за изоловање укупне РНК из лишћа и полена европске липе (*Tilia cordata*). Коришћењем комерцијално доступног прибора за изоловање РНК из биљака изолована је чиста укупна РНК из лишћа липе, док је коришћењем исте методе добијена деградирана РНК из полена липе. Успешно изолована РНК из лишћа и полена је добијено коришћењем ТРИзол реагенса. РНК изолована овим методом је контаминирана геномском ДНК, која је успешно елиминисана коришћењем ензима ДНазе. Даље су оптимизовани и услови уклањања геномске ДНК помоћу ДНазе. Изолована укупна РНК из оба извора је даље успешно искоришћена за синтезу првог и другог ланца клонске ДНК, као и у реверзо-транскриптивној PCR реакцији, доказујући тиме да је коришћењем овог метода изолована функционална укупна РНК. У закључку, добијена је чиста и функционална РНК из лишћа и полена *T. cordata* ($27,8 \pm 7,9 \mu\text{g g}^{-1}$ лишћа; $25,7 \pm 1,1 \mu\text{g g}^{-1}$ полена) која се може користити у даљим молекуларно-биолошким истраживањима.

(Примљено 30. новембра 2011, ревидирано 23. фебруара 2012)

REFERENCES

1. K. Rushforth, *Trees of Britain and Europe*, Collins, London, UK, 1999
2. N. P. Ivleva, E. R. Niessner, E. U. Panne, *Anal. Bioanal. Chem.* **381** (2005) 261
3. L. Yman, *Botanical relations and immunological cross-reactions in pollen allergy*, 2nd ed., Pharmacia Diagnostics AB, Uppsala, Sweden, 1982, p. 254
4. W. H. Lewis, P. Vinay, V. E. Zenger, *Airborne and allergenic pollen of North America*, John Hopkins University Press, Baltimore, USA, 1983, p. 194
5. P. Mur, F. Feo Brito, M. Lombardero, D. Barber, P. A. Galindo, E. Gomez, J. Borja, *Allergy* **56** (2001) 457
6. G. Loureiro, M. Rabaca, B. Blanco, S. Andrade, C. Chieira, C. Pereira, *J. Invest. Allergol. Immunopathol.* **33** (2005) 192
7. A. Krakowiak, B. Krēcis, A. Pas-Wyroślak, W. Dudek, M. Kieć-Swierzyńska, C. Palczyński, *Contact Dermatitis* **51** (2004) 34
8. M. Picardo, R. Rovina, A. Cristaudo, C. Cannistraci, B. Santucci, *Contact Dermatitis* **19** (1988) 72



9. M. Fromm, H. H. Hattemer, *Heredity* **91** (2003) 337
10. J. Sambrook, E. F. Fritsch, T. Maniatis, *Molecular Cloning: A Laboratory Manual*, 2nd ed., Cold Spring Harbour Laboratory Press, New York, USA, 1989
11. W. W. Wilfinger, M. Mackey, P. Chomczynski, *Biotechnology* **22** (1997) 474
12. N. Van den Berg, B. G. Crampton, I. Hein, P. R. J. Birch, D. K. Berger, *Biotechnology* **37** (2004) 818
13. E. Kiefer, W. Heller, D. Ernst, *Plant Mol. Biol. Rep.* **18** (2000) 33.



Microwave synthesis and spectral, thermal and antimicrobial activities of some novel transition metal complexes with tridentate Schiff base ligands

RAJENDRA K. JAIN* and ANAND P. MISHRA

Department of Chemistry, Synthetic Inorganic and Coordination Chemistry Laboratories,
Dr. H. S. Gour Central University, Sagar M.P. 470 003, India

(Received 1 October 2011, revised 1 February 2012)

Abstract: Some novel Schiff base metal complexes of Cr(III), Co(II), Ni(II) and Cu(II) derived from 2-[(5-bromo-2-hydroxybenzylidene)amino]pyridin-3-ol (BSAP) and {5-chloro-2-[(2-hydroxy-1-naphthyl)methylene]amino}phenyl-phenylmethanone (HNAC) were synthesized by conventional as well as microwave methods. These compounds were characterized by elemental analysis, FT-IR, FAB-mass, electronic and ESR spectroscopy, molar conductance, magnetic susceptibility, thermal, cyclic voltammetric and electrical conductivity measurements and XRD analyses. Analytical data revealed that all the complexes exhibited 1:1 (metal:ligand) ratio with a coordination number of 4 or 6. The IR data showed that the ligand coordinates with the metal ions in a tridentate manner. FAB-mass and thermal data showed the degradation pattern of the complexes. The thermal behaviour of the metal complexes showed that the hydrated complexes lose water molecules of hydration in the first step; with decomposition of the ligand molecules in the subsequent steps. The crystal system, lattice parameters, unit cell volume and number of molecules in a unit cell in the lattice of the complexes were determined by XRD analysis. XRD patterns indicated a crystalline nature for the complexes. The solid state electrical conductivity of the metal complexes was also measured. Solid state electrical conductivity studies reflected a semi-conducting nature of the complexes. The Schiff base and metal complexes displayed good activity against the Gram-positive bacteria *Staphylococcus aureus*, the Gram-negative bacteria *Escherichia coli* and the fungi *Aspergillus niger* and *Candida albicans*. The antimicrobial results also indicated that the metal complexes displayed better antimicrobial activity as compared to the Schiff bases.

Keywords: microwave method; tridentate ligands; thermal analyses; biological activities.

*Corresponding author. E-mail: rajendrajain85@rediffmail.com
doi: 10.2298/JSC111001023J

INTRODUCTION

Metal complexes have received considerable attention in the last many years, due to their interesting characteristics in the field of material science and biological systems. Optoelectronic, electrical and magnetic properties of metals and metalloids can be tailored by their reaction with different ligands. A large number of Schiff bases and their complexes may exhibit properties such as reversible binding of oxygen, transfer of an amino group, thermal, varied complexing/redox abilities, and as nanoprecursors. The Schiff bases have high affinity for transition metal ions; hence exhibit potential applications in various areas. Metal complexes are also suitable as molecular materials, because of the electronic properties associated with the metal centres.^{1–4}

Transition metal complexes with tridentate Schiff base ligands have been widely investigated since such ligands can bind metal centres at more than one site and thus allow the successful synthesis of metal complexes with interesting stereochemistry and model redox enzyme/biological systems. The Schiff bases of salicylaldehyde with aminopyridines have created a well-known class of predominantly thermochromic compounds and metallobiomolecules.^{5–8}

Similarly, a heterocyclic nucleus, namely pyridine based ligands, have also been reported in many biochemical reactions to design and develop molecular systems of biological and medical importance. Such ligating species on coordination with metal ions may emerge as metal-mediated drugs. A 2-hydroxy-1-naphthaldehyde-derived Schiff base has been used as a good chelating agent with 3d-metal ions. 2-Aminobenzophenone derivatives are important compounds in organic chemistry because of their application in heterocyclic synthesis and medicinal compounds.^{9–12}

Microwave-assisted synthesis is a branch of green chemistry. The application of microwave-assisted synthesis in organic, organometallic and coordination chemistry continues to develop at an astonishing pace. Microwave-irradiated reactions under solvent free or less solvent conditions offer reduced pollution, low cost and better yield, and simplicity in processing and handling. The main features of the microwave approach are shorter reaction times, simple reaction conditions and enhancement of yields. There are a few reports on the synthesis of metal complexes by microwave methods.^{13–18}

In the present paper, the coordination behaviour of Schiff bases (Fig. 1) derived from the condensation of 5-bromosalicylaldehyde with 2-amino-3-hydroxypyridine (BSAP) and 2-hydroxy-1-naphthaldehyde with 2-amino-5-chlorobenzophenone (HNAC) towards some transition elements is described, which may help in more understanding of the mode of chelation of ligands towards metals. For this purpose, the complexes of Cr(III), Co(II), Ni(II) and Cu(II) ions with BSAP and HNAC were synthesized by both conventional and microwave methods and characterized by various physico-chemical and spectral techniques.



The metal complexes prepared with these two new ligands may be used as precursors for the synthesis of new compounds. Some of them may also exhibit interesting physical and chemical properties and useful biological activities.

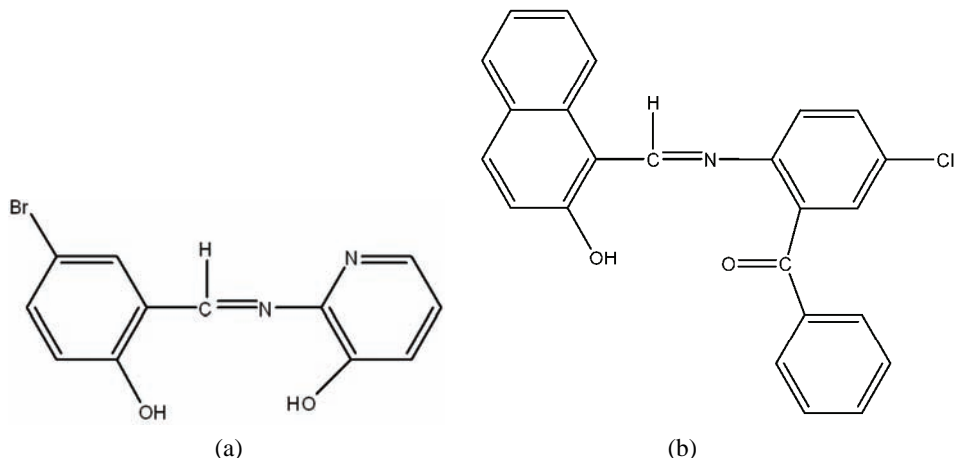


Fig.1. Structure of Schiff base ligands, a) 2-[5-bromo-2-hydroxybenzylidene]amino]pyridin-3-ol (BSAP) and b) {5-chloro-2-[(2-hydroxy-1-naphthyl)methylene]-amino}phenylmethanone (HNAC).

EXPERIMENTAL

Materials

All the chemicals and solvents used were of Anal R grade. All the reagents employed for the preparation of the Schiff bases were obtained from Sigma Aldrich. Metal salts were purchased from Loba Chemie.

Physical measurements

Elemental analyses were performed on an Elemental Vario EL III Carlo Erba 1108 analyzer. The FAB-mass spectra were recorded on a JEOL SX 102/DA 6000 Mass Spectrometer using argon/xenon (6 kV, 10 mA) as the FAB gas. The accelerating voltage was 10 kV and the spectra were recorded at room temperature. The electronic spectra (in DMSO) were recorded on Perkin Elmer Lambda-2B-spectrophotometer. The molar conductance measurements were realised using 10^{-3} M solution of the complexes in DMSO on an Elico-CM 82 conductivity bridge at room temperature. Magnetic susceptibility measurements were performed on a Gouy balance at room temperature using $\text{Hg}[\text{Co}(\text{SCN})_4]$ as the calibrant. Dia-magnetic corrections were applied in compliance with the Pascal constant. FT-IR spectra were recorded in KBr discs on a Perkin Elmer RX1 spectrophotometer in wave number range 4000–400 cm^{-1} . The $^1\text{H-NMR}$ spectra were recorded on a JEOL AL300 FTNMR spectrometer employing TMS as an internal reference and $\text{DMSO}-d_6$ as the solvent. Cyclic voltammetry was performed with a BAS-100 Epsilon electrochemical analyzer using a three-electrode electrochemical cell. Ag/AgCl was used as a reference electrode, glassy carbon as the working electrode and a platinum wire as the auxiliary electrode. 0.1 M NaClO_4 was used as the supporting electrolyte and DMSO as the solvent. All measurements were performed at room temperature under a nitrogen atmosphere. The X-band EPR spectra were recorded at room tem-

perature on a Varian E-112 spectrometer operating in the X-band region with 100 kHz modulation frequency, 5 mW microwave power and 1 G modulation amplitude using tetracyanoethylene (TCNE) as the internal standard. Thermogravimetric analysis was realised under atmospheric conditions with a heating rate 10 °C min⁻¹ on TGA Q500 universal V4.5A TA instrument. Powder X-ray diffraction (XRD) patterns were recorded on a RINT2000 wide angle goniometer. X-ray diffractometer was operated at 40 kV and 30 mA generator using the CuK_α line of 1.54056 Å as the radiation sources. The samples were scanned between 5 and 70° (2θ) at 25 °C. The solid state electrical conductivity was measured by impedance spectroscopic method using a HIOKI 3532-50 LCR Hitester at a fixed frequency of 1 KHz in the temperature range of 298–413 K. Microwave-assisted syntheses were performed in an open glass vessel using a modified microwave oven model 2001 ETB with a rotating tray and a 230 V power source. The microwave energy output was 800 W and the microwave frequency 2450 MHz. A thermocouple device was used to monitor the temperature inside the vessel of the microwave. The microwave reactions were performed using ON/OFF cycling to control the temperature.

Conventional method for the synthesis of Schiff bases

The 2-[5-bromo-2-hydroxybenzylidene)amino]pyridin-3-ol Schiff base was synthesized by the condensation of an equimolar ratio of 5-bromosalicylaldehyde (0.201 g, 10 mM) with 2-amino-3-hydroxypyridine (0.110 g, 10 mM) dissolved in ethanol. The resulting reaction mixture was refluxed on a water bath for 4.1 h and then allowed to cool overnight. The coloured solid precipitate of the obtained Schiff base was filtered, washed with cold ethanol several times and dried in air at room temperature and finally preserved under reduced pressure in a desiccator. The purity of the synthesized compounds was checked by TLC using silica gel G. Yield: 78.0 %; m.p. 179 °C; Anal. Calcd. for C₁₂H₉N₂O₂Br: C, 49.17; H, 3.07; N, 9.56 %. Found: C, 49.02; H, 3.09; N, 9.50 %. IR (KBr, cm⁻¹): 1625 (C=N, azomethine), 1268 (C=O), 1496 (C=N, pyridine). ¹H-NMR (300 MHz, DMSO-d₆, δ / ppm), 9.29 (1H, s, –CH=N), 13.80 (1H, s, –OH, salicylaldehyde moiety), 10.28 (1H, s, –OH pyridine moiety). FAB-mass (m/z), Calcd.: 292; Found: 294.

The {5-chloro-2-[(2-hydroxy-1-naphthyl)methylene]amino}phenylmethanone Schiff base was synthesized by the condensation of an equimolar ratio of 2-hydroxy-1-naphthaldehyde (0.172 g, 10 mM) with 2-amino-5-chlorobenzophenone (0.232 g, 10 mM) dissolved in ethanol. The resulting reaction mixture was refluxed on a water bath for 3.8 h and then allowed to cool overnight. The obtained coloured precipitate of the Schiff base was filtered, washed with cold ethanol several times and dried in air at room temperature and finally stored under reduced pressure in a desiccator. The purity of the synthesized compounds was checked by TLC using silica gel G. Yield: 74.9 %; m.p. 160 °C; Anal. Calcd. for C₂₄H₁₆NO₂Cl: C, 74.41; H, 4.18; N, 3.63 %. Found: C, 74.35; H, 4.11; N, 3.58 %. IR (KBr, cm⁻¹): 1613 (C=N, azomethine), 1236 (C=O), 1675 (C=O). ¹H-NMR (300 MHz, DMSO-d₆, δ / ppm), 8.65 (1H, s, –CH=N), 12.67 (1H, s, –OH phenolic). FAB-mass (m/z), Calcd.: 386, Found: 388.

Microwave method for the synthesis of the Schiff bases

An equimolar ratio of 5-bromosalicylaldehyde (0.201 g) with 2-amino-3-hydroxypyridine (0.110 g) and 2-hydroxy-1-naphthaldehyde (0.172 g) with 2-amino-5-chlorobenzophenone (0.232 g) was mixed thoroughly in a grinder. The reaction mixture was then irradiated in the microwave oven by taking 3–4 mL of dry ethanol as a solvent. The reaction was completed in a short time (4–5 min) with better yields than were obtained in the conventional



procedure. The resulting product was then recrystallized from ethanol and finally dried under reduced pressure over anhydrous CaCl_2 in a desiccator. The progress of the reaction and purity of the product was monitored by TLC using silica gel G (yield: 87.1–87.4 %).

Conventional method for the synthesis of metal complexes

The metal complexes were prepared by mixing 50 mL of a 10 mM ethanolic solution of $\text{CrCl}_3 \cdot 6\text{H}_2\text{O}$ / $\text{CoCl}_2 \cdot 6\text{H}_2\text{O}$ / $\text{NiCl}_2 \cdot 6\text{H}_2\text{O}$ / $\text{CuCl}_2 \cdot 2\text{H}_2\text{O}$ with 50 mL of a 10 mM ethanolic solution of the Schiff bases (BSAP/HNAC) in a 1:1 (metal:ligand) ratio (Figs. 2 and 3). The resulting mixture was refluxed on a water bath for 6–9 h. A coloured product appeared on standing and cooling the solution. The precipitated complexes were filtered, washed with ether and recrystallized several times from ethanol and dried under reduced pressure over anhydrous CaCl_2 in a desiccator. They were further dried in an electric oven at 50–70 °C (yield: 59.6–69.0 %).

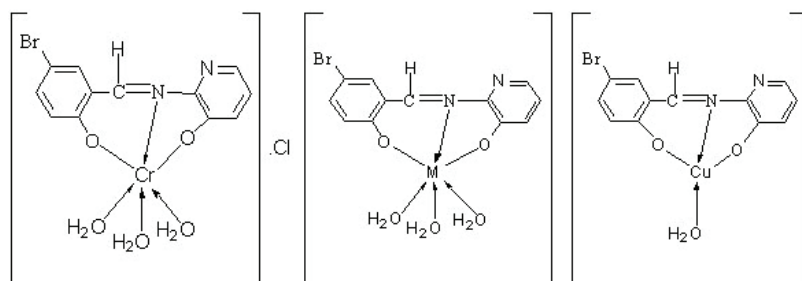


Fig. 2. The proposed structures of the Schiff base complexes of BSAP.

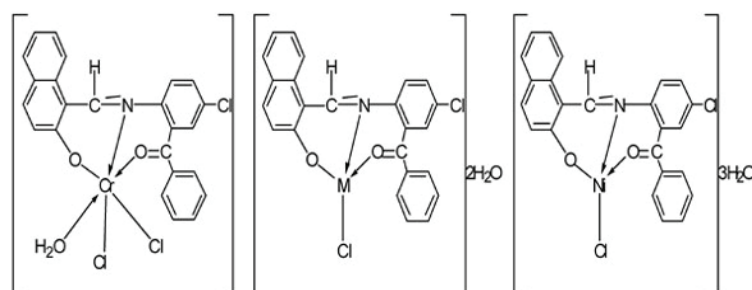


Fig. 3. The proposed structures of the Schiff base complexes of HNAC.

Microwave method for the synthesis of metal complexes

The ligands and the metal salts were mixed in a 1:1 (metal:ligand) ratio in a grinder. The reaction mixture was then irradiated in the microwave oven taking 3–5 mL of dry ethanol as the solvent. The reactions were completed in a short time (6–10 min) with better yields than were obtained in the conventional procedure. The resulting product was then recrystallized from ethanol and washed with diethyl ether and finally dried under reduced pressure over anhydrous CaCl_2 in a desiccator. The progress of the reaction and purity of the product was monitored by TLC using silica gel G (yield: 78.0–85.0 %).

Biological activity

The *in vitro* biological activity of the investigated Schiff bases and their metal complexes were tested against the bacteria *Escherichia coli* and *Staphylococcus aureus* by the disc diffusion method using nutrient agar as the medium and streptomycin as the control. The anti-fungal activities of the compounds were also tested by the well diffusion method against the fungi *Aspergillus niger* and *Candida albicans*, on potato dextrose agar as the medium and miconazole as the control. Each of the compounds was dissolved in DMSO and the solutions of concentrations 25, 50 and 100 ppm were prepared separately. In a typical procedure, a well was made on the agar medium inoculated with micro-organism. The well was filled with the test solution using a micropipette and the plate was incubated 24 h at 37 °C for the bacteria or 72 h at 30 °C for the fungi. After incubation, the diameter of the clear zone of inhibition surrounding the sample was taken as a measure of the inhibitory power of the sample against the particular test organism.

RESULTS AND DISCUSSION

As a result of the microwave-assisted synthesis, it was observed that the reaction time decreased from hours to minutes and better yields of the products were obtained compared to those attained by the conventional synthesis method. In the microwave method, homogeneity of the reaction mixture was increased by the rotation of reaction platform tray. The confirmation of the results was also checked by repeating of the synthesis process.

All the metal complexes were coloured, solid and stable towards air and moisture at room temperature. They decomposed on heating at high temperatures and were more or less soluble in common organic solvents. The results of a comparison of the two synthesis methods showed that reactions which required 3.8–8.2 h by the conventional method were completed within 4.0–7.9 min by the microwave irradiation technique and the yields were improved from 59.6–78.0 % to 78.0–87.6 %. The reaction times and yields for all the synthesised compounds are given in Table I.

All the metal chelates had 1:1 (metal:ligand) stoichiometry. The observed molar conductance of the complexes in DMSO at room temperature, given in Table S-I of the Supplementary Material to this paper, were consistent with the non-electrolytic nature of the complexes except for the Cr(III) complex of the BSAP Schiff base ligand, which was electrolytic in nature.

FAB-mass spectra

The FAB-mass spectra suggested that all the complexes have a monomeric nature. These complexes showed molecular ion peaks in good agreement with the empirical formula suggested by elemental analyses, the results of which are given in Table S-I of the Supplementary Material to this paper.

Thus, mass spectra of the complexes $[\text{Ni}(\text{BSAP})(\text{H}_2\text{O})_3]$ (FW 403.84) and $[\text{Co}(\text{HNAC})\text{Cl}] \cdot 2\text{H}_2\text{O}$ (FW 515.25), as representative complexes, showed the

highest mass peaks at m/z at 406 and 518, respectively, which agree well with the formula weights of the complexes.^{19,20}

TABLE I. Reaction times and yields for the conventional and microwave synthesis methods

Compound (colour)	Empirical formula (FW)	Reaction period		Yield, %	
		CM, h	MM, min	CM	MM
BSAP (brown)	C ₁₂ H ₉ N ₂ O ₂ Br (293.12)	4.1	4.5	78.0	87.6
[Cr(BSAP)(H ₂ O) ₃]Cl (Greenish brown)	C ₁₂ H ₇ N ₂ O ₂ BrClCr (432.60)	8.2	7.9	59.6	79.8
[Co(BSAP)(H ₂ O) ₃] (Dark brown)	C ₁₂ H ₁₃ N ₂ O ₅ BrCo (404.08)	7.3	7.2	67.5	80.8
[Ni(BSAP)(H ₂ O) ₃] (Coffee brown)	C ₁₂ H ₁₃ N ₂ O ₅ BrNi (403.84)	7.8	7.5	66.2	83.5
[Cu(BSAP)(H ₂ O)] (black)	C ₁₂ H ₉ N ₂ O ₃ BrCu (372.66)	6.9	6.5	62.0	85.0
HNAC (Yellowish brown)	C ₂₄ H ₁₆ NO ₂ Cl (385.84)	3.8	4.0	74.9	87.1
[Cr(HNAC)(H ₂ O)Cl ₂] (Dark green)	C ₂₄ H ₁₇ NO ₃ Cl ₃ Cr (525.75)	7.9	7.8	60.1	78.0
[Co(HNAC)Cl] \cdot 2H ₂ O (Tobacco green)	C ₂₄ H ₁₉ NO ₄ Cl ₂ Co (515.25)	7.8	7.0	64.5	78.9
[Ni(HNAC)Cl] \cdot 3H ₂ O (Yellowish green)	C ₂₄ H ₂₁ NO ₅ Cl ₂ Ni (533.03)	7.2	7.3	69.0	84.2
[Cu(HNAC)Cl] \cdot 2H ₂ O (Coffee brown)	C ₂₄ H ₁₉ NO ₄ Cl ₂ Cu (519.86)	7.0	7.5	66.2	82.7

¹H-NMR spectra

The proton NMR spectra of the Schiff base ligands were recorded in DMSO-*d*₆ solution using TMS as an internal standard. The ¹H-NMR spectra of the BSAP ligand showed signals at δ 6.94–7.86 (*m*) for the aromatic protons and 9.29 (*s*) for the azomethine proton. The peaks at δ 13.80 (*s*) and 10.28 (*s*) were attributed to the phenolic –OH group present in the salicylaldehyde moiety and the –OH group present in the pyridine moiety, respectively; the –OH peaks disappeared after D₂O addition.

The ¹H-NMR spectra of the HNAC ligand showed signals at δ 7.23–7.69 (*m*) for the aromatic protons and 8.65 (*s*) for the azomethine proton. The peak at 12.67 (*s*) attributed to the phenolic –OH group, disappeared upon addition of D₂O.^{21–25} The IR data support these assignments.

IR spectra

The data of the IR spectra of Schiff base ligands and their metal complexes are listed in Table S-II of the Supplementary Material to this paper. The IR spectra of the complexes were compared with those of the free ligands in order to de-

termine the involvement of the coordination sites in the chelation. Characteristic peaks in the spectra of the ligand and complexes were considered and compared.

IR spectrum of the BSAP ligand exhibited the most characteristic bands at 1625 cm^{-1} $\nu(\text{C}=\text{N}, \text{azomethine})$, 1268 cm^{-1} $\nu(\text{C}-\text{O})$ and 1496 cm^{-1} $\nu(\text{C}=\text{N}, \text{pyridine})$. The formation of the Schiff base, 2-[$(5$ -bromo- 2 -hydroxybenzylidene)amino]pyridin- 3 -ol (BSAP) was noted from the absence of $\text{C}=\text{O}$ and NH_2 peaks in the ligand. The ligand spectrum showed bands at 3150 and 1361 cm^{-1} due to the stretching and deformation of the phenolic OH. These were absent in the spectra of the complexes. The band at 1625 cm^{-1} due to the azomethine group of the Schiff base was shifted to lower frequencies (1596 – 1607 cm^{-1}) after complexation, indicating the bonding of nitrogen of the azomethine group to the metal ions. The phenolic C–O stretching vibration that appeared at 1268 cm^{-1} in Schiff base shifted towards higher frequencies (20 – 27 cm^{-1}) in the complexes. This suggests deprotonation of the phenolic OH group after its chelation with the metal ion. The appearance of broad bands at around 3343 – 3398 cm^{-1} in the spectra of complexes may be due to water molecules. A band of medium intensity at 807 – 822 cm^{-1} (OH rocking) suggests the presence of coordinated water in all four complexes. In the low frequency region, the band of weak intensity observed for the complexes in the region 522 – 540 cm^{-1} is attributed to $\text{M}-\text{O}$ and in the region 486 – 497 cm^{-1} to $\text{M}-\text{N}$. There was no appreciable change in the $\nu(\text{C}=\text{N})$ at 1496 cm^{-1} in ligand on complex formation, which indicates that the pyridine ring nitrogen does not participate in the coordination.^{26–30}

IR spectrum of the HNAC ligand showed the most characteristic bands at 1613 cm^{-1} $\nu(\text{C}=\text{N}, \text{azomethine})$, 1675 cm^{-1} $\nu(\text{C}=\text{O})$ and 1236 cm^{-1} $\nu(\text{C}-\text{O})$. The ligand spectrum showed bands at 3230 and 1336 cm^{-1} due to the stretching and deformation of the phenolic OH. These were absent in the spectra of the complexes. The band 1613 cm^{-1} due to the azomethine group of the Schiff base was shifted to lower frequencies (1582 – 1594 cm^{-1}) after complexation, indicating bonding of the azomethine nitrogen to the metal ions. This can be explained by the donation of electrons from nitrogen to the empty d-orbital of the metal atom. The band at 1675 cm^{-1} , due to the carbonyl group of the Schiff base, was shifted to lower frequencies by 23 – 35 cm^{-1} in the spectra of complexes, indicating involvement of carbonyl oxygen to metal ions in the coordination. The phenolic C–O stretching vibration that appeared at 1236 cm^{-1} in Schiff base shifted towards higher frequencies (19 – 27 cm^{-1}) in the complexes. This shift confirms the participation of oxygen in the C–O–M bond. The appearance of broad bands around at (3365 – 3408 cm^{-1}) in the spectra of the complexes may be due to water molecules. A medium intensity band at 785 cm^{-1} in the spectrum of the Cr(III) complex suggests the presence of coordinated water molecules in this complex. This band was not observed in other complexes, indicating the absence of coordinated water molecules in the Co(II), Ni(II) and Cu(II) complexes. In the low

frequency region, the band of weak intensity observed in the spectra of the complexes in the region 519–529 cm⁻¹ is attributed to (M–O) and in the region 485–492 cm⁻¹ to (M–N).^{26–30}

The IR data of both the Schiff bases and their metal complexes showed that the Schiff bases (BSAP and HNAC) were coordinated to the metal ion in a tridentate manner.

Electronic spectra and magnetic moment

The electronic spectral data of the metal complexes in DMSO solution are displayed in Table S-III of the Supplementary Material to this paper. The nature of the ligand field around the metal ion was deduced from the electronic spectra.

The electronic spectra of Cr(III) complex of BSAP showed bands at 16654 cm⁻¹, 24212 and 35982 cm⁻¹, which may be assigned to ${}^4A_{2g} \rightarrow {}^4T_{2g}(F)$ (ν_1), ${}^4A_{2g} \rightarrow {}^4T_{1g}(F)$ (ν_2) and ${}^4A_{2g} \rightarrow {}^4T_{1g}(P)$ (ν_3) transitions, respectively. The magnetic moment was 3.88 μ_B ; thus octahedral geometry is suggested for this complex. The electronic spectrum of Co(II) complex of BSAP exhibited three bands at 9486, 15823 and 20618 cm⁻¹, which were tentatively assigned to ${}^4T_{1g} \rightarrow {}^4T_{2g}(F)$ (ν_1), ${}^4T_{1g} \rightarrow {}^4A_{2g}(F)$ (ν_2) and ${}^4T_{1g} \rightarrow {}^4T_{1g}(P)$ (ν_3) transitions, respectively. The value of magnetic moment was 5.02 μ_B , which indicates the presence of Co(II) complex in an octahedral geometry. The electronic spectrum of the Ni(II) complex of BSAP showed three bands at 10691, 20360 and 23838 cm⁻¹, assignable to ${}^3A_{2g} \rightarrow {}^3T_{2g}(F)$ (ν_1), ${}^3A_{2g} \rightarrow {}^3T_{1g}(F)$ (ν_2) and ${}^3A_{2g} \rightarrow {}^3T_{1g}(P)$ (ν_3) transitions, respectively. The value of magnetic moment was 3.04 μ_B ; therefore octahedral geometry is suggested for this complex. The electronic spectrum of the Cu(II) complex of BSAP showed two bands at 15150 and 19230 cm⁻¹, assignable to ${}^2B_{1g} \rightarrow {}^2B_{2g}$ and ${}^2B_{1g} \rightarrow {}^2E_g$ transitions, respectively. Since the value of magnetic moment was found 1.92 μ_B , square planar geometry is suggested for the Cu(II) complex.^{31–34}

The Cr(III) complex of HNAC showed electronic spectral bands at 16871, 23837 and 34942 cm⁻¹; these were tentatively assigned to ${}^4A_{2g} \rightarrow {}^4T_{2g}(F)$ (ν_1), ${}^4A_{2g} \rightarrow {}^4T_{1}(F)$ (ν_2) and ${}^4A_{2g} \rightarrow {}^4T_{1g}(P)$ (ν_3) transitions, respectively. The magnetic moment value was 3.84 μ_B ; thus, an octahedral structure is suggested for this complex. The electronic spectrum of the Co(II) complex of HNAC showed bands at 14142 and 19514 cm⁻¹, these were tentatively assigned to ${}^4A_{2} \rightarrow {}^4T_{1}(F)$ (ν_2) and ${}^4A_{2} \rightarrow {}^4T_{1}(P)$ (ν_3) transitions, respectively. The magnetic moment value was 4.32 μ_B , which is indicative of tetrahedral geometry. The absorption spectrum of the Ni(II) complex of HNAC exhibited bands at 12748 and 20750 cm⁻¹, which were tentatively assigned to the transitions ${}^1A_{1g} \rightarrow {}^1E_g$ (ν_1) and ${}^1A_{1g} \rightarrow {}^1B_{2g}$ (ν_2), respectively. It is a diamagnetic complex, therefore square planar geometry is proposed. The electronic spectrum of the Cu(II) complex of HNAC showed two bands at 15110 and 19456 cm⁻¹, assignable to ${}^2B_{1g} \rightarrow {}^2B_{2g}$



and ${}^2\text{B}_{1\text{g}} \rightarrow {}^2\text{E}_\text{g}$ transitions, respectively. The value of magnetic moment for this complex was $1.81 \mu_\text{B}$; thus, square planar geometry is suggested for the Cu(II) complex.^{31–34}

The different parameters such as ligand field stabilization energy ($10Dq$), Racah inter-electronic repulsion parameter (B), nephelauxetic ratio (β), percent of covalent character ($\beta\%$) and ligand field stabilization energy ($LFSE$) were calculated. The values of these parameters are presented in Table S-III of the Supplementary Material to this paper. The complexes showed lower value of B than those of the free ions, which indicates orbital overlapping and delocalization of the d-orbital. The value of β lied in the range of 0.68–0.78, indicating appreciable covalent character of the metal–ligand bonding.^{31–34}

ESR Spectra

The ESR spectra of Cu(II) provide information about the extent of the delocalization of the unpaired electron. The X-band ESR spectra of the Cu(II) complexes were recorded in the solid state at room temperature and their g_{\parallel} , g_{\perp} , Δg , g_{av} and G were calculated. The values of ESR parameters g_{\parallel} , g_{\perp} , g_{av} , Δg and G for Cu(II) complex of BSAP were 2.2530, 2.1205, 2.1647, 0.1325 and 2.1181, respectively. Similarly, the corresponding values for Cu(II) complex of HNAC were 2.2072, 2.1342, 2.1585, 0.0730 and 1.5535, respectively.

ESR spectra of the complexes revealed two g values (g_{\parallel} and g_{\perp}). Since the g_{\parallel} and g_{\perp} values were closer to 2 and $g_{\parallel} > g_{\perp}$, a tetragonal distortion around the Cu(II) ion is suggested. The trend $g_{\parallel} > g_{\perp} > g_{\text{e}}$ (2.0023) shows that the unpaired electron is localized in the $d_{x^2-y^2}$ orbital in the ground state of Cu(II) and spectra were characteristic of axial symmetry. The value of $g_{\parallel} > 2.3$ is characteristic of an ionic environment and $g_{\parallel} < 2.3$ indicates a covalent environment in metal–ligand bonding. The g_{\parallel} values for the complexes were less than 2.3, suggesting the environment was covalent.

The exchange coupling interaction between two Cu(II) ions is explained by the Hathaway Expression:

$$G = (g_{\parallel} - 2.0023)/(g_{\perp} - 2.0023)$$

According to Hathaway, if the value G is greater than 4 ($G > 4.0$), the exchange interaction is negligible; whereas when the value of G is less than 4 ($G < 4.0$), a considerable exchange coupling is present in a solid complex. The G values for the complexes were less than four, indicating considerable exchange interaction in the complexes.^{35,36}

Thermal analyses

The thermal behaviour of the metal complexes showed that the hydrated complexes first lost molecules of hydration, followed by decomposition of the ligand molecules in the subsequent steps.

The thermal degradation behaviour of the Co(II) complex of BSAP was studied by thermogravimetric analysis. The TGA curve of the complex showed three stages of decomposition within the temperature range 30–750 °C. The complex did not show any loss in weight up to 110 °C, indicating the absence of lattice water molecules. A weight loss was observed after elimination of three coordinated molecules of water between the temperature range 110–225 °C (remaining mass %, obs./calcd.: 87.50/86.63). Above 225 °C, a weight loss was observed in general up to 380 °C, indicating decomposition of the non-coordinated part of the ligand (remaining mass %, obs./calcd.: 48.20/45.05). The decomposition of remaining ligand moiety occurred between 480–620 °C, above 620 °C a horizontal curve was observed suggesting the ultimate pyrolysis product as metal oxide (remaining mass %, obs./calcd.: 29.64/25.99).

The TGA curve of the Ni(II) complex of HNAC showed a weight loss between 72–116 °C. This corresponds to the loss of three lattice water molecules in the complex (remaining mass %, obs./calcd.: 90.10/89.87). Above 116 °C, the complex did not show any loss in weight up to 200 °C. After 200 °C, weight loss was observed up to 400 °C, which corresponded with the decomposition of thermally degradable part of the ligand (remaining mass %, obs./calcd.: 64.55/62.10). After this temperature, a weight loss was observed, suggesting the elimination of the remaining part of the ligand. Above 590 °C, a constant weight region was observed due to metal oxide, as the final pyrolysis product (remaining mass %, obs./calcd.: 25.72/20.66).^{37,38}

The thermal analysis evaluation of the thermal stability of the metal complexes aided in the characterization of the metal complexes.

Kinetic study

Kinetic evaluations of the thermal decomposition of the complexes were performed. All stages were selected for the study of kinetics of decomposition of the complexes. Based on the thermal decomposition data, the kinetic parameter, *i.e.*, activation energy (E^*), pre-exponential factor (Z), entropy of activation (ΔS^*), enthalpy of activation (ΔH^*) and free energy of activation (ΔG^*) were calculated using the Piloyan–Novikova³⁹ and Coats–Redfern⁴⁰ Equations. The determined values of the kinetic parameters are summarized in Table S-IV of the Supplementary Material to this paper.

The high values of the activation energies reflect the thermal stability of the complexes. The complexes have negative entropy, which indicates that the decomposition reactions proceed with a lower rate than normal ones. The negative value of entropy also indicates that the activated complexes have a more ordered and more rigid structure than the reactants or intermediates. The negative values of the entropies of activation are compensated by the values of enthalpies of activation, leading to almost the same values for the free energy of activation.^{41,42}



Electrochemical studies

The electrochemical properties of the two complexes of BSAP were studied by cyclic voltammetry (CV) under a nitrogen atmosphere in DMSO solution in the potential range -1.0 to 1.2 V vs. an Ag/AgCl reference electrode. The Co(II) complex of BSAP showed a reduction peak at $E_{pc} = -619$ mV with a corresponding oxidation peak at $E_{pa} = -428$ mV at a scan rate 100 mV s^{-1} . The peak separation ΔE_p was 191 mV for this couple. Thus, the cyclic voltammetric studies gave evidence to a quasi-reversible Co(II)/Co(I) couple.

The cyclic voltammogram of the Cu(II) complex of BSAP exhibited a one-electron quasi-reversible transfer process with a reduction peak at $E_{pc} = -725$ mV with an associated oxidation peak at $E_{pa} = -444$ mV at scan rate 100 mV s^{-1} which increased with scan rate. The peak separation of this couple (ΔE_p) was 281 mV. The most significant feature of the Cu(II) complex was the Cu(II)/Cu(I) couple. This redox process was consistent with a quasi-reversible process.^{43,44}

X-Ray diffraction study

X-Ray diffraction (XRD) analysis of the Ni(II) complexes was performed. The XRD patterns indicate the crystalline nature of the complex. The X-ray powder diffractogram of the complex were recorded using CuK_α as the source in the 2θ range $5\text{--}70^\circ$. The X-ray crystal system was determined by trial and error methods for finding the best fit between the observed and calculated $\sin^2\theta$. The Ni(II) complex of BSAP crystallized in an orthorhombic system. The $\sin^2\theta$ and hkl values for different lattice planes were calculated for this complex. The crystal data for this complex were $a = 12.67352\text{ \AA}$, $b = 23.79049\text{ \AA}$, $c = 16.62566\text{ \AA}$, $V = 5012.79\text{ \AA}^3$, $Z = 11$, $D_{obs} = 1.4713\text{ g cm}^{-3}$ and $D_{cal} = 1.4652\text{ g cm}^{-3}$. The observed and calculated values of density and $\sin^2\theta$ show good agreement.^{45,46}

Electrical conductivity

The temperature dependence of the solid state conductivity (σ) of the compounds in their compressed pellet form was measured at a fixed frequency of 1 kHz in the temperature range 297–413 K. The values of the solid state electrical conductivity of the Schiff bases and their complexes increased with increasing temperature and decreased upon cooling over the studied temperature range, indicating their semi-conducting behaviour. The general behaviour of electrical conductivity follows the Arrhenius Equation:

$$\sigma = \sigma_0 \exp(-E_a/kT)$$

where E_a is the thermal activation energy of conduction, σ_0 is the conductivity constant and k is the Boltzman constant. The plots of σ vs. $1000/T$ for all the compounds were found to be linear over the studied temperature range. The room temperature electrical conductivity of all the compounds lies in the range $1.241 \times 10^{-7}\text{--}3.525 \times 10^{-12}\text{ }\Omega^{-1}\text{ cm}^{-1}$. These values showed their semi-conducting



nature. The order of the electrical conductivity at room temperature for the complexes of BSAP and those of HNAC was Co>Cr>Cu>Ni. The activation energy of the compounds lie in the range 0.221–0.768 eV.^{47–49} Confirmation of the temperature dependence of the conductivity of the compounds was checked by repetition of the conductivity measurements.

Antimicrobial activities

The *in vitro* antimicrobial activities of the synthesized Schiff base ligands and their corresponding metal complexes against two selected bacteria *E. coli* and *S. aureus* and two fungi *A. niger* and *C. albicans* were determined. Any chemotherapeutic agent reduces the growth of microbes by microcidal or microstatic mechanisms. All of the tested compounds showed good biological activity against the micro-organism. On comparing the biological activities of the Schiff base ligands and their metal complexes with those of a standard bactericide and fungicide, it was shown that the metal complexes had moderate activity as compared to the standard but all the complexes were more active than their respective ligands. The higher inhibition zone of the metal complexes than those of the ligands can be explained based on the Overtone concept and the chelation theory. Upon chelation, the polarity of the metal ion is reduced to a great extent due to the overlap of the ligand orbital and the partial sharing of the positive charge of the metal ion with donor groups. Furthermore, it increases the delocalization of the π -electrons over the whole chelating ring and enhances the penetration of the complexes into lipid membranes and the blocking of the metal binding sites in the enzymes of micro-organisms. There are other factors that increase the activity, *viz.* solubility, lipophilicity/hydrophilicity, conductivity and M–L bond length.^{50–53}

The bactericidal and fungicidal data of the compounds are summarized in Tables II and III, respectively. The results of the investigations account for the antipathogenic behaviour of the compounds and this efficacy is positively modified on complexation.

TABLE II. Antibacterial screening data for the ligands and their complexes

Compound	<i>E. coli</i>						<i>S. aureus</i>					
	Diameter of inhibition zone, mm			Activity index ^a %			Diameter of inhibition zone, mm			Activity index %		
	Concentration, $\mu\text{g ml}^{-1}$						25	50	100	25	50	100
BSAP	11	13	16	50	54	57	11	14	16	61	64	67
Cr(III)	14	16	19	64	67	68	12	15	18	67	68	75
Co(II)	18	20	24	82	83	86	14	18	20	78	82	83
Ni(II)	16	19	25	73	79	89	12	15	18	67	68	75
Cu(II)	17	20	24	77	83	86	15	19	21	83	86	88
HNAC	10	12	15	45	50	54	—	10	12	—	45	50
Cr(III)	11	13	16	50	54	57	11	14	17	61	64	71



TABLE II. Continued

Compound	<i>E. coli</i>						<i>S. aureus</i>					
	Diameter of inhibition zone, mm			Activity index ^a %			Diameter of inhibition zone, mm			Activity index %		
	Concentration, $\mu\text{g ml}^{-1}$						25	50	100	25	50	100
Co(II)	15	18	22	68	75	79	14	18	21	78	82	88
Ni(II)	14	16	20	64	67	71	12	16	18	67	73	75
Cu(II)	16	19	23	73	79	82	13	17	19	72	77	79
Streptomycin (standard)	22	24	28	100	100	100	18	22	24	100	100	100

^aActivity index = $\frac{\text{Inhibition zone by test compound (diameter)}}{\text{Inhibition zone by standard (diameter)}} \times 100$

TABLE III. Antifungal screening data for the ligands and their complexes (diameter of inhibition zone, mm)

Compound	<i>A. niger</i>						<i>C. albicans</i>		
	Concentration, $\mu\text{g ml}^{-1}$						25	50	100
	25	50	100	25	50	100			
BSAP	11	14	18	12	13	17			
Cr(III)	12	15	19	14	16	20			
Co(II)	14	18	22	16	18	23			
Ni(II)	12	16	20	15	17	22			
Cu(II)	15	20	24	17	19	23			
HNAC	12	16	20	11	14	18			
Cr(III)	13	15	21	15	18	22			
Co(II)	16	21	26	18	20	25			
Ni(II)	15	20	25	16	18	23			
Cu(II)	14	19	23	19	21	26			
Miconazole (standard)	20	25	30	22	24	29			

CONCLUSIONS

In the present research study, the aim was to synthesize and characterize some new compounds prepared by the conventional and the microwave method. The microwave method is considered a green chemical route. The synthesized compounds were characterized by various physico-chemical and spectral analyses. In course of the microwave assisted syntheses, it was observed that the reaction time was decreased from hours to minutes and the products were obtained in better yield as compared to those of the conventional method. The use of solvent was also minimized. The synthesized BSAP Schiff base ligand bound with the metal ions in a tridentate manner, with ONO donor sites of the phenyl-O, azomethine-N and pyridyl-O, whereas the HNAC ligand also coordinated to the metal ions in a tridentate manner, with ONO donor sites of phenolic-O, azo-methine-N and carbonyl-O. Such metal complexes may be stereoselective and



stereoactive in nature and thus applicable in various catalytic reactions. Thermo-gravimetric studies reflected their thermal stability. The XRD patterns indicated the crystalline nature of the complexes. The electrical conductivity data suggested that all the complexes fall into the semi-conducting range. The antimicrobial data showed that the metal complexes were more biologically active compared to the parent Schiff base ligands against all the tested pathogenic species. Such studies may assist in the search for some novel chemotherapeutics to answer the emerging problem of drug resistance in health sciences.

SUPPLEMENTARY MATERIAL

Analytical, conductivity, spectral, magnetic, kinetic and thermodynamic data of the synthesized complexes are available electronically from <http://www.shd.org.rs/JSCS/>, or from the corresponding author on request.

Acknowledgements. We are thankful to I.I.T. Mumbai for the ESR analysis. We also acknowledge SAIF, CDRI, Lucknow, for the micro-analysis and spectral analysis. Thanks are also due to the Head, Department of Chemistry, Botany and Physics, Dr. Hari Singh Gour University, Sagar (M.P.), for providing the laboratory facilities.

ИЗВОД

СИНТЕЗА ПОМОЋУ МИКРОТАЛАСА И СПЕКТРАЛНА, ТЕРМИЧКА И АНТИМИКРОБНА СВОЈСТВА НЕКИХ НОВИХ КОМПЛЕКСА ПРЕЛАЗНИХ МЕТАЛА СА ТРИДЕНТАТНОКООРДИНОВАНИМ ШИФОВИМ БАЗАМА КАО ЛИГАНДИМА

RAJENDRA K. JAIN и ANAND P. MISHRA

*Department of Chemistry, Synthetic Inorganic & Coordination Chemistry Laboratories,
Dr. H. S. Gour Central University, Sagar M.P. 470 003, India*

Применом конвенционалних метода и микроталаса, синтетизовани су нови комплекси Cr(III), Co(II), Ni(II) и Cu(II) са Шифовим базама 2-[(5-брому-2-хидроксибензилиден)амино]пиридин-3-олом (BSAP) и {5-хлоро-2-[(2-хидрокси-1-нафтил)метилен]-амино}фенилметаноном (HNAC). За карактеризацију комплекса употребљени су елементална микроанализа, FT-IR и електронска спектроскопија, FAB-масена спектрометрија, мерења моларне и електричне проводљивости и магнетне сусцептибилности, термичке методе, циклична волтаметрија и XRD анализа. На основу аналитичких података нађено је да су одговарајући јон метала и лиганд у овим комплексима координовани у 1:1 молском односу, при чему је координациони број лиганда 4 или 6. На основу IR спектрскопских резултата закључено је да се лиганд координује тридентатно за наведене јоне металла. Начин разлагања ових комплекса је одређен на основу FAB-масених и термичких података, при чему је нађено да хидратисани комплекси прво губе молекуле хидратационе воде, а затим долази до разлагања лиганда. Применом XRD анализе одређене су кристалне структуре синтетизованих комплекса, као и параметри, запремина и број молекула у јединичној ћелији кристалне решетке. Измерена је електрична проводљивост комплекса у чврстом стању, при чему су ова мерења показала да су синтетизовани комплекси полуправодници. Испитивана је антибактеријска активност синтетизованог лиганда и одговарајућих комплекса на грам-позитивне (*Staphylococcus aureus*) и на грам-негативне (*Escherichia coli*) бактерије, као и антифунгална активност на сојевима *Aspergillus niger* и *Candida albicans*. Добијени резултати ових испитивања су



показали да комплекси наведених јона метала имају већу антибактеријску односно антифунгальну активност у односу на некоординоване Шифове базе.

(Примљено 1. октобра 2011, ревидирано 1. фебруара 2012)

REFERENCES

- D. Rehder, G. Santoni, G. M. Licini, C. Schulzke, B. Meier, *Coord. Chem. Rev.* **237** (2003) 53
- S. Chandra, U. Kumar, *Spectrochim. Acta, A* **61** (2005) 219
- S. M. Abdallah, M. A. Zyed, G. G. Mohammed, *Arabian J. Chem.* **3** (2010) 103
- J. M. Fraile, J. I. García, J. A. Mayoral, *Chem. Rev.* **109** (2009) 360
- T. Inabe, *New J. Chem.* **15** (1991) 129
- A. Nilgun, G. O. Selma, I. Semra, *Struct. Chem.* **18** (2007) 667
- S. G. Shirodkar, P. S. Mane, T. K. Chondhekar, *Indian J. Chem., A* **40** (2001) 1114
- S. Chandra, A. K. Sharma, *J. Coord. Chem.* **62** (2009) 3688
- Z. H. Chohan, A. Munawar, C. T. Supuran, *Met.-Based Drugs* **8** (2001) 137
- S. M. Ben-Saber, A. A. Maihub, S. S. Hudere, M. M. El-Ajaily, *Microchem. J.* **81** (2005) 191
- K. M. Khan, M. Khan, M. Ali, M. Taha, S. Rasheed, S. Perveen, M. I. Choudhary, *Bioorg. Med. Chem.* **17** (2009) 7795
- R. M. Issa, A. M. Khedr, H. Rizk, *J. Chin. Chem. Soc.* **55** (2008) 875
- K. Mahajan, N. Fahmi, R.V. Singh, *Indian J. Chem., A* **46** (2007) 1221
- K. Sharma, R. Singh, N. Fahmi, R. V. Singh, *Spectrochim. Acta, A* **75** (2010) 422
- K. Mohanan, B. S. Kumari, G. Rijulal, *J. Rare Earths* **26** (2008) 16
- Y. Sun, M. L. Machala, F. N. Castellano, *Inorg. Chim. Acta* **363** (2010) 283
- R. Garg, M. K. Saini, N. Fahmi, R. V. Singh, *Transition Met. Chem.* **31** (2006) 362
- K. Mahajan, M. Swami, R.V. Singh, *Russ. J. Coord. Chem.* **35** (2009) 179
- R. K. Dubey, U. K. Dubey, C. M. Mishra, *Indian J. Chem., A* **47** (2008) 1208
- A. P. Mishra, N. Sharma, R. Jain, *J. Indian Chem. Soc.* **88** (2011) 1429
- N. Raman, S. J. Raja, J. Joseph, J. D. Raja, *J. Chil. Chem. Soc.* **52** (2007) 1138
- A. Ourari, K. Ouari, W. Moumeni, L. Sibous, *Transition Met. Chem.* **31** (2006) 169
- I. S. Ahmed, M. A. Kassem, *Spectrochim. Acta, A* **77** (2010) 359
- B. Wrackmeyer, *Annu. Rep. NMR Spectrosc.* **16** (1985) 73
- J. M. Fernandez-G, F. del Rio-Portillo, B. Quiroz-Garcia, R. A. Toscano, R. Salcedo, *J. Mol. Struct.* **561** (2001) 197
- K. Nakamoto, *Infrared and Raman Spectra of Inorganic and Coordination Compounds*, Part A and B, 5th ed. Wiley, New York, USA, 1998
- M. M. Omar, G. G. Mohammed, *Spectrochim. Acta, A* **61** (2005) 929
- A. P. Mishra, R. K. Mishra, S. P. Shrivastava, *J. Serb. Chem. Soc.* **74** (2009) 523
- M. A. Neelakantan, S. S. Marriappan, J. Dharmaraja, T. Jeyakumar, K. Muthukumaran, *Spectrochim. Acta, A* **71** (2008) 628
- S. Samadhiya, A. Halve, *Orient. J. Chem.* **17** (2001) 119
- A. B. P. Lever, *Inorganic Electronic Spectroscopy*, 2nd ed. Elsevier, New York, 1984
- S. Chandra, D. Jain, A. K. Sharma, P. Sharma, *Molecules* **14** (2009) 174
- R. L. Dutta, A. Syamal, *Elements of Magneto Chemistry*, 2nd ed., Affiliated East West Press, New Delhi, 1993
- S. Chandra, A. K. Sharma, *Spectrochim. Acta, A* **74** (2009) 271
- A. P. Mishra, L. R. Pandey, *Indian J. Chem., A* **44** (2005) 94
- B. J. Hathaway, D. E. Billing, *Coord. Chem. Rev.* **5** (1970) 143
- A. A. Soliman, G. G. Mohamed, *Thermochim. Acta* **421** (2004) 151



38. G. G. Mohamed, M. M. Omar, A. M. Hindy, *Turk J. Chem.* **30** (2006) 361
39. G. O. Piloyan, O. S. Novikova, *Russ J. Inorg. Chem.* **12** (1966) 31
40. A. W. Coats, J. P. Redfern, *Nature* **201** (1964) 68
41. G. G. Mohamed, M. M. Omar, A. A. Ibrahim, *Eur. J. Med. Chem.* **44** (2009) 4801
42. M. Thankamony, B. Sindhu Kumari, G. Rijulal, K. Mohanan, *J. Therm. Anal. Cal.* **95** (2009) 259
43. R. N. Patel, V. L. N. Gundla, D. K. Patel, *Polyhedron* **27** (2008) 1054
44. R. N. Patel, *Indian J. Chem., A* **48** (2009) 1370
45. M. S. Sujamol, C. J. Athira, Y. Sindhu, K. Mohanan, *Spectrochim. Acta, A* **75** (2010) 106
46. V. N. Patange, B. R. Arbad, *J. Indian Chem. Soc.* **84** (2007) 1096
47. M. G. Wahed, H. A. Bayoumi, M. I. Mohamme, *Bull. Korean Chem. Soc.* **24** (2003) 1313.
48. A. P. Mishra, L. R. Pandey, *Indian J. Chem., A* **44** (2005) 1800
49. J. T. Makode, A. R. Yaul, S. G. Bhadange, A. S. Aswar, *Russ. J. Inorg. Chem.* **54** (2009) 1372
50. Z. H. Chohan, H. Pervez, A. Rauf, K. M. Khan, C. T. Supuran, *J. Enzym. Inhib. Med. Chem.* **39** (2004) 417
51. Z. H. Chohan, *Met-Based Drugs* **6** (1999) 75
52. R. R. Coombs, S. A. Westcott, A. Decken, F. J. Baerlocher, *Transition Met. Chem.* **30** (2005) 411
53. B. G. Tweedy, *Phytopathology* **55** (1964) 910.



SUPPLEMENTARY MATERIAL TO
**Microwave synthesis and spectral, thermal and antimicrobial
activities of some novel transition metal complexes
with tridentate Schiff base ligands**

RAJENDRA JAIN* and ANAND P. MISHRA

Department of Chemistry, Synthetic Inorganic and Coordination Chemistry Laboratories,
Dr. H. S. Gour Central University, Sagar M.P. 470 003, India

J. Serb. Chem. Soc. 77 (8) (2012) 1013–1–29

Table S-I. Analytical and molar conductance data of the compounds

Compound Empirical formula (FW)	Elemental analysis, Found (Calcd.), %				$\Lambda_m / \Omega^{-1} \text{cm}^2 \text{mol}^{-1}$
	C	H	N	M	
BSAP	49.02	3.07	9.50	—	—
$\text{C}_{12}\text{H}_9\text{N}_2\text{O}_2\text{Br}$ (293.12)	(49.17)	(3.09)	(9.56)		
$[\text{Cr}(\text{BSAP})(\text{H}_2\text{O})_3]\text{Cl}$	33.29	2.98	6.45	11.97	92.5
$\text{C}_{12}\text{H}_7\text{N}_2\text{O}_2\text{BrClCr}$ (432.60)	(33.32)	(3.03)	(6.48)	(12.01)	
$[\text{Co}(\text{BSAP})(\text{H}_2\text{O})_3]$	35.65	3.20	6.87	14.55	17.6
$\text{C}_{12}\text{H}_{13}\text{N}_2\text{O}_5\text{BrCo}$ (404.08)	(35.67)	(3.24)	(6.93)	(14.58)	
$[\text{Ni}(\text{BSAP})(\text{H}_2\text{O})_3]$	35.65	3.19	6.90	14.50	11.5
$\text{C}_{12}\text{H}_{13}\text{N}_2\text{O}_5\text{BrNi}$ (403.84)	(35.69)	(3.24)	(6.94)	(14.53)	
$[\text{Cu}(\text{BSAP})(\text{H}_2\text{O})]$	38.67	2.39	7.49	17.0	12.8
$\text{C}_{12}\text{H}_9\text{N}_2\text{O}_3\text{BrCu}$ (372.66)	(38.68)	(2.43)	(7.52)	(17.05)	
HNAC	74.35	4.11	3.58	—	—
$\text{C}_{24}\text{H}_{16}\text{NO}_2\text{Cl}$ (385.84)	(74.41)	(4.18)	(3.63)		
$[\text{Cr}(\text{HNAC})(\text{H}_2\text{O})\text{Cl}_2]$	54.80	3.07	2.58	9.47	56.6
$\text{C}_{24}\text{H}_{17}\text{NO}_3\text{Cl}_3\text{Cr}$ (525.75)	(54.83)	(3.10)	(2.66)	(9.89)	
$[\text{Co}(\text{HNAC})\text{Cl}] \cdot 2\text{H}_2\text{O}$	55.86	3.17	2.61	11.29	36.4
$\text{C}_{24}\text{H}_{19}\text{NO}_4\text{Cl}_2\text{Co}$ (515.25)	(55.94)	(3.72)	(2.72)	(11.44)	
$[\text{Ni}(\text{HNAC})\text{Cl}] \cdot 3\text{H}_2\text{O}$	54.00	3.91	2.55	10.95	30.6
$\text{C}_{24}\text{H}_{21}\text{NO}_5\text{Cl}_2\text{Ni}$ (533.03)	(54.08)	(3.97)	(2.63)	(11.01)	
$[\text{Cu}(\text{HNAC})\text{Cl}] \cdot 2\text{H}_2\text{O}$	55.36	3.60	2.60	12.02	49.5
$\text{C}_{24}\text{H}_{19}\text{NO}_4\text{Cl}_2\text{Cu}$ (519.86)	(55.45)	(3.68)	(2.69)	(12.22)	

*Corresponding author. E-mail: rajendrajain85@rediffmail.com

Table S-II. IR bands (cm^{-1}) of the Schiff base ligands and their complexes

Compound	$\nu(\text{OH})/\delta(\text{OH})$	$\nu(\text{C}=\text{N})$	$\nu(\text{C}-\text{O})$	$\nu(\text{C}=\text{N})$ (pyridine ring)	$\nu(\text{C}=\text{O})$	$\nu(\text{M}-\text{O})$	$\nu(\text{M}-\text{N})$
BSAP	3150/ 1361	1625	1268	1496	—	—	—
[Cr(BSAP)(H ₂ O) ₃]Cl	—	1596	1290	1495	—	522	490
[Co(BSAP)(H ₂ O) ₃]	—	1603	1295	1492	—	538	486
[Ni(BSAP)(H ₂ O) ₃]	—	1607	1288	1494	—	540	495
[Cu(BSAP)(H ₂ O)]	—	1606	1292	1495	—	526	497
HNAC	3230/ 1336	1613	1236	—	1675	—	—
[Cr(HNAC)(H ₂ O)Cl ₂]	—	1589	1260	—	1640	519	488
[Co(HNAC)Cl] \cdot 2H ₂ O	—	1594	1255	—	1652	524	492
[Ni(HNAC)Cl] \cdot 3H ₂ O	—	1590	1258	—	1647	527	489
[Cu(HNAC)Cl] \cdot 2H ₂ O	—	1582	1263	—	1645	529	485

Table S-III. Magnetic moment values, electronic spectral data and ligand field parameters data of the complexes

Complex	$\mu_{\text{eff}}/\mu_{\text{B}}$	$\lambda_{\text{max}}/\text{cm}^{-1}$	Band assignments	Ligand field parameter			
				$10Dq/\text{cm}^{-1}$	B/cm^{-1}	$\beta/\%$	$LFSE/\text{kJ mol}^{-1}$
[Cr(BSAP)(H ₂ O) ₃]Cl	3.88	16654 24212 35982	$^4\text{A}_{2g}\rightarrow^4\text{T}_{2g}(\text{F})$ $^4\text{A}_{2g}\rightarrow^4\text{T}_{1g}(\text{F})$ $^4\text{A}_{2g}\rightarrow^4\text{T}_{1g}(\text{P})$	16654	794.97	0.77	22.82
[Co(BSAP)(H ₂ O) ₃]	5.02	9486 15823 20618	$^4\text{T}_{1g}\rightarrow^4\text{T}_{2g}(\text{F})$ $^4\text{T}_{1g}\rightarrow^4\text{A}_{2g}(\text{F})$ $^4\text{T}_{1g}\rightarrow^4\text{T}_{1g}(\text{P})$	10696	822.75	0.73	26.54
[Ni(BSAP)(H ₂ O) ₃]	3.04	10691 20360 23838	$^3\text{A}_{2g}\rightarrow^3\text{T}_{2g}(\text{F})$ $^3\text{A}_{2g}\rightarrow^3\text{T}_{1g}(\text{F})$ $^3\text{A}_{2g}\rightarrow^3\text{T}_{1g}(\text{P})$	10691	808.33	0.78	22.35
[Cu(BSAP)(H ₂ O)]	1.92	15150 19230	$^2\text{B}_{1g}\rightarrow^2\text{B}_{2g}$ $^2\text{B}_{1g}\rightarrow^2\text{E}_g$	—	—	—	—
[Cr(HNAC)(H ₂ O)Cl ₂]	3.84	16871 23837 34942	$^4\text{A}_{2g}\rightarrow^4\text{T}_{2g}(\text{F})$ $^4\text{A}_{2g}\rightarrow^4\text{T}_{1g}(\text{F})$ $^4\text{A}_{2g}\rightarrow^4\text{T}_{1g}(\text{P})$	16871	704.34	0.68	31.62
[Co(HNAC)Cl] \cdot 2H ₂ O	4.32	— 14142 19514	$^4\text{A}_{2}\rightarrow^4\text{T}_2(\text{F})$ $^4\text{A}_{2}\rightarrow^4\text{T}_1(\text{F})$ $^4\text{A}_{2}\rightarrow^4\text{T}_1(\text{P})$	—	—	—	—
[Ni(HNAC)Cl] \cdot 3H ₂ O	Dia.	12748 20750 —	$^1\text{A}_{1g}\rightarrow^1\text{E}_g$ $^1\text{A}_{1g}\rightarrow^1\text{B}_{2g}$ $^1\text{A}_{1g}\rightarrow^1\text{B}_{1g}$	—	—	—	—
[Cu(HNAC)Cl] \cdot 2H ₂ O	1.81	15110 19456	$^2\text{B}_{1g}\rightarrow^2\text{B}_{2g}$ $^2\text{B}_{1g}\rightarrow^2\text{E}_g$	—	—	—	—



Table S-IV. Kinetic and thermodynamic parameters of the complexes

Complex	Method ^a	Dec. stage	E^* $t / ^\circ\text{C}$	Z kJ mol^{-1}	ΔS^* s^{-1}	ΔH^* $\text{J K}^{-1} \text{mol}^{-1}$	ΔG^* kJ mol^{-1}
$[\text{Co(BSAP)(H}_2\text{O)}_3]$	P-N	I st /185	31.39	5.47×10^{-6}	-349.28	22.62	182.59
	C-R		51.64	6.44×10^1	-213.88	42.87	140.83
	P-N	II nd /342	59.51	3.78×10^{-3}	-297.35	47.75	230.32
	C-R		87.86	1.57×10^6	-132.32	76.11	157.35
	P-N	III rd /559	64.43	9.33×10^{-7}	-368.95	48.50	355.47
	C-R		112.79	6.04×10^3	-181.10	96.86	247.53
$[\text{Ni(HNAC)Cl}] \cdot 3\text{H}_2\text{O}$	P-N	I st /98	31.61	3.03×10^{-3}	-294.99	24.51	133.95
	C-R		49.23	3.90×10^4	-158.86	42.13	101.06
	P-N	II nd /354	49.41	1.22×10^{-5}	-345.22	37.41	253.86
	C-R		71.07	4.23×10^1	-219.99	59.07	197.01
	P-N	III rd /537	81.75	1.71×10^{-3}	-306.27	66.24	314.32
	C-R		123.04	1.87×10^6	-133.16	107.53	215.39

^aP-N: Piloyan-Novikova¹; C-R: Coats-Redfern²

REFERENCES

1. G. O. Piloyan, O. S. Novikova, *Russ. J. Inorg. Chem.* **12** (1966) 31
2. A. W. Coats, J. P. Redfern, *Nature* **201** (1964) 68.



Vertex-degree-based molecular structure descriptors of benzenoid systems and phenylenes

IVAN GUTMAN* and BORIS FURTULA**

Faculty of Science, University of Kragujevac, P. O. Box 60, 34000 Kragujevac, Serbia

(Received 12 December 2011)

Abstract. Several recently published papers report expressions for various vertex-degree-based molecular structure descriptors of benzenoid systems and phenylenes. Herein, the general expression for these descriptors is deduced, and it is shown that a simple and generally valid relation exists between such structure descriptors of phenylenes and their hexagonal squeezes.

Keywords: molecular structure descriptor; topological index; degree-based molecular structure descriptor; benzenoid system; phenylene; hexagonal squeeze.

INTRODUCTION

Let G be a molecular graph¹ and v its vertex. The *degree* of the vertex v , denoted by $d(v)$, is the number of the first neighbors of v . A large number of molecular structure descriptors (topological indices), defined in terms of vertex degrees, has been considered in the literature.^{2,3} The general form of these descriptors is:

$$D = D(G) = \sum_{u \sim v} \psi(d(u), d(v)) \quad (1)$$

where the summation goes over all pairs of adjacent vertices u, v of the molecular graph G .

In particular, the function ψ in Eq. (1) has the following forms:

$$\psi(p, q) = \frac{1}{\sqrt{pq}}, \text{ for the Randić index,}^4$$

$$\psi(p, q) = (pq)^\lambda, \text{ for the general Randić index,}^5$$

where λ is an adjustable parameter,

$$\psi(p, q) = pq, \text{ for the second Zagreb index,}^6$$

Correspondence. E-mail: *gutman@kg.ac.rs; **boris.furtula@gmail.com
doi: 10.2298/JSC111212029G

$$\psi(p,q) = \sqrt{\frac{2(p+q-2)}{pq}}, \text{ for the atom-bond connectivity index,}^7$$

$$\psi(p,q) = \frac{1}{\sqrt{p+q}}, \text{ for the sum-connectivity index,}^8$$

$$\psi(p,q) = (p+q)^\lambda, \text{ for the general sum-connectivity index,}^9$$

where λ is an adjustable parameter,

$$\psi(p,q) = \frac{\sqrt{pq}}{\frac{1}{2}(p+q)}, \text{ for the geometric-arithmetic index,}^{10}$$

$$\psi(p,q) = \left(\frac{pq}{p+q-2} \right)^3, \text{ for the augmented Zagreb index,}^{11}$$

$$\psi(p,q) = \frac{2}{p+q}, \text{ for the harmonic index.}^{12}$$

In the general case, the calculation of a particular structure descriptor D is not quite easy, and finding molecular graphs possessing extremal (maximal or minimal) values of D is even more difficult. However, in the case of benzenoid systems and phenylenes, this task is much simpler. Namely, the molecular graphs of the latter systems possess only vertices of degree 2 and 3, and therefore there are only three types of contributions $\psi(p,q)$ occurring in the summation on the right-hand side of Eq. (1). Indeed, if m_{22} , m_{23} and m_{33} denote, respectively, the number of edges connecting two vertices of degree 2, the number of edges connecting vertices of degree 2 and 3, and the number of edges connecting two vertices of degree 3, then:

$$D = m_{22} \psi(2,2) + m_{23} \psi(2,3) + m_{33} \psi(3,3) \quad (2)$$

and, moreover, simple expressions for the structure-dependency of the coefficients m_{22} , m_{23} , m_{33} are available (see below). In spite of this, recently a number of papers appeared in which some of the above listed degree-based structure descriptors were studied for benzenoids and phenylenes: general Randić index,^{13,14} atom-bond connectivity index,^{14–16} general sum-connectivity index,^{14,17,18} geometric–arithmetic index.^{14,19} All these were preceded by an analogous study of the Randić index, realized more than ten years ago.²⁰

It will now be shown how the general solution of this problem can (easily) be achieved. By this, it is hoped that the appearance of additional publications of the same kind as those mentioned above^{13–20} will cease.



GENERAL EXPRESSIONS FOR THE INDEX D OF BENZENOID SYSTEMS AND PHENYLENES

The structural features of benzenoid systems are described in detail in the book.²¹ The analogous properties of phenylenes and their hexagonal squeezes were established in the paper.²⁰ Self-explanatory examples of benzenoid systems, phenylenes, and their hexagonal squeezes are provided in Fig. 1.

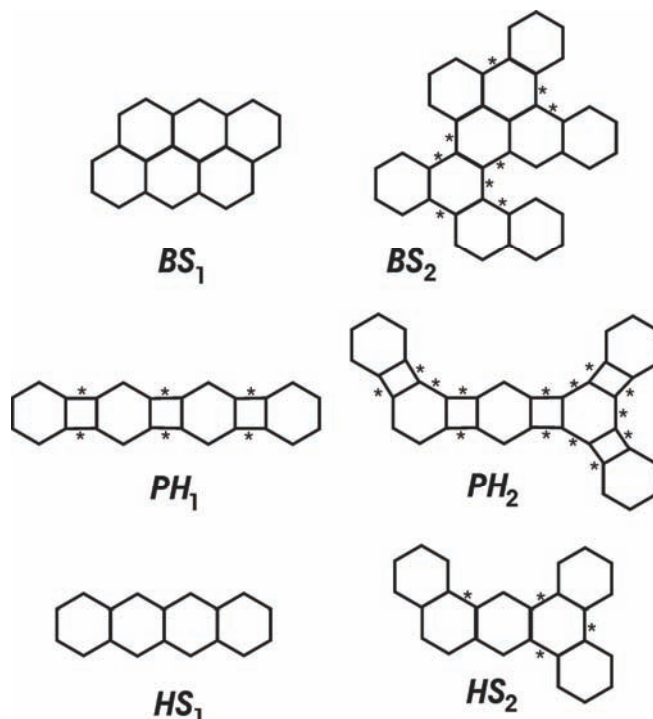


Fig. 1. Examples of benzenoid systems (BS_1 and BS_2), phenylenes (PH_1 and PH_2), and hexagonal squeezes (HS_1 and HS_2). The hexagonal squeeze HS_i corresponds to the phylene PH_i ; $i = 1, 2$. The edges on the perimeter connecting two vertices of degree 3 are indicated by asterisks; their count is b . Thus, $b(BS_1) = 0$, $b(BS_2) = 9$, $b(PH_1) = 6$, $b(PH_2) = 14$, $b(HS_1) = 0$ and $b(HS_2) = 4$.

The basic properties of a benzenoid system are determined²¹ by the number of hexagons (h) and internal vertices (n_i). For instance, the formula of the respective benzenoid hydrocarbon is $C4h+2-n_i H2h+4-n_i$. In the examples depicted in Fig. 1, $h(BS_1) = 6$, $h(BS_2) = 10$, $n_i(BS_1) = 4$, $n_i(BS_2) = 2$.

Let b be the number of edges on the perimeter, connecting two vertices of degree 3 (this parameter is usually referred to as the “number of bays”). Then, for a benzenoid system BS , one has:²¹

$$\begin{aligned}m_{22}(BS) &= b + 6 \\m_{23}(BS) &= 4h - 2b - 2n_i - 4 \\m_{33}(BS) &= h + b + n_i - 1\end{aligned}$$

which combined with Eq. (2) immediately implies:

$$\begin{aligned}D(BS) &= [6\psi(2,2) + (4h - 2n_i - 4)\psi(2,3) + (h + n_i - 1)\psi(3,3)] + \\&\quad + b[\psi(2,2) - 2\psi(2,3) + \psi(3,3)]\end{aligned}$$

Phenylenes have no internal vertices, and their structural relations are significantly simpler. One has:²⁰

$$\begin{aligned}m_{22}(PH) &= 8 - 2h + b \\m_{23}(PH) &= 8h - 2b - 8 \\m_{33}(PH) &= 2h + b - 2\end{aligned}$$

resulting in:

$$\begin{aligned}D(PH) &= [(8 - 2h)\psi(2,2) + (8h - 8)\psi(2,3) + (2h - 2)\psi(3,3)] + \\&\quad + b[\psi(2,2) - 2\psi(2,3) + \psi(3,3)]\end{aligned}$$

Interestingly, the coefficient of the parameter b is same for both BS and PH . Therefore, if this coefficient, namely $\psi(2,2) - 2\psi(2,3) + \psi(3,3)$, is positive-valued, then the benzenoid system with h hexagons and n_i internal vertices and the phylene with h hexagons will have maximal (resp. minimal) D -index if b is maximal (resp. minimal). If $\psi(2,2) - 2\psi(2,3) + \psi(3,3)$ is negative-valued, the situation is reversed.

Recall that in the case of benzenoid systems, the minimal value of the parameter b is zero (as, for instance, for BS_1), whereas in the case of phenylenes it is $2h - 2$ (as, for instance, for PH_1).

By this simple reasoning, the general solution of the problem considered is arrived at, and the benzenoid systems and phenylenes with minimal and maximal D index characterized.

RELATING THE INDEX D OF PHENYLENES AND THEIR HEXAGONAL SQUEEZES

The concept of “hexagonal squeeze” (HS) was introduced²² in the 1990s, and since then it has played an important role in the theory of phenylenes. The way in which a hexagonal squeeze (which is a catacondensed benzenoid system) is associated with a phylene is seen from Fig. 1. It is easy to recognize that for a hexagonal squeeze HS corresponding to the phylene PH the following identities hold: $m_{22}(HS) = m_{22}(PH)$ and $m_{23}(HS) = m_{23}(PH)$. This means that:

$$D(PH) - D(HS) = [m_{33}(PH) - m_{33}(HS)]\psi(3,3).$$

Because, in addition:



$$m_{33}(HS) = b(HS) + h - 1 = b(PH) - h + 1$$

one arrives at the remarkably simple formula:

$$D(PH) - D(HS) = 3(h-1)\psi(3,3)$$

the special cases of which were reported several times.^{13–15,17–20} We hope that this will not be repeated also in the future.

Acknowledgement. The authors thank the Ministry of Education, Science and Technological Development of the Republic of Serbia for support (Grant No. 174033).

ИЗВОД

НА СТЕПЕНИМА ЧВОРОВА ЗАСНОВАНИ МОЛЕКУЛСКИ СТРУКТУРНИ ДЕСКРИПТОРИ БЕНЗЕНОИДНИХ СИСТЕМА И ФЕНИЛЕНА

ИВАН ГУТМАН И БОРИС ФУРТУЛА

Природно-математички факултет Универзитета у Крагујевцу

Већи број недавно објављених радова наводи формуле за различите, на степенима чвррова засноване, молекулске структурне дескрипторе бензеноидних система и фенилена. У овом раду је дат општи израз за ове дескрипторе и показано је да у општем случају постоји једноставна релација између ових дескриптора за фенилене и за њихове хексагоналне основе.

(Примљено 12. децембра 2011)

REFERENCES

1. N. Trinajstić, *Chemical Graph Theory*, CRC Press, Boca Raton, FL, USA, 1983
2. R. Todeschini, V. Consonni, *Molecular Descriptors for Chemoinformatics*, Vols. 1 & 2, Wiley-VCH, Weinheim, Germany, 2009
3. *Novel Molecular Structure Descriptors – Theory and Applications*, I. Gutman, B. Furtula, Eds., Vols. 1 and 2, Univ. Kragujevac, Kragujevac, Serbia, 2010
4. M. Randić, *J. Am. Chem. Soc.* **97** (1975) 6609
5. X. Li, I. Gutman, *Mathematical Aspects of Randić-type Molecular Structure Descriptors*, Univ. Kragujevac, Kragujevac, Serbia, 2006
6. I. Gutman, N. Trinajstić, *Chem. Phys. Lett.* **17** (1972) 535
7. E. Estrada, L. Torres, L. Rodríguez, I. Gutman, *Indian J. Chem.* **37A** (1998) 849
8. B. Zhou, N. Trinajstić, *J. Math. Chem.* **46** (2009) 1252
9. B. Zhou, N. Trinajstić, *J. Math. Chem.* **47** (2010) 210
10. D. Vukičević, B. Furtula, *J. Math. Chem.* **46** (2010) 1369
11. B. Furtula, A. Graovac, D. Vukičević, *J. Math. Chem.* **48** (2010) 370
12. L. Zhong, *Appl. Math. Lett.* **25** (2012) 561
13. R. Wu, H. Deng, *MATCH Commun. Math. Comput. Chem.* **64** (2010) 459
14. H. Deng, J. Yang, F. Xia, *Comput. Math. Appl.* **61** (2011) 3017
15. J. Yang, F. Xia, H. Cheng, *Int. Math. Forum* **6** (2011) 2001
16. X. Ke, *Polycyclic Aromat. Compd.* **32** (2012) 27
17. S. Chen, F. Xia, J. Yang, *Iran. J. Math. Chem.* **1** (2010) 97
18. F. Ma, H. Deng, *J. Comput. Theor. Nanosci.* **8** (2011) 1878
19. L. Xiao, S. Chen, Z. Guo, Q. Chen, *Int. J. Contemp. Math. Sci.* **5** (2010) 2225



20. J. Rada, O. Araujo, I. Gutman, *Croat. Chem. Acta* **74** (2001) 225
21. I. Gutman, S. J Cyvin, *Introduction to the Theory of Benzenoid Hydrocarbons*, Springer Verlag, Berlin, Germany, 1989
22. I. Gutman, *J. Chem. Soc. Faraday Trans.* **89** (1993) 2413.





Quantum-chemical investigation of the photoproduct of the reaction of two 1-methylthymine molecules: the pyrimidine(6-4)pyrimidone adduct

MIROSLAV M. RISTIĆ[#], MILENA PETKOVIĆ^{#*} and MIHAJLO ETINSKI[#]

Faculty of Physical Chemistry, University of Belgrade, Studentski trg 12–16,
P. O. Box 47, 11158 Belgrade, Serbia

(Received 22 May 2012)

Abstract: One of the products of the photochemical reaction induced by UV irradiation of the two 1-methylthymine molecules is pyrimidine(6-4)pyrimidone. Due to the low yield of this product, it is difficult to examine its geometry and vibrational spectrum. In this study, quantum chemical methods were used to characterize the structure of pyrimidine(6-4)pyrimidone. Its three conformers were optimized and their structures compared. Their vibrational frequencies in the harmonic approximation are discussed briefly. It was shown that the most significant changes in the infrared spectra arise from the formation of hydrogen bonds. All calculations were performed both in vacuum and in D₂O.

Keywords: photochemistry, quantum chemistry, density functional theory.

INTRODUCTION

The main chromophores for the absorption of UVA and UVB radiation in DNA and RNA are the nucleic acid bases. Most of the excited-state population of the nucleic acid bases in a low-pressure gas phase relaxes radiationlessly to the electronic ground state on an ultrafast timescale.¹ This fast relaxation prevents the creation of UV damage. Nevertheless, in the pyrimidine bases uracil and thymine, a long-lived dark state is formed to a minor extent.^{2–5} Recent theoretical work^{6–8} and supersonic jet experiments⁴ have shown that this dark state is the T₁ state. In apolar solvents, a significant triplet quantum yield was observed, while in polar protic solvents, the triplet quantum yield was smaller.⁹

There is evidence that the triplet states of nucleic acids are involved in the formation of nucleic acids photo-lesions, which are mutagenic and carcinogenic for skin cells.^{10–13} The most frequent photoreaction of nucleic acids is an intra-

* Corresponding author. E-mail: milena@ffh.bg.ac.rs

[#] Serbian Chemical Society member.

doi: 10.2298/JSC120522061R

strand pyrimidine dimerization. This reaction covalently links two pyrimidine bases and yields mostly the cyclobutane pyrimidine dimer (CPD) and a small amount of the pyrimidine(6-4)pyrimidone adduct ((6-4)PP), Fig. 1. The former product is formed in a [2+2] cycloaddition reaction between adjacent bases, while the latter arises from a Paterno–Büchi cycloaddition, followed by thermal ring opening of the oxetane intermediate. The adduct exposed to UVB light can be further photochemically transformed to its Dewar valence photo-isomer, the so-called Dewar PP. In mammalian cells, UV-induced bipyrimidine photoproducts are removed *via* nucleotide excision repair (NER), by either transcription-coupled repair (TCR) or global genomic repair (GGR).¹⁴ The repair kinetics and efficiencies of UV-induced damage vary considerably from one type of phot lesion to another and also between different species.¹⁴ Both PP products are less investigated than CPD because of the low reaction yield and difficult detection. Hence, more work is required to understand the mechanism of their formation and repair.

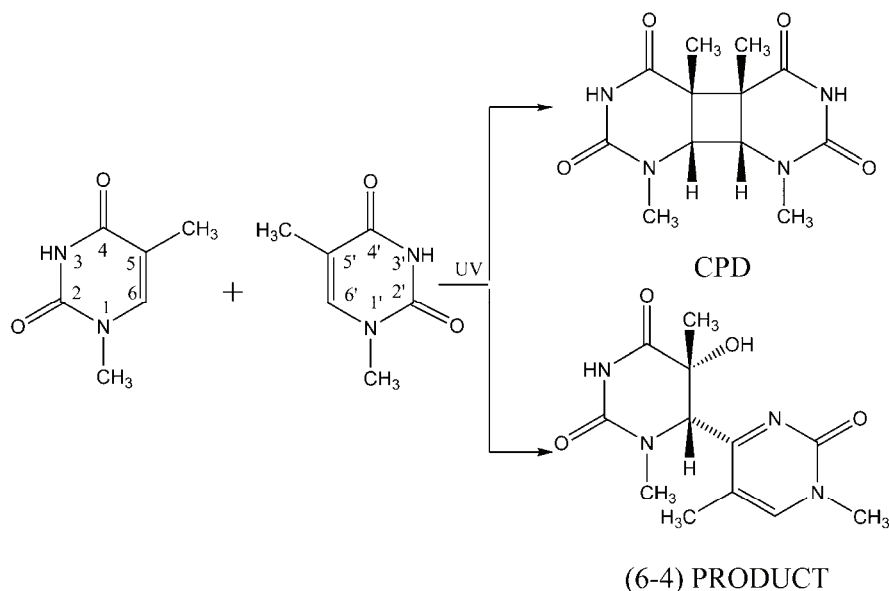


Fig. 1. Chemical structures and atom labels of the 1-methylthymine photoproducts: cyclobutane pyrimidine dimer (CPD) and pyrimidine(6-4)pyrimidone adduct.

In the present study, the pyrimidine(6-4)pyrimidone adduct, created by the photochemical reaction of two 1-methylthymine molecules, was analyzed by means of a quantum-chemical method. Thymine is a pyrimidine base that has the highest yield of dimerization photoproducts. The methylated compound was chosen for analysis because methylation in position one plays the role of sugar in

DNA. The ground state structure of (6-4)PP was characterized in vacuum and also in D₂O. The solvent D₂O was chosen because experiments concerning the detection of vibrational motion are usually performed in this solvent. Three conformers were found, and their structure and stability were characterized. In addition, their vibrational spectra were calculated and assigned.

COMPUTATIONAL DETAILS

All calculations were performed with the GAUSSIAN program package.¹⁵ The density functional theory (DFT) with B3-LYP functional¹⁶ was employed for electronic structure calculations. All calculations were realized in C₁ point-group symmetry. The optimization was performed with *tight* convergence criteria due to the presence of methyl groups and low frequency modes that involve methyl rotation. The Dunning's¹⁷ correlation-consistent basis set cc-pVTZ (C, N, O, 10s5p2d1f /4s3p2d1f; H, 5s2p1d /3s2p1d) was used. In order to take into account the electrostatic interactions in the polar solvent (D₂O), the Onsager Model,^{18,19} in which the solute is imbedded in a spherical cavity of a continuum medium characterized by its dielectric constant, was employed. The dielectric constant of D₂O was taken to be $\epsilon = 78.06$. All vibrational frequencies were calculated within the harmonic approximation.

RESULTS AND DISCUSSION

The molecular geometries

The ground state structure of (6-4)PP was optimized in vacuum and in D₂O. Three conformers were found, which were labeled K1, K2 and K3 according to their stability. Their electronic energies with and without zero-point correction and their dipole moments are presented in Table I.

TABLE I. Electronic energy (relative to the most stable conformer in D₂O), sum of the electronic and zero-point vibrational energy and dipole moment of the conformers in vacuum and in D₂O

Parameter	K1	K2	K3
E_{el} / cm^{-1}	1323	3235	3266
$E_{el+zpv} / \text{cm}^{-1}$	64309	66244	66227
μ / D	7.49	3.58	10.41
$E_{el,D_2O} / \text{cm}^{-1}$	0	2872	537
$E_{el+zpv,D_2O} / \text{cm}^{-1}$	62985	65859	63544
μ_{D_2O} / D	9.71	4.77	14.02

The K1 conformer is the most stable one. Its optimized geometry with the most significant bond lengths is presented in Fig. 2. This structure was also found by Ai *et al.* using the CASSCF(10,8)/6-31G(d) method.¹¹ Its pyrimidone ring is planar. On the other hand, the pyrimidine ring is non-planar. The dihedral angles C₂-N₃-C₄-C₅ and C₂-N₁-C₆-C₅ in the pyrimidine ring are 15 and 42 degrees, respectively. The two rings are almost orthogonal (the dihedral angle C₅-C₆-C₄-N₃ is 86 degrees). The C₂=O and C₄=O bond lengths are 1.21 and 1.22 Å, respectively. Ai *et al.*¹¹ found slightly shorter bonds, namely 1.19 and 1.20 Å.



There is a general tendency that the CASSCF bonds obtained by Ai *et al.* are shorter than are those found in this study. This is because the CASSCF method does not include the dynamic correlation required for the correct description of the electronic energy in the vicinity of the potential minimum. The C_6-N_1' bond is 1.35 Å while the $C_4'-N_3'$ bond is 1.30 Å long. This means that the former bond is weaker and is not strictly of a double bond character as is presented in the valence-bond structure in Fig. 1. The C_6-C_4' bond is 1.54 Å long and it is a single bond that allows ring rotation. The O–H bond is orientated toward the oxygen that is connected to the C_4 atom. This orientation stabilizes the energy of the molecule by the formation of an intramolecular hydrogen bond. The hydrogen bond length (defined by the distance between the bridging hydrogen and the acceptor oxygen) amounts to 2.05 Å. There are 102 normal modes, which results in large zero-point energy, 62985 cm⁻¹.

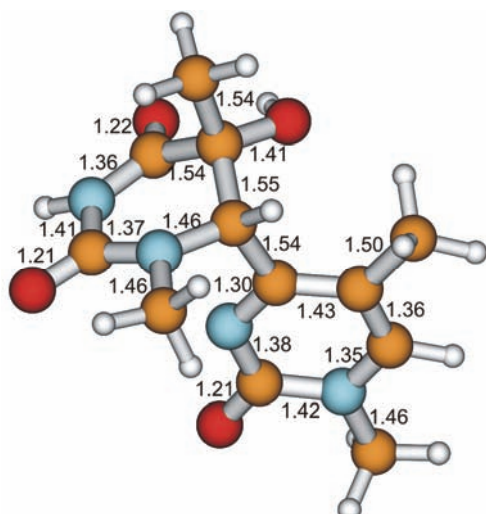


Fig. 2. The optimized geometry of the K1 conformer. All bond lengths are in Å.

The optimized geometry of the K2 conformer is displayed in Fig. 3. Its electronic energy is 1912 cm⁻¹ higher than that of the K1 conformer. Rotation around the C_6-C_4' bond can transform it into the K1 conformer. The dihedral angle $C_5-C_6-C_4'-N_3'$ between the pyrimidine and pyrimidone rings is 111 degrees. The differences in the bond lengths in the K1 and K2 conformers are not larger than 0.01 Å. The pyrimidine bonds of the two conformers are more distinctive. This is due to the steric effects induced by the interaction of the methyl group from the pyrimidone ring and the pyrimidine ring in the K2 conformer. The intramolecular hydrogen bond is 2.11 Å. The zero-point energy of the K2 conformer is 24 cm⁻¹ larger than the zero-point energy of the K1 structure.

The K3 conformer is the least stable. Its electronic energy is 31 cm^{-1} higher than that of K2 and 1943 cm^{-1} higher than that of the K1 conformer. The optimized geometry of the K3 conformer with the most significant bond lengths is presented in Fig. 4. The angle between the pyrimidine and pyrimidone rings is 57 degrees. The dihedral angles $\text{C}_2-\text{N}_3-\text{C}_4-\text{C}_5$ and $\text{C}_2-\text{N}_1-\text{C}_6-\text{C}_5$ in the pyrimidine ring are 3 and 44 degrees, respectively. The K3 conformer has the lowest zero-point energy of all three conformers, it is 25 cm^{-1} lower than the zero-point energy of K1. The hydrogen bond in the K3 conformer is formed between the two rings and is of $\text{O}-\text{H}\cdots\text{N}$ type in the contrast to hydrogen bonds in K1 and K2 conformers that are formed within the same ring, and both the donor and the acceptor are oxygen atoms. The hydrogen bond length in the K3 conformer amounts to 1.9 \AA . It lowers the dihedral angle between the two rings (it is close to 90 degrees in the most stable conformation), which increases the tension in the system, making it less stable.

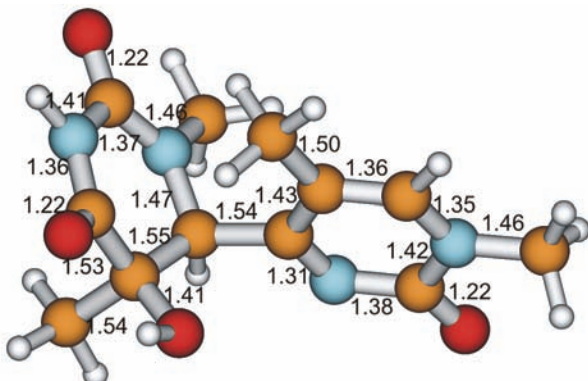


Fig. 3. The optimized geometry of the K2 conformer. All bond lengths are in \AA .

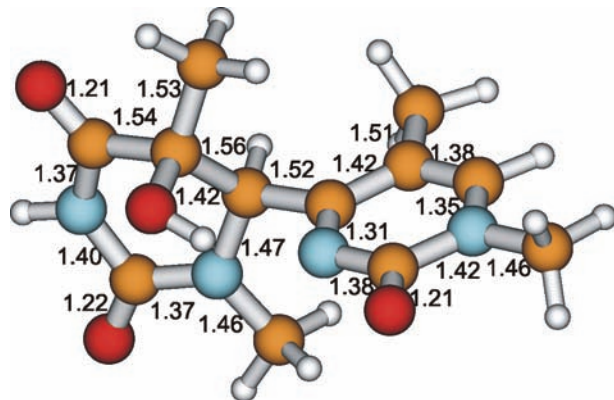


Fig. 4. The optimized geometry of the K3 conformer. All bond lengths are in \AA .

It is interesting to examine whether solvation in D₂O modifies the relative stability of the three conformers. The K3 conformer has the largest dipole moment in vacuum (10.41 D) while the K2 conformer has the smallest (3.58 D). The dipole moment in the K1 conformer is 7.49 D. Therefore, it is expected that solvation would considerably modify the electronic energy of the K3 and K1 conformers. The increase of stability due to solvation is 1323, 363 and 2730 cm⁻¹ for K1, K2 and K3 conformers, respectively. The energy of the K3 conformer decreased the most so that it became the second most stable conformer, 537 cm⁻¹ higher in energy than the K1 conformer and 2335 lower in energy than the K2 conformer. This is expected due to this conformer having the largest value of the dipole moment. The dipole moments of the conformers in D₂O are 9.71, 4.77 and 14.02 D, respectively. Although the solvation modifies the electronic energies, the bond lengths remain almost unchanged. The largest bond change was 0.01 Å.

The vibrational properties

The vibrational spectra were calculated in the harmonic approximation, Fig. 5. As mentioned before, there are 102 vibrational degrees of freedom. Attention will be focused on the O–H, N–H and C=O stretching vibrations and changes in the corresponding peak position and intensity upon conformational change will be analyzed. The frequencies and their intensities in vacuum and in D₂O are listed in Table II.

First, the high frequency region above 3000 cm⁻¹ will be analyzed. This is the region of the X–H stretching modes (X = O, N, C). There are 14 C–H bonds, resulting in 14 C–H stretching modes. Due to the small difference in electronegativity of hydrogen and carbon atoms, the dipole moment does not drastically change upon such vibrational motions, which results in the small intensity of the corresponding peaks. On the other hand, the peak intensities that correspond to O–H and N–H stretching motion are generally large. Therefore, special attention will be paid to these two modes. As mentioned before, hydrogen bonds are formed in all three cases: in conformers K1 and K2, the proton acceptor is the oxygen atom of the pyrimidone ring, whereas in the K3 conformer, the proton acceptor is the nitrogen atom of the pyrimidine ring. Although the electronegativity of the oxygen atom is greater than that of the nitrogen atom, O–H ··· N bonds are usually stronger than O–H ··· O hydrogen bonds.²⁰ This is also the case with the (6-4)PP conformers; thus the harmonic ν_{OH} frequencies equal 3659 and 3700 cm⁻¹ in K1 and K2, respectively, and 3540 cm⁻¹ in K3. The stronger hydrogen bond in K3 weakens the covalent O–H bond, which results in a lower O–H stretching frequency. In a polar solvent such as D₂O, it is expected that hydrogen bonds between the solvent and the solute are formed (in this particular case, the oxygen atom of the hydroxyl group is supposed to play the role of an acceptor, and the solvent molecule of a donor). However, in order to account for the for-



mation of these bonds, it would be necessary to treat the solvent explicitly, which would require substantial memory and CPU time. These interactions are not included in the Onsager Model used in this work; hence, the intermolecular hydrogen bonds are not included. For this reason, the ν_{OH} frequency in K1 undergoes a blue shift upon solvation. On the other hand, this band is red shifted in D₂O compared to vacuum for K2 and K3. Inclusion of the polar environment significantly increases the peak intensities in all cases. This change is especially pronounced for the K3 conformer, where the hydrogen bond is the strongest.

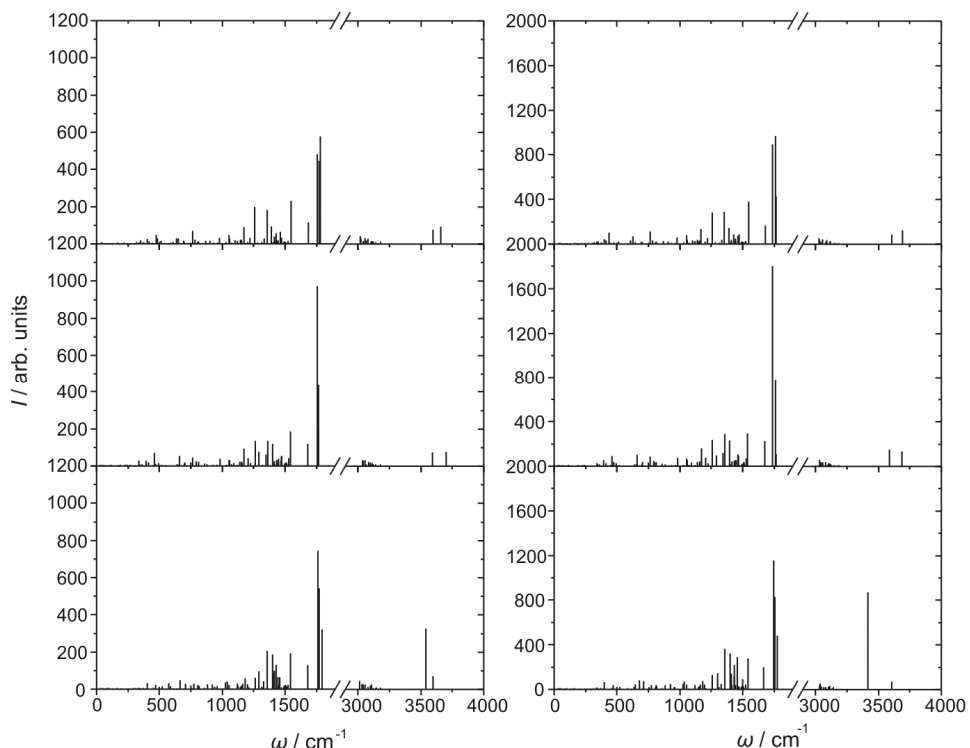


Fig. 5. Vibrational spectra of the conformers in vacuum (left) and D₂O (right). Upper row K1 conformer, middle row K2 conformer and lower row K3 conformer.
There is a break in frequency axis from 1850 to 2950 cm⁻¹.

The situation with the ν_{NH} mode is less complicated: neither the nitrogen nor the hydrogen atoms participate in hydrogen bonding. Therefore, the N–H stretching frequencies do not differ much between the three conformers, and neither after placing the molecules in D₂O. An exception is the significant intensity increase upon solvation of K2.

Considering the three C=O stretching modes, the values of the three frequencies do not drastically differ, neither in vacuum nor in D₂O. An exception is

$\nu_{\text{C}4=\text{O}}$, *i.e.*, the role of an acceptor in hydrogen bonding weakens the $\text{C}_4=\text{O}$ bond in K1 and K2 compared to that in K3; hence, in the last case, the frequency has the highest value. Inclusion of the solvent generally increases the peak intensity. An exception is the peak that corresponds to $\text{C}_2=\text{O}$ stretching motion in K1 and K2, where the presence of the polar environment decreases the peak intensity.

TABLE II. Vibrational frequencies and infrared intensities of the O–H, N–H and C=O stretching vibrations of the three conformers in vacuum/D₂O

Parameter	K1	K2	K3
$\nu_{\text{O}-\text{H}} / \text{cm}^{-1}$	3659/3691	3700/3686	3540/3416
$I_{\text{VO}-\text{H}} / \text{arb. units}$	(91/117)	(73/129)	(324/868)
$\nu_{\text{N}-\text{H}} / \text{cm}^{-1}$	3595/3607	3591/3586	3595/3606
$I_{\text{VN}-\text{H}} / \text{arb. units}$	(73/82)	(72/142)	(68/72)
$\nu_{\text{C}2=\text{O}} / \text{cm}^{-1}$	1781/1767	1767/1767	1769/1757
$I_{\text{VC}2=\text{O}} / \text{arb. units}$	(575/418)	(433/103)	(537/821)
$\nu_{\text{C}4=\text{O}} / \text{cm}^{-1}$	1771/1761	1765/1761	1792/1776
$I_{\text{VC}4=\text{O}} / \text{arb. units}$	(442/963)	(210/776)	(319/476)
$\nu_{\text{C}2'=\text{O}} / \text{cm}^{-1}$	1755/1736	1754/1736	1762/1746
$I_{\text{VC}2'=\text{O}} / \text{arb. units}$	(479/890)	(969/1796)	(741/1147)

CONCLUSIONS

In this contribution, the geometries and vibrational properties of pyrimidine(6-4)pyrimidone, a less stable product of a photoreaction of 1-methylthymine, were investigated. The bond lengths do not differ significantly between the three conformers and the factor that governs the stability of the conformers is the mutual orientation of the pyrimidine and pyrimidone rings. Due to the presence of polar groups, the order of stability of the three conformers changed when the polar environment was introduced (the polar environment mimics the solvent molecules, D₂O).

The corresponding infrared spectra (peak position and intensities) are briefly discussed. The most noticeable changes concern the O–H stretching motion, since this hydroxyl group is involved in intramolecular hydrogen bonding. The vibrational frequencies were computed within the harmonic approximation. A detailed analysis would require inclusion of mode couplings, which would cause not only red shift of the O–H stretching band comparing to the harmonic value, but also band broadening and the appearance of additional peaks.

Acknowledgements. The authors acknowledge Professor Miljenko Perić for helpful discussions and the Ministry of Education, Science and Technological Development of the Republic of Serbia for the financial support (Contract No. 172040).



И З В О Д

КВАНТНО ХЕМИЈСКО ИСПИТИВАЊЕ ФОТОПРОИЗВОДА РЕАКЦИЈЕ ДВА МОЛЕКУЛА 1-МЕТИЛТИМИНА: ПИРИМИДИН(6-4)ПИРИМИДОН АДУКТА

МИРОСЛАВ М. РИСТИЋ, МИЛЕНА ПЕТКОВИЋ и МИХАЈЛО ЕТИНСКИ

*Факултет за физичку хемију, Универзитет у Београду, Студентски трг 12–16,
б. бр. 47, 11158 Београд*

Један од производа фотохемијске реакције инициране UV зрачењем два молекула 1-метилтимина је пиримидин(6-4)пиримидон. Због малог приноса овог производа, тешко је испитати његову геометрију и вибрациони спектар. У овом раду коришћене су квантно хемијске методе да би се карактеризовала структура пиримидин(6-4)пиримидона. Његова три конформера су оптимизована и њихове структуре су поређене. Разматрана су вибрациона својства израчуната у хармонијској апроксимацији. Показано је да се најзначајније промене у инфрацрвеним спектрима јављају као последица обраズовања водоничних веза. Сви прорачуни су извршени и у вакууму и у D₂O.

(Примљено 22. маја 2012)

REFERENCES

1. C. E. Crespo-Hernandez, B. Cohen, P. M. Hare, B. Kohler, *Chem. Rev.* **104** (2004) 1977
2. Y. He, C. Wu, W. Kong, *J. Phys. Chem., A* **107** (2003) 5143
3. M. Busker, M. Nispel, T. Häber, K. Kleinermanns, M. Etinski, T. Fleig, *Chem. Phys. Chem.* **9** (2008) 1570
4. M. Kunitski, Y. Nosenko, B. Brutschy, *Chem. Phys. Chem.* **12** (2011) 1
5. J. González-Vázquez, L. González, E. Samoylova, T. Schultz, *Phys. Chem. Chem. Phys.* **11** (2009) 3927
6. M. Etinski, T. Fleig, C. M. Marian, *J. Phys. Chem., A* **113** (2009) 11809
7. M. Etinski, J. Tatchen, C. M. Marian, *J. Chem. Phys.* **134** (2011) 154105
8. M. Etinski, *J. Serb. Chem. Soc.* **76** (2011) 1649
9. P. M. Hare, C. E. Crespo-Hernández, B. Kohler, *J. Phys. Chem., B* **110** (2006) 18641
10. W.-M. Kwok, C. Ma, D. L. Phillips, *J. Am. Chem. Soc.* **130** (2008) 5131
11. Y.-J. Ai, R.-Z. Liao, S.-F. Chen, Y. Luo, W.-H. Fang, *J. Phys. Chem., B* **114** (2010) 14096
12. R. B. Zhang, L. A. Eriksson, *J. Phys. Chem., B* **110** (2006) 7556
13. Z. B. Yang, R. B. Zhang, L. A. Eriksson, *Phys. Chem. Chem. Phys.* **13** (2011) 8961
14. D. Perdiz, P. Grof, M. Mezzina, O. Nikaido, E. Moustacchi, E. Sage, *J. Biol. Chem.* **275** (2000) 26732
15. Gaussian 09, Revision A.02, Gaussian, Inc., Wallingford CT, 2009
16. A. D. Becke, *J. Chem. Phys.* **98** (1993) 5648
17. T. H. Dunning, *J. Chem. Phys.* **90** (1989) 1007
18. J. G. Kirkwood, *J. Chem. Phys.* **2** (1934) 351
19. M. W. Wong, K. B. Wiberg, M. J. Frish, *J. Chem. Phys.* **95** (1991) 8991
20. M. Petković, *J. Phys. Chem., A* **116** (2012) 364.





A mixture of dicyclohexylamine and oleylamine as a corrosion inhibitor for mild steel in NaCl solution saturated with CO₂ under both continual immersion and top of the line corrosion

IVANA JEVREMOVIĆ^{1#}, ALEKSANDRA DEBELJKOVIĆ¹, MARC SINGER²,
MOHSEN ACHOUR³, SRDAN NEŠIĆ² and VESNA MIŠKOVIĆ-STANKOVIĆ^{1#*}

¹University of Belgrade, Faculty of Technology and Metallurgy, Kargujeva 4, 11000 Belgrade, Serbia, ²Institute for Corrosion and Multiphase Technology, Ohio University, 342 West State St., Athens, OH 45701, USA and ³ConocoPhillips Company, 226 Geosciences Building, Bartlesville, OK, USA

(Received 22 February, revised 21 May 2012)

Abstract: This paper presents a comprehensive method to evaluate a mixture of dicyclohexylamine and oleylamine (DCHA+OA) as a corrosion inhibitor for mild steel in a CO₂ environment in the liquid and vapor phase. The volatile properties of the corrosion inhibitor were investigated in order to determine whether DCHA+OA could be used to control the severity of a top of the line (TLC) corrosion attack. Corrosion measurements were performed using electrochemical impedance spectroscopy, linear polarization resistance, potentiodynamic sweep measurements, as well as electrical resistance and weight loss measurements, in order to determine the inhibitive performances of dicyclohexylamine and oleylamine. In order to define the surface morphological characteristics, the scanning electron microscopy technique was applied. The electrochemical study and the weight loss measurements indicated that DCHA+OA significantly decreased the corrosion rate in the liquid phase when 50 ppm of DCHA+OA was added. Scanning electron microphotographs indicated a protective inhibitor film was formed on the steel surface and revealed that good protection was achieved, together with a decrease in the corrosion rate, as determined by weight loss and electrochemical techniques. It was shown using electrical resistance measurements in the vapor phase, that a concentration of 1000 ppm DCHA+OA significantly decreased the corrosion rate at the top of the line only when it was carried there within its own foam and not due to its volatility.

Keywords: carbon steel; corrosion inhibitors; electrochemical measurements; scanning electron microscopy; electrical resistance measurements.

* Corresponding author. E-mail: vesna@tmf.bg.ac.rs

Serbian Chemical Society member.

doi: 10.2298/JSC120222058J

INTRODUCTION

In wet gas transportation, one of the most significant internal corrosion challenges is the so-called Top of the Line Corrosion (TLC). When the fluid stream is cooled, water vapor condenses on the sides and at the top of the line, creating droplets that are very corrosive since they contain dissolved corrosive gases such as CO₂ and H₂S. It is difficult to mitigate this type of corrosion, as conventional corrosion inhibitors dissolved in the liquid phase cannot be easily transported to the top of the line.^{1–5} One possible solution may be the application of volatile corrosion inhibitors (VCI), which have been successfully used in different applications. The advantage of VCI is that the vaporized inhibitor molecules can reach the top of the line and form a relatively stable and protective layer on the metal surface.^{6–8}

An aqueous carbon dioxide-saturated system is by far one of the most common corrosive environments encountered in the oil and gas industry.^{9–11} The problems arising from CO₂ corrosion have led to the development of various methods of corrosion control and one of the most practical methods for protection is the addition of organic substances as corrosion inhibitors, especially in acidic media.^{12–14} Injected inhibitor liquids are carried along the line, thereby producing a protective film all over the internal pipeline surface.¹⁵ Most of the inhibitors are organic heterocyclic compounds with N, S, or O atoms.^{16–23} The sites of these elements have higher electron density, so they are considered to be adsorption reaction centers. It was found that most of the organic inhibitors act by adsorption on the metal surface and by blocking the active corrosion sites.^{24–26} Inhibitors adsorb on the metal surface by displacing water molecules on the surface and forming a compact film as a physical barrier to reduce the transport of corrosive species to the metal surface.²⁷ This phenomenon is influenced by the nature and surface charge of the metal, by the type of aggressive electrolyte and by the chemical structure of the inhibitors.²⁸ As most corrosion inhibitors are required to partition to the water phase, the surface tension between the oil/water interface must be lowered, which is achieved by the addition of a surfactant.^{29–31}

In this study, electrochemical impedance spectroscopy (EIS), linear polarization resistance (LPR), potentiodynamic sweep (PDS) measurements, as well as electrical resistance (ER) and weight loss (WL) measurements and scanning electron microscopy (SEM) were conducted in order to investigate the efficiency of a mixture of dicyclohexylamine and oleylamine (DCHA+OA) as a corrosion inhibitor for mild steel in a CO₂ environment in the liquid and vapor phase. Dicyclohexylamine is used for its corrosion inhibition properties, while the oleylamine is used for its surfactant properties. A mixture of DCHA+OA was chosen considering the fact that dicyclohexylamine has a relatively high vapor pressure (1.6 kPa) and good inhibition properties in the liquid phase; hence, it was anticipated that even a small concentration of dicyclohexylamine in the vapor phase

could provide sufficient inhibition at the top. Oleylamine, known as a surfactant, was added in the mixture in order to maximize the contact surface area between dicyclohexylamine and the aqueous medium. In addition, dicyclohexylamine is a water insoluble inhibitor and a surface-active agent, oleylamine, was added to increase surface area and to cause a micro emulsion to form in the water phase. The molecular structures of inhibitor components are shown in Fig. 1.

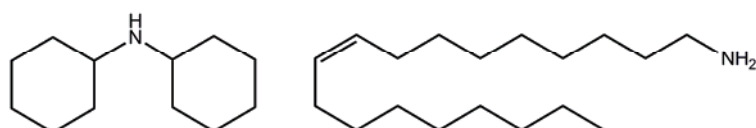
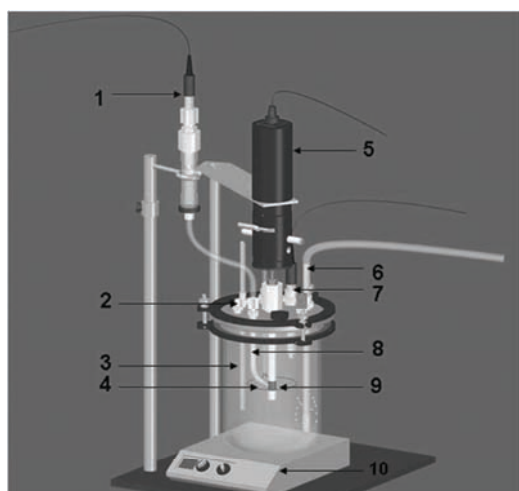


Fig. 1. Molecular structures of dicyclohexylamine and oleylamine.

EXPERIMENTAL

Investigation of the efficiency of the corrosion inhibitor in the liquid phase

The carbon steel API X65 was used in all experiments. The test specimens of surface area 5.4 cm², were sequentially polished using 240, 320, 400 and 600 grit silicon carbide paper, rinsed with 2-propanol in an ultrasonic cleaner for 1 to 2 minutes and then air-dried. The mixture of corrosion inhibitor dicyclohexylamine and oleylamine (1:1 vol. %) in a concentration of 50 ppm was added to a 3 wt. % NaCl solution. The cell temperature was monitored by a thermocouple. When the required temperature was achieved, the pH of the test solution was adjusted by addition of a deoxygenated sodium bicarbonate solution. The linear polarization resistance, electrochemical impedance spectroscopy, potentiodynamic sweep and weight loss measurements were performed in a glass cell, shown in Fig. 2. The test matrix for this experimental series is shown in Table I.



- | | |
|------------------------|-------------------------------|
| 1. Reference electrode | 2. Gas outlet |
| 3. Temperature probe | 4. Platinum counter electrode |
| 5. Rotator | 6. Gas inlet |
| 7. pH - electrode | 8. Luggin capillary |
| 9. Working electrode | 10. Hot plate |

Fig. 2. Scheme of the glass cell for the CO₂ corrosion test of mild steel.⁹

TABLE I. Test matrix for the CO₂ experiments in the liquid phase

Parameter	Value
Total pressure, kPa	100
CO ₂ partial pressure, kPa	96 and 69
Liquid temperature, °C	20 and 70
NaCl solution, wt. %	3
Concentration of DCHA+OA, ppm	50
pH	5
Measurements	OCP, EIS, LPR, PDS

Electrochemical measurements. All the electrochemical measurements were performed using a Gamry, Reference 600 potentiostat/galvanostat/ZRA. An Ag/AgCl (4M KCl) reference electrode was externally connected *via* a Luggin capillary. The counter electrode was a concentric platinum wire. The open circuit potential was monitored for 30 min, in which time a stable potential was reached, before all the electrochemical measurements were realized. The electrochemical measurements were typically conducted in the same order: linear polarization resistance, electrochemical impedance spectroscopy and potentiodynamic sweep. The linear polarization resistance (LPR) measurements were performed from a cathodic potential of -5 mV to an anodic potential of +5 mV, with respect to the corrosion potential, at a scan rate of 0.125 mV s⁻¹. The electrochemical impedance spectroscopy (EIS) measurements were performed over a frequency range of 10 kHz to 10 mHz using a 10 mV amplitude of sinusoidal voltage. The potentiodynamic sweep (PDS) measurements were realized from a cathodic potential of -0.25 V to an anodic potential of 0.25 V, with respect to the corrosion potential, at a scan rate of 0.2 mV s⁻¹.

Weight loss measurements. Typically after 24 h, pre-weighed samples were taken out of the 3 wt. % NaCl purged with CO₂ gas without and with DCHA+OA at 20 °C, and at 70 °C, rinsed with 2-propanol and wiped with a cloth to remove any salt residue and carbide scales, then air dried and weighed on an analytic balance (accuracy ±0.1 mg).

Surface morphology. A scanning electron microscope (SEM) JEOL JSM-6390 was used to analyze the morphology of the mild steel surface. Images of the specimens were recorded after 24 h exposure time in 3 wt. % NaCl purged with CO₂ gas at 20 °C, and at 70 °C without and with DCHA+OA.

Electrical resistance measurements. All measurements were realized using a Microcor Online Corrosion Monitoring System, Rohrback Cosasco Systems. API X65 steel specimens were pretreated with 78 wt. % H₂SO₄ for 30 s, rinsed with distilled water for 10 s and then polished with emery paper grit 600 and rinsed with distilled water. The solutions were deaerated by purging carbon dioxide gas for an hour before the start of the experiment, and then the bubbler was placed in the vapor phase. CO₂ injection was maintained during the entire test. When the desired conditions were achieved, the ER probe was put into the glass cell and corrosion rate was monitored. The test matrix for this experimental series is shown in Table II.

Investigation of efficiency of the corrosion inhibitor in the vapor phase

The experiments were performed in a glass cell containing 3 wt. % aqueous NaCl solutions with 1000 ppm of acetic acid added. The test solution was deoxygenated by bubbling CO₂ for an hour and then the CO₂ gas inlet was placed in the vapor phase. At the same time, the temperature was increased to 70 °C. Once the experimental conditions were attained, an



ER probe was installed flush mounted at the bottom of a stainless steel lid. When the bare steel corrosion rate was obtained, 1000 ppm of corrosion inhibitor DCHA+OA was injected into the solution.

TABLE II. Test matrix for the ER measurements

Parameter	Value
Total pressure, kPa	100
CO ₂ partial pressure, kPa	69
Liquid temperature, °C	70
NaCl solution, wt. %	3
Concentration of DCHA+OA, ppm	1000
Concentration of acetic acid, ppm	1000
pH	4
Measurement	ER

RESULTS AND DISCUSSION

Efficiency of the corrosion inhibitor in the liquid phase

The objective of this part of the experiments was to determine the basic properties of the investigated corrosion inhibitor dicyclohexylamine and oleylamine (DCHA+OA) in the liquid phase.

Electrochemical measurements. The impedance data were analyzed using the electric equivalent circuit presented in Fig. 3, where R_Q is the solution resistance, C_{dl} is the double layer capacitance and R_{ct} is the charge-transfer resistance.^{32–34}

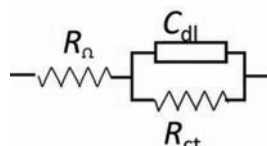


Fig. 3. Electrical equivalent circuit.

The Nyquist plots of the mild steel in 3 wt. % NaCl saturated with CO₂, pH 5, without and with 50 ppm DCHA+OA, at 20 °C are shown in Fig. 4.

From the Nyquist plots, it could be seen that the impedance response significantly changed on addition of DCHA+OA. The inhibition efficiency ($IE / \%$) after different exposure times was calculated from the impedance data using the following equation:

$$IE / \% = \frac{R_{ct} - R_{0ct}}{R_{ct}} \cdot 100 \quad (1)$$

where R_{0ct} and R_{ct} are the charge-transfer resistance values without and with inhibitor, respectively.³⁵ The values of charge-transfer resistance and inhibition efficiency obtained from the EIS measurements for mild steel in 3 wt. % NaCl at 20 °C and at 70 °C are given in Table III, from which it can be observed that the

inhibition efficiency increased upon addition of 50 ppm of DCHA+OA during the exposure time and reached a maximum inhibition efficiency of 98 % after 49 h of exposure at 20 °C.

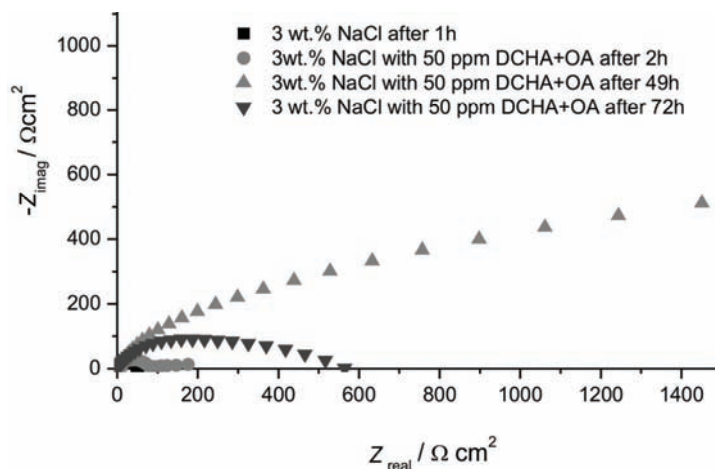


Fig. 4. Nyquist plots for mild steel in 3 wt. % NaCl solution at 20 °C, pH 5, without and with 50 ppm DCHA+OA.

TABLE III. The values of the charge-transfer resistance and inhibition efficiencies obtained from EIS measurements for mild steel in 3 wt. % NaCl solution without and with inhibitor (DCHA+OA), at 20 and 70 °C

<i>c</i> (DCHA+OA) / ppm	<i>t</i> / h	<i>t</i> / °C	<i>R</i> _{ct} / Ω cm ²	<i>IE</i> / %
0	1	20	50	–
50	2	20	90	44
50	49	20	2400	98
50	72	20	600	92
0	1	70	12	–
50	2	70	50	76
50	22	70	500	98
50	32	70	150	92

It can also be seen from Table III that the values of charge-transfer resistance at 20 °C in 3 wt. % NaCl with inhibitor increased with exposure time (up to 49 h), indicating the presence of an inhibitor layer adsorbed at the metal surface that acts as a barrier layer. After prolonged time (72 h), the charge-transfer resistance decreased, which could be explained by desorption of the inhibitor film from the metal surface and lower inhibition performances. A similar behavior was observed at 70 °C, but after shorter exposure times (22 and 32 h, respectively). It appears that inhibitor molecules probably start to desorb during time due to interactions between the inhibitor molecules already adsorbed at the metal surface and those present in solution. With increasing amount of adsorbed inhibitor, the inter-

actions become stronger, leading to secondary desorption after prolonged exposure. As could be expected, the values of the charge-transfer resistance at 70 °C were lower compared to the values at 20 °C due to the faster corrosion process and smaller amount of adsorbed inhibitor. It is well known that the amount of adsorbed inhibitor decreases with increasing temperature.

Similar behavior can be observed from the potentiodynamic sweep curves shown in Fig. 5. The addition of DCHA+OA shifted the corrosion potential to slightly more positive values and decreased the corrosion rate of mild steel. In the absence of inhibitor, the corrosion current density was calculated to be $8 \times 10^{-5} \text{ A cm}^{-2}$, which is about 10 times greater than the corrosion current density with inhibitor ($1.7 \times 10^{-6} \text{ A cm}^{-2}$). According to Fig. 5, it appears that DCHA+OA is a mixed-type inhibitor, since it reduces both the cathodic and anodic current densities. The decrease in the corrosion current density and increase in the corrosion potential confirm the inhibition properties of DCHA+OA. However, the rate of anodic dissolution of steel increased in the presence of inhibitor at more positive potentials than -300 mV (Ag/AgCl), which was previously reported as the desorption potential.^{18,35}

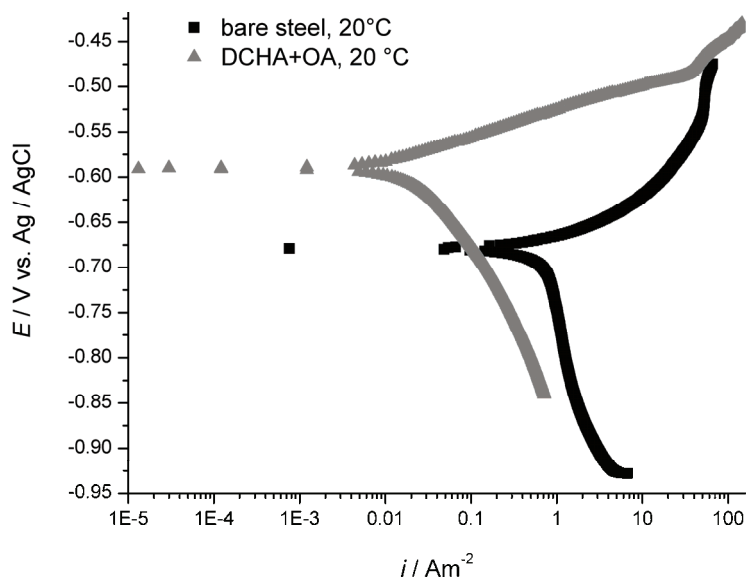


Fig. 5. Polarization curves of mild steel in 3 wt. % NaCl solution at 20 °C, pH 5, without and with 50 ppm DCHA+OA.

The value of R_p was determined using linear polarization resistance (LPR), while the corrosion rate was calculated using the following equations:

$$i_{\text{corr}} = \frac{1}{A R_p} \frac{b_a b_c}{2.303(b_a + b_c)} \quad (2)$$

$$CR = \frac{M_w}{\rho n F} i_{\text{corr}} \quad (3)$$

where, b_a and b_c are the anodic and cathodic Tafel slopes, respectively, M_w is the molecular weight of iron, A is the surface area of the sample, which is 5.4 cm^2 , ρ is the density of iron, n is the number of electrons exchanged in the electrochemical reaction and F is the Faraday constant. It was found that corrosion rate of mild steel in 3 wt. % NaCl, pH 5, at 20°C decreased to below 0.1 mm yr⁻¹ when 50 ppm of DCHA+OA was added compared to the corrosion rate of 0.6 mm yr⁻¹ for bare steel (Fig. 6). The corrosion rate at 70 °C also decreased from 2.2 mm yr⁻¹ for bare steel to 0.1 mm yr⁻¹ on addition of 50 ppm of DCHA+OA (Fig. 7). As can be seen in Figs. 6 and 7, the E_{corr} value shifted from approximately -0.7 V for the uninhibited system to -0.6 V in the presence of DCHA+OA. Namely, E_{corr} shifted to slightly more positive values from that of the uninhibited electrode when corrosion inhibitor was added. In general, DCHA+OA is considered as a mixed type of corrosion inhibitor because it affects both the metal ionization and the hydrogen evolution reaction, but the anodic action is more pronounced.

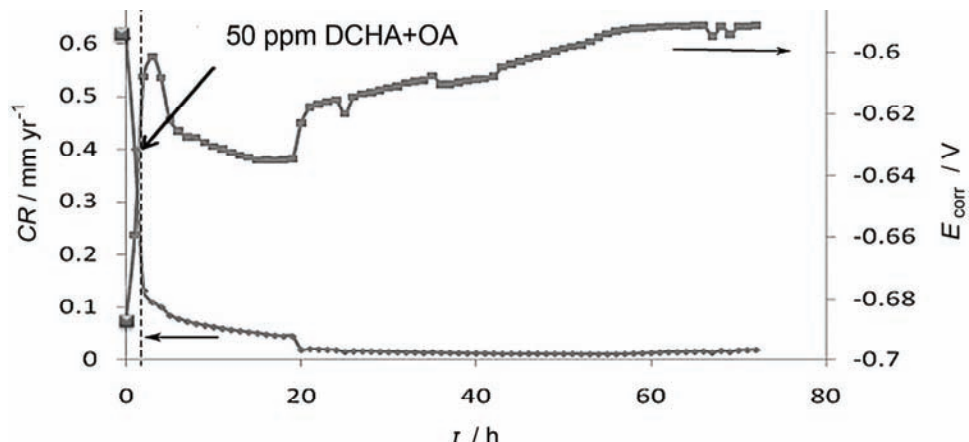


Fig. 6. Corrosion rate and corrosion potential of mild steel in 3 wt. % NaCl solution at 20 °C, pH 5, without and with 50 ppm DCHA+OA, measured by LPR during 72 h.

Weight loss measurements. The effect of addition of the DCHA+OA inhibitor on the corrosion of mild steel in 3 wt. % NaCl solution was also studied by weight loss measurements at 20 and 70 °C after a 24-h immersion period. The weight loss method was used in order to estimate average corrosion rates.³⁶ The weight loss (WL) was calculated from the equation:

$$WL = W_1 - W_2 \quad (4)$$

where W_1 and W_2 are the average weight of the specimens before and after exposure, respectively. The corrosion rate, CR , was calculated using the equation:

$$CR = \frac{WL}{S\rho t} \quad (5)$$

where, S is the surface area of specimens, ρ is the density of iron and t is the exposure time.¹⁸ It can be seen from Table IV that the corrosion rate significantly decreased on addition of the DCHA+OA corrosion inhibitor at both temperatures. The results obtained from the weight loss measurements are in accordance with the results obtained from the EIS and PDS measurements.

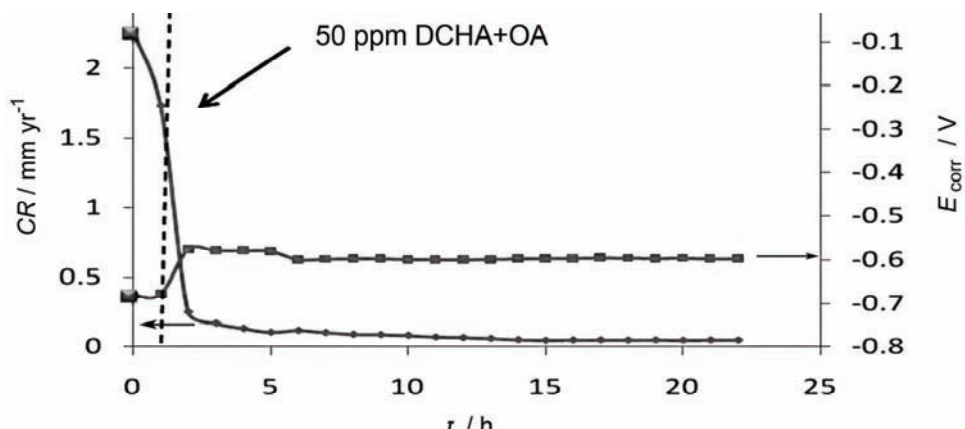


Fig. 7. Corrosion rate and corrosion potential of mild steel in 3 wt. % NaCl solution at 70 °C, pH 5, without and with 50 ppm DCHA+OA, measured by LPR during 24 h.

It can be considered that the inhibition performances of the corrosion inhibitor dicyclohexylamine and oleylamine and the reduced corrosion rate are the consequence of strong interactions established between the N atoms with unshared electron pair from the dicyclohexylamine (DCHA) and oleylamine (OA) molecules and the negatively charged metal surface. Moreover, the long alkyl chains from oleylamine can orientate the inhibitor on the metal surface. In addition, van der Waals interactions are established between the alkyl chains, so they form a firmly adsorbed hydrophobic layer that protects the steel surface against corrosion attack.

Surface morphology. The SEM microphotographs of mild steel surface after 24 h of exposure to 3 wt. % NaCl solution without and with DCHA+OA added at 20 °C and at 70 °C are shown in Fig. 8. In the absence of inhibitor (Figs. 8a and b), the mild steel surface was strongly damaged due to metal dissolution in the corrosive solution. The surface after exposure at 20 °C was very rough and uneven

while the specimen that was exposed at 70 °C (Fig. 8b) had deep and large holes at the surface. However, the appearance of steel surface was significantly different after the addition of DCHA+OA to the corrosive solution. As can be seen from Figs. 8c and 8d, the dissolution rate of mild steel was reduced and a uniform, smooth surface appeared due to formation of a protective inhibitor film on the metal surface. The SEM results are in accordance with the results of the weight loss and electrochemical measurements.

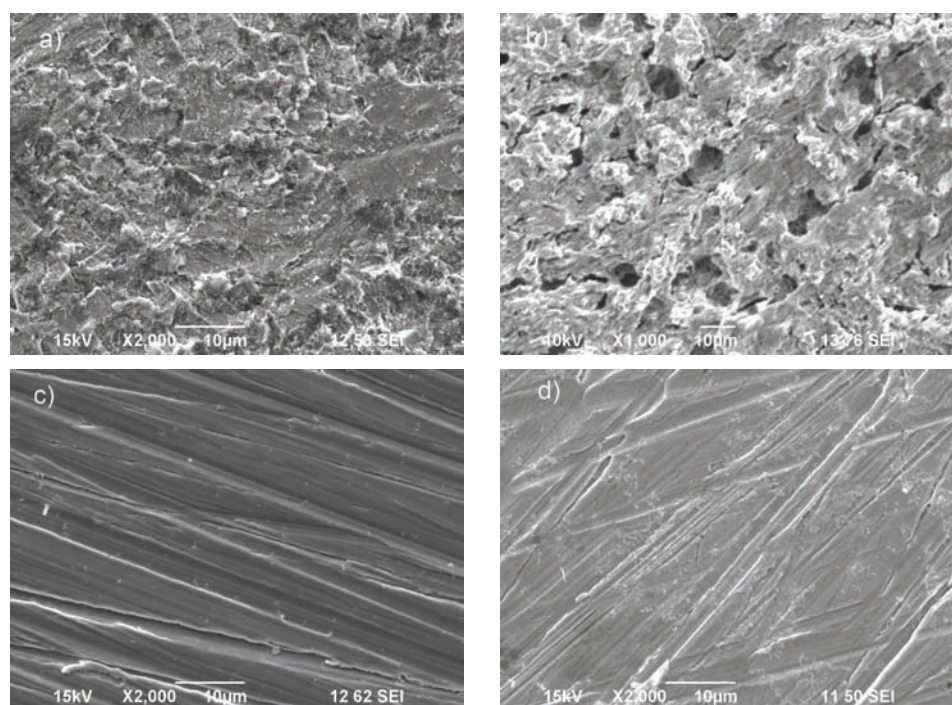


Fig. 8. SEM Microphotographs of mild steel after exposure to 3 wt. % NaCl solution at: a) 20 and b) 70 °C; c) with 50 ppm DCHA+OA at 20 °C and d) with 50 ppm DCHA+OA at 70 °C.

Electrical resistance measurements. The time dependences of the decrease metal thickness and corrosion rate when 1000 ppm DCHA+OA was added in 3 wt. % NaCl solution are shown in Fig. 9, indicating that the corrosion rate after 20 h was around 0.1 mm yr^{-1} . After the baseline conditions were established, the corrosion rate of bare steel in solution was around 4.5 mm yr^{-1} . Consequently, it can be considered that a concentration of 1000 ppm DCHA+OA significantly decreased the corrosion rate in the liquid phase. Similar results were obtained using LPR (Fig. 7) and weight loss measurements (Table IV).

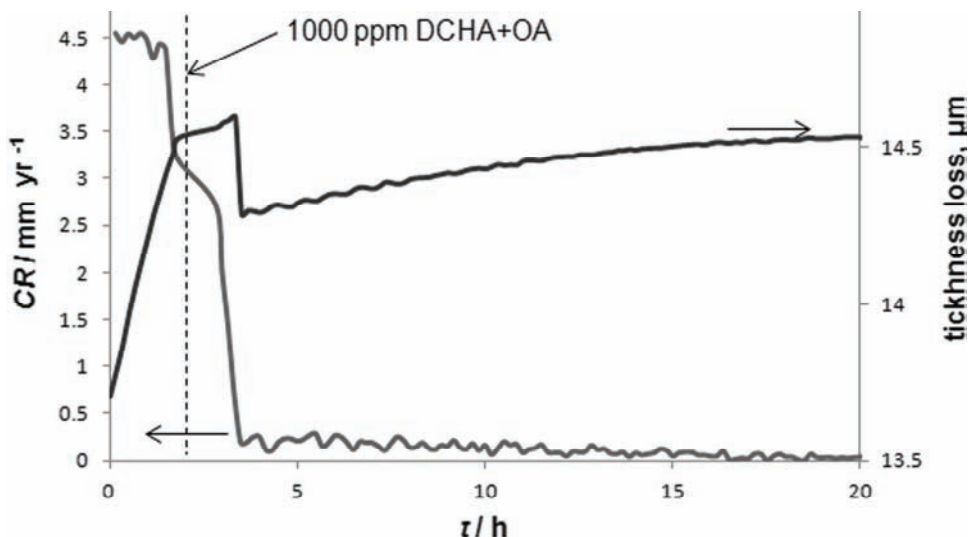


Fig. 9. The time dependence of the decrease in metal thickness and corrosion rate for mild steel in the liquid phase when 1000 ppm DCHA+OA was added to 3 wt. % NaCl solution at 70 °C, pH 4, with 1000 ppm of acetic acid.

TABLE IV. Weight loss measurements after 24 h for mild steel in 3 wt. % NaCl solution without and with inhibitor (DCHA+OA), at 20 and 70 °C

c (DCHA+OA) / ppm	t / °C	WL / mg	CR / mm yr ⁻¹
0	20	0.017	0.96
50	20	0.0002	0.012
0	70	0.074	4.3
50	70	0.0016	0.095

Efficiency of the corrosion inhibitor in the vapor phase

The aim of this part of the study was to investigate the volatile properties of the corrosion inhibitor DCHA+OA using electrical resistance (ER) measurements. The time dependences of the decrease in the metal thickness and the corrosion rate in vapor phase when 1000 ppm DCHA+OA was added to a 3 wt. % NaCl solution are shown in Fig. 10. The rate of decrease of the metal thickness was constant when 1000 ppm of corrosion inhibitor DCHA+OA was injected (Fig. 10), indicating that the inhibitor DCHA+OA has poor volatile properties and did not protect the carbon steel at the top of the line.

The corrosion rate increased during the first 2 h and reached approximately 0.5 mm yr⁻¹ (Fig. 10). After the corrosion rate of bare steel was established, 1000 ppm of corrosion inhibitor DCHA+OA was injected directly into the solution. It can be seen that the added inhibitor had no effect on the corrosion rate in the vapor phase.

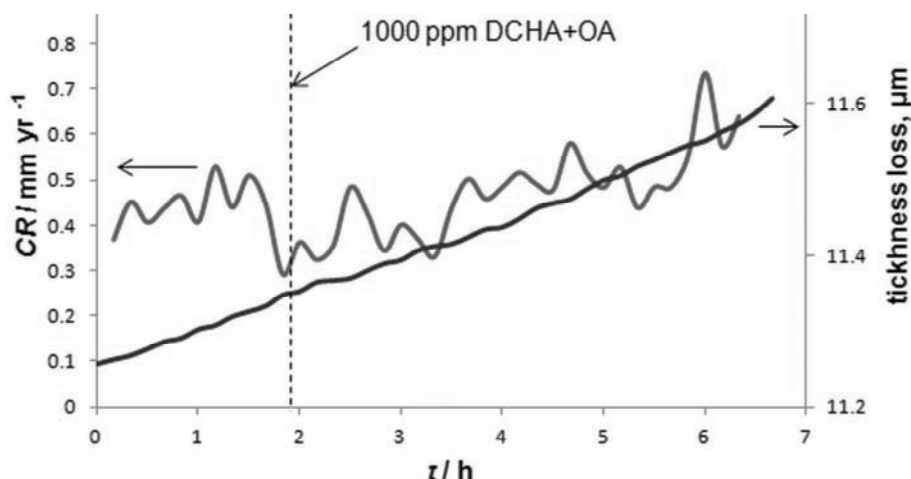


Fig. 10. The time dependence of the decrease in metal thickness and corrosion rate for mild steel in the vapor phase when 1000 ppm DCHA+OA was added to 3 wt. % NaCl solutions at 70 °C, pH 4, with 1000 ppm of acetic acid.

In an additional experiment foam was created inside the glass cell by placing the bubbler in the liquid phase instead of in the vapor phase after addition of the corrosion inhibitor DCHA+OA to the solution. The time dependences of the decrease in the metal thickness and the corrosion rate in vapor phase when foam was created after the addition of 1000 ppm DCHA+OA to the 3 wt. % NaCl solution are shown in Fig. 11.

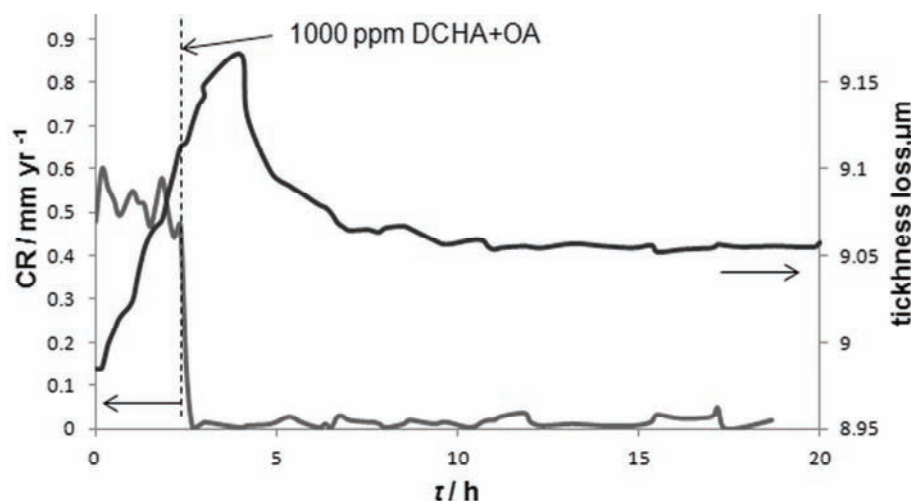


Fig. 11. The time dependence of the decrease in metal thickness and corrosion rate for mild steel in the vapor phase with foam created when 1000 ppm DCHA+OA was added to 3 wt. % NaCl solution at 70 °C, pH 4 with 1000 ppm of acetic acid.

The corrosion rate in the vapor phase increased during the first 2.5 h and reached approximately 0.5 mm yr^{-1} and then decreased to below 0.1 mm yr^{-1} after the foam contacted the ER probe (Fig. 11). Consequently, it could be concluded that a concentration of 1000 ppm DCHA+OA significantly decreased the corrosion rate at the top only when it was carried to the top within its own foam and not due to its volatility.

CONCLUSIONS

The electrochemical study of the efficiency of the corrosion inhibitor dicyclohexylamine and oleylamine (DCHA+OA) in liquid phase showed that the corrosion rate of mild steel in 3 wt. % NaCl solution at pH 5 and at 20°C decreased to below 0.1 mm yr^{-1} when 50 ppm of DCHA+OA was added, compared to bare steel corrosion rate of 0.6 mm yr^{-1} . The corrosion rate also decreased from 2.2 mm yr^{-1} for bare steel to 0.1 mm yr^{-1} by adding 50 ppm of DCHA+OA at 70°C . The protective action of the added inhibitor can be explained by the strong interactions established between the unshared electron pair of the N atoms of the dicyclohexylamine (DCHA) and oleylamine (OA) molecules and the negatively charged metal surface. Scanning electron microphotographs of mild steel surface also revealed that DCHA+OA inhibits the corrosion process and a uniform, smooth surface appeared due to formation of a protective inhibitor film on the metal surface. Electrical resistance measurements in the liquid phase showed that the corrosion rate at 70°C after 20 h was below 0.1 mm yr^{-1} when 1000 ppm of DCHA+OA was added. From electric resistance measurements in the vapor phase, it could be concluded that the inhibitor DCHA+OA has poor volatile properties and does not protect the carbon steel at the top of the line. On the other hand, it was shown that a concentration of 1000 ppm DCHA+OA significantly decreased the corrosion rate at the top when it was carried to the top within its own foam.

Acknowledgements. The authors would like to express their gratitude to ConocoPhillips, USA, and the Ministry of Education, Science and Technological Development of the Republic of Serbia (Grant No. III 45019) for financial support.

ИЗВОД

СМЕСА ДИЦИКЛОХЕКСИЛАМИНА И ОЛЕИЛАМИНА КАО ИНХИБИТОР КОРОЗИЈЕ НИСКОУГЉЕНИЧНОГ ЧЕЛИКА У РАСТВОРУ NaCl ЗАСИЋЕНОМ СА CO_2

ИВАНА ЈЕВРЕМОВИЋ¹, АЛЕКСАНДРА ДЕБЕЉКОВИЋ¹, MARC SINGER², MOHSEN ACHOUR³,
СРЂАН НЕШИЋ² и ВЕСНА МИШКОВИЋ-СТАНКОВИЋ¹

¹Технолошко-мештаришки факултет, Универзитет у Београду, Карнеијева 4, Београд, ²Institute for Corrosion and Multiphase Technology, Ohio University, 342 West State St., Athens, OH 45701, USA и

³ConocoPhillips Company, 226 Geosciences Building, Bartlesville, OK, USA

У овом раду испитивана је заштита нискоугљеничног челика од корозије под дејством CO_2 применом смесе дициклохексиламина и олеиламина (DCHA+OA) као инхи-



битора у течној и гасовитој фази. Испарљивост смесе DCHA+OA је испитивана у циљу потенцијалне примене DCHA+OA као лако испарљивог инхибитора за смањење брзине корозије у условима кондензације. При испитивању инхибиторских својстава смесе дигиклохекциламина и олеиламина примењене су следеће технике карактеризације: спектроскопија електрохемијске импедансије, метода линеарне поларизационе отпорности, метода поларизације линеарно променљивим потенцијалом, мерење електричне отпорности, гравиметријска метода одређивања губитка масе, као и скенирајућа електронска микроскопија. Резултати електрохемијских мерења и гравиметријске методе одређивања губитка масе показују да додата смеса DCHA+OA у концентрацији од 50 ppm значајно смањује брзину корозије у течној фази у односу на систем без инхибитора. Микрофотографије површине челика потврђују да се у присуству смесе DCHA+OA смањује степен корозије као последица формирања заштитног филма инхибитора на површини нискоугљеничног челика. Применом технике мерења електричне отпорности у гасовитој фази показано је да додатак смесе инхибитора DCHA+OA у концентрацији од 1000 ppm доводи до значајног смањења брзине корозије у условима кондензације, само у случају када се транспорт инхибитора до површине челика остварује у облику пене, а не због испарљивости самог инхибитора.

(Примљено 22. фебруара, ревидирано 21. маја 2012)

REFERENCES

1. F. Vitse, S. Nesic, Y. Gunaltun, D. Larrey de Torreben, P. Duchet-Suchaux , *Corrosion* **59** (2003) 1075
2. Z. Zhang, D. Hinkson, M. Singer, H. Wang, S. Nesic, *Corrosion* **63** (2007) 1051
3. M. Singer, A. Camacho, B. Brown, S. Nesic, *Corrosion* **67** (2011) B1
4. D. Hinkson, Z. Zhang, M. Singer, S. Nesic, *Corrosion* **66** (2010) A1
5. I. Jevremović, M. Singer, M. Achour, D. Blumer, T. Baugh, V. Mišković-Stanković, S. Nešić, *Corrosion* (2012), <http://dx.doi.org/10.5006/0617>
6. E. Cano, D. M. Bastidas, J. Simancas, J. M. Bastidas, *Corrosion* **61** (2005) 473
7. D. M. Bastidas, E. Cano, E. M. Mora, *Anti-Corros. Meth. M.* **52** (2005) 71
8. R. L. Martin, *Mater. Perform.* **48** (2009) 48
9. F. Haitao, *Low temperature and high salt concentration effect on general CO₂ corrosion for carbon steel*, MS thesis, The Russ College of Engineering and Technology of Ohio University (2006).
10. X. Liu, Y. G. Zheng, *Corros. Eng. Sci. Techn.* **43** (2008) 87
11. L. Zhaoling, F. Chaoyang, G. Xingpeng, *Anti-Corros. Meth. M.* **54** (2007) 301
12. F. Bentiss, M. Lagrenée, M. Traisnel, J. C. Hornez, *Corros. Sci.* **41** (1999) 789
13. G. Achary, H. P. Sachin, Y. A. Naik, T. V. Venkatesha, *Mater. Chem. Phys.* **107** (2008) 44
14. S. D. Shetty, P. Shetty, H. V. S. Nayak, *J. Serb. Chem. Soc.* **71** (2006) 1073
15. S. Nesic, *Corros. Sci.* **49** (2007) 4308
16. S. A. Ali, M. T. Saeed, S. U. Rahman, *Corros. Sci.* **45** (2003) 253
17. A. Döner, G. Kardas, *Corros. Sci.* **53** (2011) 4223
18. A. Döner, R. Solmaz, M. Özcan, G. Kardas, *Corros. Sci.* **53** (2011) 2902.
19. V. R. Saliyan, A. V. Adhikari, *Corros. Sci.* **50** (2008) 55
20. F. Bentiss, M. Traisnel, H. Vezin, H. F. Hildebrand, M. Lagrenée, *Corros. Sci.* **46** (2004) 2781



21. M. El. Azhar, B. Mernari, M. Traisnel, F. Bentiss, M. Lagrenée, *Corros. Sci.* **43** (2001) 2229
22. M. Finšgar, I. Milošev, *Mater. Corros.* **62** (2011) 956
23. M. Finšgar, J. Kovač, I. Milošev, *J. Electrochem. Soc.* **157** (2010) C52
24. B. Wang, M. Du, J. Zhang, C. J. Gao, *Corros. Sci.* **53** (2011) 353
25. D. M. Dražić, Lj. Vračar, V. J. Dražić, *Electrochim. Acta* **39** (1994) 1165
26. Lj. M. Vračar, D. M. Dražić, *Corros. Sci.* **44** (2002) 1669
27. M. Lebrini, M. Lagrene, H. Vezin, L. Gengembre, F. Bentiss, *Corros. Sci.* **47** (2005) 485
28. R. A. Prabhu, T. V. Venkatesha, A. V. Shanbhag, G. M. Kulkarni, R. G. Kalkhambkar, *Corros. Sci.* **50** (2008) 3356
29. W. Wang, M. L. Free, *Corros. Sci.* **46** (2004) 2601
30. M. L. Free, *Corros. Sci.* **44** (2002) 2865
31. M. L. Free, *Corros. Sci.* **46** (2004) 3101
32. W. Guo, S. Chen, H. Ma, *J. Serb. Chem. Soc.* **71** (2006) 167
33. J. B. Bajat, V. B. Mišković-Stanković, *Prog. Org. Coat.* **49** (2004) 183
34. J. B. Bajat, V. B. Mišković-Stanković, Z. Kačarević-Popović, *Prog. Org. Coat.* **47** (2003) 49
35. A. Chetouani, A. Aouniti, B. Hammouti, N. Benchat, T. Benhadda, S. Kertit, *Corros. Sci.* **45** (2003) 1675
36. S. Muralidharan, M. A. Quraishi, S. V. K. Iyer, *Corros. Sci.* **37** (1995) 1739.





SHORT COMMUNICATION

Application of UV–Vis spectrophotometric and chemiluminescent methods for the evaluation of the antioxidant action of curcumin

STANCHO STANCHEV^{1*}, IVANKA PENCHEVA², SPIRO KONSTANTINOV³,
DANKA OBRESHKOVA⁴ and VERA HADJIMITOVA⁵

¹*Institute of Organic Chemistry and Biochemistry, Czech Academy of Sciences, 2 Flemingovo namesti, CZ-16610 Prague 6, Czech Republic,* ²*Department of Pharmaceutical Chemistry, Faculty of Pharmacy, Medical University, 2 Dunav St. BG-1000 Sofia, Bulgaria,* ³*Department of Pharmacology and Toxicology, Faculty Pharmacy, Medical University, 2 Dunav St., BG-1000 Sofia, Bulgaria,* ⁴*Department of Pharmaceutical Chemistry, Faculty of Pharmacy, Medical University, 2 Dunav St. BG-1000 Sofia and* ⁵*Department of Physics and Biophysics, Faculty of Medicine, Medical University, 2 Zdrave St. BG-1431 Sofia, Bulgaria*

(Received 11 June 2011, revised 8 January 2012)

Abstract: Curcumin (1,7-bis(4-hydroxy-3-methoxyphenyl)-1,6-heptadiene-3,5-dione) is a natural biologically active substance with antioxidant activity. The ability of curcumin to inhibit free radical reactions can be used in the prevention of diseases such as cancer and coronary heart disease. UV–Vis spectrophotometric and chemiluminescent dynamic methods for determination of the antioxidant activity of curcumin were developed. The spectrophotometric method includes investigation of the interaction between DNA, isolated from HL-60 cells, and curcumin. The decreasing absorption of curcumin in the presence of HL-60 DNA against the blank sample can be a measurement for some complex formation between curcumin and DNA. The chemiluminescent method involves three tests for the detection of luminol-dependent chemiluminescence based on model systems that generate superoxide, hydroxide and hypochlorite radicals. The strongest decay of chemiluminescence was registered at the highest concentration of curcumin ($100 \mu\text{mol L}^{-1}$).

Keywords: curcumin; antioxidant; UV–Vis spectrophotometry; DNA complexation; chemiluminescence.

INTRODUCTION

Curcumin (1,7-bis(4-hydroxy-3-methoxyphenyl)-1,6-heptadiene-3,5-dione) is the principal curcuminoid of the popular spice *Curcuma longa* L. (turmeric),

*Corresponding author. E-mail: stancho_stanchev@yahoo.com
doi: 10.2298/JSC110621032S

which is a member of the ginger family (Zingiberaceae). The curcuminoids are polyphenols and are responsible for the yellow color. Curcumin (Fig. 1) can exist in at least two tautomeric forms - keto and enol. The enol form is more energetically stable in the solid phase and in solution.¹

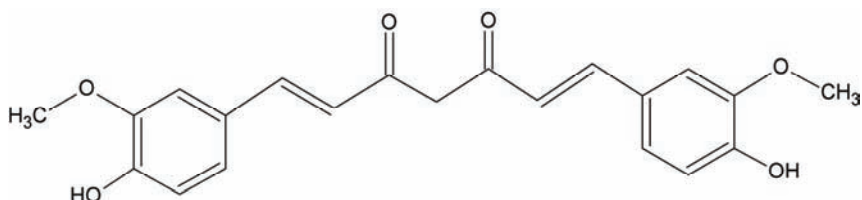


Fig. 1. Chemical structure of curcumin.

In vitro and animal studies suggested a wide range of potential therapeutic or preventive effects associated with curcumin on numerous diseases, including multiple myeloma, pancreatic cancer, myelodysplastic syndromes, colon cancer, psoriasis, Alzheimer's disease, gastric ulcer and dermal wound healing and liver protection.^{2–9} Curcumin has been tested in the clinical stage for anticancer activity – phase 1 and it showed very low toxicity (even at a dosage of 12 g day⁻¹).¹⁰ The major problem is its very low bioavailability due to poor absorption and rapid metabolism and elimination. Many methods were used, in order to increase its bioavailability, such as combination with piperine, which interferes with glucuronidation, and application as liposomes and nanoparticles.¹¹

The antioxidant properties of curcumin were evaluated by different methods (mainly spectrophotometric and spectrofluorimetric), including the determination of thiobarbituric acid reactive substances (TBARS), as a result of lipid peroxidation caused by AAPH (2,2'-azobis (2-amidinopropane) hydrochloride),¹² the decrease in the reduction of Tetrazolnitro Blue to formazane caused by superoxide radicals, generated in the xantine/xantine oxidase system, and the scavenging of the DPPH radical, based on the decrease in the absorption of the stable radical at 517 nm.^{13–14} The other methods are based on electronic paramagnetic resonance.^{15–16}

A mononuclear (1:1) copper complex of curcumin was synthesized and examined for its superoxide dismutase (SOD) activity. The complex was found to be regenerated completely, indicating catalytic activity in neutralizing superoxide radicals. The SOD mimicking activity of the complex was determined by the xanthine/xanthine oxidase assay, from which it was found that 5 µg of the complex is equivalent to 1 unit of SOD. The complex inhibited radiation-induced lipid peroxidation and showed radical-scavenging ability.¹⁴

Curcumin is used as a supplement and food additive because of its broad antioxidant activity for the prevention of different diseases caused by the over-production of free radicals. As a food additive, its E number is E100. The aim of

this study was to develop a spectrophotometric and chemiluminescent method for the evaluation of its antioxidant activity in different model systems, which could find application in the quality control of drugs and food additives containing curcumin.

EXPERIMENTAL

Collection of cells from an HL-60 cell culture

5×10^6 cells with the ordinary number of chromosomes were centrifuged for 5 min at 300 rpm in 1.5 mL centrifuge test tubes. The supernatant was removed carefully in order to keep the cell pellets intact.

Liberation of DNA from the collected cells

Collected cell pellets are suspended in phosphate buffer up to a final volume of 200 μL . 20 μL of QIAGEN-protease (protease K) and 200 μL buffer AL were added to the suspension. The mixture was vortexed for 15 s in order to obtain homogenous suspension, followed by incubation at 56 °C for 10 min. The suspension was centrifuged shortly in order to remove the drops from the inner side of the lid. Ethanol (200 μL , 96–100 %) was added to the sample and the latter was vortexed for 15 s and then centrifuged shortly, in order to remove the drops from the lid.

Purification of DNA by QIAamp ion-exchange column

A QIAamp DNA Blood Mini Kit (QIAGEN, UK), consisting of proteolytic enzymes (lyophilized QIAGEN-protease) and a series of buffer solutions (buffer AL, buffer AW1, buffer AW2), was used for the step-by-step purification of DNA from leukemic HL-60 cells using an ion-exchange column QIAamp (QIAGEN).

The mixture, obtained in the previous step was loaded onto a QIAamp-rotating column (with a 2 mL collection tube), without wetting of the edge of the column. The whole system was centrifuged at 6000 rpm for 1 min. The collection test-tube was changed with a clean one.

The column was eluted in the same manner subsequently with 500 μL of buffer AW1 and 500 μL of buffer AW2. The centrifugation of the buffer AW2 was performed at 20000 rpm for 3 min. The final centrifugation was performed at full rate for 1 min., in order to remove the residual quantities of buffer AW2 in a new test tube. The final elution was performed with 200 μL of distilled water, followed by incubation for 1 min and centrifugation at 6000 rpm for 1 min. The yield of the isolated DNA was around 6 μg .

Analysis of the isolated DNA by UV–VIS spectrophotometry

Two samples of DNA were prepared as aqueous solutions, 5 and 20 μL mL^{-1} . These solutions were analyzed on Hewlet-Packard UV–Vis spectrophotometer (Hewlet-Packard, USA, with a diode array matrix with a 1 cm cell). This spectrophotometer was connected with PC and the data were collected and processed by integrated software.

The absorptions (A_1 and A_2) were measured at the wavelengths 248 and 280 nm and the factor of resolution was calculated as the ratio between A_1 and A_2 at λ_1 and λ_2 .

UV–Vis spectrophotometric assay of the interaction between DNA and curcumin

Two samples of curcumin reference substance (Fluka, Switzerland) were prepared in Eppendorf tubes: sample 1 – containing 100 μL DNA, 400 μL distilled water and 5 μL 10000 M solution of curcumin, sample 2 – containing 495 μL distilled water and 5 μL 10000 M solution of curcumin (blank sample).



Samples 1 and 2 were incubated 24 h at room temperature. Sample 1 was filtered through paper filter and subsequently diluted to 3 mL with distilled water. The spectrophotometric analysis of this sample was made before and after filtration and dilution at $\lambda = 422$ nm. The absorption of sample 2 (blank sample) was measured at 422 nm after dilution to 3 mL with distilled water.

Chemiluminescent assay

For registration of active oxygen species, a luminol-dependent chemiluminescence was detected using a chemiluminometer LKB 1251 (Bioorbit, Turku, Finland). The chemiluminometer was connected with IBM computer system (IBM, USA) and the obtained data were collected and analyzed with the MultiUse program version 1.08 (Bioorbit). All tests were made at a fixed temperature of 37 °C. The chemiluminescence responses of all the systems described below were measured. The ratio in percentage between the magnitude of the chemiluminescence in the presence and the absence of curcumin was termed chemiluminescence-scavenging index (*CL-SI*).

Xanthine/xanthine oxidase system. This test for the determination of the luminol-dependent chemiluminescence is based on the model system in which superoxide is generated from xanthine/xanthine oxidase: To 1 mL PBS (0.1 mmol L⁻¹ luminol and 1 mmol L⁻¹ xanthine), curcumin in different concentrations in DMSO was added. In parallel, blank samples were prepared without curcumin. After 10 min incubation at 37 °C to 20 µL xanthine oxidase (100 IU L⁻¹) were added to the samples and the chemiluminescence was measured against reference sample for 5 min.

Fe–ethylenediaminetetraacetic acid(EDTA)–H₂O₂ system. This test for the determination of the luminol-dependent chemiluminescence is based on the model system in which hydroxide radicals are generated from Fe-EDTA, ascorbic acid and peroxide. Luminol (100 µmol L⁻¹), Fe³⁺ (100 µmol L⁻¹ and EDTA, 100 µmol L⁻¹), ascorbic acid (100 µmol L⁻¹) and peroxide (1 mmol L⁻¹) were dissolved in 1 mL phosphate buffer of pH 7.4 (50 mM K₂HPO₄/KH₂PO₄). Curcumin in the three different concentrations as a DMSO solution was added. The chemiluminescence was measured against the reference sample for 1 min.

Hypochlorite system. This test for the determination of luminol-dependent chemiluminescence is based on the model system in which hypochlorite ions are generated. To 1 mL phosphate buffer of pH 7.4 (50 mM K₂HPO₄/KH₂PO₄), luminol (100 µmol L⁻¹), sodium hypochlorite (30 µmol L⁻¹) and curcumin in the investigated concentrations were added. The chemiluminescence was measured against the reference sample for 1 min.

RESULTS AND DISCUSSION

UV–Vis spectrophotometric evaluation of the interaction between DNA and curcumin

Purity of DNA, isolated from HL-60 cells by the above-described procedure was evaluated by UV–Vis spectrophotometry. Two samples, containing DNA with concentration respectively 5 µL DNA/mL water and 20 µL DNA/mL water were analyzed. The absorbances (A_1 and A_2) were measured at the wavelengths 248 and 280 nm and the factor of resolution was calculated. Factor of resolution was measured as the ratio between A_1 and A_2 at 248 and 280 nm respectively, which is an indicator for purity of DNA and normally must be between 1.7 and



1.9. The measured value in our case is 1.86, which corresponds to the requirement of purity.

The absorption maxima of the complex DNA–curcumin were at 248, 250, 252, 260 and 422 nm. The range of the minimal overlapping between DNA and curcumin is the visible area and for this reason, all the measurements were made at 422 nm. The absorption of the complex DNA–curcumin decreased by 24.5 % and after filtration by 66 %, compared to the blank sample 1. The decrease of the absorbance (resp. concentration) of curcumin in the sample containing DNA and curcumin, compared to the blank sample, containing only curcumin, can serve as proof for an interaction between DNA and curcumin. This complex was probably formed by hydrogen bonds and/or van der Waals interactions between phenolic hydroxyl groups and the keto-groups of curcumin and the keto-, amino- and imino-groups of the nucleotide bases.

Chemiluminescent assay

The most significant decay of the luminal-dependent chemiluminescence in the three tested systems: xanthine–xanthine oxidase, generating superoxide radicals, Fe–EDTA/H₂O₂, generating hydroxyl radicals, and NaOCl, generating ClO⁻, was at the highest concentration (100 μmol L⁻¹), referred to DMSO (Fig. 2). There was no significant decrease in the chemiluminescence between the lowest

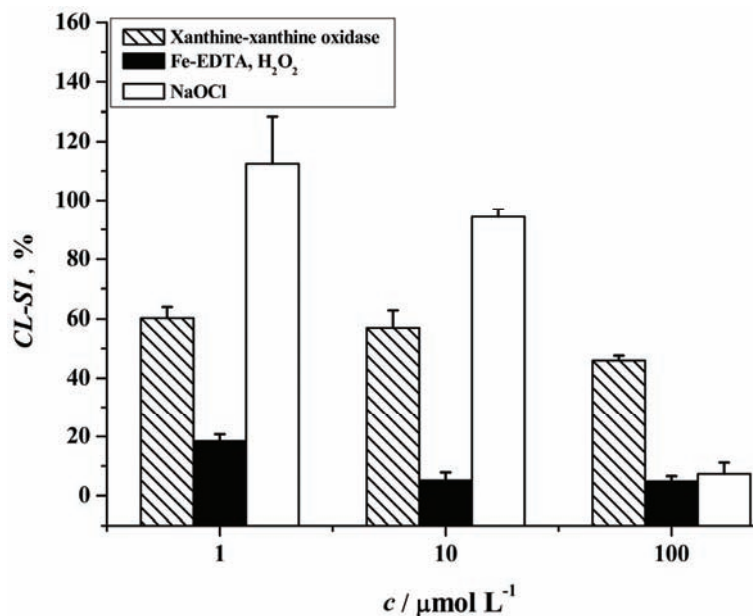


Fig. 2. Chemiluminescent scavenging index (CL-SI) as a marker of the antioxidant effect of curcumin in the three model systems: xanthine–xanthine oxidase, Fe–EDTA–H₂O₂ and NaOCl at the three concentrations c in $\mu\text{mol L}^{-1}$.

(1 $\mu\text{mol L}^{-1}$) and the middle concentration (10 $\mu\text{mol L}^{-1}$) for the systems xanthine–xanthine oxidase and NaOCl. In the Fe–EDTA/H₂O₂ model system, the decay of chemiluminescence at the highest (100 $\mu\text{mol L}^{-1}$) and the middle concentration (10 $\mu\text{mol L}^{-1}$) were relatively similar.

The most important functional groups from a structural point of view are conjugated double bonds, phenol and methoxy groups. Double bonds are probably oxidized and form epoxides and/or diols, especially under the influence of superoxide and hydroxyl radicals. The ClO⁻ can probably cause the formation of chlorohydrins at the double bonds of curcumin. Phenols have expressed redox properties, which can explain the neutralization of free radicals, singlet oxygen species and peroxides. Methoxy groups also have a free radical scavenging activity.

CONCLUSIONS

Three different model systems generating free radicals, *i.e.*, xanthine–xanthine oxidase, Fe–EDTA/H₂O₂ and NaOCl, were used in the investigation of the antioxidant properties of curcumin, based on the decay of luminol-dependent chemiluminescence. The decay was most expressed at the highest concentration, 100 $\mu\text{mol L}^{-1}$, of curcumin.

The developed methods could be very useful in the qualitative and quantitative control of the natural antioxidant curcumin in medicine and in the drug and food industries.

The interaction between DNA and curcumin was also investigated by UV–Vis spectroscopy. The obtained results evidenced some interaction between curcumin and DNA, probably based on hydrogen bonding and van der Waals interactions. This “complex” deserves further investigation, because it can be a part of the mechanism of protection of DNA against free radical damage.

ИЗВОД

ПРИМЕНА UV–Vis СПЕКТРОФОТОМЕТРИЈСКЕ И ХЕМОЛУМИНИСЦЕНТНЕ МЕТОДЕ У ЕВАЛУАЦИЈИ АНТИОКСИДАНТНОГ ДЕЈСТВА КУРКУМИНА

STANCHO STANCHEV¹, IVANKA PENCHEVA², SPIRO KONSTANTINOV³,
DANKA OBREŠKOVA⁴ и VERA HADJIMITOVA⁵

¹Institute of Organic Chemistry and Biochemistry, Czech Academy of Sciences, 2 Flemingovo namesti, CZ-16610 Prague 6, Czech Republic, ²Department of Pharmaceutical Chemistry, Faculty of Pharmacy, Medical University, 2 Dunav St. BG-1000 Sofia, Bulgaria, ³Department of Pharmacology and Toxicology, Faculty of Pharmacy, Medical University ,2 Dunav St., BG-1000 Sofia, Bulgaria, ⁴Department of Pharmaceutical Chemistry, Faculty of Pharmacy, Medical University, 2 Dunav St. BG-1000 Sofia Bulgaria
и ⁵Department of Physics and Biophysics, Faculty of Medicine, Medical University,
2 Zdrave St. BG-1431 Sofia, Bulgaria

Куркумин (1,7-бис(4-хидрокси-3-метоксифенил)-1,6хептадиен-3,5-дион) је природна, биолошки активна супстанца са антиоксидантним дејством. Својство куркумина да инхибира механизме формирања слободних радикала користи се у превенцији



канцера и срчаних оболења. Развијене су УВ–ВИС спектрофотометријска и хемолуминисцентна динамичка метода за одређивање антиоксидантне активности куркумина. Спектрофотометријска метода укључује испитивање интеракција између ДНК, изоловане из ХЛ-60 ћелија, и куркумина. Мери се смањење апсорбације формираних комплекса ХЛ-60 ДНК и куркумина у односу на слепу пробу. Хемолуминисцентна метода укључује три теста за детекцију луминола, на основу модел система који генерише супероксид, хидроксид и хипохлорит радикале. Највеће опадање интензитета хемолуминисценције је регистровано на концентрационом нивоу од $100 \mu\text{mol L}^{-1}$ куркумина.

(Примљено 11. јуна 2011, ревидирано 8. јануара 2012)

REFERENCES

1. T. Kolev, E. Valcheva, B. Stamboliiska, M. Spiteller, *Int. J. Quantum Chem.* **102** (2005) 1069
2. H. Hatcher, R. Planalp, J. Cho, F. Torti, S. Torti, *Cell. Mol. Life Sci.* **65** (2008) 1631
3. S. Swarnakar, K. Ganguly, P. Kundu, A. Banerjee, P. Maiti, A. Sharma, *J. Biol. Chem.* **280** (2005) 9409
4. M. Panchatcharam, S. Miriyala, V. Gayathri, L. Suguna, *Mol. Cell Biochem.* **290** (2006) 87
5. F. Marotta, Y. Shield, T. Bamba, Y. Naito, E. Minelli, E. Yoshioka, *Chin. J. Digestive Diseases* **4** (2003) 122
6. K. Maiti, K. Mukherjee, A. Gantait, B. Saha, P. Mukherjee, *Int. J. Pharm.* **330** (2007) 155
7. B. Aggarwal, S. Shishodia, *Biochem. Pharmacol.* **71** (2006) 1397
8. H. Choi, Y. Kim, S. Kim, M. Park, J. Wan, *Mol. Pharmacol.* **70** (2006) 1664
9. J. M. Matés, J. A. Segura, F. J. Alonso, J. Márquez, *Curr. Med. Chem.* **18** (2011) 2315
10. G. Sa, T. Das, S. Banerjee, J. Chakraborty, *Al Ameen J. Med. Sci.* **3** (2010) 21
11. F. Yen, T. Wu, C. Tzeng, L. Lin, C. Lin, *J. Agric. Food Chem.* **58** (2010) 7376
12. A. Banerjee, A. Kunwar, B. Mishra, K. Priydarsini, *Chem. Biol. Interact.* **174** (2008) 134
13. F. Bonte, M. Noel-Hudson, J. Wepierre, A. Maybeck, *Planta Med.* **63** (1997) 265
14. A. Barik, B. Mishra, L. Shen, H. Mohan, R. M. Kadam, S. Dutta, H. Y. Zhang, K. I. Priyadarsini, *Free Radic. Biol. Med.* **39** (2005) 811
15. H. Ahsan, N. Parveen, N. Khan, S. Hadi, *Chem. Biol. Interact.* **12** (1999) 161
16. K. Das, C. Das, *Biochem. Biophys. Res. Commun.* **295** (2002) 62.





Solvent-free preparation of poly(lactic acid) fibers by melt electrospinning using an umbrella-like spray head and alleviation of the problematic thermal degradation

YONG LIU¹, FENGWEN ZHAO¹, CHI ZHANG², JIANMING ZHANG³
and WEIMIN YANG^{1*}

¹College of Mechanical and Electrical Engineering, Beijing University of Chemical Technology, Beijing 100029, China, ²Engineering Research Center of Biomass Materials, Ministry of Education, Southwest University of Science and Technology, Mianyang, Sichuan 621010, China and ³College of Polymer Science and Engineering, Qingdao University of Science and Technology, Qingdao 266042, China

(Received 11 July 2011, revised 20 March 2012)

Abstract: Melt electrospinning is an even simpler and safer method compared to solution electrospinning in the production of ultra-fine fibers. Poly(lactic acid) (PLA) is a biodegradable and resorbable aliphatic ester that has received significant attention in recent years. PLA is easily degradable at high temperatures during the process of melt electrospinning. Highly efficient fibers were made using a self-designed umbrella-like spray head spinning facility in. Differential scanning calorimeter and X-ray diffraction analysis were used to determine how to alleviate the problematic degradation, as well as which factors could be relevant to the degradation, temperature and relative molecular mass, by comparing the results obtained before and after spinning. The results showed that fibers spun at 245 °C were facile, shorter and fractured while the relative molecular mass of PLA fibers had decreased markedly as compared with those spun at 210 °C. In attempts to hinder the degradation, several experiments were implemented with the addition of antioxidants, raising the spinning voltage, lowering the temperature and reducing the residence time. After such modifications, it was observed that the relative molecular mass of the PLA fibers was higher than that of those without the modifications. The addition of the antioxidant 1010 was found to be the most promising method for the alleviation of the problematic thermal degradation of PLA.

Keywords: PLA fibers; melt electrospinning; X-ray diffraction; antioxidants.

INTRODUCTION

Since the 1990s, with the quick development of nanomaterials and nanotechnology, increasing interest and attention have been focused and paid on electro-

*Corresponding author. E-mail: yongsd@iccas.ac.cn
doi: 10.2298/JSC110711027L



spinning, primarily due to its simplicity, validity, and directness in producing nanofibers.^{1–3} Electrospinning can be conducted by two methods: solution electrospinning and melt electrospinning^{4,5}. Most researchers utilize solution electrospinning because of its simple instrumentation and ease of operation. Melt electrospinning, on the other hand, is commonly ignored because of its complexity in instrumentation and thickness of the resulting fibers.

However, solution electrospinning has some disadvantages: 1) some solvents are expensive and extremely hazardous to the environment, and thus, must be recovered through highly complicated retrieval processes;⁶ 2) in the spinning process, the capillary are often blocked, hence seriously affecting the continuity of spinning;⁷ 3) it is difficult to find suitable solvents for some polymer, such as poly(propylene) and polyethylene, when spun at ambient temperatures although it is not relevant to this current study; 4) the evaporation of the solvent in the spinning process can leave defects on the fiber, leading to relatively low mechanical strength⁸ and 5) the concentration of the solution is low, and its corresponding evaporation greatly reduces the yield and production efficiency.

In view of these intrinsic problems with solution electrospinning, melt electrospinning has gradually gained increasing attention since melt electrospinning produces fibers directly from polymer melts in absence of solvent. Therefore, it is considered as a safer, economic and environmentally friendly method compared with solution electrospinning.^{9,10}

The raw material, lactic acid, is derived from natural resources and is easily prepared in high yield by fermentation of molasses of potato starch or dextrose from corn.^{11,12} Then lactic acid is polymerized into poly(lactic acid) (PLA) which can be spun further into PLA fibers.¹³ PLA is one of the most promising biodegradable polymers owing to the profile of its mechanical properties, thermoplastic processibility and biological properties. L-Lactic acid provides a polymer with higher mechanical strength than the DL-form,¹² particularly in terms of tensile strength¹⁴ as the pure L-form has a high degree of crystallinity, and thus sufficient mechanical strength only in its fully isotactic form.¹⁵ In some chitosan-based composites, the addition of PLA leads to an improvement in the modulus.¹⁶ Moreover, the degradation products of polylactides are non-toxic which enhances practical applications in biomedicine and other fields.^{11,17} PLA is well-known as biodegradable polymer in daily applications, such as disposable cutlery, plates, cups, lids, packaging bags, films, and containers for liquid foods.¹⁸ In most applications of biodegradable polymers and composites, PLA is one of the important candidates for high value side and specific applications, such as tissue engineering, prosthetic devices, implants, catheters, sutures and anticancer drug delivery.¹⁷ In addition to biomedical usages, the employment of the biodegradability of PLA in packaging¹⁹ and agricultural materials is worth highlighting because PLA and its fibers can eventually be decomposed into carbon



dioxide and water through the actions of microorganism actions and finally these degraded species become recyclable materials.^{15,20,21} Due to the biodegradability and recyclability of PLA in nature, PLA has been referred to as the environmental cycle material of the 21st century.²² Many investigations have recently been conducted on PLA fibers.^{23–26}

It was reported that PLA fibers can be obtained easily through solution electrospinning, but that it is relatively difficult to accomplish under melt electrospinning.²⁷ Recently, PLA fibers were obtained through a series of melt electrospinning experiments using a uniquely designed umbrella-like spray head, when it was found that the molecular mass of PLA fiber was significantly influenced by the melt electrospinning.²⁸ In order to alleviate the problematic degradation of PLA in melt electrospinning, several attempts were undertaken to hinder the degradation of the polymer, *i.e.*, through the addition of additives, refining the processing conditions and examination of aspects of the equipment.

EXPERIMENTAL

Materials

L-PLA (melting point: 210 °C) was purchased from Nature Works LLC of America (trademark: 2002D). The PLA sample was baked at 70 °C for about 4 h before spinning. Antioxidants 1010 and 168 were purchased from Beijing Additive Institute.

Equipment

A diagram of the melt electrospinning equipment,^{28,29} specifically self-designed for this study, is shown in Fig. 1. The cylinder, piston, and spray head were made of steel. The heating system included electrical heating rings, thermal sensors, and a temperature control subsystem. The spray head was a cone-type instead of the traditional capillary tube. The melts

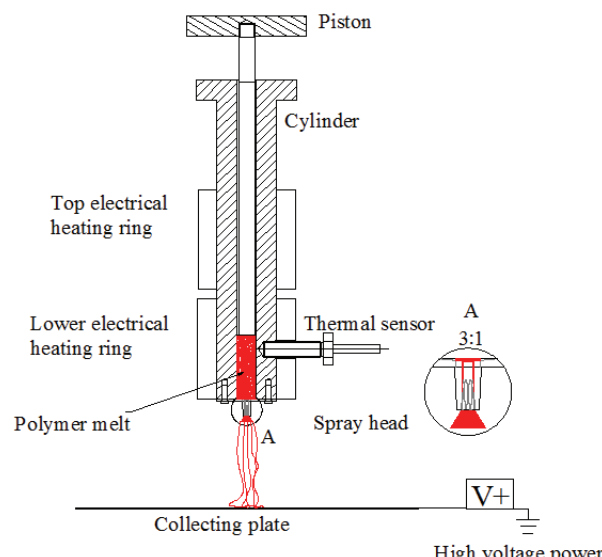


Fig. 1. Scheme of the melt electrospinning apparatus.

flowed onto the surface of an umbrella-like spray head and then formed Taylor's cones automatically at the bottom edge of the head in the high voltage electrostatic field.²⁹

Preparation of PLA fibers

The cylinder was heated to the required temperature (200–250 °C). Then, the granular or powdery material was put into the cylinder at the pre-set temperature for approximately 10 min (*i.e.*, until the melts were spread uniformly on the spray head), the high voltage supply device was switched on and adjusted to an appropriate value (30–100 KV). Thus, the melts were formed several cones along the bottom edge of the spray head, and several stripes of the PLA melt flew to the collecting mesh, as shown in Fig. 2. The distance between collecting mesh and spray head was set at around 10–23 cm.



Fig. 2. Melt electrospinning with an umbrella-like spray head.

Characterization

The morphologies of the electospun fibers were observed by scanning electron microscopy (SEM, Hitachi S4700). Fiber samples were coated with a 10 nm layer of platinum before observation. Scanning voltage was 20 KV. The relative molecular mass of the PLA fibers was measured by a gel permeation chromatograph (Shimadzu LC-6A). X-Ray diffraction (XRD) patterns of the fibers were recorded using a Rigaku D/Max-IIIC (CuK α radiation). The thermal transition curves of the PLA samples was recorded using a differential scanning calorimetry (DSC, Perkin Elmer Pyrisl) to demonstrate the crystalline state of the PLA before and after electrospinning.

RESULTS AND DISCUSSION

Effect of temperature on the spun fiber morphology

It is well-known that temperature has significant effects on melt electrospinning.^{4,5,29} Overheating at high temperatures leads to a sharp decrease in the melt viscosity, indicating a molecular weight decrease; consequently, the polymer melts flow faster and the residence time in the spinning device is shorter. The SEM micrograph of the PLA fibers obtained from melt electrospinning with the

cylinder temperature set at 210° C and at a voltage of 60 KV is shown in Fig. 3. The average diameter of the resultant fibers was 7.65 μm with a fiber diameter variance of 0.21 μm and the spinning efficiency of electrospinning was 4 g h^{-1} when using the abovementioned conditions. It was noticed that in Fig. 3 that the surface of the PLA fiber was quite smooth, suggesting the fibers had higher tensile strength compared with those with defects on the surface; such defects results in the typical poor mechanical properties from solution electrospinning.

However, if the temperature is higher than some limit, the polymer will start to degrade, especially for an easy-degradable polymer. From a DSC scan, it was evidenced that PLA starts to degrade significantly at 250 °C.¹⁵ An SEM image of PLA fibers fabricated at a spinning temperature of 245 °C is shown in Fig 4. Apparently, many of the PLA fibers were broken into short fibers and the fiber diameter distribution was broader. However, during spinning, fibers were seen on the collection mesh with continuity and unbroken. It could be reasoned that the short fibers might be due to the pressing force from the tweezers when the electron microscopy samples were prepared. Although such an augmentation might

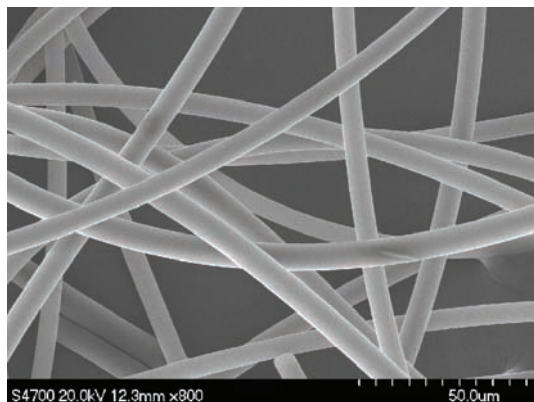


Fig. 3. SEM Micrograph of PLA fibers spun at 210 °C. The distance between the spray head and collection mesh was 11 cm.

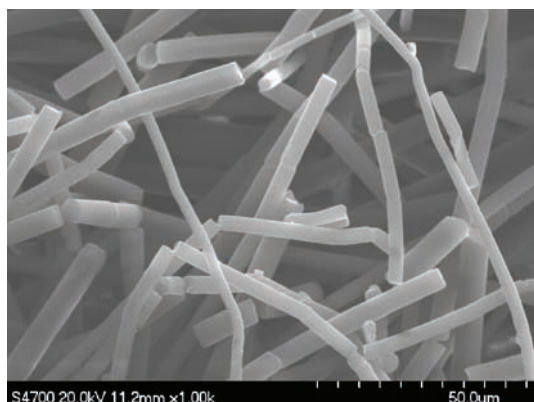


Fig. 4. SEM Micrograph of PLA fibers spun at 245 °C. The distance between the spray head and collection mesh was 11 cm.

be reasonable, it must be born in mind bear in mind that the pressing force was also applied to the fibers resulting from lower temperature spinning (*e.g.*, 210 °C). However, under the same action and pressing force from the tweezers, only the PLA fibers that had undergone chain scission and a decrease in molecular mass with the resulting compromised mechanical properties would be brittle with shorter fibers and hence easily powderized. Thus, temperature is a key parameter necessary to take into consideration and to be well controlled during PLA melt spinning.

Effect of temperature on the relative molecular mass of spun PLA fibers

As heating is a necessary condition to realize melt electrospinning, it is important to know the extent of degradation of spun fibers. To determine the intrinsic relationship between thermal spinning at a certain temperature and the extent of degradation, the relative molecular mass (M_p , as a function of molecular mass *vs.* eluent volume) of PLA before and after melt electrospinning at 245 °C was measured. A comparison of the M_p of the PLA before and after melt electrospinning at 245 °C is shown in Fig. 5 and given in Table I. The M_p of the PLA had clearly decreased (by 56.2 %) after melt electrospinning. The possible reason for this is that high spinning temperatures (*e.g.*, above 230 °C) causes thermal degradation of the PLA molecules. It was reported from some available experimental data at temperatures above 200 °C that PLA may experience a minimum of four

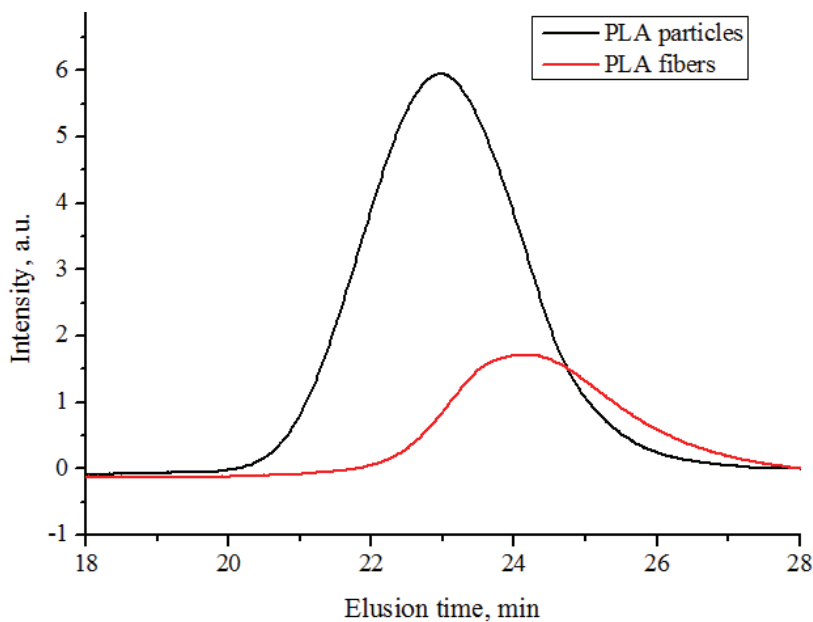


Fig. 5. Comparison of relative molecular mass of PLA before (Particles) and after (Fibers) melt electrospinning at 245 °C.

reaction pathways during thermal decomposition:¹⁵

- 1) intra- and intermolecular ester exchange to produce lactide and cyclic oligomers;
- 2) *cis*-elimination to generate acrylic acid and acyclic oligomers;
- 3) radical and concerted non-radical reactions to produce CH₃CHO and CO;
- 4) radical reactions to generate CH₃CH=C=O, CH₃CHO and CO₂.

Among these possible pathways, Kopinke³⁰ believed that there are two principal pyrolysis mechanisms for polyesters: *cis*-elimination and *trans*-esterification, but that at temperatures above 300 °C, non-selective radical reactions may also occur. Therefore, the outcome in Fig. 5 and Table I for PLA breaking down into short-chain molecules can be readily understood. It can be concluded that melt electrospinning for pure PLA material will naturally lead to a certain extent of degradation of PLA at above 200 °C because heating is necessary for PLA melting and then for the spinning process.

TABLE I. Relative molecular mass of PLA before and after melt electrospinning

PLA	M_p	M_n	M_w/M_n
Particles	131277	92736	1.8
Fibers	57497	34733	2.0

XRD and DSC investigations before and after spinning

Degradation leads to a decrease in tensile strength because PLA is either a crystalline or a partially crystalline polymer and tensile strength is relevant to its isotactic form.¹⁵ The tensile strength of individual fibers is difficult to measure because the fibers are very fine and thin. The degree of Crystallinity can reflect the strength in an aspect. Hence, the XRD and DSC patterns of PLA were recorded, as shown in Figs. 6 and 7. From Fig. 6, it can be seen that the PLA particles had a clear crystalline peak before electrospinning. After spinning, however, the sharp crystalline peak had disappeared and a smooth and broad amorphous band peaked at round $2\theta = 17^\circ$. The raw PLA from the polymerization reaction of L-lactic acid can form a high degree or partial isotactic structure of polymer and the isotactic structure constructs a lattice during polymerization. Consequently, a sharp crystalline peak existed in the XRD scan of the raw PLA. Comparatively, after electrospinning, the relative molecular mass of PLA became lower due to the thermal decomposition of the molecular chains. Although the chains underwent strong orientation, they could not crystallize as well because the chains were short and the decomposition impurities generated amorphous domains and caused high defects in the existing lattices. The DSC thermograms of PLA before and after spinning (Fig. 7) demonstrates this well. It can be seen that the PLA particles have two sharp melting peaks at 140 and 146 °C. However, after spinning, the sharp melting peak had disappeared. The small and smooth



melting peak indicates an incomplete crystalline state. Although crystallization occurred, the amount of crystallinity was too small to be registered in the XRD patterns.

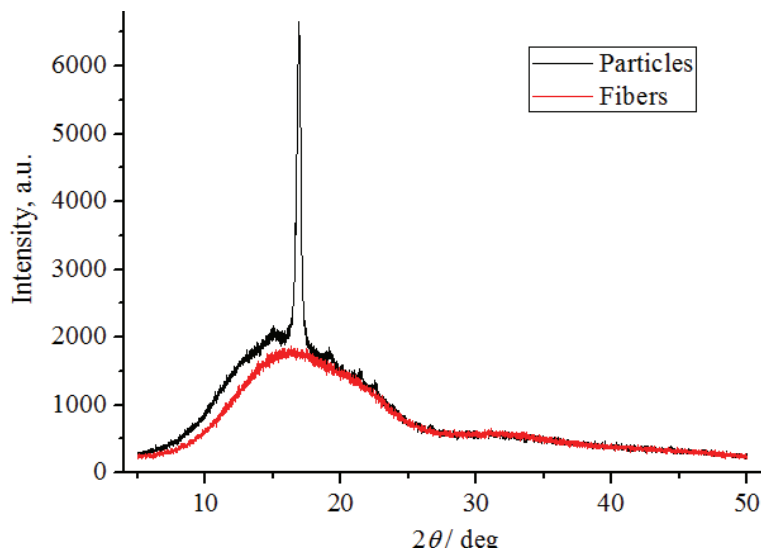


Fig. 6. XRD Patterns of PLA particles and fibers.

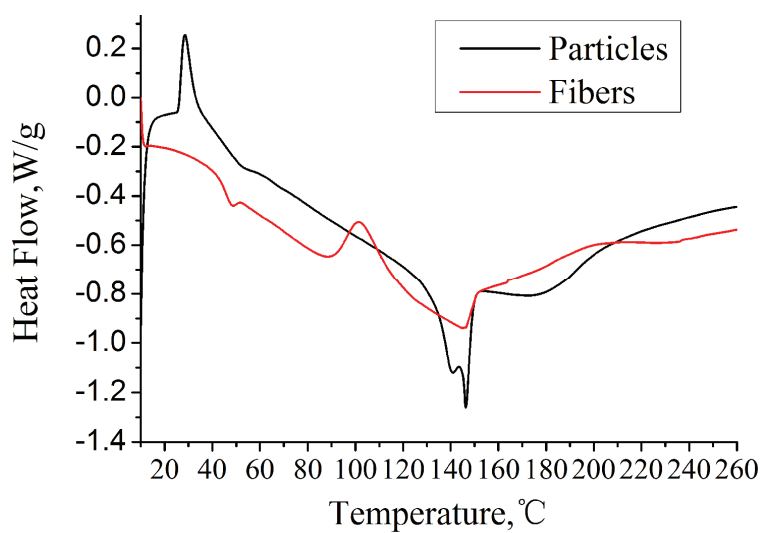


Fig. 7. DSC Thermograms of PLA particles and fibers.

Methods in alleviating the problematic degradation of PLA spun fibers

In order to minimize the side effects of thermal decomposition or to alleviate the thermal degradation for PLA in the melt electrospinning process, the initial electrospinning process was modified in terms of addition of antioxidants, the equipment and the processing conditions.

For the additives, antioxidant 1010 and antioxidant 168 were added to reduce the chain scission reaction. The antioxidant 1010 is a hindered phenolic antioxidant, the molecule of which loses a hydrogen atom to form a stable aryl radical. This radical captures chain-free radicals generated from thermo-oxidative degradation of PLA, thus partially terminating reactions at the chain break. Antioxidant 168 is a phosphite ester antioxidant. It is able to trap peroxy radicals³¹ and effectively decompose hydroperoxides produced during the processing of polymeric materials and hence inhibits the PLA from undergoing thermal degradation.

In terms of equipment, a low- and a high-temperature electrical heating ring, rather than two high-temperature heating rings, were installed and used to reduce the high temperature shock/input for avoiding unwanted longer residence times of PLA feed in the cylinder. The gap between the spinning head and the cylinder was increased to ensure that the viscous melt could flow down continuously and constantly along the conical surface of the spray head, thereby decreasing the residence time of the PLA in the hot cylinder.

As for the processing conditions of electrospinning, the spinning temperature was reduced from the usual 230 down to 210 °C. A new high voltage supply device with a maximum output of 100 kV replaced the initial one that had a maximum output 60 kV. The spinning voltage could then be increased from lower to higher, that is, from the initial 60 up to 100 kV.

Effect of additives on degradation of PLA

Antioxidants as additives can alleviate the problematic degradation of PLA fibers. After adjusting the heating temperature and adopting a new electrospinning device, a considerably higher efficiency (about 6 g h⁻¹) of fiber formation, as opposed to 4 g h⁻¹ obtained using the initial device settings, was obtained. The detailed effects of temperature and voltage on PLA fiber properties was reported previously.²⁹ In the present study, the impact of antioxidants on PLA degradation was examined in detail (shown in Fig. 8 and Table II). The mass ratio of the antioxidant and PLA in the feed was 3:1000. In case of a mixture of antioxidants, the mass ratio of antioxidant 168 to antioxidant 1010 was 1:1. The spinning voltage was set at 100 kV with a spinning distance of 12 cm. On comparing curves a and b in Fig. 8, it could be seen that the antioxidant 168 had little effect in moderating the degradation of PLA fibers. A comparison of curves a and c indicates that the 1:1 mixture of antioxidant 168 and antioxidant 1010 had enhanced effects in alle-



viating degradation. In the case of the mixed antioxidants, the relative molecular mass (curve c) was 18.05 % higher than that of the antioxidant-free counterpart (curve a). The antioxidant 1010 showed the most distinct effect in hindering the degradation of PLA fibers among the cases shown by curves b, c and d. The M_p of the PLA fibers processed in the presence of antioxidant 1010 (curve d) was 35.5 % higher than that of the fibers fabricated in the absence of antioxidant (curve a).

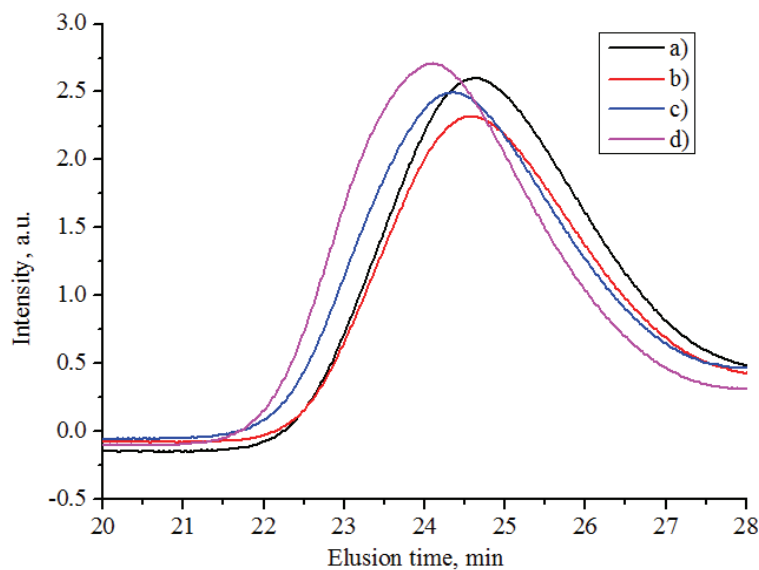


Fig. 8. Comparison of the relative molecular mass of PLA fibers spun under the same temperature and processing parameters: a) PLA fibers; b) PLA fibers + antioxidant 168; c) PLA fibers + antioxidant 168 + antioxidant 1010; d) PLA fibers + antioxidant 1010.

Finally, a comparison of Figs. 5 and 8a shows that the PLA fibers produced in this study in the absence of antioxidant had a relatively lower molecular mass than those obtained in a previous study performed several months earlier. It is possible that the PLA used in the present study, which had been stored under natural conditions, had been degraded by the oxygen in the air in presence of moisture.

TABLE II. Relative molecular mass of PLA fibers electrospun under the same temperature and processing parameters

PLA	M_p	M_n	M_w/M_n
PLA fibers	35367	7970	4.2
PLA fibers + antioxidant 168	36919	7403	6.0
PLA fibers + antioxidants 168 and 1010	41751	6437	4.5
PLA fibers + antioxidant 1010	48482	9664	4.9

CONCLUSIONS

The problematic degradation of facile degradable PLA in melt electrospinning was studied and alleviated by means of hindering thermal degradation of the spun PLA fibers by the addition of antioxidants, and modification of the equipment and processing parameters, particularly, temperature. Lowering the temperature and addition of antioxidant were found effective in alleviating the degradation of PLA in melt electrospinning. The effects of two antioxidants, individually and as a mixture, were compared and it was found that antioxidant 1010 had a remarkable capability to hinder the thermal degradation of PLA during melt electrospinning.

Acknowledgements. The authors would like to thank Professor Ping Hu, Xiaogong Wang of Tsinghua University, Professor Xiaozhen Yang, Dadong Yan and Delu Zhao of the Institute of Chemistry, Chinese Academy of Science (ICCAS) for their support and valuable discussions. The study was supported by the Open Project of State Key Laboratory Cultivation Base for Nonmetal Composites and Functional Materials (10zxfk16).

ИЗВОД

ИЗРАДА ВЛАКАНА ПОЛИ(МЛЕЧНЕ КИСЕЛИНЕ) ПОСТУПКОМ ЕЛЕКТРОСПИННИНГА ИЗ РАСТОПА ПРИМЕНОМ ГЛАВЕ У ОБЛИКУ КИШОБРАНА И СМАЊЕЊЕ ПРОЦЕСА ТЕРМИЧКЕ ДЕГРАДАЦИЈЕ

YONG LIU¹, FENGWEN ZHAO¹, CHI ZHANG², JIANMING ZHANG³ and WEIMIN YANG¹

¹College of Mechanical and Electrical Engineering, Beijing University of Chemical Technology, Beijing 100029, China, ²Engineering Research Center of Biomass Materials, Ministry of Education, Southwest University of Science and Technology, Mianyang, Sichuan 621010, China and ³College of Polymer Science and Engineering, Qingdao University of Science and Technology, Qingdao 266042, China

Израда ултра-финих влакана поступком електроспининга из растопа је једноставнији и сигурнији поступак у односу на електроспининг из раствора. Поли(млечна киселина) (PLA) је алифатски полиестар који у последње време привлачи све већу пажњу због својих биодеградабилних и ресорбујућих својстава. PLA лако деградира на високим температурама у процесу израде влакана електроспинингом из растопа. У овом раду је приказана израда високо-квалитетних влакна коришћењем специјално дизајниране главе у облику кишобрана. У намери да се елиминише термичка деградација растопа полимера, анализиран је утицај температуре на моларну масе, термичка својства и степен кристаличности полимера, поређењем DSC термограма и WAXS дифрактограма полимерних узорака пре и после обликовања. Резултати су показали да се добијају краћа и оштећена влакна уколико се обликовање изводи на температури 245 °C, док је моларна маса PLA значајно опала у односу на влакна добијена на температури 210 °C. Да би се смањила термичка деградација полимера примењене су различите експерименталне технике: повећање напона при извлачењу влакана, снижење температуре и времена задржавања растопа полимера као и додатак антиоксиданаса. Побољшање експерименталних услова извођења електроспининга довело је до повећања моларне масе PLA влакана. Примена антиоксиданса 1010 дала је најбоље резултате у погледу смањења термичке деградације PLA.

(Примљено 11. јула 2011, ревидирано 20. марта 2012)



REFERENCES

1. H. L. Jiang, Y. Q. Hu, Y. Li, P. C. Zhao, K. J. Zhu, W. Chen, *J. Controlled Release* **108** (2005) 237
2. Z. M. Huang, Y. Z. Zhang, M. Kotaki, S. Ramakrishna, *Compos. Sci. Technol.* **63** (2003) 2223
3. Y. Dzenis, *Science* **304** (2004) 1917
4. L. Jason, K. Frank, *Polym. News* **30** (2007) 170
5. J. Lyons, C. Li, F. Ko, *Polymer* **45** (2004) 7597
6. M. C. Bottino, V. Thomas, G. M. Janowski, *Acta Biomater.* **7** (2011) 216
7. F. L. Zhou, R. H. Gong, I. Porat, *Polym. Eng. Sci.* **49** (2009) 2475
8. S. H. Lee, B. S. Kim, S. H. Kim, S. W. Kang, Y. H. Kim, *Macromol. Biosci.* **4** (2004) 802
9. R. F. Service, *Science* **328** (2010) 304
10. D. W. Hutmacher, P. D. Dalton, *Chem. Asian J.* **6** (2011) 44
11. Y. J. Wee, J. N. Kim, J. S. Yun, H. W. Ryu, *Enzyme. Microb. Technol.* **35** (2004) 568
12. B. Gupta, N. Revagade, J. Hilborn, *Prog. Polym. Sci.* **32** (2007) 455
13. E. B. Bond (L. W. Lewis; A. M. Stone), US 6783854B2 (2004)
14. I. Engelberg, J. Kohn, *Biomaterials* **12** (1991) 292
15. F. D. Kopinke, M. Remmler, K. MacKenzie, M. Moeder, O. Wachsen, *Polym. Degrad. Stab.* **53** (1996) 329
16. X. Cai, H. Tong, X. Shen, W. Chen, J. Yan, J. Hu, *Acta Biomater.* **5** (2009), 2693
17. O. Benny, O. Fainaru, A. Adini, F. Cassiola, L. Bazinet, I. Adini, E. Pravda, Y. Nahmias, S. Koirala, G. Corfas, R. J. D'Amato, J. Folkman, *Nat. Biotechnol.* **26** (2008), 799
18. R. E. Conn, J. J. Kolstad, J. F. Borzelleca, D. S. Dixler, L. J. Filer, B. N. LaDu, M. W. Pariza, *Food Chem. Toxicol.* **33** (1995) 273
19. G. Glenn, A. Klamczynski, C. Ludvik, B. S. Chiou, S. Imam, J. Shey, W. Orts, D. Wood, *Packag. Technol. Sci.* **20** (2007) 77
20. R. Iovino, R. Zullo, M. A. Rao, L. Cassar, L. Gianfreda, *Polym. Degrad. Stab.* **93** (2008) 147
21. P. Rychter, R. Biczak, B. Herman, A. Smylla, P. Kurcok, G. Adamus, M. Kowalcuk, *Biomacromolecules* **7** (2006) 3125
22. M. T. Hunley, T. E. Long, *Polym. Int.* **57** (2007) 385
23. Y. Mizutani, M. Hattori, M. Okuyama, T. Kasuga, M. Nogami, *Polymer* **46** (2005) 3789
24. S. D. McCullen, K. L. Stano, D. R. Stevens, W. A. Roberts, N. A. Monteiro-Riviere, L. I. Clarke, R. E. Gorga, *J. Appl. Polym. Sci.* **105** (2007) 1668
25. T. Xu, P. P. S. Lee, Z. Xue, Y. Chen, Y. Wang, H. Wang, C. Huang, J. H. Xin, K. K. L. Cheuk, *Polym. Prepr.* **51** (2010) 640
26. A. R. Cho, D. M. Shin, H. W. Jung, J. C. Hyun, J. S. Lee, D. H. Cho, Y. L. Joo, *J. Appl. Polym. Sci.* **120** (2011) 752
27. H. Zhou, T. B. Green, Y. L. Joo, *Polymer* **47** (2006) 7497
28. R. J. Deng, Y. Liu, Y. M. Ding, P. C. Xie, L. Luo, W. M. Yang, *J. Appl. Polym. Sci.* **114** (2009) 166
29. Y. Liu, R. J. Deng, M. F. Hao, H. Yan, W. M. Yang, *Polym. Eng. Sci.* **50** (2010) 2074
30. F. D. Kopinke, K. MacKenzie, *J. Anal. Appl. Pyrol.* **40–41** (1997) 43
31. K. Schwetlick, T. Koenig, J. Pionteck, D. Sasse, W. D. Habicher, *Polym. Degrad. Stab.* **22** (1988) 357.





SHORT COMMUNICATION

Correlation of the liquid mixture viscosities

ANDELA B. KNEŽEVIĆ-STEVANOVIĆ¹, GORAN M. BABIĆ², MIRJANA LJ. KIJEVČANIN^{2#}, SLOBODAN P. ŠERBANOVIĆ^{2#} and DUŠAN K. GROZDANIĆ^{2*}

¹Metro Vancouver, 4330 Kingsway, Burnaby, British Columbia, V5H 4G8, Canada and

²Chemical Engineering Department, Faculty of Technology and Metallurgy, University of Belgrade, Kariđelova 4, 11000 Belgrade, Serbia

(Received 27 January, revised 18 April 2012)

Abstract: In this paper, forty-two selected correlation models for liquid mixture viscosities of organic compounds were tested on 219 binary and 41 ternary sets of experimental data taken from the literature. The binary sets contained 3675 experimental data points for 70 different compounds. The ternary sets contained 2879 experimental data points for 29 different compounds. The Heric I, Heric–Brewer II, and Krishnan–Laddha models demonstrated the best correlative characteristics for the binary mixtures (overall absolute average deviation < 2 %). The Heric I, Heric–Brewer II, Krishnan–Laddha and Heric II models demonstrated the best correlative characteristics for the ternary mixtures (overall absolute average deviation < 3 %).

Keywords: binary mixture; ternary mixture; liquid mixture viscosity; correlation model.

INTRODUCTION

The study of thermodynamic properties of liquid mixtures contributes to an understanding of the behavior of various liquids and functional groups. This information is very useful in the design of industrial processes and in the development of the liquid state theories and predictive methods. Knowledge of the liquid mixture viscosities are required for the solution of many engineering problems, including heat and mass transfer, and fluid flow.

A number of correlation models have been developed for liquid mixture viscosities.^{1–18} These equations are empirical or at the best semi-theoretical. The aim of this work is to compare the correlation capabilities of these models on the experimental viscosities of binary and ternary liquid mixtures of alkanes, haloalkanes, alcohols, aromates, amines, ketones, etc.

* Corresponding author. E-mail: dule@tmf.bg.ac.rs

Serbian Chemical Society member.

doi: 10.2298/JSC120127038K

Selection of models

There are numerous correlation models for liquid mixture viscosities. From these, the models Dolezalek–Schulze,¹ Grunberg–Nissan,² Tamura–Kurata,³ McAllister 3,⁴ McAllister 4,⁴ McAllister–Chandramouli–Laddha,⁵ Katti–Chaudhri,⁶ Ausländer,⁷ Modified Wilson,⁸ Heric I,⁹ Heric II,⁹ Heric–Brewer I,¹⁰ Heric–Brewer II,¹⁰ Krishnan–Laddha,¹¹ Stephan–Heckenberger,¹² McAllister–Soliman–Marschall (McASM),¹³ Mehrotra,¹⁴ Baylaucq–Daugé–Boned,¹⁵ Dimitrov–Kamenski I,¹⁶ Dimitrov–Kamenski II,¹⁶ Dimitrov–Kamenski III,¹⁶ Dimitrov–Kamenski IV,¹⁶ Dimitrov–Kamenski V,¹⁶ Dimitrov–Kamenski VI,¹⁶ Dimitrov–Kamenski VII,¹⁶ Dimitrov–Kamenski VIII,¹⁶ Dimitrov–Kamenski IX,¹⁶ Dimitrov–Kamenski X,¹⁶ Dimitrov–Kamenski XI,¹⁶ Dimitrov–Kamenski XII,¹⁶ Dimitrov–Kamenski XIII,¹⁶ modified Dimitrov–Kamenski,¹⁶ Focke–Du Plessis I,¹⁷ Focke–Du Plessis II,¹⁷ Focke–Du Plessis III,¹⁷ Focke–Du Plessis IV,¹⁷ Focke–Du Plessis V,¹⁷ Focke–Du Plessis VI,¹⁷ Focke–Du Plessis VII,¹⁷ Focke–Du Plessis VIII,¹⁷ Focke–Du Plessis IX,¹⁷ and Focke–Sandrock–Kok,¹⁸ in chronological order, were selected for the present study. The equations related to the selected models are given in the Supplementary material to this paper. The number of parameters in these models varies from one to nine.

McAllister 3, McAllister 4, Stephan–Heckenberger, Dimitrov–Kamenski I–XIII and Focke–Du Plessis I–IX are models for binary mixtures, whereas McAllister–Chandramouli–Laddha, Heric II and Modified Dimitrov–Kamenski are models for ternary mixtures. All models except the Ausländer, Modified Wilson, Stephan–Heckenberger and Focke–Sandrock–Kok are linear or can be linearized per parameters. A preliminary investigation indicated that these non-linear equations do not result in correlations significantly better than those obtained with linear equations with the same number of parameters. The linear models were investigated in this work as correlations with the nonlinear models resulted in problems of convergence and global optima. These models are based on the model of ideal mixture with additional correction terms and therefore their parameters have not physical meaning.

SELECTION OF EXPERIMENTAL DATA POINTS

The performance of selected linear models was tested on 219 binary and 41 ternary sets of literature experimental data. The binary sets contained 3675 experimental data points for 70 different compounds. The ternary sets contained 2879 experimental data points for 29 different compounds. The selected binary and ternary liquid mixtures are presented in Tables SI and SII in the Supplementary material to this paper.

RESULTS AND DISCUSSION

The results for the selected linear models are presented in Table I, where N_{all} is a total number of data points in the correlation. Only sets of experimental data with $n \geq N_m + 2$ were used in the correlation, where N_m is the number of model



parameters. Sets with experimental data for different temperatures and pressures were correlated with only one set of parameters. The deviation from the experimental values is expressed as the absolute average deviation p_{av} for each data set point:

$$p_{av} = (100 / n) \sum_{i=1}^n |(\eta_{l,m,i,\text{exp}} - \eta_{l,m,i,\text{cal}}) / \eta_{l,m,i,\text{exp}}| \quad (1)$$

where $\eta_{l,m}$ is the viscosity of a liquid mixture, and n is the number of experimental data points per set. The overall absolute average deviation P_{av} for each model is expressed as:

$$P_{av} = \sum_{i=1}^N n_i p_{av,i} / \sum_{i=1}^N n_i \quad (2)$$

where N is the number of data sets.

TABLE I. Results for the selected linear models

No.	Correlation model	Binary mixtures		Ternary mixtures	
		$P_{av} / \%$	N_{all}	$P_{av} / \%$	N_{all}
1	Dolezalek–Schulze	6.83	3675	8.32	2879
2	Grunberg–Nissan	3.37	3675	4.24	2879
3	Tamura–Kurata	5.14	3360	8.75	2879
4	McAllister 3	5.29	3264	—	—
5	McAllister 4	6.07	3249	—	—
6	McAllister–Chandramouli–Laddha	—	—	7.84	2861
7	Katti–Chaudhri	2.45	3264	4.18	2879
8	Heric I	1.73	3264	2.91	2879
9	Heric II	—	—	2.62	2861
10	Heric–Brewer I	8.21	3660	9.30	2861
11	Heric–Brewer II	1.23	3249	2.46	2861
12	Krishnan–Laddha	1.76	3264	2.92	2879
13	McAllister–Soliman–Marschall	5.31	3264	7.69	2861
14	Mehrotra	2.98	3675	5.10	2879
15	Baylaucq–Daugé–Boned	4.30	486	12.00	810
16	Dimitrov–Kamenski I	20.72	3675	—	—
17	Dimitrov–Kamenski II	10.48	2212	—	—
18	Dimitrov–Kamenski III	16.03	3576	—	—
19	Dimitrov–Kamenski IV	13.08	3675	—	—
20	Dimitrov–Kamenski V	10.32	2212	—	—
21	Dimitrov–Kamenski VI	20.10	3675	—	—
22	Dimitrov–Kamenski VII	13.72	2212	—	—
23	Dimitrov–Kamenski VIII	3.77	3660	—	—
24	Dimitrov–Kamenski IX	9.42	2212	—	—
25	Dimitrov–Kamenski X	44.67	3675	—	—
26	Dimitrov–Kamenski XI	3.63	2212	—	—
27	Dimitrov–Kamenski XII	32.96	3660	—	—



TABLE I. Continued

No.	Correlation model	Binary mixtures		Ternary mixtures	
		P_{av} / %	N_{all}	P_{av} / %	N_{all}
28	Dimitrov–Kamenski XIII	2.10	2212	—	—
29	Modified Dimitrov–Kamenski	—	—	11.17	2879
30	Focke–Du Plessis I	15.89	3576	—	—
31	Focke–Du Plessis II	9.86	3401	—	—
32	Focke–Du Plessis III	16.96	3375	—	—
33	Focke–Du Plessis IV	20.61	3576	—	—
34	Focke–Du Plessis V	15.64	3401	—	—
35	Focke–Du Plessis VI	11.85	3393	—	—
36	Focke–Du Plessis VII	25.15	3401	—	—
37	Focke–Du Plessis VIII	29.67	3393	—	—
38	Focke–Du Plessis IX	47.03	3357	—	—

The results presented in Table I indicate that the Heric I, Heric–Brewer II, and Krishnan–Laddha models have the best correlation ability for the binary mixtures (with overall absolute average deviations of 1.73, 1.23 and 1.76 %, respectively), while the Heric I, Heric II, Heric–Brewer II and Krishnan–Laddha models demonstrated the best correlation ability for the ternary mixtures (with overall absolute average deviations of 2.91, 2.62, 2.46 and 2.92 %, respectively). These models also have the best correlation results for different group of mixtures, such as *n*-alkane+*n*-alkane (34 data sets), *n*-alkylalcohol+*n*-alkylalcohol (31 data sets), etc. For many experimental data sets, the models with rational form gave average percent errors of about 1 %. However, in some instances, the denominator had a very small value that resulted in very large percent and average percent errors, making the models with rational form unreliable. The large differences in viscosities of the pure substances (2,6,10,15,19,23-hexamethyltetracosane + butane, 2,6,10,15,19,23-hexamethyltetracosane + hexane) resulted in poor correlation results for all models. The experimental data in all sets have monotonically descent or monotonically ascent trend between the viscosities of pure components at constant temperature and constant pressure and therefore models with smaller number of parameters gave better results.

CONCLUSIONS

Selected correlation models were tested on 219 binary and 41 ternary mixtures with 3675 and 2879 experimental data points, respectively. The Heric I, Heric–Brewer II, and Krishnan–Laddha models have the best correlative characteristics (overall absolute average deviations < 2 %) for binary, while the Heric I, Heric–Brewer II, Krishnan–Laddha, and Heric II models (overall absolute average deviations < 3 %) for ternary mixtures.



SUPPLEMENTARY MATERIAL

The equations of the selected correlation models as well as the data of selected binary and ternary liquid mixtures [1–49] are available electronically at <http://www.shd.org.rs/JSCS/>, or from the corresponding author on request.

Acknowledgements. This work was supported by a grant from the Research Fund of the Republic of Serbia (Project No. 172063) and the Faculty of Technology and Metallurgy, University of Belgrade.

NOMENCLATURE

m	Number of mixture components
n	Number of experimental data points per set
N	Number of data sets
N_{all}	Total number of data points in a correlation
N_m	Number of model parameters
M	Molar mass, g mol ⁻¹
T_m	Temperature of mixture, K
p_m	Pressure of mixture, bar
x	Mole fraction
ϕ	Volume fraction
η	Viscosity, mPa s
ρ	Density, g cm ⁻³
v	Molar volume, cm ³ mol ⁻¹
P_{av}	Absolute average deviation, %
P_{av}	Overall absolute average deviation, %.

ИЗВОД

КОРЕЛИСАЊЕ ВИСКОЗИТЕТА ТЕЧНИХ СМЕША

АНЂЕЛА Б. КНЕЖЕВИЋ-СТЕВАНОВИЋ¹, ГОРАН М. БАБИЋ², МИРЈАНА Љ. КИЈЕВЧАНИН²,
СЛОБОДАН П. ШЕРБАНОВИЋ² и ДУШАН К. ГРОЗДАНИЋ²

¹*Metro Vancouver, 4330 Kingsway, Burnaby, British Columbia, V5H 4G8, Canada* и

²*Технолошко-мештапуришки факултет, Универзитет у Београду, Карнеијева 4, 11000 Београд*

У овом раду тестирана су 42 одабрана модела за корелисање вискоситета течних смеша на литературним експерименталним подацима за 219 бинарних и 41 тернерну смешу. Бинарни сетови имају 3675 експерименталних података за 70 различитих супстанци, а тернерни 2879 експерименталних података за 29 различитих супстанци. Heric I, Heric-Brewer II и Krishnan-Laddha модели показали су најбоље корелационе особине са укупном средњом процентуалном грешком мањом од 2 % за бинарне смеше. Heric I, Heric-Brewer II, Krishnan-Laddha и Heric II модели показали су најбоље корелационе особине са укупном средњом процентуалном грешком мањом од 3 % за тернерне смеше.

(Примљен 27. јануара, ревидиран 18. априла 2012)

REFERENCES*

1. F. Dolezalek, A. Schulze, *Z. Phys. Chem.* **83** (1913) 45
2. L. Grunberg, A. H. Nissan, *Nature* **164** (1949) 799

*The references 18–49 relate to the data presented in the Supplementary material.



3. M. Tamura, M. Kurata, *Bull. Chem. Soc. Jpn.* **25** (1952) 32
4. R. A. McAllister, *AIChE J.* **6** (1960) 427
5. V. V. Chandramouli, G. S. Laddha, *Indian J. Technol.* **1** (1963) 199
6. P. K. Katti, M. M. Chaudhri, *J. Chem. Eng. Data* **9** (1964) 442
7. G. Ausländer, *Brit. Chem. Eng.* **9** (1964) 610
8. G. M. Wilson, *J. Am. Chem. Soc.* **86** (1964) 127
9. E. L. Heric, *J. Chem. Eng. Data* **11** (1966) 66
10. E. L. Heric, J. G. Brewer, *J. Chem. Eng. Data* **12** (1967) 574
11. M. R. V. Krishnan, G. S. Laddha, *Ind. Eng. Chem. Fundam.* **7** (1968) 324
12. K. Stephan, T. Heckenberger, *Thermal Conductivity and Viscosity Data of Fluid Mixtures*, DECHEMA Chemistry Data Series, Vol. X(1), Frankfurt am Maine, Germany, 1989
13. K. Soliman, E. Marschall, *J. Chem. Eng. Data* **35** (1990) 375
14. A. K. Mehrotra, *Can. J. Chem. Eng.* **68** (1990) 839
15. A. Baylaucq, P. Daugé, C. Boned, *Int. J. Thermophys.* **18** (1997) 1089
16. S. D. Dimitrov, D. I. Kamenski, *Comp. Chem. Eng.* **23** (1999) 1011
17. W. W. Focke, B. Du Plessis, *Ind. Eng. Chem. Res.* **43** (2004) 8369
18. W. W. Focke, C. Sandrock, S. Kok, *Ind. Eng. Chem. Res.* **46** (2007) 4660.
19. R. J. Fort, W. R. Moore, *Trans. Faraday Soc.* **62** (1966) 1112
20. C. Yang, P. Ma, F. Jing, D. Tang, *J. Chem. Eng. Data* **48** (2003) 836
21. M. Dizechi, E. Marschall, *J. Chem. Eng. Data* **27** (1982) 358
22. Z. Shan, A.-F. A. Asfour, *Fluid Phase Equilib.* **143** (1998) 253
23. Z. Shan, A.-F. A. Asfour, *J. Chem. Eng. Data* **44** (1999) 118
24. M. G. Prolongo, R. M. Masegosa, I. Hernandez-Fuentes, A. Horta, *J. Phys. Chem.* **88** (1984) 2163
25. P. J. Petrino, Y. H. Gaston-Bonhomme, L. E. Chevalier, *J. Chem. Eng. Data* **40** (1995) 136
26. N. M. Hussein, A.-F. A. Asfour, *J. Chem. Eng. Data* **55** (2010) 1075
27. H. Casas, L. Segade, O. Cabeza, C. Franjo, E. Jimenez, *J. Chem. Eng. Data* **46** (2001) 651
28. A. Baylaucq, C. Boned, P. Daugé, B. Lagourette, *Int. J. Thermophys.* **18** (1997) 3
29. K. E. Spells, *Trans. Faraday Soc.* **32** (1936) 530
30. A. Kumagai, S. Takahashi, *Int. J. Thermophys.* **16** (1995) 773
31. I.-C. Wei, R. L. Rowley, *J. Chem. Eng. Data* **29** (1984) 332
32. J. Kendall, K. P. Monroe, *J. Am. Chem. Soc.* **39** (1917) 1787
33. L. Grunberg, *Trans. Faraday Soc.* **50** (1954) 1293
34. S. Kouris, C. Panayiotou, *J. Chem. Eng. Data* **34** (1989) 200
35. A.-F. A. Asfour, F. A. L. Duillen, *J. Chem. Eng. Data* **26** (1981) 312
36. S. L. Oswal, H. S. Desai, *Fluid Phase Equilib.* **161** (1999) 191
37. A. J. Queimada, I. M. Marrucho, J. A. P. Coutinho, E. H. Stenby, *Int. J. Thermophys.* **26** (2005) 47
38. J. Wu, A. H. Nhaesi, A.-F. A. Asfour, *J. Chem. Eng. Data* **44** (1999) 990
39. J. Wu, A. H. Nhaesi, A.-F. A. Asfour, *Fluid Phase Equilib.* **164** (1999) 285
40. A. F. Moreiras, J. Gracia, L. Lugo, M. J. P. Comunas, E. R. Lopez, J. Fernandez, *Fluid Phase Equilib.* **204** (2003) 233
41. A.-F. A. Asfour, M. H. Siddique, T. D. Vavanellos, *J. Chem. Eng. Data* **35** (1990) 199
42. E. F. Cooper, A.-F. A. Asfour, *J. Chem. Eng. Data* **36** (1991) 285
43. A. S. Teja, P. Rice, *Chem. Eng. Sci.* **36** (1981) 7



44. H. Casas, L. Segade, C. Franjo, E. Jimenez, M. Inmaculada Paz Andrade, *J. Chem. Eng. Data* **43** (1998) 756
45. J. Nath, S. N. Dubey, *J. Phys. Chem.* **85** (1981) 886
46. M. Sovilj, Bull. Chem. Technol. Macedonia **14** (1995) 73
47. I.-C. Wei, R. L. Rowley, *J. Chem. Eng. Data* **29** (1984) 336
48. A. H. Nhaesi, A.-F. A. Asfour, *J. Chem. Eng. Data* **45** (2000) 991
49. M. N. Sovilj, *J. Chem. Eng. Data* **40** (1995) 1058.



SUPPLEMENTARY MATERIAL TO
Correlation of the liquid mixture viscosities

ANĐELA B. KNEŽEVIĆ-STEVANOVIĆ¹, GORAN M. BABIĆ², MIRJANA LJ.
KIJEVČANIN^{2#}, SLOBODAN P. ŠERBANOVIĆ^{2#} and DUŠAN K. GROZDANIĆ^{2*}

¹*Metro Vancouver, 4330 Kingsway, Burnaby, British Columbia, V5H 4G8, Canada and*
²*Chemical Engineering Department, Faculty of Technology and Metallurgy, University of Belgrade, Karnegijeva 4, 11000 Belgrade, Serbia*

J. Serb. Chem. Soc. 77 (8) (2012) 1083–1089

SELECTED CORRELATION MODELS FOR THE VISCOSITIES OF LIQUID MIXTURES*

Dolezalek-Schulze¹:

$$\eta_{l,m} = \sum_{i=1}^m x_i^2 \eta_{l,i} + \sum_{i=1}^m \sum_{\substack{j=1 \\ j \neq i}}^m x_i x_j A_{ij}, \quad A_{ij} = A_{ji} \quad (1)$$

Grunberg-Nissan²:

$$\ln(\eta_{l,m}) = \sum_{i=1}^m x_i \ln(\eta_{l,i}) + (1/2) \sum_{i=1}^m \sum_{\substack{j=1 \\ j \neq i}}^m x_i x_j A_{ij} \quad , \quad A_{ij} = A_{ji} \quad (2)$$

Tamura-Kurata³:

$$\eta_{l,m} = \sum_{i=1}^m x_i \varphi_i \eta_{l,i} + \sum_{i=1}^m \sum_{\substack{j=1 \\ j \neq i}}^m (x_i x_j \varphi_i \varphi_j)^{0.5} A_{ij}, \quad A_{ij} = A_{ji} \quad (3)$$

McAllister 3⁴:

* Corresponding author. E-mail: dule@tmf.bg.ac.rs

Serbian Chemical Society member.

*The reference numbers in the Supplementary material relate to the Reference list of the corresponding paper: J. Serb. Chem. Soc. 77 (8) (2012) 1083–1089.

$$\begin{aligned} \ln(\eta_{l,m} / \rho_{l,m}) = & x_1^3 \ln(\eta_{l,1} / \rho_{l,1}) + x_2^3 \ln(\eta_{l,2} / \rho_{l,2}) + x_2^3 \ln(M_2 / M_1) - \\ & - \ln(x_1 + x_2 M_2 / M_1) + 3x_1^2 x_2 \ln[(2 + M_2 / M_1) / 3] + \\ & + 3x_1 x_2^2 \ln[(1 + 2M_2 / M_1) / 3] + 3x_1^2 x_2 A_{l2} + 3x_1 x_2^2 A_{21} \end{aligned} \quad (4)$$

McAllister 4⁴:

$$\begin{aligned} \ln(\eta_{l,m} / \rho_{l,m}) = & x_1^4 \ln(\eta_{l,1} / \rho_{l,1}) + x_2^4 \ln(\eta_{l,2} / \rho_{l,2}) + x_2^4 \ln(M_2 / M_1) - \\ & - \ln(x_1 + x_2 M_2 / M_1) + 4x_1^3 x_2 \ln[(3 + M_2 / M_1) / 4] + \\ & + 6x_1^2 x_2^2 \ln[(1 + M_2 / M_1) / 2] + 4x_1 x_2^3 \ln[(1 + 3M_2 / M_1) / 4] + \\ & + 4x_1^3 x_2 A_{1112} + 6x_1^2 x_2^2 A_{1122} + 4x_1 x_2^3 A_{2221} \end{aligned} \quad (5)$$

McAllister-Chandramouli-Laddha⁵:

$$\begin{aligned} \ln(\eta_{l,m} / \rho_{l,m}) = & \sum_{i=1}^m x_i^3 \ln(\eta_{l,i} M_i / \rho_{l,i}) - \ln(\sum_{i=1}^m x_i M_i) + \\ & + 3 \sum_{i=1}^m \sum_{\substack{j=1 \\ j \neq i}}^m x_i^2 x_j \ln[\nu_{ij}(2M_i + M_j) / 3] + \\ & + 6 \sum_{i=1}^{m-2} \sum_{j=i+1}^{m-1} \sum_{k=i+2}^m x_i x_j x_k \ln[\nu_{ijk}(M_i + M_j + M_k) / 3] \\ & A_{ij} = \ln(\nu_{ij}), \quad A_{ijk} = \ln(\nu_{ijk}) \end{aligned} \quad (6)$$

Katti-Chaudhri⁶:

$$\ln(\eta_{l,m} / \rho_{l,m}) = \sum_{i=1}^m x_i \ln(\eta_{l,i} / \rho_{l,i}) + (1/2) \sum_{i=1}^m \sum_{\substack{j=1 \\ j \neq i}}^m x_i x_j A_{ij}, \quad A_{ij} = A_{ji} \quad (7)$$

Ausländer⁷:

$$\sum_{i=1}^m x_i (\sum_{j=1}^m A_{ij} x_j) (\eta_{l,m} - \eta_{l,i}) = 0 \quad (8)$$

Modified Wilson⁸:

$$\ln(\eta_{l,m}) = \sum_{i=1}^m x_i \ln(\eta_{l,i}) - \sum_{i=1}^m x_i \ln(x_i + \sum_{\substack{j=1 \\ j \neq i}}^m x_j A_{ij}) \quad (9)$$

Heric I⁹:



$$\ln(\eta_{l,m} / \rho_{l,m}) = \sum_{i=1}^m x_i \ln(\eta_{l,i} / \rho_{l,i}) + (1/2) \sum_{i=1}^m \sum_{\substack{j=1 \\ j \neq i}}^m x_i x_j [A_{ij} + (x_i - x_j)B_{ij}] \quad , \quad (10)$$

$$A_{ij} = A_{ji}, \quad B_{ij} = B_{ji}$$

Heric II⁹:

$$\ln(\eta_{l,m} / \rho_{l,m}) = \sum_{i=1}^3 x_i \ln(\eta_{l,i} / \rho_{l,i}) + \sum_{i=1}^3 \sum_{\substack{j=1 \\ j > i}}^3 x_i x_j [A + B(x_i - x_j)] + x_1 x_2 x_3 C \quad (11)$$

Heric-Brewer I¹⁰:

$$\eta_{l,m} = \sum_{i=1}^m x_i \eta_{l,i} + (1/2) \sum_{i=1}^m \sum_{\substack{j=1 \\ j \neq i}}^m x_i x_j [A_{ij} + (x_i - x_j)B_{ij} + (x_i - x_j)^2 C_{ij}], \quad (12)$$

$$A_{ij} = A_{ji}, \quad B_{ij} = B_{ji}, \quad C_{ij} = C_{ji}$$

Heric-Brewer II¹⁰:

$$\ln(\eta_{l,m} / \rho_{l,m}) = \sum_{i=1}^m x_i \ln(\eta_{l,i} / \rho_{l,i}) + (1/2) \sum_{i=1}^m \sum_{\substack{j=1 \\ j \neq i}}^m x_i x_j [A_{ij} + (x_i - x_j)B_{ij} + (x_i - x_j)^2 C_{ij}] \quad , \quad (13)$$

$$A_{ij} = A_{ji}, \quad B_{ij} = B_{ji}, \quad C_{ij} = C_{ji}$$

Krishnan-Laddha¹¹:

$$\ln(\eta_{l,m} / \rho_{l,m}) = \sum_{i=1}^m x_i \ln(\eta_{l,1} M_i / \rho_{l,i}) - \ln(\sum_{i=1}^m x_i M_i) +$$

$$+ (2,303/2) \sum_{i=1}^m \sum_{\substack{j=1 \\ j \neq i}}^m x_i x_j [A_{ij} + (x_i - x_j)B_{ij}] \quad , \quad (14)$$

$$A_{ij} = A_{ji}, \quad B_{ij} = B_{ji}$$

Stephan-Heckenberger¹²:

$$\ln(\eta_{l,m}) = \sum_{i=1}^2 x_i \ln(\eta_{l,i}) + \ln\{1 + x_1 x_2 / [A + BT_m + (C + DT)x_1^2]\} \quad (15)$$

McAllister-Soliman-Marschall (McASM)¹³:

$$\begin{aligned} \ln(\eta_{l,m} / \rho_{l,m}) = & \sum_{i=1}^m x_i^3 \ln(\eta_{l,i} / \rho_{l,i}) + 3 \sum_{i=1}^{m-1} \sum_{j=i+1}^m x_i x_j A_{ij} + \\ & + \sum_{i=1}^{m-1} \sum_{j=i+1}^m (x_i + x_j)^3 x_i x_j B_{ij} / [(M_i / M_j)^2 x_i + x_j] + \\ & + 6 \sum_{i=1}^{m-2} \sum_{j=i+1}^{m-1} \sum_{k=i+2}^m x_i x_j x_k A_{ijk} \end{aligned} \quad (16)$$

Mehrotra¹⁴:

$$\begin{aligned} \log(\eta_{l,m} [\text{mPas}] + 0,8) = & \sum_{i=1}^m x_i (M_i / M_m)^{0,5} \log(\eta_{l,i} [\text{mPas}] + 0,8) + \\ & + \sum_{i=1}^{m-1} \sum_{j=i+1}^m x_i x_j (M_i M_j / M_m^2)^{0,5} A_{ij} \\ M_m = & \sum_{i=1}^m x_i M_i \end{aligned} \quad (17)$$

Baylaucq-Daugé-Boned¹⁵:

$$\ln(\eta_{l,m}) = \sum_{i=1}^m x_i \ln(\eta_{l,i}) + \left(\sum_{i=1}^m \sum_{\substack{j=1 \\ j \neq i}}^i x_i x_j \right) [(A + B p_m) / T_m] [1 / (1 + C \sum_{i=1}^m x_i M_i)] \quad (18)$$

Dimitrov-Kamenski I¹⁶:

$$\eta_{l,m} = x_1 \eta_{l,1} + x_2 \eta_{l,2} + \frac{x_1 x_2 A}{x_1 + x_2 B} \quad (19)$$

Dimitrov-Kamenski II¹⁶:

$$\eta_{l,m} = x_1 \eta_{l,1} + x_2 \eta_{l,2} + \frac{x_1 x_2 (A + B T_m)}{x_1 + x_2 (C + D T_m)} \quad (20)$$

Dimitrov-Kamenski III¹⁶:

$$\eta_{l,m} = x_1 \eta_{l,1} + x_2 \eta_{l,2} + \frac{x_1 x_2 A + x_1 x_2 (x_1 - x_2) B}{x_1 + x_2 C + x_1 x_2 (x_1 - x_2) D} \quad (21)$$

Dimitrov-Kamenski IV¹⁶:

$$\eta_{l,m} = (x_1 \eta_{l,1} + x_2 \eta_{l,2}) \frac{x_1 + x_2 A}{x_1 + x_2 A + x_1 x_2 B} \quad (22)$$

Dimitrov-Kamenski V¹⁶:

$$\eta_{l,m} = (x_1\eta_{l,1} + x_2\eta_{l,2}) \frac{x_1 + x_2(A + BT_m)}{x_1 + x_2(A + BT_m) + x_1x_2(C + DT_m)} \quad (23)$$

Dimitrov-Kamenski VI¹⁶:

$$\eta_{l,m} = (x_1\eta_{l,1} + x_2\eta_{l,2}) \frac{x_1 + x_2A + x_1x_2B}{x_1 + x_2A} \quad (24)$$

Dimitrov-Kamenski VII¹⁶:

$$\eta_{l,m} = (x_1\eta_{l,1} + x_2\eta_{l,2}) \frac{x_1 + x_2(A + BT_m + CT_m^2) + x_1x_2(D + ET_m + FT_m^2)}{x_1 + x_2(A + BT_m + CT_m^2)} \quad (25)$$

Dimitrov-Kamenski VIII¹⁶:

$$\eta_{l,m} = (x_1\eta_{l,1} + x_2\eta_{l,2}) \frac{x_1 + x_2A + x_1x_2B}{x_1 + x_2A + x_1x_2C} \quad (26)$$

Dimitrov-Kamenski IX¹⁶:

$$\eta_{l,m} = (x_1\eta_{l,1} + x_2\eta_{l,2}) \frac{x_1 + x_2A + x_1x_2B}{x_1 + x_2A + x_1x_2(C + DT_m)} \quad (27)$$

Dimitrov-Kamenski X¹⁶:

$$\eta_{l,m} = (\eta_{l,1}^{x_1}\eta_{l,2}^{x_2}) \frac{x_1 + x_2A + x_1x_2B}{x_1 + x_2A} \quad (28)$$

Dimitrov-Kamenski XI¹⁶:

$$\eta_{l,m} = (\eta_{l,1}^{x_1}\eta_{l,2}^{x_2}) \frac{x_1 + x_2A + x_1x_2(B + CT_m)}{x_1 + x_2A} \quad (29)$$

Dimitrov-Kamenski XII¹⁶:

$$\eta_{l,m} = (\eta_{l,1}^{x_1}\eta_{l,2}^{x_2}) \frac{x_1 + x_2A + x_1x_2B}{x_1 + x_2A + x_1x_2(x_1 - x_2)C} \quad (30)$$

Dimitrov-Kamenski XIII¹⁶:

$$\eta_{l,m} = (\eta_{l,1}^{x_1}\eta_{l,2}^{x_2}) \frac{x_1 + x_2A + x_1x_2(B + CT_m)}{x_1 + x_2A + x_1x_2(x_1 - x_2)(D + ET_m)} \quad (31)$$

Modified Dimitrov-Kamenski¹⁶:

$$\begin{aligned} \eta_{l,m} = & \eta_{l,1}^{x_1}\eta_{l,2}^{x_2}\eta_{l,3}^{x_3} + \\ & + \frac{x_1x_2A + x_1x_3B + x_2x_3C}{1 + x_2D + x_3E + x_1x_2(x_1 - x_2)F + x_1x_3(x_1 - x_3)G + x_2x_3(x_2 - x_3)H} \end{aligned} \quad (32)$$

Focke-Du Plessis I¹⁷:



$$\eta_{l,m} = x_1\eta_{l,1} + x_2\eta_{l,2} + \frac{x_1^2 A + 2x_1x_2B + x_2^2 C}{x_1 + x_2 D} \quad (33)$$

Focke-Du Plessis II¹⁷:

$$\eta_{l,m} = x_1\eta_{l,1} + x_2\eta_{l,2} + \frac{x_1^3 A + 3x_1^2 x_2 B + 3x_1 x_2^2 C + x_2^3 D}{x_1 + x_2 E} \quad (34)$$

Focke-Du Plessis III¹⁷:

$$\eta_{l,m} = x_1\eta_{l,1} + x_2\eta_{l,2} + \frac{x_1^4 A + 4x_1^3 x_2 B + 6x_1^2 x_2^2 C + 4x_1 x_2^3 D + x_2^4 E}{x_1 + x_2 F} \quad (35)$$

Focke-Du Plessis IV¹⁷:

$$\eta_{l,m} = x_1\eta_{l,1} + x_2\eta_{l,2} + \frac{x_1 A + x_2 B}{x_1^2 + 2x_1 x_2 C + x_2^2 D} \quad (36)$$

Focke-Du Plessis V¹⁷:

$$\eta_{l,m} = x_1\eta_{l,1} + x_2\eta_{l,2} + \frac{x_1^2 A + 2x_1 x_2 B + x_2^2 C}{x_1^2 + 2x_1 x_2 D + x_2^2 E} \quad (37)$$

Focke-Du Plessis VI¹⁷:

$$\eta_{l,m} = x_1\eta_{l,1} + x_2\eta_{l,2} + \frac{x_1^3 A + 3x_1^2 x_2 B + 3x_1 x_2^2 C + x_2^3 D}{x_1^2 + 2x_1 x_2 E + x_2^2 F} \quad (38)$$

Focke-Du Plessis VII¹⁷:

$$\eta_{l,m} = x_1\eta_{l,1} + x_2\eta_{l,2} + \frac{x_1 A + x_2 B}{x_1^3 + 3x_1^2 x_2 C + 3x_1 x_2^2 D + x_2^3 E} \quad (39)$$

Focke-Du Plessis VIII¹⁷:

$$\eta_{l,m} = x_1\eta_{l,1} + x_2\eta_{l,2} + \frac{x_1^2 A + 2x_1 x_2 B + x_2^2 C}{x_1^3 + 3x_1^2 x_2 D + 3x_1 x_2^2 E + x_2^3 F} \quad (40)$$

Focke-Du Plessis IX¹⁷:

$$\eta_{l,m} = x_1\eta_{l,1} + x_2\eta_{l,2} + \frac{x_1^3 A + 3x_1^2 x_2 B + 3x_1 x_2^2 C + x_2^3 D}{x_1^3 + 3x_1^2 x_2 E + 3x_1 x_2^2 F + x_2^3 G} \quad (41)$$

and Focke-Sandrock-Kok¹⁸:

$$\eta_{l,m} = 1 / \left[\sum_{i=1}^m x_i / \left(\sum_{j=1}^m x_j A_{ij}^{1/2} \right) \right]^{5/3} \quad , \quad A_{ii} = \eta_{l,i} \quad (42)$$

where m is a number of mixture components, T_m is a temperature of a mixture, p_m is a pressure of a mixture, x_i is a mole fraction of the component i , ϕ_i is a volume



fraction of the component i , M_i is a molar mass of the component i , $\eta_{l,m}$ is a liquid viscosity of a mixture, $\eta_{l,i}$ is a liquid viscosity of the component i , $\rho_{l,m}$ is a liquid density of a mixture, $\rho_{l,i}$ is a liquid density of the component i , and A, B, C, D, E, F, G and H are parameters. A volume fraction of component i is defined as:

$$\varphi_i = x_i v_i / \sum_{j=1}^m v_j \quad , \quad i = 1, 2, \dots, m \quad (43)$$

where v is a molar volume of pure mixture component, and m is a number of mixture components.

TABLE SI. Selected experimental data points for viscosities of the binary liquid mixtures (the reference numbers reffer to the Reference list in the paper *J. Serb. Chem. Soc.* 77 (8) (2012) 1083–1089)

No.	Mixture	Reference	n	T / K	p / bar
1	1,1,2,2-Tetrachloroethane+2-propanone	19	6	298.15	1
2	1,2-Ethandiol+water	20	77	293.15–353.15	1
3	1,2-Ethandiol+water	21	15	303.15	1
4	1-Butanol+1-decanol	22	16	308.15–313.15	1
5	1-Butanol+1-decanol	23	16	293.15–298.15	1
6	1-Butanol+1-nonal	22	16	308.15–313.15	1
7	1-Butanol+1-nonal	23	16	293.15–298.15	1
8	1-Butanol+1-pentanol	22	16	308.15–313.15	1
9	1-Butanol+1-pentanol	23	16	293.15–298.15	1
10	1-Chlorobutane+penty ethanoate	24	11	298.15	1
11	1-Chlorohexadecane+1,4-dimethylbenzene	25	7	298.15	1
12	1-Chlorohexadecane+benzene	25	7	298.15	1
13	1-Chlorohexadecane+cyclohexane	25	11	298.15	1
14	1-Chlorohexadecane+methylbenzene	25	7	298.15	1
15	1-Chlorohexadecane+methylcyclohexane	25	7	298.15	1
16	1-Chlorohexane+1,2-dimethylbenzene	25	7	298.15	1
17	1-Chlorohexane+benzene	25	7	298.15	1
18	1-Chlorohexane+cyclohexane	25	11	298.15	1
19	1-Chlorohexane+methylbenzene	25	7	298.15	1
20	1-Chlorohexane+methylcyclohexane	25	7	298.15	1
21	1-Decanol+1-undecanol	22	16	308.15–313.15	1
22	1-Decanol+1-undecanol	23	16	293.15–298.15	1
23	1-Heptanol+1-nonal	26	22	293.15–298.15	1
24	1-Heptanol+1-octanol	22	16	308.15–313.15	1
25	1-Heptanol+1-octanol	23	16	293.15–298.15	1
26	1-Heptanol+1-undecanol	26	22	293.15–298.15	1
27	1-Hexanol+benzene	27	14	298.15	1
28	1-Methylnaphthalene+methylcyclohexane	28	162	303.15–343.15	1–1000
29	1-Nonanol+1-decanol	23	16	293.15–298.15	1
30	1-Nonanol+1-undecanol	26	22	293.15–298.15	1



TABLE SI. Continued

No.	Mixture	Reference	n	T / K	p / bar
31	1-Pentanol+1-heptanol	26	22	293.15–298.15	1
32	1-Pentanol+1-nonanol	26	22	293.15–298.15	1
33	1-Pentanol+1-octanol	22	16	308.15–313.15	1
34	1-Pentanol+1-octanol	23	16	293.15–298.15	1
35	1-Pentanol+1-undecanol	26	22	293.15–298.15	1
36	1-Propanol+1-butanol	22	16	308.15–313.15	1
37	1-Propanol+1-butanol	23	16	293.15–298.15	1
38	1-Propanol+1-heptanol	26	22	293.15–298.15	1
39	1-Propanol+1-nonanol	26	22	293.15–298.15	1
40	1-Propanol+1-pentanol	22	16	308.15–313.15	1
41	1-Propanol+1-pentanol	23	16	293.15–298.15	1
42	1-Propanol+1-pentanol	26	22	293.15–298.15	1
43	1-Propanol+1-undecanol	26	22	293.15–298.15	1
44	1-Propanol+benzene	29	14	295.15	1
45	1-Propanol+water	21	12	303.15	1
46	2,6,10,15,19,23-Hexamethyl-tetracosane+butane	30	24	273.15–333.15	1
47	2,6,10,15,19,23-Hexamethyl-tetracosane+hexane	30	23	273.15–333.15	1
48	2-Bromobutane+hexane	10	11	298.15	1
49	2-Butanone+1-chlorohexadecane	25	11	298.15	1
50	2-Butanone+1-chlorohexane	25	11	298.15	1
51	2-Butanone+benzene	25	7	298.15	1
52	2-Butanone+ethyl ethanoate	25	11	298.15	1
53	2-Butanone+methylbenzene	25	7	298.15	1
54	2-Butanone+methylcyclohexane	25	11	298.15	1
55	2-Butanone+propyl propanoate	25	11	298.15	1
56	2-Methyl-2-propanol+benzene	29	15	298.15	1
57	2-Propanone+1,2-dimethylbenzene	25	7	298.15	1
58	2-Propanone+1,2-dimethylcyclohexane,cis	25	11	298.15	1
59	2-Propanone+1,4-dimethylbenzene	25	7	298.15	1
60	2-Propanone+1-chlorohexane	25	11	298.15	1
61	2-Propanone+2-propanol	31	10	298.15	1
62	2-Propanone+benzene	25	7	298.15	1
63	2-Propanone+cyclohexane	31	10	298.15	1
64	2-Propanone+cyclohexane	25	11	298.15	1
65	2-Propanone+ethanol	31	10	298.15	1
66	2-Propanone+ethyl ethanoate	25	10	298.15	1
67	2-Propanone+hexane	31	10	298.15	1
68	2-Propanone+methanol	31	10	298.15	1
69	2-Propanone+methylbenzene	25	7	298.15	1
70	2-Propanone+propyl propanoate	25	11	298.15	1
71	2-Propanone+tetrachloromethane	31	10	298.15	1
72	2-Propanone+water	19	6	298.15	1



TABLE SI. Continued

No.	Mixture	Reference	n	T / K	p / bar
73	3-Methyl-1-butanol+benzene	29	21	293.15	1
74	3-Pentanol+benzene	29	25	293.15	1
75	4-Methylcyclohexanone+hexadecane	10	11	298.15	1
76	4-Methylcyclohexanone+hexane	10	12	298.15	1
77	4-Methylcyclohexanone+tetradecane	10	11	298.15	1
78	Benzene+1,2-dichloroethane	19	6	298.15	1
79	Benzene+bzyl benzoate	32	7	298.15	1
80	Benzene+cyclohexane	33	5	298.15	1
81	Benzene+cyclohexane	19	6	298.15	1
82	Benzene+ethanol	34	11	298.15	1
83	Benzene+ethyl benzoate	32	8	298.15	1
84	Benzene+hexane	10	12	298.15	1
85	Benzene+hexane	35	10	298.15	1
86	Benzene+methylbenzene	35	10	298.15	1
87	Benzene+tetrachloromethane	19	6	298.15	1
88	Benzene+trichloromethane	19	6	298.15	1
89	Benzyl ethanoate+1,4-dioxane	6	9	313.15	1
90	Benzyl Ethanoate+m-Methylphenol	6	7	313.15	1
91	Benzyl ethanoate+phenylamine	6	9	303.15	1
92	Butylamine+1-butanol	36	22	303.15–313.15	1
93	Butylamine+1-decanol	36	22	303.15–313.15	1
94	Butylamine+1-heptanol	36	22	303.15–313.15	1
95	Butylamine+1-hexanol	36	22	303.15–313.15	1
96	Butylamine+1-octanol	36	22	303.15–313.15	1
97	Butylamine+1-pentanol	36	22	303.15–313.15	1
98	Butylamine+1-propanol	36	22	303.15–313.15	1
99	Butylamine+ethanol	36	22	303.15–313.15	1
100	Chlorobenzene+tetrachloromethane	19	6	298.15	1
101	Cyclohexane+2-propanol	31	10	298.15	1
102	Decane+docosane	37	21	323.15–343.15	1
103	Decane+eicosane	37	28	313.15–343.15	1
104	Decane+pentadecane	38	22	293.15–298.15	1
105	Decane+pentadecane	39	22	308.15–313.15	1
106	Decane+tetracosane	37	14	333.15–343.15	1
107	Decane+tridecane	38	22	293.15–298.15	1
108	Decane+tridecane	39	22	308.15–313.15	1
109	Diethyl carbonate+1,4-dimethylbenzene	40	13	298.15	1
110	Diethyl carbonate+dodecane	40	12	298.15	1
111	Diethyl carbonate+octane	40	16	298.15	1
112	Dimethyl carbonate+1,4-dimethylbenzene	40	12	298.15	1
113	Dimethyl carbonate+dodecane	40	12	298.15	1
114	Dimethyl carbonate+octane	40	17	298.15	1
115	Dimethyl sulfoxide+acetic acid	19	6	298.15	1
116	Dimethyl sulfoxide+methanol	31	10	298.15	1



TABLE SI. Continued

No.	Mixture	Reference	n	T / K	p / bar
117	Dimethyl sulfoxide+methanol	19	6	298.15	1
118	Dimethyl sulfoxide+methyl cyanide	19	6	298.15	1
119	Dimethyl sulfoxide+trichloromethane	31	10	298.15	1
120	Dimethyl sulfoxide+water	19	6	298.15	1
121	Ethanol+1-propanol	21	12	303.15	1
122	Ethanol+2-propanol	31	10	298.15	1
123	Ethanol+cyclohexane	31	10	298.15	1
124	Ethanol+heptane	34	12	298.15	1
125	Ethanol+water	21	80	283.15–323.15	1
126	Ethyl ethanoate+1,2-dimethylbenzene	25	7	298.15	1
127	Ethyl ethanoate+1-chlorohexadecane	25	11	298.15	1
128	Ethyl ethanoate+1-chlorohexane	25	11	298.15	1
129	Ethyl ethanoate+benzene	25	7	298.15	1
130	Ethyl ethanoate+cyclohexane	25	11	298.15	1
131	Ethyl ethanoate+methylbenzene	25	7	298.15	1
132	Ethylbenzene+hexadecane	41	24	293.15–298.15	1
133	Ethylbenzene+octane	41	23	293.15–298.15	1
134	Ethylbenzene+tetradecane	41	24	293.15–298.15	1
135	Heptane+1-methylnaphthalene	28	162	303.15–343.15	1–1000
136	Heptane+benzene	34	13	298.15	1
137	Heptane+decane	42	11	293.15	1
138	Heptane+dodecane	42	11	293.15	1
139	Heptane+methylcyclohexane	28	162	303.15–343.15	1–1000
140	Heptane+octane	42	11	293.15	1
141	Heptane+tetradecane	42	11	293.15	1
142	Hexadecane+2-bromobutane	10	12	298.15	1
143	Hexadecane+benzene	10	11	298.15	1
144	Hexadecane+hexane	10	22	298.15	1
145	Hexadecane+tetrachloromethane	10	12	298.15	1
146	Hexadecane+tetradecane	10	13	298.15	1
147	Hexane+benzene	43	21	298.15–323.15	1
148	Hexane+benzene	44	14	298.15	1
149	Hexane+cyclohexane	31	10	298.15	1
150	Hexane+decane	42	11	293.15	1
151	Hexane+ethanol	31	10	298.15	1
152	Hexane+ethylbenzene	43	24	298.15–323.15	1
153	Hexane+heptane	42	11	293.15	1
154	Hexane+methylbenzene	43	27	298.15–323.15	1
155	Hexane+octane	42	11	293.15	1
156	Hexane+trichloromethane	31	10	298.15	1
157	Methanol+1-propanol	21	14	303.15	1
158	Methanol+2-propanol	31	10	298.15	1
159	Methanol+ethanol	31	10	298.15	1
160	Methanol+ethanol	21	106	283.15–323.15	1



TABLE SI. Continued

No.	Mixture	Reference	n	T / K	p / bar
161	Methanol+water	21	70	283.15–323.15	1
162	Methyl cyanide+1-chlorobutane	24	16	298.15	1
163	Methyl cyanide+pentyl ethanoate	24	12	298.15	1
164	Methyl cyanide+tetrachloromethane	24	11	298.15	1
165	Methyl ethanoate+hexane	31	10	298.15	1
166	Methyl ethanoate+trichloromethane	31	10	298.15	1
167	Methylbenzene+benzyl benzoate	32	7	298.15	1
168	Methylbenzene+decane	41	24	293.15–298.15	1
169	Methylbenzene+dodecane	41	24	293.15–298.15	1
170	Methylbenzene+ethyl benzoate	32	7	298.15	1
171	Methylbenzene+hexadecane	41	24	293.15–298.15	1
172	Methylbenzene+octane	41	24	293.15–298.15	1
173	Methylbenzene+tetradecane	41	24	293.15–298.15	1
174	<i>o</i> -Chlorophenol+1,4-dioxane	19	6	298.15	1
175	Octane+decane	42	11	293.15	1
176	Octane+pentadecane	38	22	293.15–298.15	1
177	Octane+pentadecane	39	22	308.15–313.15	1
178	Octane+tetradecane	42	11	293.15	1
179	Octane+tridecane	38	22	293.15–298.15	1
180	Octane+tridecane	39	22	308.15–313.15	1
181	Octane+undecane	38	22	293.15–298.15	1
182	Octane+undecane	39	22	308.15–313.15	1
183	Propyl propanoate+1,4-dimethylbenzene	25	7	298.15	1
184	Propyl propanoate+1-chlorohexadecane	25	11	298.15	1
185	Propyl propanoate+1-chlorohexane	25	11	298.15	1
186	Propyl propanoate+1-hexanol	27	16	298.15	1
187	Propyl propanoate+benzene	44	12	298.15	1
188	Propyl propanoate+benzene	25	7	298.15	1
189	Propyl propanoate+hexane	44	14	298.15	1
190	Propyl propanoate+methylbenzene	25	7	298.15	1
191	Propyl propanoate+methylcyclohexane	25	11	298.15	1
192	Tetrachloromethane+2-propanol	31	10	298.15	1
193	Tetrachloromethane+benzene	10	11	298.15	1
194	Tetrachloromethane+benzene	33	5	298.15	1
195	Tetrachloromethane+cyclohexane	31	9	298.15	1
196	Tetrachloromethane+cyclohexane	33	5	298.15	1
197	Tetrachloromethane+hexane	10	10	298.15	1
198	Tetradecane+2-bromobutane	10	11	298.15	1
199	Tetradecane+hexadecane	42	11	293.15	1
200	Tetradecane+hexane	10	12	298.15	1
201	Trichloroethene+1,4-dimethylbenzene	45	9	303.15	1
202	Trichloroethene+benzene	45	10	303.15	1
203	Trichloroethene+methylbenzene	45	10	303.15	1
204	Trichloroethene+tetrachloromethane	45	7	303.15	1



TABLE SI. Continued

No.	Mixture	Reference	n	T / K	p / bar
205	Trichloroethene+trichloromethane	45	11	303.15	1
206	Trichloromethane+1,4-dioxane	19	6	298.15	1
207	Trichloromethane+2-propanone	19	6	298.15	1
208	Trichloromethane+benzene	35	10	298.15	1
209	Trichloromethane+methanol	31	10	298.15	1
210	Trichloromethane+methylbenzene	35	10	298.15	1
211	Tridecane+pentadecane	38	22	293.15–298.15	1
212	Tridecane+pentadecane	39	22	308.15–313.15	1
213	Triethylamine+chlorobenzene	40	10	298.15	1
214	Triethylamine+methanol	31	10	298.15	1
215	Triethylamine+trichloromethane	31	10	298.15	1
216	Undecane+pentadecane	38	22	293.15–298.15	1
217	Undecane+pentadecane	39	22	308.15–313.15	1
218	Undecane+tridecane	38	22	293.15–298.15	1
219	Undecane+tridecane	39	22	308.15–313.15	1

TABLE SII. Selected experimental data points for viscosities of the ternary liquid mixtures (the reference numbers reffer to the Reference list in the paper *J. Serb. Chem. Soc.* 77 (8) (2012) 1083–1089)

No.	Mixture	Reference	n	T / K	p / bar
1	2-Propanol+2-butanol+ethanol	46	48	293.15–308.15	1
2	2-Propanone+ethanol+2-propanol	47	39	298.15	1
3	2-Propanone+ethanol+methanol	47	39	298.15	1
4	2-Propanone+hexane+cyclohexane	47	39	298.15	1
5	2-Propanone+hexane+ethanol	47	39	298.15	1
6	2-Propanone+tetrachloromethane+cyclohexane	47	38	298.15	1
7	Decane+eicosane+tetracosane	37	37	333.15–343.15	1
8	Dimethyl sulfoxide+2-propa- none+trichloromethane	47	23	298.15	1
9	Dimethyl sulfoxide+tetra- chloromethane+methanol	47	22	298.15	1
10	Dimethyl sulfoxide+tetra- chloromethane+trichloromethane	47	23	298.15	1
11	Dimethyl sulfoxide+tri- chloromethane+methanol	47	39	298.15	1
12	Ethanol+1-propanol+water	21	62	303.15	1
13	Ethanol+2-propanol+cyclohexane	46	38	298.15	1
14	Ethanol+benzene+heptane	34	27	298.15	1
15	Ethanol+cyclohexane+2-propanol	47	39	298.15	1
16	Ethylbenzene+tetradecane+hexadecane	48	58	293.15–298.15	1
17	Hexane+cyclohexane+ethanol	47	39	298.15	1
18	Methane+methylcyclo- hexane+methylnaphthalene	15	810	303.15–343.15	1–1000
19	Methanol+1-propanol+water	21	61	303.15	1



TABLE SII. Continued

No.	Mixture	Reference	n	T / K	p / bar
20	Methanol+ethanol+1-propanol	21	68	303.15	1
21	Methanol+ethanol+2-propanol	47	38	298.15	1
22	Methanol+ethanol+water	21	357	283.15–323.15	1
23	Methyl ethanoate+cyclohexane+ethanol	47	23	298.15	1
24	Methyl ethanoate+trichloromethane+methanol	47	31	298.15	1
25	Methylbenzene+ethylbenzene+hexadecane	48	58	293.15–298.15	1
26	Methylbenzene+ethylbenzene+tetradecane	48	58	293.15–298.15	1
27	Methylbenzene+octane+ethylbenzene	48	58	293.15–298.15	1
28	Methylbenzene+octane+hexadecane	48	58	293.15–298.15	1
29	Methylbenzene+octane+tetradecane	48	58	293.15–298.15	1
30	Methylbenzene+tetradecane+hexadecane	48	58	293.15–298.15	1
31	Octane+ethylbenzene+hexadecane	48	57	293.15–298.15	1
32	Octane+ethylbenzene+tetradecane	48	57	293.15–298.15	1
33	Octane+tetradecane+hexadecane	48	18	293.15–298.15	1
34	Propyl propanoate+1-hexanol+benzene	27	80	298.15	1.
35	Propyl propanoate+hexane+benzene	44	72	298.15	1.
36	Tetrachloromethane+cyclohexane+2-propanol	47	38	298.15	1
37	Trichloromethane+2-propanol+2-butanol	49	56	293.15–308.15	1
38	Trichloromethane+ethanol+methanol	47	31	298.15	1
39	Triethylamine+ethanol+1-propanol	47	15	298.15	1
40	Triethylamine+methanol+ethanol	47	31	298.15	1
41	Triethylamine+methanol+trichloromethane	47	39	298.15	1



NOTE

Phase composition of Bi_2O_3 specimens doped with Ti, Zr and Hf

DEJAN POLETI^{1*}, LJILJANA KARANOVIĆ², MIODRAG ZDUJIĆ^{3#}
and ČEDOMIR JOVALEKIĆ⁴

¹Department of General and Inorganic Chemistry, Faculty of Technology and Metallurgy, University of Belgrade, Karnegijeva 4, 11000 Belgrade, Serbia, ²Laboratory of Crystallography, Faculty of Mining and Geology, University of Belgrade, Dušina 7, 11000 Belgrade, Serbia, ³Institute of Technical Sciences of the Serbian Academy of Science and Arts, Knez Mihailova 35, 11000 Belgrade, Serbia and ⁴Institute for Multidisciplinary Research, Kneza Višeslava 1a, 11000 Belgrade, Serbia

(Received 14 September, revised 17 December 2011)

Abstract: Powder mixtures of α - Bi_2O_3 containing 2, 5 and 10 mol % of TiO_2 , ZrO_2 or HfO_2 were homogenized, heated at 820 °C for 24 h and quenched in air. The X-ray powder diffraction technique was used to characterize the prepared samples. In all cases, metastable Bi_2O_3 polymorphs, γ - Bi_2O_3 or β - Bi_2O_3 , were found as single or major phases. The addition of Ti^{4+} stabilizes the γ - Bi_2O_3 polymorph, while both Zr^{4+} and Hf^{4+} stabilize the β - Bi_2O_3 polymorph. In the samples with 2 and 5 mol % of TiO_2 the presence of even two γ - Bi_2O_3 phases (the $\text{Bi}_{12}\text{TiO}_{20}$ compound and a very low Ti-doped γ - Bi_2O_3) was established. Similarly, in the sample with 2 mol % of HfO_2 , two β - Bi_2O_3 phases were found. The phase composition of the prepared samples, the values of the unit cell parameters and the appearance of two polymorphs with identical crystal structure but different unit cell parameters are discussed and compared with known data.

Keywords: bismuth(III) oxide; dopants; 4th group elements; X-ray powder diffraction; phase composition; unit cell parameters.

INTRODUCTION

Due to the great diversity of the polymorphic modifications and many useful physical properties, pure or doped bismuth(III) oxide, Bi_2O_3 , is permanently in the focus of scientific interest. In addition to four well-known polymorphs: α -, β -, γ - and δ - Bi_2O_3 ,^{1–4} three new Bi_2O_3 polymorphs were described recently.^{5,6} There is general agreement that only the α - Bi_2O_3 form is stable at room tempe-

* Corresponding author. E-mail: dejan@tmf.bg.ac.rs

Serbian Chemical Society member.

doi: 10.2298/JSC110914215P



rature.^{2,7,8} However, various metastable or high-temperature polymorphs, such as β -, γ - and δ - Bi_2O_3 , can be readily stabilized by addition of proper dopants, which can be cations of any charge, usually added as the corresponding oxides.^{4,6,7,9–11} Some bismuth(III) oxides of this kind, such as γ - Bi_2O_3 , have valuable optical (photorefractive, photoluminescent, photoconductive) properties,¹² some other, such as β - and δ - Bi_2O_3 , belong to the group of high oxide ion conductors.^{13,14}

Although the Bi_2O_3 – TiO_2 system should be considered as well-characterized since detailed phase diagrams are known,¹⁵ in a previous study⁹ the quite unusual co-existence of two Ti-doped γ - Bi_2O_3 phases was observed in the Bi_2O_3 -rich region. At the same time, Bi_2O_3 – MO_2 systems, where M = Zr or Hf, are not so well known and the data are often contradictory, both for the Bi_2O_3 -rich^{7,10,11,16} and MO_2 -rich^{17,18} region. For these reasons, a systematic crystallographic study of Bi_2O_3 samples low-doped (2, 5 and 10 mole %) with Ti, Zr and Hf as 4th group elements is described herein.

EXPERIMENTAL

Four commercial powders: Bi_2O_3 (> 99 % purity), TiO_2 (99.8 %), ZrO_2 (> 99 %) and HfO_2 (> 98.5 %) were used in this study. By means of the X-ray powder diffraction technique (XRPD), Bi_2O_3 and TiO_2 were identified as being in the α - Bi_2O_3 (bismite) and rutile form, respectively; ZrO_2 was mostly present as the baddeleyite modification, but contained about 5 mass % of the high-temperature tetragonal polymorph (JCPDS card No. 42-1164), whereas HfO_2 was in the monoclinic, analogous to baddeleyite, modification (JCPDS Card No. 34-0104) with about 1.5 mass % of ZrO_2 as an impurity.

Powder mixtures of α - Bi_2O_3 containing 2, 5 and 10 mole % of TiO_2 , ZrO_2 or HfO_2 were dry homogenized in an agate mortar, pressed into tablets ($d = 8$ mm, $h \approx 1.5$ mm) under a pressure of 50 MPa, calcined in Pt-crucibles at 820 °C for 24 h and air-quenched to room temperature.

After regrinding, XRPD data of the prepared samples were collected on a Philips PW1710 diffractometer equipped with a graphite monochromator ($\text{Cu-K}\alpha$ radiation, $\lambda = 1.5418$ Å) in the 2θ range 10–90° (step-length: 0.02° 2θ , scan time: 1 s). The program PowderCell¹⁹ was used for a semi-quantitative phase analysis. The unit cell parameters were calculated by the least-squares method using the program LSUCRIPC.²⁰

RESULTS AND DISCUSSION

The results are summarized in Table I and can be commented as follows.

Bi_2O_3 – TiO_2 system. The definite composition of the body-centered cubic γ - Bi_2O_3 phase in this system is $\text{Bi}_{12}\text{TiO}_{20}$ (14.3 mol % TiO_2),³ which was confirmed several times by crystal structure determination.⁹ As briefly mentioned in the Introduction, if the quantity of TiO_2 was reduced to 7.7 mol %, a mixture of two phases, both with the γ - Bi_2O_3 structure, was previously obtained.⁹ The same feature was observed in this study (Fig. S1 of the Supplementary material to this note), but the results showed that the actual range of the two-phase region extends toward very low TiO_2 content. Thus, a quantity of only 2 mol % (0.35 mass %)



was sufficient to obtain mixed-phase specimens. One unit cell parameter (a_{Ti} , Table I) is in agreement with the literature data for the unit cell parameter of the Bi₁₂TiO₂₀ phase ($a \approx 10.18 - 10.19 \text{ \AA}$), while the other (a_{ss} , Table I) corresponds to the unit cell parameter of undoped γ -Bi₂O₃ ($a \approx 10.26 \text{ \AA}$).⁹ As expected, with increasing Ti-content, the amount of the Bi₁₂TiO₂₀ phase increased, showing the significance of the initial mixture stoichiometry. The co-existence of two phases with a γ -Bi₂O₃ structure was also noticed and discussed by Guha *et al.*²¹ in the Bi₂O₃-rich region of the Bi₂O₃-ZnO₂ system. After comprehensive research, they concluded that one phase was Bi₃₈ZnO₅₈ (equivalent to Bi₁₂TiO₂₀), whereas the second phase was described as a γ -Bi₂O₃ solid solution with no more than 2.2 mol % of ZnO. Very likely, an analogous solid solution exists in the Bi₂O₃-TiO₂ system, although this was not predicted in the phase diagram. Preliminary results of EDS analysis also revealed traces of Ti in the present γ -Bi₂O₃ solid solution.

TABLE I. Phase composition of the investigated samples and calculated unit cell parameters of the Bi₂O₃ phases

Dopant	Amount of dopant, mol %	Phase composition and mass ratio of present phases, %	Unit cell parameters of Bi ₂ O ₃ phases, Å, and unit cell volume of β -Bi ₂ O ₃ phase, V / Å ³
TiO ₂	2	Mixture of two γ -Bi ₂ O ₃ phases, Bi ₁₂ TiO ₂₀ : γ -Bi ₂ O _{3(ss)} = 24:76	$a_{\text{Ti}} = 10.186(1)$, $a_{\text{ss}} = 10.2627(6)$
	5	Bi ₁₂ TiO ₂₀ : γ -Bi ₂ O _{3(ss)} = 75:25	$a_{\text{Ti}} = 10.1877(7)$, $a_{\text{ss}} = 10.263(2)$
	10	Mixture of Bi ₁₂ TiO ₂₀ and Bi ₄ Ti ₃ O ₁₂ , Bi ₁₂ TiO ₂₀ :Bi ₄ Ti ₃ O ₁₂ = 90:10	$a_{\text{Ti}} = 10.1790(9)$
ZrO ₂	2	Single β -Bi ₂ O ₃ phase	$a_{\beta} = 7.731(1)$, $c_{\beta} = 5.629(2)$, $V = 336.4$
	5	Single β -Bi ₂ O ₃ phase	$a_{\beta} = 7.714(2)$, $c_{\beta} = 5.632(3)$, $V = 335.1$
	10	Single β -Bi ₂ O ₃ phase	$a_{\beta} = 7.722(1)$, $c_{\beta} = 5.637(2)$, $V = 336.1$
HfO ₂	2	Mixture of two β -Bi ₂ O ₃ phases, β_1 -Bi ₂ O ₃ : β_2 -Bi ₂ O ₃ = 84:16	$a_{\beta_1} = 7.716(3)$, $c_{\beta_1} = 5.636(4)$, $V = 335.5$, $a_{\beta_2} = 7.726(4)$, $c_{\beta_2} = 5.768(5)$, $V = 344.2$
	5	Mixture of β -Bi ₂ O ₃ and δ -Bi ₂ O ₃ with traces (< 5 mass %) of δ -Bi ₂ O ₃ ^a	$a_{\beta} = 7.735(2)$, $c_{\beta} = 5.654(2)$, $V = 338.3$
	10	Mixture of β -Bi ₂ O ₃ , δ -Bi ₂ O ₃ and HfO ₂ , β -Bi ₂ O ₃ : δ -Bi ₂ O ₃ :HfO ₂ = 86:10:4	$a_{\beta} = 7.744(2)$, $c_{\beta} = 5.649(3)$, $V = 338.8$, $a_{\delta} = 5.568(4)$

^aDue to the low content, it was not possible to calculate the precise lattice constant of the δ -Bi₂O₃ phase

The appearance of Bi₄Ti₃O₁₂ in the sample with 10 mol % of TiO₂ was also surprising because under similar conditions Bi₈TiO₁₄, but not Bi₄Ti₃O₁₂, may arise according to the phase diagram.¹⁵



Bi₂O₃–ZrO₂ system. As seen from Table I and Fig. S2 of the Supplementary material, in the Bi₂O₃–ZrO₂ system containing ≤ 10 mol % of ZrO₂, single-phase β -Bi₂O₃ specimens that can be described as solid solutions with the general formula Bi_{2-x}Zr_xO_{3+x/2} were obtained in all cases. Therefore, stabilization by Zr⁴⁺ is the simplest way to obtain a tetragonal β -Bi₂O₃ phase at room temperature. While the values of the *c*-axis were nearly constant (Table I), the values of the *a*-axes and unit cell volume pass through minimum at about $x = 0.05$. When compared with the unit cell volume of undoped β -Bi₂O₃,²² the unit cell volumes of the Zr-doped β -Bi₂O₃ were smaller due to the smaller radius of Zr⁴⁺ with respect to Bi³⁺.²³ This also confirmed the presence of Zr⁴⁺ in the prepared solid solutions. These results are in general agreement with data published by Abrahams and co-workers,¹⁰ but their samples with $x < 0.05$ were not single-phase and contained α -Bi₂O₃ as a secondary phase. A plausible explanation for such discrepancy could be different heat treatments applied.

Bi₂O₃–HfO₂ system. Apparently, Hf⁴⁺ also tend to stabilize β -Bi₂O₃, since this phase predominated in all samples (Table I, Fig. S3 of the Supplementary material). With one exception, the unit cells of Bi_{2-x}Hf_xO_{3+x/2} were larger than the unit cells of the corresponding Bi_{2-x}Zr_xO_{3+x/2} solid solutions and undoped β -Bi₂O₃, implying a larger effective ionic radius of Hf⁴⁺ in the Bi₂O₃ host lattice. In comparison to the Bi₂O₃–ZrO₂ system, the main difference is that single-phase samples were not obtained, while in samples with higher Hf-contents, cubic δ -Bi₂O₃ appeared as a minor phase. In fact, trace amounts of HfO₂ were also observed in the sample doped with 10 mol % of HfO₂, suggesting that thermodynamic equilibrium was not achieved. However, due to the long annealing time applied, this should be related to the upper limits of solubility of Zr⁴⁺ and Hf⁴⁺ in the corresponding solid solutions with β -Bi₂O₃ structure. According to Sorokina and Sleight, the solubility of Hf⁴⁺ is smaller than that of Zr⁴⁺ and the limiting formulae are Bi_{1.84}Zr_{0.16}O_{3.08} and Bi_{1.94}Hf_{0.06}O_{3.03}.¹¹ Similarly, Ayala and López-Garcia¹⁷ found that the maximum concentration of Hf⁴⁺ ions in Bi_{2-x}Hf_xO_{3+x/2} solid solution was only about 5 mol %. An increased tendency of Hf⁴⁺ to stabilize the cubic δ -Bi₂O₃ phase, as described in previous papers,^{24,25} could also have some influence. The unit cell parameter of the δ -phase in the sample doped with 10 mol % of HfO₂ was higher than the values reported (5.266–5.459 Å) for the corresponding δ -phases containing Hf⁴⁺,¹¹ but lower than the values (5.655–5.665 Å) for undoped δ -Bi₂O₃.^{2,26}

The most interesting result of this study was the appearance of two β -Bi₂O₃ phases in the sample with 2 mol % of HfO₂. To the best of our knowledge, this has never been reported before and shows that there are some analogies between γ - and β -Bi₂O₃, *i.e.*, that the coexistence of two crystallographically identical phases with different unit cell parameters in very low-doped samples can be expected. Unit cell parameters of major, β_1 -Bi₂O₃ phase (Table I) are close to the



literature values¹⁷ and JCPDS Card No. 43-0207 but the obtained very high unit cell parameters of the minor β_2 -Bi₂O₃ phase are difficult to explain. The proper rationalization of this system requires additional studies and will be the issue of our future work.

In conclusion, the described differences between Bi₂O₃ samples doped with Ti and doped with Zr or Hf can be judged as expected. However, the somewhat distinct behavior of Zr- and Hf-doped samples could be considered as quite surprising, bearing in mind the close chemical similarity, and identical metal and ionic radii of the elements. Nevertheless, similar discrepancies were observed previously during the investigation of Bi₂O₃-MO₂ systems, M = Zr or Hf,¹¹ and studies of mechanochemically treated 2Bi₂O₃·3ZrO₂²⁶ and 2Bi₂O₃·3HfO₂²⁷ mixtures.

SUPPLEMENTARY MATERIAL

Figures S1, S2 and S3, showing the experimental X-ray powder diffraction patterns, are available electronically at <http://www.shd.org.rs/JSCS/>, or from the corresponding author on request.

Acknowledgements. This study was financially supported by the Ministry of Education, Science and Technological Development of the Republic of Serbia (Grant Nos. 45007, 45001 and 45015), which is gratefully acknowledged.

И З В О Д

ФАЗНИ САСТАВ УЗОРАКА Bi₂O₃ ДОПИРАНИХ Ti, Zr И Hf

ДЕЈАН ПОЛЕТИ¹, ЉИЉАНА КАРАНОВИЋ², МИОДРАГ ЗДУЛИЋ³ и ЧЕДОМИР ЈОВАЛЕКИТ⁴

¹Каљегра за оштину и неорганску хемију, Технолошко-мешавински факултет, Универзитет у Београду, Карнеијева 4, 11000 Београд, ²Лабораторија за кристалографију, Рударско-геолошки факултет, Универзитет у Београду, Бушића 7, 11000 Београд, ³Институт за техничких наука САНУ, Кнез Михаилова 35, 11000 Београд и ⁴Институт за мултидисциплинарна истраживања, Универзитет у Београду, Кнеза Вишеслава 1а, 11000 Београд

Хомогенизоване смеше прахова α -Bi₂O₃ са 2, 5 и 10 mol % TiO₂, ZrO₂ или HfO₂ загреване су током 24 h на 820 °C и нагло хлађене на ваздуху до собне температуре. Тако припремљени узорци охарактерисани су методом рентгенске дифракције на поликристалним узорцима. Уочено је да у свим случајевима долази до стабилизације метастабилних модификација, γ -Bi₂O₃ или β -Bi₂O₃, које се појављују као једине или доминантне фазе. Показано је да додатак Ti⁴⁺ стабилизује γ -модификацију, док присуство Zr⁴⁺ и Hf⁴⁺ стабилизује β -модификацију. У узорцима са 2 и 5 mol % TiO₂ нађено је присуство чак две γ -Bi₂O₃ фазе (једињење Bi₁₂TiO₂₀ и допирани γ -Bi₂O₃ са веома малим садржајем Ti). Слично томе, у узорку са 2 mol % HfO₂ идентификоване су две β -Bi₂O₃ фазе. У раду су дискутовани фазни састави узорака, вредности параметара јединичних ћелија, као и истовремена појава две модификације са идентичном кристалном структуром а различитим параметрима јединичне ћелије.

(Примљено 14. септембра, ревидирано 17. децембра 2011)



REFERENCES

1. E. M. Levin, R. S. Roth, *J. Res. Natl. Bur. Stand.* **68A** (1964) 189
2. H. A. Harwig, *Z. Anorg. Allg. Chem.* **444** (1978) 151
3. M. Valant, D. Suvorov, *Chem. Mater.* **14** (2002) 3471
4. L. E. Depero, L. J. Sangaletti, *J. Solid State Chem.* **122** (1996) 439
5. N. Cornei, N. Tancret, F. Abraham, O. Mentré, *Inorg. Chem.* **45** (2006) 4886
6. S. Ghedia, T. Locherer, R. Dinnebier, D. L. V. K. Prasad, U. Wedig, M. Jansen, A. Senyshyn, *Phys. Rev. B* **82** (2010) 024106
7. E. M. Levin, R. S. Roth, *J. Res. Natl. Bur. Stand.* **68A** (1964) 197
8. H. A. Harwig, J. W. Weenk, *Z. Anorg. Allg. Chem.* **444** (1978) 167
9. D. Poleti, Lj. Karanović, A. Hadži-Tonić, *Z. Kristallogr.* **222** (2007) 59 and references therein
10. I. Abrahams, A. J. Bush, S. C. M. Chan, F. Krok, W. Wrobel, *J. Mater. Chem.* **11** (2001) 1715
11. S. L. Sorokina, A. W. Sleight, *Mater. Res. Bull.* **33** (1998) 1077
12. M. T. Borowiec, *Database of Sillenites*, available from http://www.ifpan.edu.pl/PERSONAL/borow/baz_sill.html (accessed on November, 27 2011)
13. P. Shuk, H. D. Wiemhöfer, U. Guth, W. Göpel, M. Greenblatt, *Solid State Ionics* **89** (1996) 179
14. J. C. Boivin, G. Mairesse, *Chem. Mater.* **10** (1998) 2870
15. Phase Equilibria Diagrams Database, Version 3.0, American Ceramic Society and National Institute of Standards and Technology, 2004, Figs. No. 00328C and 02360
16. A. Ayala, A. López-Garcia, A. G. Leyva, M. A. R. De Benyacar, *Solid State Commun.* **99** (1996) 451
17. F. Hund, *Z. Anorg. Allg. Chem.* **333** (1964) 248
18. I. De Meatza, J. P. Chapman, F. Mauvy, J. I. De Larramendi, M. I. Arriortua, T. Rojo, *Mater. Res. Bull.* **39** (2004) 1841
19. W. Kraus, G. Nolze, *PowderCell for Windows*, V.2.4, Federal Institute for Materials Research and Testing, Berlin, Germany, 2000
20. R. G. Garwey, *Powder Diff.* **1** (1986) 114
21. J. P. Guha, Š. Kunej, D. Suvorov, *J. Mater. Sci.* **39** (2004) 911
22. S. K. Blower, C. Greaves, *Acta Crystallogr.* **C44** (1988) 587
23. R. D. Shannon, *Acta Crystallogr.* **A32** (1976) 751
24. Č. Jovalekić, M. Zdujić, D. Poleti, Lj. Karanović, M. Mitrić, *J. Solid State Chem.* **181** (2008) 1321
25. M. Zdujić, D. Poleti, Č. Jovalekić, Lj. Karanović, *J. Serb. Chem. Soc.* **74** (2009) 1401
26. S. Kashida, K. Nakamura, *Philos. Mag. Lett.* **73** (1996) 279.





J. Serb. Chem. Soc. 77 (8) S144–S147 (2012)

Journal of the Serbian Chemical Society

JSCS@tmf.bg.ac.rs • www.shd.org.rs/JSCS

Supplementary material

SUPPLEMENTARY MATERIAL TO

Phase composition of Bi₂O₃ specimens doped with Ti, Zr and Hf

DEJAN POLETI^{1*}, LJILJANA KARANOVIĆ², MIODRAG ZDUJIĆ³
and ČEDOMIR JOVALEKIĆ⁴

¹Department of General and Inorganic Chemistry, Faculty of Technology and Metallurgy,
University of Belgrade, Karnegijeva 4, 11000 Belgrade, Serbia, ²Laboratory of Crystallography,
Faculty of Mining and Geology, University of Belgrade, Dušina 7, 11000 Belgrade,
Serbia, ³Institute of Technical Sciences of the Serbian Academy of Science and Arts, Knez
Mihailova 35, 11000 Belgrade, Serbia and ⁴Institute for Multidisciplinary Research,
Kneza Višeslava 1a, 11000 Belgrade, Serbia

J. Serb. Chem. Soc. 77 (8) (2012) 1091–1096

*Corresponding author. E-mail: dejan@tmf.bg.ac.rs



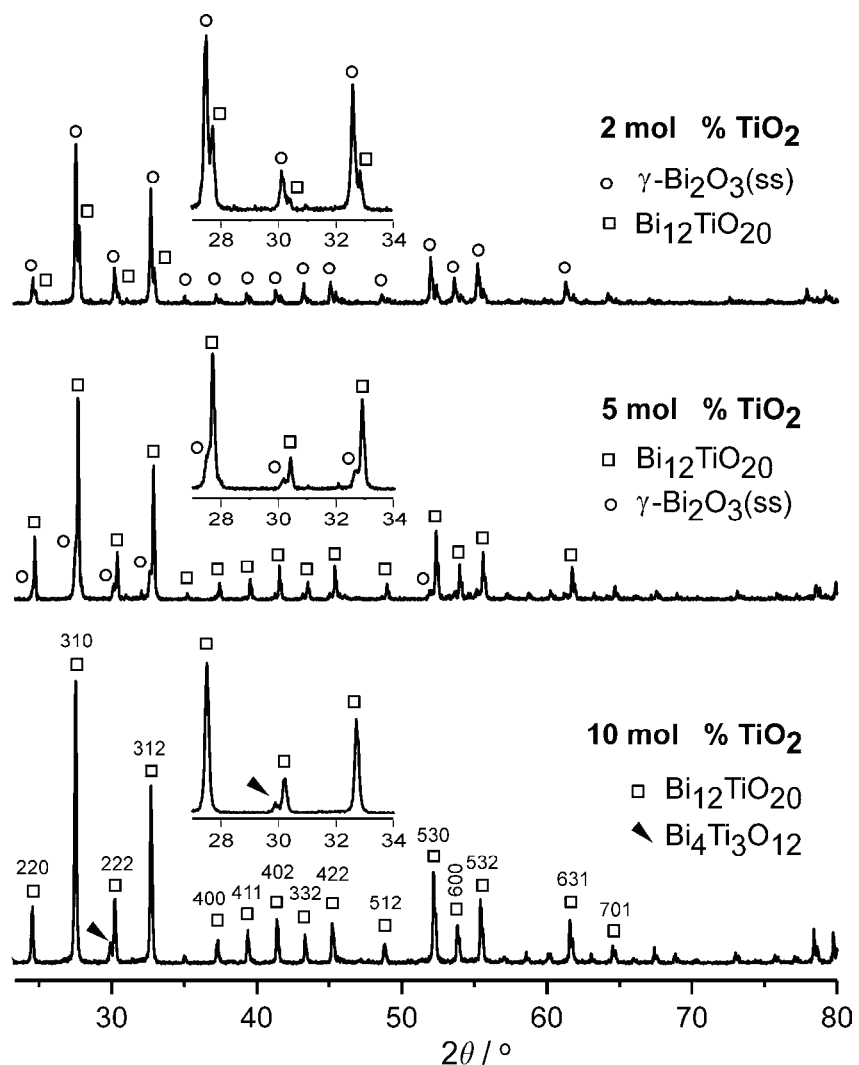


Fig. S1. XRPD Patterns for Bi₂O₃ specimens doped with 2, 5 and 10 mol % of TiO₂ (only strong reflection are indexed). Characteristic parts of the patterns are enlarged in the insets.

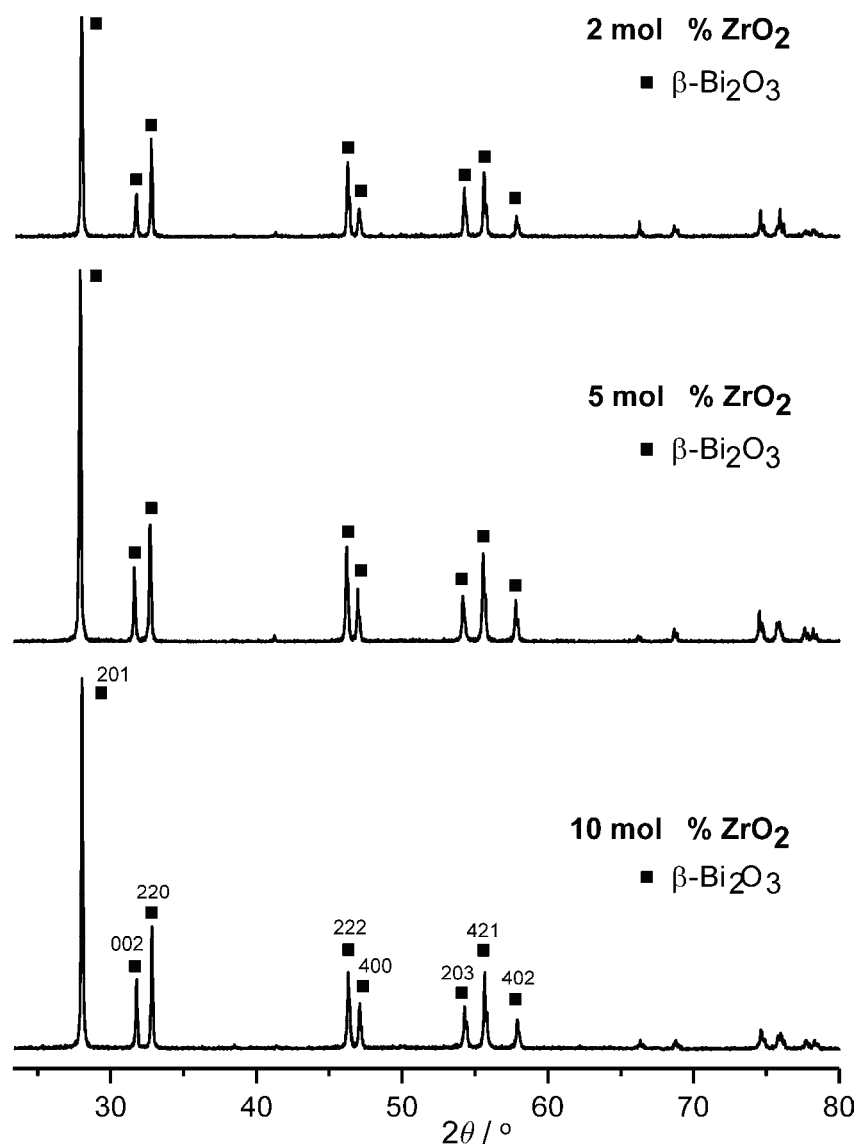


Fig. S2. XRPD Patterns for Bi_2O_3 specimens doped with 2, 5 and 10 mol % of ZrO_2 (only strong reflection are indexed).

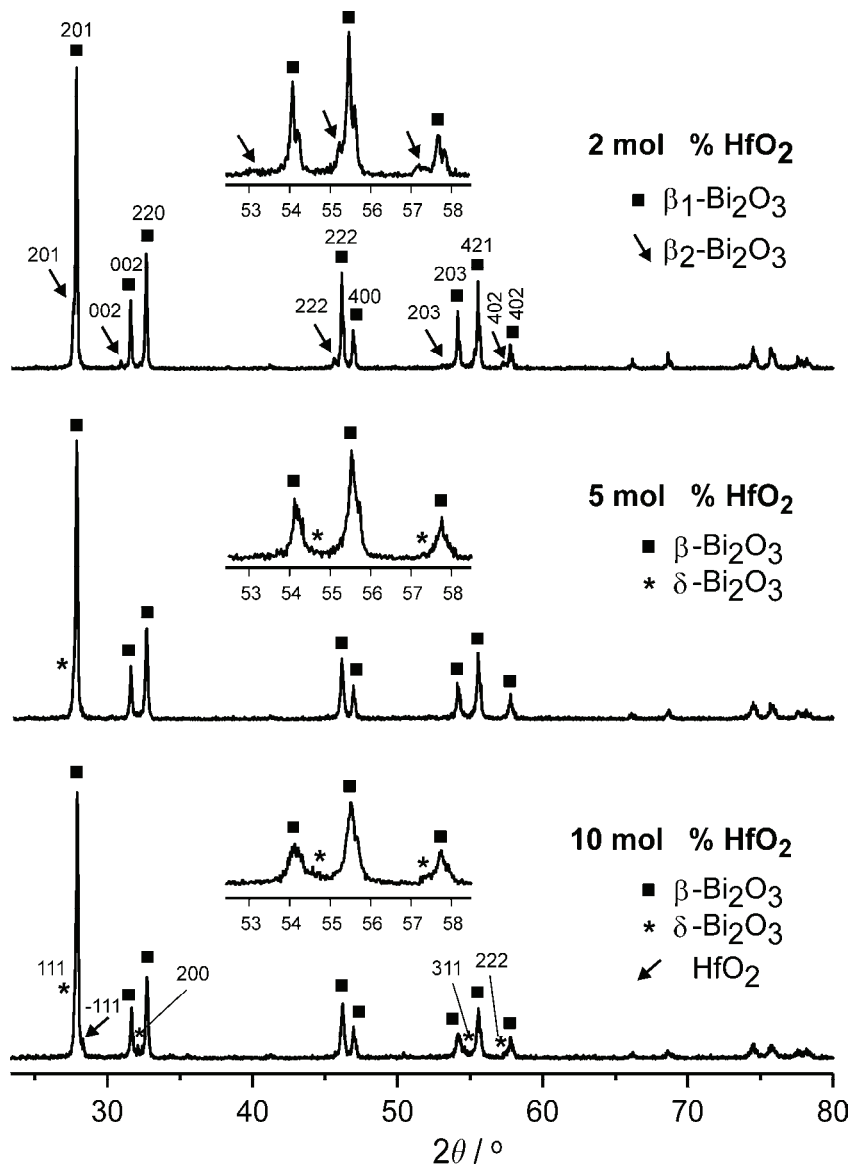


Fig. S3. XRPD Patterns for Bi_2O_3 specimens doped with 2, 5 and 10 mol % of HfO_2 (only strong reflection are indexed). Characteristic parts of the patterns are enlarged in the insets.



The use of cardboard factory sludge in the remediation of zinc-contaminated sediment

MILJANA PRICA^{1*}, MILENA DALMACIJA^{2#}, BOŽO DALMACIJA^{2#},
JELENA TRIČKOVIĆ^{2#} and SNEŽANA MALETIĆ^{2#}

¹*University of Novi Sad, Faculty of Technical Sciences, Trg Dositeja Obradovica 6, 21000 Novi Sad* and ²*University of Novi Sad, Faculty of Sciences and Mathematics, Department for Chemistry, Biochemistry and Environmental Protection, Trg Dositeja Obradovica 3, 21000 Novi Sad, Serbia*

(Received 11 November 2011, revised 6 March 2012)

Abstract: Paper and cardboard factory sludges are generated by various processes during pulp, cardboard and paper production, and the increasing quantities produced make the disposal of this sludge a problem. This study investigates the use of cardboard factory sludge as a stabilizing agent in the solidification/stabilization (S/S) treatment of zinc polluted sediment. Semi-dynamic and toxicity leaching tests were conducted to assess the effectiveness of the solidification/stabilization treatment and long-term zinc leaching behaviour. A diffusion-based model was used to elucidate the controlling leaching mechanisms. The applied S/S treatment was effective in immobilizing zinc, and the controlling leaching mechanism appeared to be diffusion, which indicates that a slow leaching of zinc could be expected when cardboard mill sludge is applied as a S/S agent.

Keywords: solidification/stabilization; leaching mechanism; leaching test.

INTRODUCTION

Zinc from various sources (industrial, mining, municipal sewage, agricultural and other activities) has entered water ways over time. Depending on their physico-chemical behaviour, heavy metals may adsorb onto suspended solids and subsequently accumulate in sediments, where they can pose a significant contamination problem.¹ However, heavy metals are not bound to sediments forever. With variations in the physical-chemical characteristics of the water conditions, some of the metals will re-enter the supernatant water and become available to living organisms.^{2,3} Symptoms of zinc toxicity in human beings include vomi-

* Corresponding author. E-mail: miljana@uns.ac.rs

Serbian Chemical Society member.

doi: 10.2298/JSC11111022P

ting, dehydration, electrolyte imbalance, abdominal pain, nausea, lethargy, dizziness and lack of muscular coordination. Zinc imparts an undesirable, bitter astringent taste to water in elevated concentrations. Concentrations of zinc above the recommended maximum value also cause adverse effects on the morphology of fish by inducing cellular breakdown of the gills.^{1,4}

It is now widely accepted that the toxicity and the mobility of elements depend strongly on their distribution in sediments. Hence, identification of the main binding sites and phase associations of heavy metals in sediments, based on the results of sequential extraction procedures, can help in understanding the remobilisation potential and the risks induced.⁵ Based on the Tessier procedure,⁶ the European Community Bureau of Reference produced a definition of an extraction protocol (the BCR protocol) and a purely operational definition of sequential fractionation. This method partitions the heavy metals into four fractions: exchangeable and carbonate bound, iron and manganese oxides bound, organic matter bound and residual metal. The distribution of metals in different phases obtained by the sequential extraction procedure offers an indication of their availability, which in turn allows a risk assessment of their presence in aquatic environments. The Risk Assessment Code (RAC) gives an idea of the possible risk by applying a scale to the percentage of metals present in the exchangeable and carbonate fractions, *i.e.*, labile phases.⁷ According to the RAC, if this fraction is < 1 %, there is no risk for the aquatic system, 1–10 % exhibits a low risk, 11–30 % medium risk, 31–50 % high risk and > 75% a very high risk.

In some cases, due to different factors, sediments may need dredging and remediation treatments. Currently, dredged sediment in Serbia is deposited in landfills whether it is contaminated or not. However, landfill capacity is limited, and can cause a serious threat if it is contaminated. In this study, stabilization/solidification (S/S) was used in order to remediate zinc-contaminated sediment, since this is a widely accepted treatment process for the immobilization of heavy metals contained in wastes.^{8,9} At the moment, there is not enough data about S/S treatments of contaminated sediments, especially those contaminated with zinc. There are a few studies regarding soil treatment with paper mill sludge but none for sediment treatment, and the conclusions obtained for soils that can be found in the literature may not be completely valid for sediments.

Paper and cardboard factory sludges are generated by various processes in the production of pulp, cardboard and paper, and the increasing quantities produced make the disposal of this sludge a problem.^{10,11} Waste is mainly generated from pulping, de-inking unit operations and wastewater treatment. The amount and composition of the waste depends on the paper grade produced, the raw materials used, the process techniques applied and the paper and cardboard properties to be achieved. The wastes can be reused and valorised in a safe and environ-



mental way, but landfill disposal of paper and cardboard sludges is the only waste disposal method used in Serbia.

The paper and cardboard factory sludges could be effective stabilizers due to their organic matter, silicate and carbonate contents. Organic matter is able to form stable complexes with several metals; the silicates are materials with high cation exchange capacity (CEC) and the bicarbonate/carbonate system is able to increase the pH value of soil. These chemical properties were able to reduce the harmful mobile metals in polluted soils when paper factory sludge was added to them.¹²

The long-term performance of S/S waste forms is difficult to predict. The mechanisms governing heavy metals leachability of contaminants from monolithic solidified waste forms, and the evaluation of the long-term behaviour of S/S wastes can be effectively examined using the American Nuclear Society's (ANS) semi-dynamic leaching test.¹³ The ANS 16.1 provides substantially more information regarding the "real time" rate at which heavy metals are released from a solidified product as compared to other leaching tests (toxicity characteristic leaching procedure – TCLP). The leaching results extend over a 90-day period instead of a single result at the end of the test (toxicity characteristic leaching procedure). The ANS 16.1 method was modified by including acetic acid (AA) and humic acid (HA) solutions as leachates instead of deionised water (DI). This was applied with the objective to mimic the worst possible conditions for S/S waste disposed in a landfill. It should be noted that this was used for the first time in the experiments with cardboard factory sludge and sediment.

The most commonly used leaching test, recommended by the USEPA, is the TCLP test, but it only provides one result to define waste toxicity.¹⁴ The TCLP was specifically designed to mimic acidic conditions in a sanitary landfill and identify wastes that have potential to contaminate ground water.

In view of the above, the objectives of this study were: 1) to define the zinc distribution in dredged sediment and evaluate its environmental risk based on the results of the sequential extraction procedure; 2) to assess the effectiveness of zinc immobilization using S/S treatments with cardboard factory sludge; 3) to evaluate the effectiveness of zinc immobilization by the S/S treatments under conditions which mimic a landfill environment and 4) to determine the controlling leaching mechanisms of zinc in the treated sediment samples.

EXPERIMENTAL

The cardboard factory sludge used was obtained after physical-chemical wastewater treatment from cardboard mill situated in Belgrade and its chemical characteristics were: pH 8.6 ± 0.3 , CEC 14.8 (cmol kg⁻¹), water content 39 %, organic matter 31 %, carbonates 25 %, silicates 47 % and Zn 10.1 mg kg⁻¹. The sludge was dried, crushed and passed through a 2.0 mm sieve, then characterised and used in the experiments.



Fresh sediment was collected using an Eijkelkamp core sampler, from the middle sediment on a stretch of the Veliki Bački Canal (Serbia), and was placed in a sealed plastic, acid-rinsed box (15 cm×15 cm and 20 cm deep) immediately after sampling.

Sediment initial water content was 75 %. Organic matter content, $4.48 \pm 0.1 \%$,¹⁵ was determined as loss on ignition. Sediment pH of 7.3 ± 0.4 ,¹⁶ was measured according to ASTM D 4972-01. The given values represent the means of three measurements.

The pseudo-total zinc content was assessed in triplicate after *aqua regia* digestion¹⁷ and determined using an atomic absorption spectrometer (AAS, Perkin Elmer AAnalyst 700, USA) or an inductively coupled plasma mass spectrometer (ICP-MS, Perkin Elmer ELAN 5000, USA) according to the standard procedures.¹⁸ The standard deviations (% RSD) obtained ($n = 3$) were below 10 %. The results of the sediment zinc pseudo-total concentrations are discussed in reference to the Canadian guidelines¹⁹ and the Dutch regulations,²⁰ since Serbia has neither an established system of continual sediment quality monitoring nor regulations covering quality standards.

The microwave assisted sequential extraction procedure (MWSE) was performed using identical operating conditions for each individual BCR fraction.²¹ Mean values were used and the RSD values ($n = 3$) were below 5 %. The sum of the four steps of the sequential procedure and the pseudo-total zinc contents differed by less than 10 %. Zinc contents in the sequential extraction procedure steps were analyzed by AAS or ICP-MS according to standard procedures.¹⁸

Sediment and cardboard factory sludge were dried to constant mass at 105 °C. The sediment and cardboard factory sludge were mixed in proportions of 95:5 (M1), 90:10 (M2), 80:20 (M3), 70:30 (M4) and 50:50 (M5) by mass. The samples were prepared in the form of monolithic cubes ($(3 \pm 0.1)^3 \text{ cm}^3$) by compaction. The compaction was performed according to ASTM D 1557-00,²² providing a compaction force of 2700 kN m m⁻³. The samples were cured at 20 °C in sealed sample bags for 28 days and then subjected to the leaching tests, *i.e.*, the standard TCLP leaching method and ANS 16.1.

According to the USEPA protocol,¹⁴ a 0.1 M acetic acid solution of pH 2.88 was used to extract the control sample and the S/S-treated samples since the pH was above 5. The sediment samples were extracted at a liquid to solid (L/S) ratio of 20 in capped polypropylene bottles on a rotary tumbler at 30 rpm for 18 h. After extraction, the final pH of the leachate was measured and the liquid was separated from the solids by filtration through a 0.45 µm pore size membrane filter. This test was applied on every sample in triplicate and the RSD values were below 5 %.

The ANS 16.1 test was applied in duplicate only on the M2 sample using deionised water as the leachate, and the RSD values were below 10 %. The ANS 16.1 method was modified by including 0.014 M acetic acid pH 3.25 and humic acid solutions (20 mg TOC L⁻¹, pH 6.55) as leachate instead of deionised water (DI). All materials in contact with the leachate were pre-cleaned with HNO₃ and subsequently rinsed with deionised water. All results are expressed with respect to sediment dry matter.

Evaluation of the leaching behaviour diffusion model

The long-term leachability of zinc from the S/S treated sediments was evaluated using the ANS method 16.1.¹³ By applying this test, the cumulative fraction of zinc leached *versus* time was obtained. The ANS has standardized the Fick's Law-based mathematical diffusion model as follows:



$$D_e = \pi \left[\frac{\frac{a_n}{A_0}}{(\Delta t)_n} \right]^2 \left[\frac{V}{S} \right]^2 T_n \quad (1)$$

where a_n is the contaminant loss (mg) during the particular leaching period with subscript n; A_0 is the initial amount of contaminant present in the specimen (mg); V is the specimen volume (cm^3); S is the surface area of the specimen (cm^2); $\Delta(t)_n$ is the duration of the leaching period in seconds; T_n is the elapsed time to the middle of the leaching period n (s), and D_e is the effective diffusion coefficient ($\text{cm}^2 \text{ s}^{-1}$).

The relative mobility of zinc can be evaluated by this coefficient, which varies from $D_e = 10^{-5} \text{ cm}^2 \text{ s}^{-1}$, (very mobile) to $D_e = 10^{-15} \text{ cm}^2 \text{ s}^{-1}$ (immobile).²³

Determination of the controlling leaching mechanism

The type of leaching mechanism that controls the release of metals can be determined based on the values of the slope of the logarithm of the cumulative fraction release, $\log(B_t)$, versus the logarithm of time, $\log(t)$:²⁴

$$\log(B_t) = S \log(t) + \log \left[U_{\max} d \sqrt{\left(\frac{D_e}{\pi} \right)} \right] \quad (2)$$

where D_e is the effective diffusion coefficient in $\text{m}^2 \text{ s}^{-1}$ for component x ; B_t is the cumulative maximum release of the component in mg m^{-2} ; t is the contact time in seconds; U_{\max} is the maximum leachable quantity in mg kg^{-1} and d is the bulk density of the product in kg m^{-3} .

When the slope (S) is close to 1 (0.60–1.00), the process is defined as dissolution. In such a case, the dissolution of the material proceeds faster than diffusion. If the slope is around 0.50 (0.40–0.60), the release of heavy metals will be slow and diffusion will be the controlling mechanism. If the slope is less than 0.40, the release of metal is probably due to surface wash-off.²⁴

RESULTS AND DISCUSSION

Pseudo-total metal concentrations and sequential extraction of the untreated sample

The pseudo-total zinc concentration in the sediment was $1137 \pm 54 \text{ mg kg}^{-1}$. According to Dutch standards,²⁰ the sediment is polluted with zinc (class 4). Class 4 sediments are of unacceptable quality and have the highest urgency for action: dredging, disposal in special storage reservoirs and, if possible, sediment clean-up measures.²⁰ Compared with the Canadian Sediment Quality Guidelines for aquatic life protection,¹⁹ the metal contents are above the PEL value. Sediment concentrations above the PEL values are expected to be frequently associated with adverse biological effects. Although the PEL is considered to be applicable to a variety of sediment types, it cannot define uniform values of sediment pollution as the bioavailability (and hence toxicity) of the contaminants may be different.¹⁹



The percentage of extracted zinc in the most available, mobile fraction was 24.4 %. The percentages of zinc in the other modified BCR fractions according to their relative contents are as follows: 12.7 % in the reducible fraction, 1.9 % in oxidisable form, and 61.2 % in the residual fraction.

The sequential extraction results are not in full agreement with the results of the pseudo-total metal concentration in the sediment, which only confirms the opinion that the total metal concentration is not sufficient to define the real danger presented to the environment. According to the risk assessment code (RAC), 24.4 % of zinc in the carbonate phases comes under the medium risk category.⁷

The total non-residual fraction (exchangeable+reducible+oxidisable) of zinc was 39 %. This indicates that these zinc fractions in the sediment are potentially available for exchange and/or release into the environment.

Leaching tests: ANS 16.1 and TCLP

Samples of sediment-cardboard factory sludge mixtures were subjected to the semi-dynamic leaching test ANS 16.1.¹³ This test has not been previously applied to mixtures of metal-contaminated sediments with cardboard factory sludge. The total cumulative fractions of zinc leached (%) after completion of the ANS 16.1 test using deionised water, acetic acid and humic acid solutions as leachates are presented in Table I.

TABLE I. Total cumulative fraction of zinc leached (*CFL*) after completion of the ANS 16.1 test using deionised water, acetic acid and humic acid solutions as leachates and the mean effective diffusion coefficient D_e for untreated (SO) and treated sediment samples (M1, M2, M3, M4 and M5)

Parameter	SO	M1	M2	M3	M4	M5
Deionised water						
<i>CFL</i> / %	17.1	5.13	4.52	4.30	3.21	4.40
D_e / $\text{cm}^2 \text{s}^{-1}$	4.84×10^{-8}	7.94×10^{-13}	5.01×10^{-13}	3.16×10^{-12}	2.51×10^{-13}	6.34×10^{-13}
Acetic acid solution						
<i>CFL</i> / %	19.8	7.17	6.33	6.05	4.49	6.40
D_e / $\text{cm}^2 \text{s}^{-1}$	5.62×10^{-6}	6.62×10^{-10}	4.01×10^{-10}	2.04×10^{-10}	7.95×10^{-11}	3.12×10^{-10}
Humic acid solution						
<i>CFL</i> / %	18.3	6.16	5.42	5.16	3.85	5.34
D_e / $\text{cm}^2 \text{s}^{-1}$	2.72×10^{-7}	3.16×10^{-11}	2.52×10^{-11}	1.58×10^{-11}	7.93×10^{-11}	1.96×10^{-11}

The amount of zinc released during the ANS 16.1 tests for the untreated samples did not exceed 20 % of the total mass of the contaminant in the waste, which is the upper limit for the diffusion model to be still applicable.¹³ The cardboard factory sludge exhibited good sorption properties, significantly reducing zinc leachability compared to the untreated sample. This is in agreement with literature data.^{10,12,25–30}



The humic acid leachate extracted more zinc than deionised water from all samples. Humic acids are very important in the formation of stable organo-mineral complexes because of their physico-chemical and biological stability. Due to their amphipathic nature and structural features, HAs play an important role in environmental processes governing the fate and transport of organic and inorganic pollutants in natural systems. They include binding sites with different complexion strength and are able to form inert and labile complexes with inorganic cations and organic compounds. Based on some previous studies, zinc shows a pronounced tendency for complexing with humic acids.^{31–34}

The amount of metal leached increased with high sorbent loading (M5). Similar results were reported by other authors.^{35–37} This may be attributed to two reasons: *i*) a large amount of adsorbent effectively reduces the unsaturation of the adsorption sites and correspondingly, the number of such sites per unit mass decreases resulting in comparatively lower adsorption at higher adsorbent amounts, and *ii*) higher amounts of adsorbent create particle aggregation, resulting in a decrease in the total surface area and an increase in diffusion path length, both of which contribute to decreasing the amount adsorbed per unit mass.

The diffusion coefficients D_e for the treated samples, calculated using Eq. (1), are listed in Table I. The mobility of zinc in this study was reduced by treatment possibly due to the high sorption capacity of the sludge.^{10,12,25–30} The diffusion coefficients are in agreement with the results of the cumulative release of zinc from the treated samples. The diffusion coefficients for metals in the treated samples ranged from 10^{-10} to $10^{-13} \text{ cm}^2 \text{ s}^{-1}$ (low mobility).

At present, TCLP is used by the USEPA to evaluate whether a particular S/S process is effective in treating a given waste in terms of reduction of the contaminant mobility and toxicity.¹⁴ The results of the TCLP leaching test are presented in Table II.

TABLE II. Results of the TCLP leaching test (mg L^{-1} , mean value $\pm SD$) for untreated (SO) and treated sediment samples (M1, M2, M3, M4 and M5)

SO	M1	M2	M3	M4	M5
0.94 ± 0.02^a	0.40 ± 0.01	0.32 ± 0.01	0.28 ± 0.01	0.21 ± 0.01	0.25 ± 0.01

^adata obtained from triplicate, standard deviation

A comparison of the concentrations obtained in the TCLP test showed that the zinc concentrations in the treated samples were below the concentration obtained for untreated sediment, meaning the zinc had been successfully incorporated into the treated matrix.

Overall, bearing in mind the high initial zinc concentration of the sediment sample, the treatment was very effective. This may be difficult to readily explain due to the degree of complexity in natural sediment samples. In nature there are many constituents that could participate in and influence zinc leachability. Fur-



ther research is required to obtain some of this information in order to evaluate zinc speciation and subsequent mechanisms of incorporation and release in these samples.

Controlling leaching mechanism

The controlling leaching mechanisms were evaluated using the diffusion model (Eq. (2)). The slope (S) and R^2 values obtained from the diffusion model are presented in Table III.

TABLE III. Slope (S) and R^2 values obtained from the diffusion model for untreated (SO) and treated sediment samples (M1, M2, M3, M4 and M5)

Parameter	SO	M1	M2	M3	M4	M5
Deionised water						
S	0.22	0.43	0.47	0.47	0.48	0.47
R^2	0.99	0.99	0.99	0.98	0.99	0.99
Acetic acid solution						
S	0.20	0.41	0.40	0.53	0.54	0.60
R^2	0.98	0.99	0.96	0.98	0.96	0.92
Humic acid solution						
S	0.29	0.42	0.45	0.54	0.56	0.58
R^2	0.98	0.96	0.99	0.99	0.97	0.99

The slope values for the mixtures ranged from 0.41 to 0.60 for all the treated samples. This indicates that diffusion was the dominant leaching mechanism. In the untreated sediment sample, the slope values ranged from 0.20 to 0.29, indicating that the dominant leaching mechanism was surface wash-off.

Further research should be focused on a more detailed analysis aimed at elucidating the encapsulation of zinc into the sediment structure and its leaching mechanism, relying on studies of mineralogy (qualitative and quantitative X-ray diffraction) as well as micromorphology (scanning electron microscopy and optical microscopy).

CONCLUSIONS

Assessment of the sediment quality based on the pseudo-total zinc content showed it to be severely contaminated according to the corresponding Dutch standards and Canadian guidelines. The zinc seems to pose a medium risk based on the modified BCR sequential extraction procedure and the risk assessment code.

The immobilization treatment applying cardboard factory sludge appeared to be effective in the remediation of the zinc-contaminated sediment. Based on the cumulative fraction of zinc leached, the diffusion coefficients and the results of the TCLP tests, it appears that the treatment efficiently reduced zinc mobility. In all samples, the controlling zinc leaching mechanism after S/S treatment ap-



peared to be diffusion. Hence, only small amounts of zinc could be expected to leach into the environment over time from the treated sediment.

Due to the large volumes of waste generated in the paper, cardboard and pulp industry, it is necessary to continue to increase environmental awareness about the different applications of wastes, while taking into account the environmental and economic factors influencing these waste treatments. Conventional waste management methods, which might have been acceptable in the past, might not be optimal to meet present and future requirements. The utilisation of cardboard factory sludge to “remediate” a contaminated sediment could be an interesting approach.

Acknowledgement. The authors acknowledge the financial support of the Ministry of Education and Science of the Republic of Serbia (Grant Nos. III43005 and TR37004).

ИЗВОД

КОРИШЋЕЊЕ ОТПАДА КАРТОНСКЕ ИНДУСТРИЈЕ ЗА РЕМЕДИЈАЦИЈУ СЕДИМЕНТА КОНТАМИНИРАНОГ ЦИНКОМ

МИЉАНА ПРИЦА¹, МИЛЕНА ДАЛМАЦИЈА², БОЖО ДАЛМАЦИЈА², ЈЕЛЕНА ТРИЧКОВИЋ² И СНЕЖАНА
МАЛЕТИЋ²

¹Универзитет у Новом Саду, Факултет техничких наука, Трг Доситеја Обрадовића 6, 21000 Нови Сад и

²Универзитет у Новом Саду, Природно-математички факултет, Департман за хемију, биохемију и
защиту животне средине, Трг Доситеја Обрадовића 3, 21000 Нови Сад

Отпад у индустрији папира, картона и пулпе настаје као последица бројних процеса, а његова све већа производња доводи до настајања проблема његове диспозиције. У овом раду је приказана могућност коришћења отпадног муља картонске индустрије као стабилизационог агенса у третману солидификације/стабилизације (С/С) седимента загађеног цинком. Да би се испитала ефикасност примењеног третмана и процена потенцијала излуживања цинка у дужем временском периоду примењени су семидинамички тест излуживања и тест излуживања токсичности. Модел базиран на дифузији је послужио за процену механизма који је доминантан током излуживања. Примењени третман се показао ефикасним за имобилизацију цинка, а доминантан механизам излуживања је дифузија. Резултати указују на то да би требало очекивати споро излуживање цинка када се отпадни муљ картонске индустрије примени као стабилизациони агенс у С/С третману.

(Примљено 11. новембра 2011, ревидирано 6. марта 2012)

REFERENCES

1. S. Tautkus, L. Steponeniene, R. Kazlauskas, *J. Serb. Chem. Soc.* **72** (2007) 579
2. I. Planojević, I. Teodorović, K. Bartova, A. Tubić, T. Jurca, W. Kopf, J. Machat, L. Blaha, R. Kovačević, *J. Serb. Chem. Soc.* **76** (2011) 459
3. Ž. Vuković, M. Radenković, S. Stanković, D. Vuković, *J. Serb. Chem. Soc.* **76** (2011) 795
4. N. Dali-Youcef, B. Ouddane, Z. Derriche, *J. Hazard. Mater.* **137** (2006) 1263
5. D. L Wise, D. J., Trantolo, E. J. Cichon, H. I. Inyang, U. Stottmeister, *Remediation Engineering of Contaminated Soils*, Marcel Decker, NY, USA (2000)
6. A. Tessier, P. G. C. Campbell, M. Bisson, *Anal. Chem.* **51** (1979) 844



7. C. K. Jain, *Water Res.* **38** (2004) 569
8. D. H. Moon, D. Dermatas, *J. Hazard. Mater.* **141** (2007) 388
9. A. Coz, A. Andrés, S. Soriano, J. R. Viguri, M. C. Ruiz, J. A. Irabien, *J. Hazard. Mater.* **164** (2009) 755
10. A. Battaglia, N. Calace, E. Nardi, B. M. Petronio, M. Pietroletti, *Bioresour. Technol.* **98** (2007) 2993
11. M. C. Monte, E. Fuente, A. Blanco, C. Negro, *Waste Manage.* **29** (2008) 293
12. N. Calace, T. Campisi, A. Iacondini, M. Leonia, B. M. Petronio, M. Pietroletti, *Environ. Pollut.* **136** (2005) 485
13. ANS (American National Standard) ANSI/ANS 16.1. *Measurement of the Leachability of Solidified Low-Level Radioactive Wastes by Short-Term Tests Procedures*, (1986)
14. USEPA (United States Environmental Protection Agency), 2002, Method 1311
15. NEN 5754 *Determination of organic matter content in soil as loss-on-ignition* (1994)
16. ASTM D 4972-01 Standard test method for pH of soils (2007)
17. ISO 11466 (1995) *Soil quality. Extraction of trace elements soluble in aqua regia*
18. NEN 5759 *Determination of zinc content by atomic absorption spectrometry (flame technique)* (1990)
19. CCME (Canadian Council of Ministers of the Environment) *Protocol for the derivation of Canadian Sediment quality guidelines for the protection of aquatic life*. CCME EPC-98E (1995)
20. Ministry of Housing, Spatial Planning and Environment Directorate-General for Environmental Protection (2000) *Circular on target values and intervention values for soil remediation*, Netherlands Government Gazette No. 39
21. M. K. Jamali, T. G. Kazi, M. B. Arain, H. I. Afridi, N. Jalbani, G. A. Kandhro, A. Q. Shah, J. A. Baig, *J. Hazard. Mater.* **163** (2009) 1157
22. ASTM D 1557-00 Standard test method for laboratory compaction characteristics of soil using modified effort (2000)
23. J. S. Nathwani, C. R. Phillips, *Water Air Soil Pollut.* **14** (1980) 389
24. G. J. de Groot, H. A. van der Sloot, *Determination of Leaching Characteristics of Waste Materials Leading to Environmental Product Certification*, in *Stabilization and Solidification of Hazardous, Radioactive, and Mixed Wastes*, T. M. Gilliam, C. C. Wiles, Eds., ASTMSTP 1123, American Society for Testing Materials, Philadelphia, PA, 1992, p.p. 149–170
25. N. Calace, B. M. Petronio, M. Picciolo, M. Pietrantonio, M. Pietroletti, *Ann. Chim.* **90** (2000) 655
26. S. K. Lister, M. Line, *Bioresour. Technol.* **79** (2001) 35
27. N. Calace, A. di Muro, E. Nardi, B. M. Petronio, M. Pietroletti, *M. Ind. Eng. Chem. Res.* **41** (2002) 5491
28. A. Battaglia, N. Calace, E. Nardi, B. M. Petronio, M. Pietroletti, *Microchem. J.* **75** (2003) 97
29. N. Calace, E. Nardi, B. M. Petronio, M. Pietroletti, G. Tosti, G. *Chemosphere* **51** (2003) 797
30. X. He, L. Yao, Z. Liang, J. Ni, *J. Environ. Sci.* **22**(3) (2010) 413
31. F. S. Mowat, K. J. Bundy, *Adv. Environ. Res.* **6** (2002)
32. V. P. Utkigar, N. Chaudhary, A. Koeniger, H. H. Tabak, J. R. Haines, R. Govind, *Water Res.* **38** (2004) 3651



33. V. Tsiridis, M. Petala, P. Samaras, S. Hadjispypou, G. Sakellaropoulos, A. Kungolos, *Ecotox. Environ. Safe.* **63** (2006) 158
34. Y. Li, Q. Yue, B. Gao, *J. Hazard. Mater.* **178** (2010) 455
35. K. G. Bhattacharyya, S. S. Gupta, *Adv. Colloid Interface Sci.* **140** (2008) 114
36. C. Pérez-Novo, M. Pateiro-Moure, F. Osorio, J. C. Novoa-Muñoz, E. Lopez-Periago, M. Arias-Estevez, *J. Colloid Interface Sci.* **322** (2008) 33
37. J. M. De la Rosa, M. Santos, M. F. Araújo, *Estuarine Coastal Shelf Sci.* **93** (2011) 478.



J. Serb. Chem. Soc. 77 (8) 1109–1127 (2012)
JSCS-4338

Journal of the Serbian Chemical Society

JSCS-info@shd.org.rs • www.shd.org.rs/JSCS

UDC 553.96.:550.86:547(497.11-92)

Original scientific paper

Drmno lignite field (Kostolac Basin, Serbia): origin and palaeoenvironmental implications from petrological and organic geochemical studies

KSENIJA STOJANOVIĆ^{1**#}, DRAGANA ŽIVOTIĆ², ALEKSANDRA ŠAJNOVIĆ³,
OLGA CVETKOVIĆ^{3#}, HANS PETER NYTOFT⁴ and GEORG SCHEEDER⁵

¹University of Belgrade, Faculty of Chemistry, Studentski trg 12–16, 11000 Belgrade, Serbia,

²University of Belgrade, Faculty of Mining and Geology, Djušina 7, 11000 Belgrade, Serbia,

³University of Belgrade, Centre of Chemistry, ICTM, Studentski trg 12–16, 11000 Belgrade;

Serbia, ⁴Geological Survey of Denmark and Greenland, Øster Voldgade 10, DK-1350

Copenhagen, Denmark and ⁵Federal Institute for Geosciences and Natural

Resources, Steveledge 2, 30655 Hanover, Germany

(Received 26 November 2011, revised 17 February 2012)

Abstract: The objective of the study was to determine the origin and to reconstruct the geological evolution of lignites from the Drmno field (Kostolac Basin, Serbia). For this purpose, petrological and organic geochemical analyses were used. Coal from the Drmno field is typical humic coal. Peat-forming vegetation dominated by decay of resistant gymnosperm (coniferous) plants, followed by prokaryotic organisms and angiosperms. The coal forming plants belonged to the gymnosperm families *Taxodiaceae*, *Podocarpaceae*, *Cupressaceae*, *Araucariaceae*, *Phyllocladaceae* and *Pinaceae*. Peatification was realised in a neutral to slightly acidic, fresh water environment. Considering that the organic matter of the Drmno lignites was deposited at the same time, in a relatively constant climate, it could be supposed that climate probably had only a small impact on peatification. Therefore, variations in compositions of macerals and biomarkers indicate changes in the water level, due to seasonal drying of the mire, which caused vegetation differences in the palaeoplant communities and changes in the redox conditions (from anoxic to slightly oxic) during peatification. Diagenetic transformations of the organic matter were mainly governed by microbial activity, rather than thermal alteration.

Keywords: lignites; Kostolac Basin; organic matter; macerals; biomarkers; palaeoenvironment.

* Corresponding author. E-mail: ksenija@chem.bg.ac.rs; xenasyu@yahoo.com

Serbian Chemical Society member.

doi: 10.2298/JSC111126017S



INTRODUCTION

Standard methods for the investigation of peat and coal bearing sediments include a complex of petrological, palynological, palaeobotanical and geochemical techniques to acquire information about the sedimentary environment, type of vegetation and its transformation during diagenesis.

The maceral composition is directly dependent on the type of the source material and the environmental settings. Therefore, maceral analysis is widely used to interpret the conditions of peat formation.^{1–4} In addition to maceral percentages, two parameters based on the maceral composition, the tissue preservation index (*TPI*) and the gelification index (*GI*), are of great importance. The *TPI* provides valuable data about peat forming plant communities, water column level, pH and climatic settings.^{5–7} The *GI* could be used as an indirect measure for the water column level, as well as for an estimation of the redox conditions of the environment and microbial activity.^{4–7}

Elemental analysis, Rock–Eval analysis and other bulk geochemical parameters (*e.g.*, ash content, organic carbon and sulphur contents, and group composition of soluble organic matter) provide basic data for characterizing coals.^{8,9}

In the past few decades, molecular organic geochemistry has played an important role in the exploration of coals and fossil fuels generally. It involves the analysis of the soluble organic matter and identification of organic compounds with hydrocarbon skeletons related to biological molecules present in the tissues of living organisms.^{10,11} These biomarkers allow for the recognition of the main input of organic matter (OM), an estimation of the palaeoenvironment in which they were deposited and determination of the thermal maturity. For these purposes, numerous biomarkers, *n*-alkanes, isoprenoid aliphatic alkanes, steroids, hopanoids, sesquiterpenoids, diterpenoids, non-hopanoid triterpenoids, were used.

The production of energy in Serbia is based on coal sources (52 %), followed by crude oil (28 %), natural gas (13 %) and hydroenergy (7 %).¹² The largest resources of coals in Serbia represent soft brown coals, *i.e.*, lignites (92 %).¹³ The main lignite deposits are located in the Kosovo, Kolubara, Kostolac and Metohija Basins, and in the Kovin deposit.¹⁴ Although the lignite deposits are widespread in Serbia, petrological and geochemical data are either scarce or completely missing.^{15,16} The objective of this study was to determine the origin and to reconstruct the geological evolution of lignites from the Drmno field, Kostolac Basin (Serbia), based on comprehensive petrological and organic geochemical analyses.

Geological settings of the Kostolac Basin

The Kostolac Coal Basin, covering an area of 145 km², is located about 90 km east of Belgrade. It is divided into three coal fields: the Drmno field in the eastern, the Čirikovac field in the central and the Smederevsko Podunavlje field



in the western part of the Basin (Fig. 1). The Drmno and Ćirikovac fields are exploited, while the Smederevsko Podunavlje field is still under preliminary exploration.

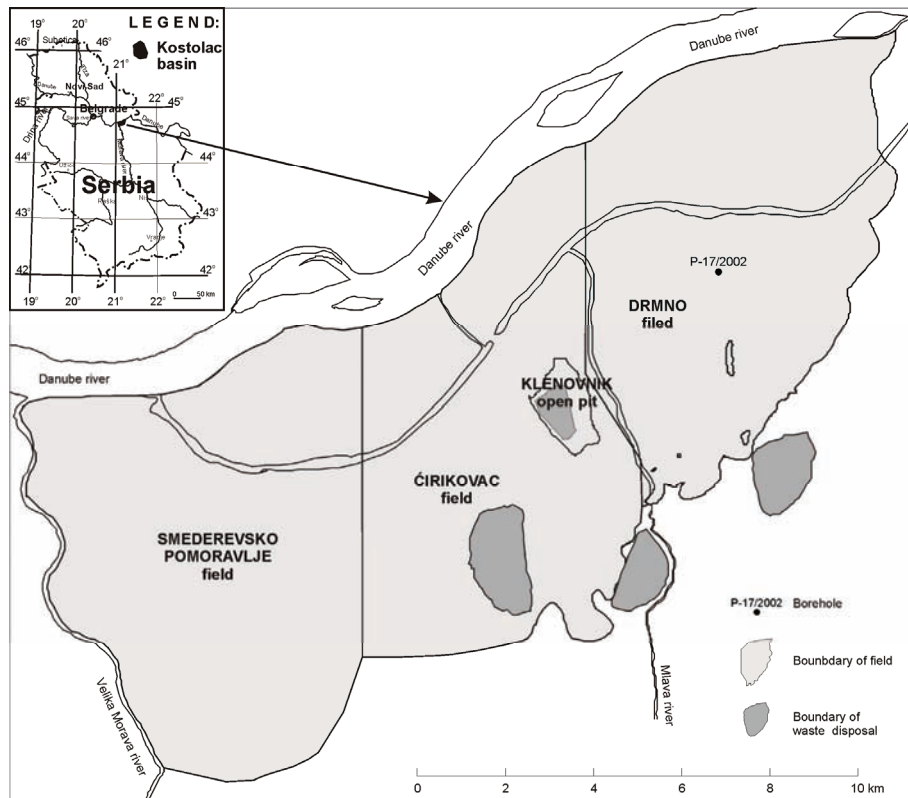


Fig. 1. Location and coal fields of the Kostolac Basin.

The basement of the Kostolac Basin is formed of Devonian crystalline rocks overlain by Neogene sediments. The total thickness of the Neogene sediments ranges from 300 to 5000 m in the central part of the depression.¹⁷ The complete Neogene generally dips towards NW at the low angle of 5–15°; the coal seams following the same dip, as well. The Neogene complex consists of several units:¹⁷

1. Lower Miocene, formed of fluvio-lacustrine and marine metaclastic rocks, siltstone, sandstone, and shales (“redeposited series”), breccia-type material (“transitional zone”), and red to violet sandy marlstone, sandstone, and conglomerate (“red series”);
2. Ottnangian–Karpathian, consisting of fluvial brackish and marine conglomerate, sandstone, siltstone, shale, and marlstone, with local transitions to laminated limestone and tuffaceous sandstone;

3. Badenian, formed of marine sandstone, marlstone, and siltstone;
4. Sarmatian, consisting of clayey and sandy marlstone, marly clay, marly and clayey sandstone, subordinately of gravel and quartz sand, in a shallow brackish-marine environment;
5. Pannonian, made of clastic sediments with two coal seams, the lower up to 6 m in thickness, and the upper of maximum 1 m in thickness;¹⁸
6. Pontian, consisting of clastic sediments, with economic coal resources. The total thickness of the Pontian sediments is more than 200 m. The Pontian coal-bearing series consists of five coal seams, namely seam III (the oldest and deepest) and the seams II-a, II, I-a, and I. Only coal seams III, II and I have been explored in the Drmno, Ćirikovac and Klenovnik open pits. The average thickness of coal seam III throughout whole basin is 19.38 m, while it is 1.43 m for IIa, 4.14 m for II, 1.53 for Ia and 13.90 m for I coal seam.¹⁹ Average huminite reflectance of coal from the Drmno and Ćirikovac fields (seams II and III) is 0.30 %;^{19,20} thus, placing the coal in the soft brown coal (lignite) stage of coalification;
7. Romanian, includes sand, clay, silt, and gravel, disconformably overlying Pannonian or Pontian sediments;
8. Quaternary, formed of fluvial gravel, sand and sandy clay, eolian loess and loess-like clays, all of Pleistocene age.

The lignite samples investigated in this study are of Upper Pontian age (c. 6 Ma) and originated from the borehole P-17/2002 of the Drmno field (Kostolac Basin; Fig. 1). The samples were collected from the two coal seams, II at a depth interval 23.20 to 24.90 m, and III at a depth interval 100.60 to 123.70 m (Table I). The thickness of each sample interval was determined as per the changes in macroscopic lithology of the coal.

TABLE I. The list of investigated samples

Coal seam	Sample	Depth interval, m	Lithology
II	1	23.20–23.40	Mixture of xylitic and matrix coal
	2	23.40–24.40	Mixture of matrix and xylite-rich coal
	3	24.40–24.53	Xylite-rich coal
	4	24.80–24.90	Matrix coal
III	5	100.60–101.00	Mixture of matrix and xylite-rich coal
	6	102.10–102.20	Xylite-rich coal
	7	103.00–104.20	Matrix coal
	8	104.80–104.90	Xylite-rich coal
	9	112.00–112.60	Mixture of matrix and xylite-rich coal
	10	121.40–123.70	Mineral-rich coal

EXPERIMENTAL

For the maceral analyses, the coal samples were crushed to a maximum particle size of 1 mm, mounted in epoxy resin and polished. The maceral analysis was performed on a LEITZ DMLP microscope under monochromatic and UV reflected light on 500 points. The maceral



description used in this article follows the terminology developed by the International Committee for Coal Petrology for low-rank coal.²¹

Elemental analysis was applied to determine the contents of sulphur and organic carbon (C_{org}). The organic carbon content was determined after removal of carbonates with dilute hydrochloric acid (1:3, v/v). The measurements were performed using a Vario EL III, CHNOS elemental analyser, Elementar Analysensysteme GmbH. The measurements of the ash content followed the standard procedure ISO 1171 (1997).²²

Soluble organic matter (bitumen) was extracted from pulverized lignites (<150 µm) using a Dionex ASE apparatus with a mixture of *iso*-hexane and acetone (1:1, v:v) at a temperature of 80 °C and a pressure of 8 MPa. After extraction, most of the solvent was removed using a vacuum rotary evaporator. The extract yields were weighed. The asphaltenes were precipitated from the bitumen with petroleum-ether and the remainder (maltenes) was separated into three fractions (saturated hydrocarbons, aromatic hydrocarbons and NSO compounds) using column chromatography over silica gel and aluminium oxide. The saturated hydrocarbons fraction was eluted with *iso*-hexane, the aromatic hydrocarbons with dichloromethane and the NSO fractions (polar fraction, which contains nitrogen, sulphur and oxygen compounds) with a mixture of dichloromethane and methanol (1: 1, v:v).

The saturated and aromatic fractions isolated from the bitumen were analyzed by gas chromatography-mass spectrometry (GC-MS). A gas chromatograph Agilent 7890A GC (H5-MS capillary column, 30 m×0.25 mm, He carrier gas 1.5 cm³ min⁻¹, FID) coupled to an Agilent 5975C mass selective detector (70 eV) was used. The column was heated from 80 to 310 °C at a rate of 2 °C min⁻¹, and the final temperature of 310 °C was maintained for an additional 25 min. The individual peaks were identified by comparison with literature data^{10,23-26} and on the basis of the total mass spectra (library: NIST5a). Biomarker parameters were calculated from the GC-MS chromatogram peak areas (software GCMS Data Analysis).

RESULTS AND DISCUSSION

Maceral analysis

Coal from the Drmno field is typical humic coal with huminite concentrations between 50.8 and 89.3 vol. %, liptinite less than 7 vol. % and inertinite between 4.0 and 12.5 vol. %. The most abundant huminite macerals are textinite, ulminite and densinite. Liptodetrinite and sporinite dominated among liptinite macerals, whereas inertodetrinite and fusinite are the most abundant inertinite macerals (Table II).

The tissue preservation index (*TPI*),^{27,28} taken as the ratio between structured and unstructured macerals of the huminite and inertinite group, ranges from 0.7 to 4.2 (Table II). The variations of the *TPI* with depth could reflect, at least to some extent, the differences in the type of peat forming plant communities. On the other hand, it was suggested that tissue preservation depends mostly on the relative height of the water level, pH and climatic settings, rather than from the botanical properties of the vegetation.²⁹ Namely, lowering the water level within the basins during the dry seasons contributes to the establishment of more oxic conditions, resulting in more extensive tissue degradation. Considering that the OM of the Drmno lignites was deposited in the same time, in the relatively



constant climate, it could be supposed that the climate probably had only a small impact on peatification. Therefore, the variations in the maceral composition and the *TPI* could be attributed mainly to changes in the water column level, due to seasonal drying of the mire, which caused vegetation differences in the palaeo-plant communities and changes of redox potential (*Eh*) during peatification.

TABLE II. Maceral composition (vol. %) and petrographic indices of the Drmno field coals

Maceral	Sample									
	1	2	3	4	5	6	7	8	9	10
Textinite	17.1	19.7	48.3	16.1	17.3	14.3	15.7	15.8	11.4	3.7
Ulminite	10.6	5.4	15.8	11.8	15.5	26.7	13.1	32.8	38.9	15.3
(Total telohuminite)	27.7	25.1	64.1	27.9	32.8	41.0	28.8	48.6	50.3	19.0
Attrinite	3.0	13.6	3.9	14.5	7.9	6.6	3.5	2.4	0.6	2.7
Densinite	30.0	25.8	9.4	31.0	31.5	32.3	39.1	19.7	17.1	22.6
(Total detrohuminite)	33.0	39.4	13.3	45.5	39.4	38.9	42.6	22.1	17.7	25.3
Gelinite	4.0	2.3	3.1	3.0	3.2	3.0	0.5	4.0	7.2	5.5
Corpohuminite	1.5	1.8	2.0	5.0	5.4	6.4	0.9	6.3	4.7	1.0
(Total gelohuminite)	5.5	4.1	5.1	8.0	8.6	9.4	1.4	10.3	11.9	6.5
Total huminite	66.2	68.5	82.6	81.4	80.8	89.3	72.8	81.0	79.9	50.8
Sporinite	1.4	1.5	1.3	2.0	1.4	0.6	0.7	0.5	1.1	0.8
Cutinite	0.1	0.2	0.0	0.4	0.2	0.0	0.2	0.0	0.1	0.3
Resinite	0.1	0.0	0.2	0.4	0.2	0.4	0.2	0.5	0.2	0.4
Suberinite	0.1	0.2	0.0	0.9	0.2	0.2	0.2	0.4	0.9	0.0
Alginite	0.4	0.5	0.0	0.0	0.2	0.0	0.2	0.0	0.0	0.3
Liptodetrinite	1.2	2.1	1.1	2.7	1.9	1.2	1.2	1.1	0.2	1.3
Other – liptinite	1.0	1.2	0.7	0.4	0.2	0.4	0.7	0.5	0.0	0.0
Total liptinite	4.3	5.7	3.3	6.8	4.3	2.8	3.4	3.0	2.5	3.1
Fusinite	1.5	2.3	2.7	0.6	0.5	0.4	1.1	1.1	4.0	1.8
Semifusinite	0.3	1.0	0.4	0.4	0.4	0.0	1.2	0.4	3.8	1.2
Macrinite	0.0	0.2	0.2	0.0	0.2	0.0	0.2	0.5	0.2	0.8
Funginite	1.2	0.3	0.2	1.7	0.9	0.8	0.5	0.7	0.4	0.5
Inertodetrinite	1.0	3.9	2.4	1.4	3.0	0.7	9.2	1.3	4.1	6.1
Total inertinite	4.0	7.7	5.9	4.1	5.0	1.9	12.2	4.0	12.5	10.4
Total coal	74.5	82.0	91.7	92.3	90.1	94.0	88.4	88.0	94.9	64.3
Clay	21.8	11.1	1.4	5.3	8.3	3.5	6.1	9.7	4.3	31.6
Pyrite	2.3	2.2	1.8	0.9	0.5	1.9	3.2	1.8	0.8	1.9
Carbonates	0.7	0.8	0.9	0.4	0.4	0.0	1.6	0.0	0.0	0.9
Other minerals	0.7	3.9	4.2	1.1	0.7	0.6	0.7	0.5	0.0	1.3
Total mineral	25.5	18.0	8.3	7.7	9.9	6.0	11.6	12.0	5.1	35.7
<i>TPI</i> ^a	0.8	0.7	4.2	0.7	0.9	1.1	0.7	2.1	2.5	0.7
<i>GI</i> ^b	1.9	0.9	0.5	1.5	1.8	3.0	1.7	2.8	2.8	2.6

^a*TPI* = (textinite+ulminite+corpohuminite+fusinite+semifusinite)/(gelinite+macrinite+detrohuminite),^{27,28} ^b*GI* = = (ulminite+densinite+gelinite+corpohuminite)/(textinite+attrinite+inertinite)^{27,28}

The gelification index (*GI*),^{27,28} expressed as the ratio of gelified (ulminite, densinite, gelinite and corpohuminite) to non-gelified (textinite and attrinite) macerals, is used as an indirect measure for the height of the water level, because



gelification of the tissues requires the continuous presence of water. Lignites from the Drmno field have a *GI* value ranging between 0.5 and 3.0 (Table II). The variation of this ratio with depth also indicates changes in the height of the water level and consequently changes of the *Eh* conditions during peatification. Based on the generally higher *TPI* and *GI* values in coal seam III than in coal seam II, it could be assumed that the water column level during peatification was lower in coal seam II.

The content of mineral matter shows a comparatively wide range 5.1–35.7 % (Table II). An increase in the mineral content is often related to more intensive degradation of organic matter and/or contribution of clastic material. The domination of clays and very low carbonate content in the mineral matter (Table II) suggest a neutral to slightly acidic environment. As expected, a significant positive correlation (correlation coefficient, $r = 0.98$) is observed between the mineral matter content (Table II) and the ash content (Table III).

TABLE III. Values of group organic geochemical parameters

Coal seam	Sample	Ash, %, db ^a	C_{org} , %, db ^b	S, %, db	Bitumen, ppm	Asp ^c , %	Saturated HC ^d , %	Aromatic HC, %	NSO, %
II	1	35.62	38.41	0.85	15333	59.22	2.56	2.67	35.54
	2	18.44	49.13	3.42	12292	42.03	5.71	3.60	48.67
	3	8.72	58.09	1.80	98666	64.54	2.33	3.79	29.33
	4	9.82	55.12	1.58	11628	51.23	2.63	3.58	42.56
III	5	10.52	54.58	0.63	10631	41.41	3.90	4.51	50.18
	6	4.53	N.D. ^e	N.D.	79400	70.93	13.22	2.17	13.69
	7	13.17	51.32	1.03	6645	42.20	3.25	4.20	50.35
	8	17.26	51.04	1.32	40000	63.63	6.50	3.71	26.15
	9	9.66	56.67	0.90	18272	45.87	6.90	3.40	43.83
	10	47.04	30.72	1.23	14950	42.40	2.23	5.50	49.87

^aDry basis; ^borganic carbon content; ^casphaltenes; ^dhydrocarbons; ^enot determined

Group organic geochemical parameters

The contents of organic carbon (C_{org}) are within the limits typical for lignite^{7,30} and vary between 30.72 and 58.09 % (Table III). The significant negative correlation between C_{org} and the mineral matter content ($r = 0.98$) indicates that the differences in the C_{org} contents of the lignites are mainly controlled by the varying amounts of mineral matter. The content of sulphur does not exceed 2 %, with exception of sample 2 (Table III). This result implies the relatively low sulphate content of the waters within the peat (peatification in fresh water environment).^{3,31}

The yield of the soluble organic matter (bitumen) varies over a wide range 6645–98666 ppm, in concordance with the variation in C_{org} . The soluble organic matter is mainly represented by asphaltenes (41.41–70.93 %) and polar, NSO compounds (13.69–50.35 %). The relative contents of saturated and aromatic



hydrocarbons are low, which is in accordance with the low maturity of the organic matter (Table III).

Molecular composition of the organic matter

General characteristics. The main constituents of the saturated fraction of the coals are diterpenoids, followed by *n*-alkanes and hopanoids. Steroids and non-aromatic, non-hopanoid triterpenoids were identified in relatively low amounts (Fig. 2). The main components in the aromatic fractions of the Drmno coals are diterpenoids. Other constituents of the aromatic fractions are non-hopanoid triterpenoids, sesquiterpenoids, aromatized hopanoids, long-chain acyclic alkan-2-ones, monoaromatic steroids and perylene (Fig. 3).

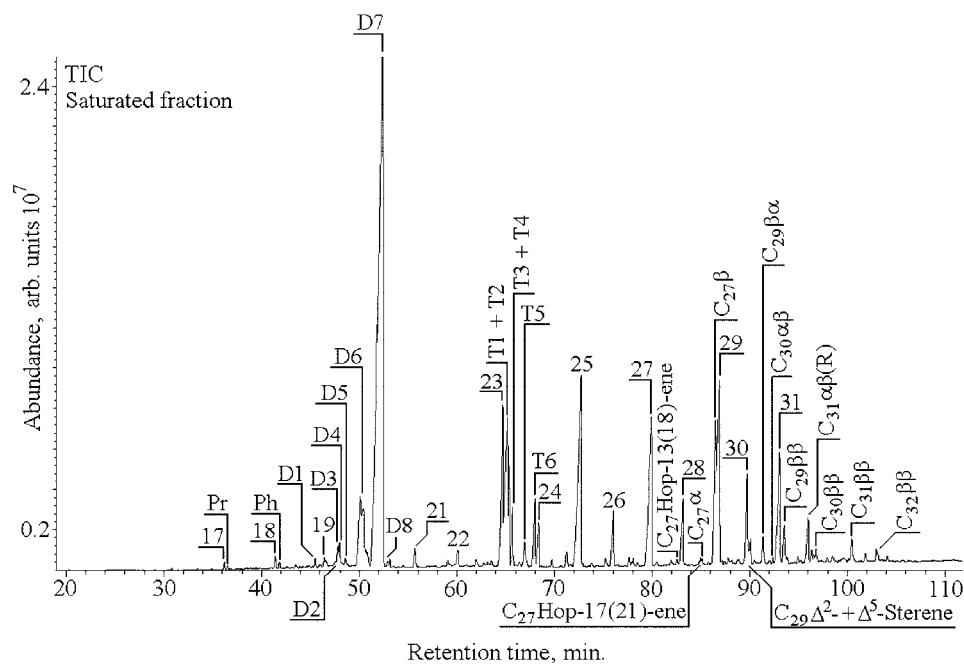


Fig. 2. TIC (total ion current) of a saturated fraction typical for the investigated samples. Peak assignments: *n*-alkanes are labelled according to their carbon number; Pr – pristane; Ph – phytane; D1 – isopimaradiene; D2 – norabietane; D3 – norpimarane; D4 – beyerane; D5 – isophyllocladene; D6 – pimarane; D7 – 16 α (*H*)-phyllocladane; D8 – 16 α (*H*)-kaurane; T1 – des-A-olean-13(18)-ene; T2 – des-A-olean-12-ene; T3 – des-A-olean-18-ene; T4 – des-A-urs-13(18)-ene; T5 – des-A-urs-12-ene; T6 – des-A-lupane; $\beta\beta$, $\beta\alpha$ and $\alpha\beta$ designate configurations at C₁₇ and C₂₁ in hopanes, *R* designates configuration at C₂₂ in hopanes.

The domination of diterpenoids in both the saturated and aromatic fractions shows that the main sources of organic matter were gymnosperms (conifers). The presence of hopanoid biomarkers indicates the contribution of prokaryotic orga-

nisms, such as bacteria and fungi, whereas the identification of non-hopanoid triterpenoids implies a contribution of angiosperms to the lignite organic matter (Figs. 2 and 3).

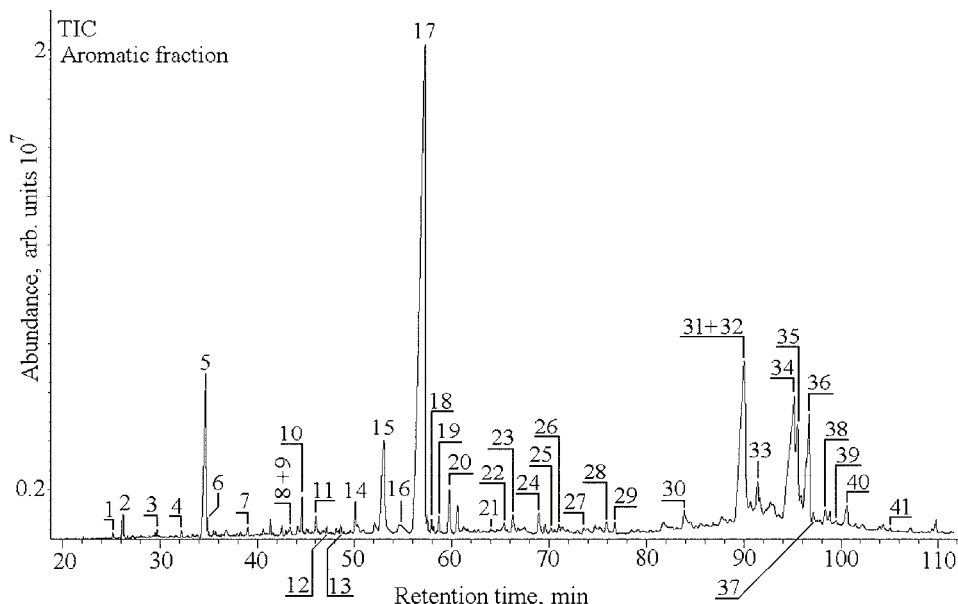


Fig. 3. TIC (total ion current) of an aromatic fraction typical for the investigated samples. Peak assignments: **1** – cuparene; **2** – calamenene; **3** – cadina-1(10),6,8-triene; **4** – 5,6,7,8-tetrahydrocadalene; **5** – cadalene; **6** – isocadalene; **7** – phenanthrene; **8** – 19-norabiet-8,11,13-triene; **9** – 6,10,14-trimethylpentadecan-2-one; **10** – 18-norabiet-6,8,11,13-tetraene; **11** – 16,17-bisnordehydroabietane; **12** – hibane; **13** – 16,17-bisnorsimonellite; **14** – 18-norabiet-8,11,13-triene; **15** – dehydroabietane; **16** – 1,2,3,4-tetrahydrotetene; **17** – simonellite; **18** – totarane; **19** – sempervirane; **20** – retene; **21** – ferruginol; **22** – pentamethylocatahyd-rochrysene; **23** – 2-methylretene; **24** – 3,4,7,12a-tetramethyl-1,2,3,4,4a,11,12,12a-octahydrochrysene; **25** – 3,3,7,12a-tetramethyl-1,2,3,4,4a,11,12,12a-octahydrochrysene; **26** – penta-methyldecahydrochrysene; **27** – triaromatic des-A-lupane; **28** – 3,4,7-trimethyl-1,2,3,4-tetrahydrochrysene; **29** – 3,3,7-trimethyl-1,2,3,4-tetrahydrochrysene; **30** – perylene; **31** – 24,25-dinoroleana-1,3,5(10)-12-tetraene; **32** – D-ring monoaromatic hopane; **33** – 24,25-dinorlupa-1,3,5(10)-triene; **34** – 1,2,4a,9-tetramethyl-1,2,3,4,4a,5,6,14b-octahydropicene; **35** – 2,2,4a,9-tetramethyl-1,2,3,4,4a,5,6,14b-octahydropicene; **36** – 24,25-dinoroleanapentaene; **37** – 4-methyl-24-ethyl-19-norcholesta-1,3,5(10)-triene; **38** – 7-methyl-3'-ethyl-1,2-cyclopentanochrysene; **39** – C₃₁ n-alkan-2-one; **40** – 1,2,9-trimethyl-1,2,3,4-tetrahydropicene; **41** – C₃₃ n-alkan-2-one.

n-Alkanes and isoprenoids. *n*-Alkanes are relatively abundant in the total ion current (TIC) of the saturated fraction (Fig. 2). Based on the *m/z* 71 mass chromatogram of the saturated fraction (Fig. 4a), *n*-alkanes were identified in the range C₁₇ to C₃₅. The *n*-alkane patterns of the coal samples are dominated by long-

chain homologues (C_{27} – C_{31}) with a maximum at $n\text{-}C_{29}$ and a marked odd over even predominance, indicating a significant contribution of epicuticular waxes.¹¹ The values of the *CPI* (carbon preference index) and *OEP* 2 (odd–even predominance) range between 3.21–5.61 and 3.24–6.30, respectively (Table IV), which are in accordance with the low rank of the lignites.

TABLE IV. Values of parameters calculated from distributions and abundances of n -alkanes, isoprenoids and terpenoids

Coal seam	Sample	CPI ^a	OEP 1 ^b	OEP 2 ^c	Pr/Ph ^d	Di/(Di+Tri) ^e
II	1	3.23	0.89	3.58	0.27	0.66
	2	5.24	1.65	4.57	0.38	0.84
	3	4.37	0.94	3.36	1.20	0.99
	4	5.08	0.92	5.13	1.26	0.95
III	5	4.36	1.65	4.39	0.41	0.97
	6	N.D. ^f	N.D.	N.D.	N.D.	0.99
	7	4.97	1.40	6.30	0.08	0.96
	8	3.21	1.25	3.75	N.D.	0.99
	9	3.92	1.89	3.24	N.D.	0.88
	10	5.61	5.50	4.52	0.62	0.62

^aCarbon preference index determined for the full distribution of n -alkanes C_{23} – C_{33} (mass chromatogram m/z 71), $CPI = 1/2[\Sigma \text{odd}(n\text{-}C_{23}\text{--}n\text{-}C_{33})/\Sigma \text{even}(n\text{-}C_{22}\text{--}n\text{-}C_{32}) + \Sigma \text{odd}(n\text{-}C_{23}\text{--}n\text{-}C_{33})/\Sigma \text{even}(n\text{-}C_{24}\text{--}n\text{-}C_{34})]$; ^b $OEP\ 1 = 1/4[(n\text{-}C_{21}+6\ n\text{-}C_{23}+n\text{-}C_{25})/(n\text{-}C_{22}+n\text{-}C_{24})]$; ^c $OEP\ 2 = 1/4[(n\text{-}C_{25}+6\ n\text{-}C_{27}+n\text{-}C_{29})/(n\text{-}C_{26}+n\text{-}C_{28})]$; ^dPr/Ph = pristane/phytane; ^eDi/(Di+Tri) = Σ aromatic diterpenoids/(Σ aromatic diterpenoids + Σ aromatic triterpenoids), calculated from the TIC of aromatic fraction, Σ aromatic diterpenoids = (18-norabiet-6,8,11,13-tetraene + 19-norabiet-8,11,13-triene + 18-norabiet-8,11,13-triene + 2-methyl-1-(4'-methylpentyl)-6-isopropylnaphthalene + dehydroabietane + simonellite + retene + sempervirane + totarane + hibaene + ferruginol + 6,7-dehydroferruginol + 2-methylretene + 12-hydroxysimonellite + 16,17-bisnordehydroabietane + 16,17-bisnorSimonellite + 1,2,3,4-tetrahydrodoretere), Σ aromatic triterpenoids = (24,25-dinoroleana-1,3,5(10),12-tetraene + 24,25-dinoroleana-1,3,5(10),12,14-pentaene + 24,25-dinorursa-1,3,5(10),12-tetraene + 24,25-dinorlupa-1,3,5(10)-triene + pentamethyllocatahydrochrysene + pentamethyldecabhydrochrysene + 3,4,7,12a-tetramethyl-1,2,3,4,4a,11,12,12a-octahydrochrysene + 3,3,7,12a-tetramethyl-1,2,3,4,4a,11,12,12a-octahydrochrysene + 3,4,7-trimethyl-1,2,3,4-tetrahydrochrysene + 3,3,7-trimethyl-1,2,3,4-tetrahydrochrysene + 1,2,4a,9-tetramethyl-1,2,3,4,4a,5,6,14b-octahydropicene + 2,2,4a,9-tetramethyl-1,2,3,4,4a,5,6,14b-octahydropicene + 1,2,9-trimethyl-1,2,3,4-tetrahydropicene + triaromatic des-A-lupane); ^fnot determined due the absence of n -alkanes and isoprenoids

The mid-chain n -alkanes ($n\text{-}C_{21}$ – C_{25}), originating from vascular plants, microalgae, cyanobacteria, sphagnum and aquatic macrophytes,^{32–34} are present in a lower amount in comparison with the long-chain homologues. The slight predominance of odd over even carbon-numbered n -alkanes in the mid-range n -alkanes (parameter *OEP* 1; Table IV) in the samples from coal seam III suggests a microbial origin. Moreover, the relatively high abundance of C_{23} and C_{25} n -alkane homologues implies an input of aquatic macrophytes to the organic matter.

Short chain n -alkanes (< $n\text{-}C_{20}$) are found mostly in algae and microorganisms.¹¹ In the studied lignites, short chain n -alkanes are absent or present in low quantities (Fig. 4a), which is consistent with the results of the maceral analysis (low liptinite content; Table II).



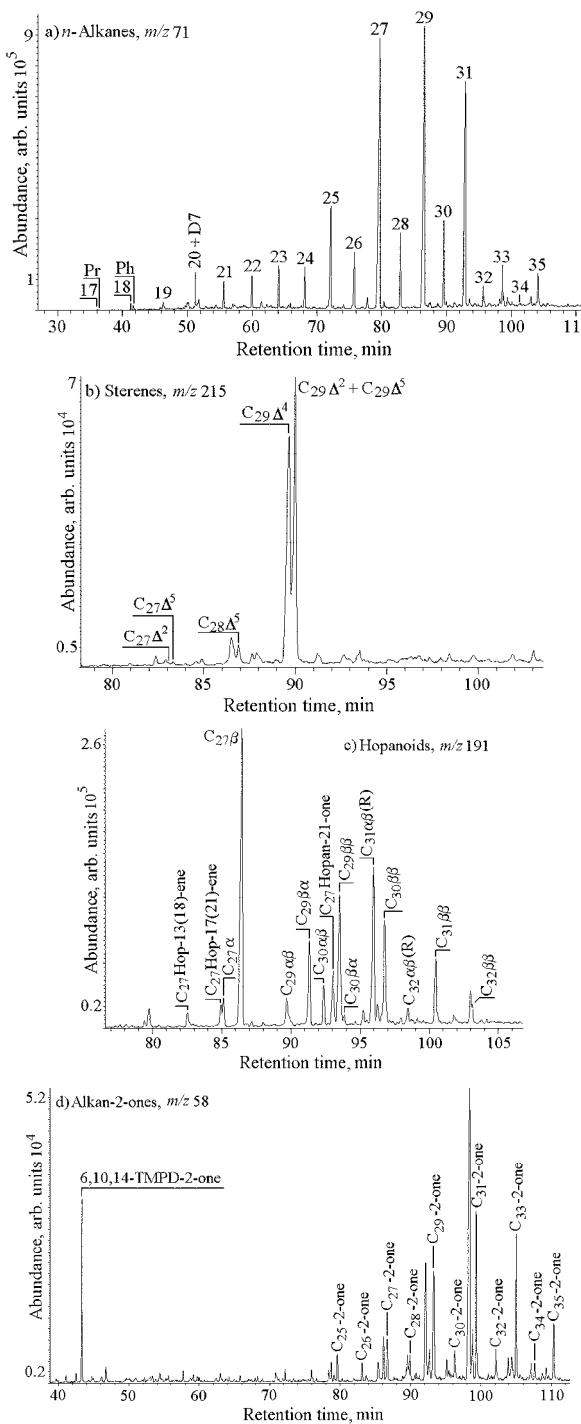


Fig. 4. GC-MS Mass chromatograms of *n*-alkanes, m/z 71 (a), sterenes, m/z 215 (b), hopanoids, m/z 191 (c) and alkan-2-ones, m/z 58; d) typical for the investigated samples 6,10,14-TMPD-2-one – 6,10,14-trimethylpentadecan-2-one; for other peak assignments, see the legend to Fig. 2.

The isoprenoids pristane (Pr) and phytane (Ph) are present in Drmno lignites in low amounts or are not identified (Fig. 2; Table IV). Low concentrations of pristane and phytane are often reported in immature organic matter.^{35–37} This is probably related to the fact that isoprenoid precursors incorporate into the macromolecular kerogen matrix either by esterification³⁸ or natural sulphurization³⁹ during early diagenesis and the release of saturated isoprenoids occurs after the thermal maturity of the organic matter increases.³⁷ The Pr/Ph ratio is widely used as indicator for the *Eh* settings of the depositional environment. However, this parameter is known to be also affected by maturation.¹¹ For this sample set, the influence of maturity on the pristane/phytane ratios can be ruled out. Therefore, the Pr/Ph ratio varying between 0.08 and 1.26 (Table IV) may be considered as an indicator of changing of Eh settings from anoxic to slightly oxic during peat deposition in the Drmno seam.⁴⁰ This result is consistent with the variations in the *TPI* and *GI* parameters.

Sesquiterpenoids, diterpenoids and triterpenoids with a non-hopanoid skeleton. In all samples, aromatic sesquiterpenoids were observed in low quantities (Fig. 3). Cadalene predominates over isocadalene, calamenene and 5,6,7,8-tetrahydrocadalene. Other sesquiterpenoid constituents of the lignite extracts are cuparene and cadina-1(10),6,8-triene, whereas dihydro-ar-curcumene, 1-methyl-7-isopropyltetrahydronaphthalene and 1-methyl-7-isopropynaphthalene (eudalene) were identified only in two samples. Sesquiterpenoids are used as markers for higher land plants. However, sesquiterpenoid biomarkers are often not useful for an unambiguous determination of the precursor plant community,^{25,41,42} with exception of cuparene, the presence of which clearly indicates a contribution of *Cupressaceae*, a family of gymnosperms, to the precursor OM.^{43,44}

Diterpenoids are the main constituents of both the saturated and aromatic fraction, indicating a significant contribution of gymnosperms to the precursor OM. Pimarane and particularly 16 α (H)-phyllocladane are dominant by far in the saturated fractions. Other diterpenoid-type constituents of the saturated fraction are norpimarane, norabietane, beyerane, 16 α (H)-kaurane, isopimaradiene, iso-phyllocladene and abietane (Fig. 2). The high amount of 16 α (H)-phyllocladane indicates that the coal forming plants belonged to the conifer families *Taxodiaceae*, *Podocarpaceae*, *Cupressaceae*, *Araucariaceae* and *Phyllocladaceae*, while the high abundance of pimarane suggests *Pinaceae*, *Taxodiaceae* and *Cupresaceae*.^{41,43,45,46}

The aromatic diterpenoids consist of norabieta-6,8,11,13-tetraenes, norabieta-8,11,13-trienes, 2-methyl-1-(4'-methylpentyl)-6-isopropynaphthalene, 16,17-bisnordehydroabietane, dehydroabietane, simonellite, retene, sempervirane, totarane, hibaene, ferruginol, 6,7-dehydroferruginol, 12-hydroxysimonellite, 16,17-bisnorsimonellite and 2-methylretene. Simonellite is the predominant aromatic



diterpenoid, with the exception of two samples in which the most prominent are dehydroabietane and retene, respectively (Fig. 3).

Almost of all the aromatic diterpenoids are non-specific conifer markers, because they are the diagenetic products of a great variety of abietane-type precursors that are common constituents of all conifers except *Phyllocladaceae*.^{41,46,47} In contrast, the presence of cuparene, ferruginol, totarane and hinbaene in the aromatic fraction of the Drmno lignite extracts clearly indicates the contribution of *Cupressaceae*, *Taxodiaceae*, *Podocarpaceae* and *Araucariaceae* to the precursor biomass,⁴³ which is consistent with the observation derived from the analysis of the saturated diterpenoids.

The non-hopanoid triterpenoids are present in relatively low amounts in the saturated fraction of the Drmno lignites and consist of olean-12-ene, olean-13,18-ene, des-A-oleanenes, des-A-ursenes and des-A-lupane. A marked domination of des-A-ring degraded compounds is observed, and only in two samples were non-degraded oleanenes identified (Fig. 2).

Although the non-hopanoid triterpenoids represent a minor component of the saturated fraction, these compounds are slightly more abundant in the aromatic fraction of the coal extracts (Fig. 3). This result shows that angiosperms also contributed to the organic matter. The higher abundance of aromatized in comparison to non-aromatized angiosperm triterpenoids indicates significant aromatization of the triterpenoids during diagenesis. The same result that aliphatic angiosperm-derived triterpenoids are more easily altered to aromatic derivatives, in comparison with gymnosperm-derived diterpenoids, resulting in the selective loss of such aliphatic compounds, was also reported by Kalkreuth *et al.* (1998)⁴⁸ and Nakamura *et al.* (2010).⁴⁹

All samples contain des-A-ring degraded aromatic triterpenoids, represented by tetramethyloctahydrochrysene and trimethyltetrahydrochrysene. In four samples (1, 2, 9 and 10), which have generally higher amounts of triterpenoids (see next paragraph and Table IV), in addition to the des-A-ring degraded aromatic triterpenoids, pentacyclic aromatic triterpenoids (ring-A-monoaromatic triterpenoids, tetramethyloctahydriopinene and trimethyl-tetrahydriopinene) were also identified. Degradation of the A-ring of triterpenoids followed by intensive aromatization suggests microbial activity, which is consistent with relatively abundant hopanoids (Figs. 2 and 3).

In order to estimate the contribution of gymnosperm and angiosperm vegetation in the ancient peat bogs, the ratio of diterpenoid and angiosperm-derived triterpenoid aromatic biomarkers ($\text{Di}/(\text{Di}+\text{Tri})$) was used, Table IV). The values of this parameter show the dominant role of gymnosperms for peat formation in the Drmno field. The lower values of $\text{Di}/(\text{Di}+\text{Tri})$ ratio in upper part of upper seam (samples 1 and 2) and lower part of lower seam (samples 9 and 10), indicate the higher contribution of angiosperms to precursor biomass (Table IV). This result

implies changes in palaeoenvironment in the mire during coal formation, consistent with conclusions derived from the TPI, the GI and the Pr/Ph ratio.

Steroids and hopanoids. The analysis of the aliphatic fraction revealed low contents of steroids (Fig. 2). Steroid biomarkers (based on the *m/z* 215 mass chromatogram of the saturated fraction; Fig. 4b) consist predominantly of C₂₉ Δ⁴-, Δ²- and Δ⁵-sterenes. C₂₈-sterenes (Δ⁴-, Δ²- and Δ⁵) were identified in low amounts, whereas the corresponding C₂₇ homologues are present in several samples. The marked predominance of C₂₉ sterenes (Fig. 4b; Table V) clearly indicates peat formation from terrigenous plants.

TABLE V. Values of parameters calculated from the distributions and abundances of steroids and hopanoids

Coal seam	Sample	% C ₂₇ ^a	% C ₂₈ ^b	% C ₂₉ ^c	Ster Hop ^d	C ₃₀ ββ (ββ+aβ) ^e
II	1	2.30	6.44	91.25	0.07	0.80
	2	2.43	5.28	92.29	0.08	0.72
	3	0.00	0.00	100.00	0.17	0.53
	4	4.55	3.00	92.45	0.11	0.90
	5	1.45	5.93	92.62	0.24	0.70
	6	N.D. ^f	N.D.	N.D.	N.D.	N.D.
III	7	1.07	3.59	95.34	0.25	0.87
	8	0.00	15.94	84.06	0.22	0.84
	9	0.26	6.00	93.74	0.18	0.77
	10	0.00	3.04	96.96	0.09	0.78

^a%C₂₇ = 100C₂₇(Δ² + Δ⁴ + Δ⁵)-sterenes/Σ(C₂₇–C₂₉)(Δ² + Δ⁴ + Δ⁵)-sterenes; ^b%C₂₈ = 100C₂₈(Δ² + Δ⁴ + Δ⁵)-sterenes/Σ(C₂₇–C₂₉)(Δ² + Δ⁴ + Δ⁵)-sterenes; ^c%C₂₉ = 100C₂₉(Δ² + Δ⁴ + Δ⁵)-sterenes/Σ(C₂₇–C₂₉)(Δ² + Δ⁴ + Δ⁵)-sterenes; ^dSter/Hop = [Σ(C₂₇–C₂₉)(Δ² + Δ⁴ + Δ⁵)-sterenes]/[Σ(C₂₉–C₃₂)17α(H)21β(H)-hopanes + Σ(C₂₉–C₃₀)17β(H)21α(H)-hopanes + Σ(C₂₉–C₃₁)17β(H)21β(H)-hopanes + C₂₇17α(H)-hopane + C₂₇17β(H)-hopane + Σ(C₂₉–C₃₀)-hop-17(21)-enes + C₂₇-hop-17(21)-ene + C₂₇-hop-13(18)-ene]; ^eC₃₀ββ/(ββ+aβ) = C₃₀17β(H)21β(H)-hopane/(C₃₀17β(H)21β(H)-hopane + C₃₀17α(H)21β(H)-hopane). The sterenes were quantified from the *m/z* 215 mass chromatogram, and the hopenes and hopanes from the *m/z* 191 mass chromatogram; ^fnot determined due to the absence of sterenes and hopanes

Hopanoids are more abundant than steroid biomarkers in the Drmno lignite extracts (Ster/Hop ratio < 0.25; Table V). This result indicates a bacteria-influenced facies and argues for the role of microorganisms in the degradation of plant tissue.

Based on the *m/z* 191 mass chromatogram of the saturated fraction, the hopane composition in all samples is characterized by the presence of 17α(H)21β(H), 17β(H)21α(H) and 17β(H)21β(H) compounds with 27 and 29–31 carbon atoms, with exception of C₃₁17β(H)21α(H) moretane. Other hopanoid-type constituents of the saturated fraction are C₂₇ hop-13(18)-ene, C₂₇ hop-17(21)-ene and C₂₇hopan-21-one. Several samples contain C₃₂αβ(R)-hopane and C₃₀ hop-17(21)-ene (Fig. 4c).



The presence of unsaturated hopenes and the domination of $\beta\beta$ -isomers in range C₂₇, C₂₉–C₃₀ over $\alpha\beta$ -hopanes confirm an immature stage of the organic matter. The ratio of 17 $\beta(H)21\beta(H)$ to (17 $\beta(H)21\beta(H)$ + 17 $\alpha(H)21\beta(H)$) C₃₀-hopanes (Table V) is within the limits established for lignite, 0.5–0.7,⁵⁰ or even higher, consistent with deposition of the OM in an anoxic to slightly oxic environment.⁵¹

The C₂₇17 $\beta(H)$ -hopane and the C₂₉17 $\beta(H)21\beta(H)$ -hopane dominate the distribution of C₂₇–C₃₁ $\beta\beta$ -homologues (Fig. 4c). The predominance of the short-chain homologues can be interpreted as being indicative of rather oxidizing palaeoconditions, but may also indicate that the precursor hopanoid lipids were functionalized at position 29, such as aminobacteriohopanepentol that is abundant in methanotrophic bacteria (*e.g.*, *Methylococcus capsulatus* or *Methyloimonas methanica*).⁵² This particular hopanoid functionalized at position 29 cannot, however, be taken as the exclusive precursor of C₂₉ hopanes, considering the high sensitivity of the side chains from biologic hopanoids.⁵³

The identification of the D-ring monoaromatic hopanes, 7-methyl-3'-ethyl-1,2-cyclopentanochrysene and 4-methyl-24-ethyl-19-norcholesta-1,3,5(10)-triene¹⁰ in the aromatic fraction of all the investigated samples (Fig. 3) suggests partial aromatization of the hopanoids and steroids during diagenesis, in accordance with the aromatization of the diterpenoids and particularly the triterpenoids.

Alkan-2-ones. Based on the *m/z* 58 mass chromatogram of the aromatic fraction (Fig. 4d), *n*-alkan-2-ones were identified in the range C₂₅ to C₃₅, with the even C₂₆–C₃₀ homologues being absent in several samples. Similar to the distribution of the *n*-alkane, the *n*-alkan-2-ones patterns of the coal samples are dominated by odd long-chain homologues C₂₉–C₃₃. Although the distributions of the *n*-alkanes and the *n*-alkanones are generally similar, two main differences could be seen. First, even C₂₆–C₃₀ homologues of *n*-alkan-2-ones are absent in several samples, although *n*-alkanes with the same number of carbons were identified. Secondly, in almost all of the samples, *n*-alkanes have maximum at C₂₉, followed by C₂₇, whereas the most abundant *n*-alkan-2-one is C₃₁ followed by C₃₃. The obtained results indicate that *n*-alkan-2-ones probably have few sources: a) the direct contribution of ketones from higher plant waxes, which consist of C₂₃–C₃₃ homologues with a significant odd C number predominance and C_{max} at C₂₉ or C₃₁; b) microbially mediated β -oxidation of the corresponding *n*-alkanes in the sediments or prior to incorporation into the sediments; c) oxidative decarboxylation of *n*-fatty acids and oxidized alcohols as well as elongation of a suitable fatty acid precursor and subsequent decarboxylation, which would yield longer-chain alkanones with a pronounced odd C predominance and C₂₇, C₂₉ and C₃₁ as major constituents.²⁶



In addition to *n*-alkan-2-ones, 6,10,14-trimethylpentadecan-2-one (6,10,14-TMPD-2-one), an isoprenoidal ketone, was also found in half of the studied samples (Fig. 4d). Since pristane was identified in low amounts, it could be supposed that the main pathways of TMPD-2-one formation are bacterial degradation³⁸ and photosensitized oxidation⁵⁴ of free phytol and/or photodegradation of chlorophyll-*a*.⁵⁵

The presence of alkan-2-ones in the lignite extracts confirms microbial activity, assumed also basis on the distribution of hopanoids and angiosperm derived triterpenoids.

CONCLUSIONS

The origin and geological evolution of organic matter of upper Miocene lignites from the Drmno field, Kostolac Basin (Serbia) were evaluated using coal petrology and the composition of biomarkers.

Coal from the Drmno field is typical humic coal. The composition of the biomarkers shows that the peat-forming vegetation dominated by decay resistant gymnosperm plants, followed by prokaryotic organisms and angiosperms. Based on the composition of the saturated and aromatic diterpenoids, it was established that the coal forming plants belonged to the gymnosperm families *Taxodiaceae*, *Podocarpaceae*, *Cupressaceae*, *Araucariaceae*, *Phyllocladaceae* and *Pinaceae*.

Peatification was performed in a limnic, neutral to slightly acidic environment. The variations in the maceral and biomarker ratios showed that the lignite seams were formed under variable *Eh* conditions (anoxic to slightly oxic), probably as a result of seasonal drying of the mire. The water column level was lower in coal seam II than in coal seam III during peatification. Changes in the water level also caused vegetation differences in the palaeoplant communities.

Group organic geochemical parameters and biomarker compositions indicate low OM maturity (phase of intensive diagenetic processes). The abundance of hopanoid biomarkers, intensive degradation of the A-ring of triterpenoids followed by aromatization and the presence of alkan-2-ones indicate that the diagenetic changes in the organic matter were mainly governed by bacterial activity, rather than thermal degradation.

Acknowledgements. This study was financed by the Ministry of Education, Science and Technological Development of the Republic of Serbia (Project No. 176006). We are also grateful to the anonymous reviewers.

И З В О Д

ЛИГНИТИ ЛЕЖИШТА ДРМНО (БАСЕН КОСТОЛАЦ): ПОРЕКЛО И ПАЛЕОУСЛОВИ
СТВАРАЊА НА ОСНОВУ ПЕТРОГРАФСКИХ И ОРГАНСКО-ГЕОХЕМИЈСКИХ
ИСТРАЖИВАЊА

КСЕНИЈА СТОЈАНОВИЋ¹, ДРАГАНА ЖИВОТИЋ², АЛЕКСАНДРА ШАЈНОВИЋ³, ОЛГА ЦВЕТКОВИЋ³,
HANS PETER NYTOFT⁴ и GEORG SCHEEDER⁵

¹Хемијски факултет Универзитета у Београду, Студентски трг 12–16, 11000 Београд, ²Рударско-геолошки факултет Универзитета у Београду, Ђушина 7, 11000 Београд, ³Центар за хемију ИХТМ, Универзитет у Београду, Студентски трг 12–16, 11000 Београд, ⁴Geological Survey of Denmark and Greenland, Øster Voldgade 10, DK-1350 Copenhagen, Denmark и ⁵Federal Institute for Geosciences and Natural Resources, Steinbogen 2, 30655 Hannover, Germany

Циљ рада био је да се утврди порекло и геолошка еволуција лигнита лежишта Дрмно басена Костолац. Примењене су петрографске и органско геохемијске методе. Лигнити лежишта Дрмно су типични хумусни угљеви. Главни извор органске супстанце биле су гимносперме (голосеменице), а затим прокариотски организми и ангиосперме (скривеносеменице). Утврђено је да прекурсорски органски материјал потиче од следећих фамилија гимносперми: *Taxodiaceae*, *Podocarpaceae*, *Cupressaceae*, *Araucariaceae*, *Phyllocladaceae* и *Pinaceae*. Таложење и хумификација органске супстанце лигнита одвијали су се у слатководној, неутралној до слабо киселој средини. Узимајући у обзир да се стварање лигнита у лежишту Дрмно одигравало у исто време, претпостављено је да климатски фактор није могао значајније утицати на састав органске супстанце. Разлике у саставу маџерала и биомаркера у испитиваним лигнитима последица су колебања нивоа воденог стуба у средини таложења услед сезонских промена у количини падавина. Ово колебање воденог стуба узроковало је промене како у саставу палеовегетације, тако и у редокс потенцијалу средине таложења (од аноксичне до благо оксичне). Дијагентске промене органске супстанце одвијале су се уз интензивну микробну активност, док је термичка деградација била готово беззначајна.

(Примљено 26. новембра 2011, ревидирано 17. фебруара 2012)

REFERENCES

- W. Kalkreuth, T. Kotis, C. Papanikolaou, P. Kokkinakis, *Int. J. Coal Geol.* **17** (1991) 51
- A. Bechtel, R. Gratzer, R. F. Sachsenhofer, *Int. J. Coal Geol.* **46** (2001) 27
- A. Bechtel, M. Markic, B. Jelen, R. F. Sachsenhofer, R. Gratzer, A. Lücke, W. Püttmann, *Int. J. Coal Geol.* **57** (2004) 23
- D. Životić, B. Jovančićević, J. Schwarzbauer, O. Cvetković, I. Gržetić, M. Ercegovac, K. Stojanović, A. Šajnović, *Int. J. Coal Geol.* **81** (2010) 227
- A. Bechtel, R. F. Sachsenhofer, I. Kolcon, R. Gratzer, A. Otto, W. Püttmann, *Int. J. Coal Geol.* **51** (2002) 31
- A. Bechtel, R. F. Sachsenhofer, R. Gratzer, A. Lücke, W. Püttmann, *Org. Geochem.* **33** (2002) 1001
- A. Zdravkov, A. Bechtel, R. F. Sachsenhofer, J. Kortenski, R. Gratzer, *Org. Geochem.* **42** (2011) 237
- P. A. Philp, R. Ishiwatari, *Org. Geochem.* **20** (1993) 867
- J. Yang, P. G. Stansberry, J. W. Zondlo, A. H. Stiller, *Fuel Process. Technol.* **79** (2002) 207
- R. P. Philp, *Fossil Fuel Biomarkers. Applications and Spectra*. Elsevier, Amsterdam, The Nederlands, 1985, pp. 12–33, 188, 259



11. K. E. Peters, C.C. Walters, J. M. Moldowan, *The Biomarker Guide, Vol. 2: Biomarkers and Isotopes in the Petroleum Exploration and Earth History*, Cambridge University Press, Cambridge, UK, 2005, p. 483–486, 499–500
12. http://www.seea.gov.rs/Downloads/karticeProjekata/Elaborat_Nacionalni_Izvestaj.pdf (last accessed August, 2012)
13. <http://www.smeits.rs/include/data/docs0066.doc> (last accessed August, 2012)
14. R. Jelenković, A. Kostić, D. Životić, M. Ercegovac, *Geol. Carpathica* **59** (2008) 345
15. Z. Milićević, M. Šaban, B. Jovančićević, J. Nedeljković, *J. Serb. Chem. Soc.* **61** (1996) 823
16. G. Dević, B. Jovančićević, *Acta Geol. Sin.* **82** (2008) 1168
17. A. Kostić, *Conceptions and methodology of petroleum exploration on the example of the Drmno Depression*, MSc Thesis, Faculty of Mining and Geology, University of Belgrade, Serbia, 1995, p. 160–167 (in Serbian)
18. S. Milošević, R. Miletić, in: *Geology of Serbia, Fossil fuels, VII*, V. Aksin, B. Maksimović, Eds., Faculty of Mining and Geology, University of Belgrade, Serbia, 1975, p. 144–149 (in Serbian)
19. D. Životić, *Petrography and quality of coal from the Kostolac Basin and its energetic potential*, MSc Thesis, Faculty of Mining and Geology, University of Belgrade, Serbia, 2001, p. 29–49 (in Serbian)
20. M. Ercegovac, *First proposal of the classification and the codification of the low-rank coals of Serbia*, Faculty of Mining and Geology, University of Belgrade, Belgrade, Serbia, 1998, p. 12–40 (in Serbian).
21. I. Sykorova, W. Pickel, K. Christianis, M. Wolf, G. H. Taylor, D. Flores, *Int. J. Coal Geol.* **62** (2005) 85
22. ISO 1171, Solid mineral fuels – Determination of ash content (1997), International Organization for Standardization http://www.techstreet.com/standards/iso/1171_1997?product_id=232633 (last accessed August, 2012)
23. S. G. Wakeham, C. Schaffner, W. Giger, *Geochim. Cosmochim. Acta* **44** (1980) 415
24. S. Stout, *Org. Geochem.* **18** (1992) 51
25. A. Otto, B. R. T. Simoneit, *Org. Geochem.* **33** (2002) 1241
26. J. Tuo, Q. Li, *Appl. Geochem.* **20** (2005) 553
27. C. F. K. Diessel, *On the correlation between coal facies and depositional environments*, in *Proceedings of the 20th Newcastle Symposium “Advances in the Study of the Sydney Basin”*, (1986), Newcastle, N.S.W., Australia, 1986, p. 19
28. M. Ercegovac, D. Pulejković, *Ann. Géol. Péninsule Balkanique* **55** (1991) 223
29. J. Dehmer, *Int. J. Coal Geol.* **28** (1995) 111
30. A. Bechtel, M. Hámor-Vidó, R. F. Sachsenhofer, D. Reischenbacher, R. Gratzer, W. Püttmann, *Int. J. Coal Geol.* **72** (2007) 33
31. D. J. Casagrande, in *Coal and Coal-Bearing Strata: Recent Advances*, A.C. Scott, Ed., Geol. Soc. Spec. Publ., London, UK, 1987, p. 87
32. G. I. Matsumoto, M. Akiyama, K. Watanuki, T. Torii, *Org. Geochem.* **15** (1990) 403
33. C. J. Nott, S. Xie, L. A. Avsejs, D. Maddy, F. M. Chambers, R. P. Evershed, *Org. Geochem.* **31** (2000) 231
34. K. J. Ficken, B. Li, D. L. Swain, G. Eglinton, *Org. Geochem.* **31**, (2000) 745
35. L. I. P. Dzou, R. A. Noble, J. T. Senftle, *Org. Geochem.* **23** (1995) 681
36. W. B. Hughes, A. G. Holba, L. I. P. Dzou, *Geochim. Cosmochim. Acta* **59** (1995) 3581
37. T. T. A. Vu, K. G. Zink, K. Mangelsdorf, R. Sykes, H. Wilkes, B. Horsfield, *Org. Geochem.* **40** (2009) 963



38. P. W. Brooks, J. R. Maxwell, R. L. Patience, *Geochim. Cosmochim. Acta* **42** (1978) 1175
39. S. C. Brassell, C. A. Lewis, J. W. de Leeuw, F. de Lange, J. S. Sininghe Damste, *Nature* **320** (1986) 160
40. B. M. Didyk, B. R. T. Simoneit, S. C. Brassell, G. Eglinton, *Nature* **272** (1978) 216
41. A. Otto, H. Walther, W. Püttmann, *Org. Geochem.* **26** (1997) 105
42. B. G. K. van Aarsen, H. C. Cox, P. Hoogendoorn, J. W. de Leeuw, *Geochim. Cosmochim. Acta* **54** (1990) 3021
43. A. Otto, V. Wilde, *Bot. Rev.* **67** (2001) 141
44. M. R. Haberer, K. Mangelsdorf, H. Wilkes, B. Horsfield, *Org. Geochem.* **37** (2006) 519
45. M. Stefanova, D. R. Oros, A. Otto, B. R. T. Simoneit, *Org. Geochem.* **33** (2002) 1079
46. M. Stefanova, K. Markova, S. Marinov, B. R. T. Simoneit, *Bull. Geosci.* **80** (2005) 93
47. A. Otto, B. R. T. Simoneit, *Geochim. Cosmochim. Acta* **65** (2001) 3505
48. W. Kalkreuth, C. Keuser, M. Fowler, M. Li, D. McIntyre, W. Püttmann, R. Richardson, *Org. Geochem.* **29** (1998) 799
49. H. Nakamura, K. Sawada, M. Takahashi, *Org. Geochem.* **41** (2010) 975
50. A. S. Mackenzie, R. L. Patience, J. R. Maxwell, in *Origin and Chemistry of Petroleum*, G. Atkinson, J. J. Zuckermann, Eds., Pergamon Press, Oxford, UK, 1981, p. 1
51. L. Marynowski, M. Zatón, *Appl. Geochem.* **25** (2010) 933
52. S. Neunlist, M. Rohmer, *Biochem. J.* **231** (1985) 635
53. R. Y. P. Burhan, J.M. Trendel, P. Adam, P. Wehrung, P. Albrecht, A. Nissenbaum, *Geochim. Cosmochim. Acta* **66** (2002) 4085
54. J.-F. Rontani, P. J.-P. Giral, *Int. J. Environ. Anal. Chem.* **42** (1990) 61
55. J.-F. Rontani, G. Baillet, C. Aubert, *J. Photochem. Photobiol., A* **59** (1991) 369.

